Degradation of Emerging Micropollutants by Combined Advanced Oxidation with Immobilized Plasmon Titanium Dioxide Nanocomposites in an Electrohydraulic Discharge Reactor

Report to the
Water Research Commission

by

LF Petrik, OO Fatoba, JO Tijani, P Nyamukamba, E Mouele, LTichagwa

Environmental and Nano Sciences Group, Department of Chemistry,
University of the Western Cape, South Africa

WRC Report No. 2364/1/18
ISBN 978-0-6392-0036-1

September 2018

Obtainable from
Water research Commission
Private Bag X03
GEZINA, 0031

orders@wrc.org.za or download from www.wrc.org.za

Printed in the Republic of South Africa

EXECUTIVE SUMMARY

BACKGROUND

The production and use of chemically manufactured products have increased significantly due to the rapid population growth, industrialization and, of course, extensive agricultural activities. These activities are responsible for the presence and accumulation of different recalcitrant organic compounds in the environment. One class of compounds currently identified and detected in the global water cycle is endocrine disrupting compounds (EDCs). Among the EDCs, phenolic compounds such as bisphenol-A and nitrophenols have become a subject of considerable environmental concern and a public health issue. Emerging micropollutants such as dyes, or bisphenol-A and 2-nitrophenol present a great threat in drinking and wastewater due to their adverse health effects on living organisms. Most conventional technologies in water and wastewater treatment are not designed to eliminate these xenobiotics, instead pollutants are merely transferred from one phase to another (liquid to solids). Titanium (IV) oxide has continued to attract considerable and diverse interest in the field of material science as a result of its promising photocatalytic activity in the area of wastewater purification and destruction of microbes and organic pollutants in water. Unfortunately, the photosensitivity and photocatalytic activity of TiO_2 is limited as a consequence of its relatively high band gap energy (3.2 eV for anatase) and lower ultraviolet range of 400 nm. Apart from this, the post-separation and recovery of the powdered, used TiO_2 photocatalyst from wastewater after treatment remains a major hurdle which increases the overall capital and running cost of the treatment. In order to overcome these challenges, it becomes imperative to synthesize supported, composite semiconductor catalytic materials with a band gap capable of utilizing the photons in the visible light range or that are able to prevent recombination of the hole and electron pair in order to achieve high photon efficiency, in composite, stabilized format.

OBJECTIVES

The objectives of the project were as follows:

1. To synthesize and characterize novel immobilized Ag-TiO_2, and plasmon enhanced TiO_2 composite photocatalyst for water treatment.
2. To apply the combined synthesized Ag-immobilized or plasmon enhanced TiO_2 composites and electrohydraulic discharge reactor to degrade pharmaceutical and personal care products, antiscalants and endocrine disruption compounds in contaminated/wastewater.
3. To assess the removal efficiencies of the PPCPs, antiscalants and EDCs by the combined plasmon or Ag immobilised TiO_2 nanocomposites and electrohydraulic discharge reactor.
4. To evaluate the degradation of these micro pollutants and the antiscalants using the combined plasmon or Ag doped titania nano composites and electrohydraulic discharge reactor.

5. To determine the effect of interaction time, pH of the solution and dosage of the catalyst in the electrohydraulic discharge reactor on the effectiveness of degradation.
6. To establish the degradation mechanism of the reaction using immobilised nanocomposites and propose a kinetic model through kinetic study.
7. To determine the scalability of the combined advanced oxidation system for treating effluents contaminated with PPCPs, EDCs and antiscalants.

METHOD

Because of these limitations stated above, the aims of this study were to immobilize the photocatalyst TiO_2 on different supports, namely stainless steel mesh or fused silica, whilst also doping the photocatalyst with plasmonic metals, either to lower the recombination rate, or to alter the band gap in order to increase the absorption threshold into the visible region. The research approach for immobilization of the photocatalyst on a stainless steel mesh was to use the sol-gel method to coat TiO_2 precursors on a stable, stainless steel mesh support followed by calcination of the gel-coated support at various temperatures and times, where after different amounts of Ag were deposited on the TiO_2 supported nanocrystals via a thermal evaporation technique. The thickness of deposited Ag layers on TiO_2 was in the range of 5-15 nm.

Furthermore, in the case of a fused silica support, thin films of copper and silver of various thicknesses (5-25 nm) were deposited on 3-mercaptopropyltrimethoxysilane (MPTMS) coated, fused silica using a thermal evaporation technique. A 100 nm film of titanium dioxide (TiO_2) was either deposited before or after, on or underneath, the plasmonic metal films using a sputter coating technique. QPod.exe software was used for the film thickness determination. Bimetallic films were also prepared using the same procedure. The metal films were deposited one at a time, layer by layer. The use of a bilayer system and the effect of order of deposition were also investigated.

High Resolution Scanning Electron Microscopy (HRSEM) and High Resolution Transmission Electron Microscopy (HRTEM) were used to analyse the size, morphology and composition of the supported nanomaterials. Fourier Transform Infrared Spectroscopy (FTIR) was utilized to identify functional groups in the synthesised materials. Selected Area Electron Diffraction (SAED), Ultraviolet-vis (UV-vis)/diffuse reflectance spectroscopy and X-ray diffraction (XRD) were used to determine the crystalline nature and phases as well as the band gap of the synthesized material. Rutherford backscattering spectrometry (RBS) showed the geometric dispersion of the doped metals.

RESULTS

In the case of the fused silica supported photocatalytic composites, the effect of plasmonic metal film thickness, order of deposition and the use of bimetallic layers on the photocatalytic activity of the TiO_2 photocatalyst under UV light of wavelength 254 nm or sunlight was evaluated using methyl orange as a model pollutant. It was shown that the increase in Ag film thickness underneath the TiO_2 layer increased the photocatalytic activity of the TiO_2 photocatalyst until an optimum film thickness of 20 nm was attained. The thicker the Ag metal film,

the better was the displacement of the electrons to lower layers of the metal film. This implies that there are more chances of the electrons to be far from the TiO_2 photocatalyst layer where electron holes are confined. Hence, the charge separation is better when compared with thin metal films and recombination is prevented. This would result in the surface of TiO_2 being enriched with holes which can directly degrade methyl orange and oxidize water to produce hydroxyl radicals that degrade organics effectively. In the case of copper, the increase in film thickness led to reduced photocatalytic activity. Silver was found to be a better plasmonic metal than copper in enhancing the photocatalytic activity of TiO_2 under UV light illumination. Cu was found to perform better when deposited underneath the TiO_2 film whereas Ag performed better when deposited on top of the TiO_2 photocatalyst film.

The use of bimetallic layers was found to enhance TiO_2 photocatalytic activity more than monometallic layers. Activity under solar irradiation was lower than under UV radiation showing that the plasmonic metals mainly acted to reduce the recombination rate of holes and electrons, not to lower the band gap. The reason for the observed increase in photocatalytic activity of the metal coated TiO_2 photocatalyst under UV irradiation is ascribed to the Schottky barriers formed between the TiO_2 and the Ag nanoparticles. These barriers may facilitate the transfer of electrons from TiO_2 nanoparticles with high Fermi level to silver nanoparticles which have a low Fermi level, resulting in reduced electron-hole recombination rates.

In the case of the stainless steel mesh supported composites, the XRD patterns and HRTEM micrograph showed that the supported carbon doped TiO_2 catalyst developed upon the support by thermal treatment of the 8%PAN/DMF/$TiCl_4$ sol gel precursor was highly polycrystalline with anatase structure. The crystallite size of the synthesized TiO_2 nanomaterial as calculated from XRD ranged from 4.9 to 19.8 nm depending upon the applied thermal conditions where temperatures were increased at constant heating rate of 50 ºC/min and calcination was performed from 300ºC to 400ºC for between 1 to 4 hrs holding time. The peak intensity of TiO_2 nanoparticles remained the same and diffraction angles hardly changed despite depositing different amounts of Ag. Therefore, the anatase phase was retained and particle size did not change as such with an increase in Ag content.

Moreover, XPS data showed that the PAN precursor had carbon doped the photocatalyst during the calcination process applied during stabilization and that the carbon content could be controlled by the calcination time and temperature. The band gap energy (E_g) values of the supported TiO_2 nanoparticle were narrowed from 3.15 to 3.02 eV by deposition of Ag on the supported TiO_2 matrix. The deposition of Ag on TiO_2 prevented the recombination reaction as evidenced in the band gap energy value obtained. The present investigation has demonstrated that surface modification of sol-gel supported TiO_2 nanoparticles prepared thermally by calcination and coated with Ag via thermal evaporation of plasmonic metal is a viable route to achieve stable, supported composite plasmonic assisted TiO_2 photocatalysts.

The photocatalytic activity of the various synthesised composite photocatalysts supported upon stainless steel mesh was conducted under ultra-violet light irradiation (278 nm) using methylene blue (MB) as a model pollutant. The influence of solution pH, initial concentration of MB, calcination temperature on the photocatalytic efficiency of the synthesised catalysts was examined. The optimum catalyst was selected and the effect of addition of Ag onto TiO_2 upon the MB removal rate was further investigated. The results indicated that the

percentage MB removal decreased with increasing solution pH and initial concentration of MB. The study demonstrated that supported TiO_2 photocatalysts modified with Ag resulted in a higher photocatalytic activity than bare, supported TiO_2 nanocrystals. The concentration and percentage MB removed decreased with irradiation time in the following order: 10 nm Ag/TiO_2 > 5 nm Ag/TiO_2 > 15 nm Ag/TiO_2 > TiO_2. The addition of 10 nm layer of plasmonic Ag enhanced the MB removal rate by 13.3%. The increased photocatalytic activity was linked to the free electrons in metallic Ag which acted as electron trappers and supressed the electron-hole pair recombination rate and ultimately increased the surface hydroxyl radicals. The study demonstrated that surface modification of supported TiO_2 nanocrystals with plasmonic Ag is a viable route to achieve stable plasmonic assisted TiO_2 photocatalysts.

The plasmonic metal decorated TiO_2 photocatalyst sample (2 nm Ag on TiO_2/stainless steel mesh) applied in the photodegradation of methyl orange was also tested for its photocatalytic activity towards bisphenol-A (BPA) which is an endocrine disruptor. In this study, a dielectric barrier discharge (DBD) system and its combination with supported Ag doped TiO_2 photocatalyst, (2.4% Ag doped TiO_2 nanocomposites) were applied to decompose BPA or 2-NP as model pollutants in aqueous solution. The combined DBD with 2.4% Ag doped TiO_2 nanocomposites achieved 89% or 81% removal efficiency for BPA or 2-NP respectively after 80 min compared to 67.22% or 56.8% obtained while using the DBD system alone. This shows that the incorporation of supported Ag doped TiO_2 photocatalysts (JT14) in the DBD system, improved BPA or 2-NP removal efficiency by 21.8% and 24.2% respectively, compared to DBD alone. The photocatalyst degraded 61.86% of BPA after 300 minutes which was 23.99% lower when compared to methyl orange photodegradation (ca. 85.85%). The same trend was also observed using pure TiO_2 photocatalyst which degraded 47.10% of BPA which was 10.06% lower than that of methyl orange (ca. 57.16%). These results show that BPA is more difficult to degrade than methyl orange under the same conditions. Methyl orange had more electron withdrawing groups than BPA, and the azo bonds in the azo compounds are active and are more easily degraded.

The supported Ag loaded carbon doped catalyst could be reused due to maintenance of its crystalline nature and pure anatase polymorph after four repeated applications. The results obtained for the change of TOC in wastewater was rather low due to formation of intermediate, reaction byproducts that were quite refractory to complete mineralisation. Using DBD alone or the combined systems, fourteen and nine different major oxidation by-products of bisphenol-A and 2-nitrophenol were identified. Five new transformation products namely: 4-nitrophenol ($C_6H_5NO_3$), 4-nitrosophenolate ($C_6H_4NO_2$), 4-(prop-1-en-2-yl) cyclohexa-3,5-diene-1,2-dione, ($C_9H_8O_2$), 4-(2-hydroxylpropan-2-yl)cyclohexane-3,5-diene-1,2-dione ($C_9H_{10}O_3$), and 1,2-dimethyl-4-(2-nitropropan-2-yl)benzene ($C_9H_{10}NO_4$) were identified during the degradation of BPA. While, three aromatic intermediate compounds such as 2-nitro-1,3,5-benzenetriolate ($C_6H_2NO_5$), 2-nitro-1,4-benzoquinone ($C_6H_3NO_4$), and 2,5-dihydroxyl-1,4-benzoquinone ($C_6H_4O_4$) respectively were identified for the first time using LC-MS after the degradation of 2-NP using the DBD combined with supported Ag doped TiO_2 photocatalysts.

These intermediate compounds have never been reported in the literature, thereby expanding the number of BPA or 2-NP intermediates in the data base. BPA degradation in the DBD/Ag doped TiO_2 system proceeded via ozonation, hydroxylation, dimerization, and decarboxylation and nitration step, while 2-NP degradation proceeded via hydroxylation, nitration and denitration respectively. The DBD alone and combined DBD with

catalyst produced more of the OH^{o} radical than H_2O_2 and O_3. The OH^{o} that readily formed in acidic medium was the most significant species responsible for the degradation of BPA and 2-NP. The major shortcoming of the supported Ag doped TiO_2 photocatalyst was the leaching of metallic species such as Fe, Cr and Ni from the stainless steel mesh support over time due to the oxidation reactions. The leaching of Fe, Cr, and Ni into the solution inhibited and interfered with the TiO_2 nanocrystals based on the proximity of the ionic radii of these elements with Ti. This appeared as one of the major drawbacks responsible for lower conversion rate of BPA or 2-NP by combined DBD/supported photocatalysts over time. In future work the support type used in the DBD system should be varied to prevent corrosion.

CONCLUSION

The results presented in this study have clearly demonstrated that the combination of the DBD system with Ag doped TiO_2 can be applied as a method to decompose recalcitrant pollutants such as BPA or 2-NP remaining in water after conventional treatment. Moreover, the report presents two feasible ways of preparing and presenting the supported and doped photocatalyst to the UV light generated in the DBD system or to visible light, namely supported on metal or fused silica. The integration of a plasmon metal doped photocatalyst to the DBD system significantly enhanced the degradation rate of both dyes and persistent organic pollutants. The study furthermore showed that a combination of advanced oxidation techniques is more efficient at degradation of organic pollutants than each system on its own. Moreover, the degradation achieved was of the primary pollutant, and complete mineralization of the pollutants was more difficult to achieve. The mechanism of secondary breakdown products was elaborated, showing that simplistic measurement of the primary pollutant left in the wastewater after treatment is not an accurate reflection of the degree of purification achieved, since secondary breakdown products may be difficult to identify and quantify. In all studies where degradation of persistent organics is claimed, the secondary breakdown products should be identified and quantified. Toxicological studies of the treated water should be performed to ensure that the treated water is safe for reuse or release into the environment.

FURTHER READING:

Further reading on aspects of the study include the following:

1. NYAMUKAMBA, P., TICHAGWA, L., MAMPHWELI, S. and PETRIK, L.F. (2017). Silver/Carbon Codoped Titanium Dioxide Photocatalyst for Improved Dye Degradation under Visible Light. International Journal of Photoenergy, Volume 2017, Article ID 3079276, 9 pages, DOI:10.1155/2017/3079276

2. MAKENE, V.W., TIJANI, J.O., PETRIK, L.F. and POOL, E.J. (2016). Evaluation of cytotoxicity and inflammatory activity of wastewater collected from a textile factory before and after treatment by coagulation-flocculation methods. Environmental Monitoring Assessment, 188, pp. 471. DOI 10.1007/s10661-016-5441-x.

3. MOUELE, E.S.M., TIJANI, J.O., FATOBA, O.O. and PETRIK, L.F. (2015). Degradation of organic pollutants and microorganisms from wastewater using different dielectric barrier discharge configurations – a critical review. Environmental Science and Pollution Research, 22(23), pp. 18345-18362. DOI 10.1007/s11356-015-5386-6.

4. ROSSOUW, A., ARTOSHINA, O.V., NECHAEV, A.N., APEL, P., PETRIK, L.F, PEROLD, W.J., PINEDA-VARGAS, C.A. (2015). Stable Ion Beam Analysis (RBS and PIXE) Study of Photocatalytic Track-Etched Membranes. Exotic Nuclei, pp. 591-596. DOI: 10.1142/9789814632041_0065

5. BADMUS, K.O., TIJANI, J.O., EZE, C.P., FATOBA, O.O. and PETRIK L. F. (2016). Quantification of Radicals Generated in a Sonicator. Analytical and Bioanalytical Chemistry Research, 3(1), pp.139-147.

6. TIJANI, J.O., FATOBA, O.O., BABAJIDE, O.O. and PETRIK, L.F. (2015). Pharmaceuticals, endocrine disruptors, personal careproducts, nanomaterials and perfluorinated pollutants: A review. Environmental Chemistry Letters, pp. 1-23. DOI 10.1007/s10311-015-0537-z

7. TIJANI, J.O., FATOBA, O.O., MADZIVIRE, G., PETRIK, L.F. (2014). A review of combined advanced oxidation technologies for the removal of organic pollutants from water. Water, Air, & Soil Pollution, 225, pp. DOI 10.1007/s11270-014-2102-y.

8. HINTSHO, N., PETRIK, L., NECHAEV, A., TITINCHI, S., NDUNGU, P. (2014). Photo-Catalytic Activity of Titanium Dioxide Carbon Nanotube Nano-composites Modified with Silver and Palladium Nanoparticles. Applied Catalysis B: Environmental, 156-157, pp. 273-283.

9. TIJANI, J.O., FATOBA, O.O., PETRIK L.F. (2013). A review of pharmaceuticals and endocrine disrupting compounds: sources, effects, removal and detections. Water, Air and Soil Pollution, 224, pp. 1770-1799. DOI 10.1007/s11270-013-1770-3.

10. Swartz, C.D., Genthe, B., Chamier, B., Petrik, L.F., Tijani, J.O., Adeleye, A., Coomans, C.J., Ohlin, A., Falk, D. and Menge, J.G. (2016). Emerging Contaminants In Wastewater Treated For Direct Potable Re-Use: The Human Health Risk Priorities In South Africa. Final Report WRC K5 2369

11. Petrik, L.F., Fatoba, O.O., Totito, T. (2015). Advanced oxidative water treatment process for water disinfection using an Electrohydraulic Discharge Reactor and TiO_2 immobilized on Nano fibres. 2015/08/01; WRC Research Report No.2132/1/15. ISBN No: 978-1-4312-0692-6

12. NYAMUKAMBA, P. (2016). PhD Thesis UFort Hare. Preparation and Application of Plasmon Metal Enhanced Titanium Dioxide Photocatalysts for the Removal of Organics in Water

13. TIJANI, J.O. (2015). PhD thesis UWC. Degradation of Bisphenol-A and 2-Nitriphenol by Combined Advanced Oxidation Technologies

14. TOTITO, T. (2015). MSc Thesis UWC: Photocatalytic Activity of Supported TiO_2 Nanocrystals.

15. GURA, A. (2015). MSc Thesis UWC: Synthesis and photocatalytic activity of carbon doped and carbon-nitrogen co-doped TiO_2 nanocomposites

16. MOUELE, E.S.M. (2015). MSc Thesis UWC: Water Treatment Using Electrohydraulic Discharge System.

17. OKOLONGO, G.N. (2015). PHD Thesis UWC: Advanced Oxidative Water Treatment Process Using An Electrohydraulic Discharge Reactor And Titanium Oxide Immobilised On Nanofibres.

18. HINTSHO, N.C. (2011). MSc thesis UWC: Synthesis of nanostructured Titanium Dioxide and Application in Water Treatment.

ACKNOWLEDGEMENTS

The project team wishes to thank the following people for their contributions to the project.

Reference Group	Affiliation
Dr N Kalebaila	Chairperson
Dr M Lutz	Stellenbosch University
Prof. JC Ngila	University of Johannesburg (UJ)
Prof. SD Mhlanga	UJ/Unisa
Prof. VL Pillay	Stellenbosch University
Prof. EP Jacobs	Stellenbosch University
Dr V Somerset	Cape Peninsula University of Technology
Dr PG Ndungu	University of Johannesburg
Prof. RWM Krause	Rhodes University
Prof. N Revaprasadu	University of Zululand
Prof. EMN Chirwa	University of Pretoria
Prof. EM Cukrowska	University of the Witwatersrand
Dr N Khan	Cape Peninsula University of Technology
Dr V Jacobs	CSIR

TABLE OF CONTENTS

LIST OF FIGURES

LIST OF TABLES

ACRONYMS & ABBREVIATIONS

AOTs	Advanced Oxidation Technologies
DBD	Dielectric barrier discharge
EHD	Electrohydraulic discharge
HPLC	High Performance Liquid Chromatography
HRSEM	High-Resolution Scanning Electron Microscopy
LC-MS	Liquid chromatography-mass spectrometry
XRD	X-Ray Diffraction Spectroscopy

This page was deliberately left blank

CHAPTER 1: BACKGROUND

1.1 INTRODUCTION

The increasing economic growth coupled with higher energy and resource consumption has been globally identified as a driver of severe water pollution. Consequently, with the increase demand for safe drinking water globally coupled with a growing concern about the adverse health effects of anthropogenic contaminants, several research and development strategies have recently focused on synthesising novel nanocomposites capable of detoxifying and degrading refractory, complex organic pollutants. In the last couple of years, there has been remarkable progress in the application of advanced oxidation technologies (AOTs) for environmental remediation particularly wastewater treatment. Besides AOTs, heterogeneous photocatalysis has been widely considered as a promising technique that can be used to supplement existing wastewater treatment technologies.

Apart from other recognized metal-oxide semiconductors such as ZnO, SnO_2 and Fe_2O_3, titanium (IV) oxide (TiO_2) has attracted significant attention from fundamental research in comparison to other oxides due to its outstanding characteristics such as stability, low cost and affordability, high photosensitivity, environmental friendliness, availability, strong oxidizing power and above all, ease of use over other oxides (Dolat et al., 2012). TiO_2 is often referred to as titania, titanium white, titanic anhydride, or titanic acid anhydride and occurs naturally as an oxide of titanium. It exists in four different polymorphs namely rutile, anatase, brookite and titanium (IV) oxide B. These four crystal structures differ appreciably from one another through the bond angle distortion of the octahedral chains. Out of these polymorphs, anatase and rutile are photocatalytically active. Heterogeneous photocatalysis involves the absorption of photoenergy (hv) by TiO_2 to produce electron excitation that initiates a sequence of reaction steps and pathways (Palomino et al., 2008; Klauson et al., 2010; Elmolla and Chaudhuri, 2010; Chong et al., 2010).

Historically, the discovery of TiO_2 as a heterogeneous photocatalyst began in 1970s when Fujishima and Honda used a photochemical cell comprising an inert cathode and rutile TiO_2 anode to split water into hydrogen and oxygen (Fukushima et al., 2000; Fujishima et al., 2008). This incident marked a new beginning in the field of photocatalysis and over the last four decades, heterogeneous photocatalysis has expanded rapidly to solve various environmental problems, particularly wastewater treatment. To buttress this fact, more than 75% of the articles published in the last three years on advanced oxidation technologies were based on the use of semiconductor titanium (iv) oxide nanoparticles or its immobilized form (Di Paola et al., 2012). Nano TiO_2 can be synthesised via different techniques such as the sol-gel method, solvothermal method, hydrothermal treatment, chemical vapour deposition, chemical precipitation methods, ball milling, micro-emulsions, to mention but a few (Karami, 2010). Of all these methods, the sol-gel technique appeared the most promising due to production of nanoparticles with good homogeneity and high surface area at relatively low cost (Monreal et al., 2009).

The advantages of the sol-gel deposition method are numerous and briefly outlined by Bestetti et al. (2010) as follows: (i) the application of sol-gel technique for different support materials; (ii) easily conducted with ordinary laboratory equipment; (iii) permits uniform coating of high contact areas and complex shapes; (iv) the properties of the resulting film can be easily manipulated and controlled via changing some parameters; and (v) dopants can easily be co-deposited. In addition, an extensive review on most of these techniques, as well as the basic principle of heterogeneous photocatalysis, particularly semiconductor TiO_2 have been widely reported in literature (Nainani et al., 2012; Gaya and Abdullah, 2008; Chong et al., 2010). An interesting new synthetic technique that could be used to control the size and the surface properties of TiO_2 nanoparticles obtained via calcination is by the utilization of a polymeric precursor method, which is considered in this study.

The mechanism of electron-hole pair formation on TiO_2 surface such as photo-excitation, diffusion, trapping, recombination, oxidation and eventual generation of hydroxyl radicals that are responsible for the degradation of target pollutants into carbon dioxide, water, and inorganic ions (Figure 1.1) have been discussed extensively in literature (Fujishima et al., 2008; Di Paolo et al., 2009; Chong et al., 2010; Chong and Jin, 2012; Teoh et al., 2012; Weir et al., 2012). The absorption of a photon of light either from sunlight or from an illuminated light source by a semiconductor metal oxide such as titanium dioxide (TiO_2), produces electron (e^-) – hole (h^+) pairs on the valence and conduction band. The valence band becomes excited and oxidised while the conduction band of titanium dioxide accepts the transferred electron and is reduced. At this point, the semiconductor TiO_2 has become photo-excited. The positive hole (h^+) of the catalyst is responsible for the breaking down of water molecules into hydrogen gas and hydroxyl radicals while the negative electron combines with oxygen molecules and produces super oxide anions (Figure 1.1).

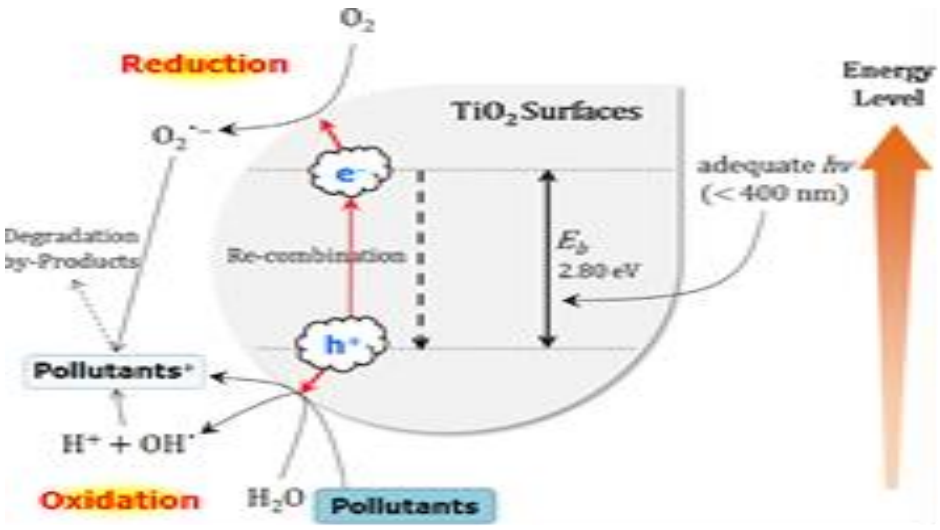

Figure 1-1: Schematic illustration on removal of pollutants by the formation of photoinduced charge carriers (e_/h+) in a semiconductor TiO_2 particle surfaces (Lee and Park, 2013)

The hydroxyl radicals then react and degrade the pollutants to harmless inorganic pollutants such as carbon dioxide and water. This cycle continues as long as light is available. Nano-TiO_2 degrades recalcitrant organic pollutants and micro-organisms in water due to its ability to utilize radiant energy directly, although the mechanisms are still subject to debate due to lack of mechanistic models as predicted in the process (Dalrymple et al., 2010). The application of nano TiO_2 to destroy cancer cells, viruses, bacteria and other microorganisms under UV light in water treatment has been limited to laboratory bench scale studies, while only a very few pilot plants using solar energy are in operation in some parts of the world. The efficiency of the laboratory scale and the pilot-plant differ with the latter being affected by the complexities of the wastewater to be treated. Presently, research and development of large scale water treatment plants based on TiO_2 photocatalysis and solar energy system is on-going (Dalrymple et al., 2007).

The technical hurdles that diminish the photocatalytic efficiency of TiO_2 and even constitute inherent difficulties include: Low light penetration into the solution because TiO_2 particulates impede the light; difficult post-separation of the particulate nano-TiO_2 after water treatment; high recombination rate of photo-generated electron-hole pairs; the high band gap of TiO_2 and lower ultraviolet range of 400 nm confines its photosensitivity and limits its photo-activity leading to low quantum efficiency as a result of ineffective visible light harvesting; difficulty to support powder TiO_2 on substrates; and catalyst deactivation (Chong et al., 2010; Ahmed et al., 2011; Li et al., 2012). To date, several approaches have been proposed towards improving the photocatalytic activity vis-a-viz extending the absorption threshold in the visible region and eliminating post separation challenges. It is imperative to modify TiO_2, with electron scavengers such as plasmonic metals to reduce recombination rates as well as to immobilise TiO_2 on a solid support (Chong et al., 2010; Ismail et al., 2010; Pan et al., 2010; Ismail and Bahnemann, 2011; Han et al., 2012; Hen et al., 2012; Joo et al., 2012; Liu et al., 2012; Roben et al., 2012; Nakada and Fujishima, 2012; Wang et al., 2012; Zhao et al., 2012).

Very recently, doping of TiO_2 towards extending the absorption threshold to the visible light region in order to maximise solar energy utilisation has attracted the attention of the scientific community. For instance, doping TiO_2 with plasmonic elements such as silver significantly reduce the recombination of photogenerated electron-hole pairs and improve the surface electron excitation (Nainani et al., 2012). Silver particles act electron trappers. This dopant could furthermore be used to tailor the band gap to allow light to be absorbed in the visible range. There are a few other advantages such as higher surface area, superior adsorption properties and increased surface hydroxyl groups (Zhu and Zou, 2009; Jin and Dai, 2012; Manoj et al., 2012; Hintsho et al., 2014). Several support materials such as a glass, wooden fibre cloth, carbon fibre, stainless steel mesh have been used to immobilize the semiconductor catalyst. Most of these support material are chosen because of their higher surface area. This is to guarantee highly active reaction centres as well as improved light penetration and reflection by the support (Kleiman-Shwarsctein et al., 2008; Friedmann et al. 2010).

So far, many studies have focused on preparing silver doped TiO_2 nanocomposites showing photocatalytic activity under visible and ultra violet light irradiation (Suwarnkar et al., 2014). Only a very few studies actually immobilised the silver doped TiO_2 nanocomposites on a suitable support such as stainless steel mesh. However, this study considers synthesising supported TiO_2 on a stainless steel mesh using a polymer enhanced sol-gel method and thereafter applied calcination for developing nano crystals followed by a thermal

evaporation technique to deposit different thickness of stable plasmonic metal (silver) onto TiO_2 surface. Furthermore, this study investigates a fused silica support with different metal and TiO_2 layers deposited thereon by vapour deposition.

1.2 PROJECT AIMS

The following were the aims of the project:

1. To synthesize and characterize novel immobilised Ag-TiO_2, and plasmon enhanced TiO_2 composite photocatalysts for water treatment
2. To apply the combined synthesised Ag-immobilized or plasmon enhanced TiO_2 composites and electrohydraulic discharge reactor to degrade persistent organic pollutants (POPs) in contaminated/wastewater.
3. To assess the removal efficiencies of the POPs by the combined plasmon or Ag immobilised TiO_2 nanocomposites and dielectric barrier discharge (DBD) reactor
4. To evaluate the degradation of these micro pollutants and the antiscalants using the combined plasmon or Ag-doped titania nano composites and dielectric barrier discharge reactor.
5. To determine the effect of interaction time, pH of the solution and dosage of the catalyst in the electrohydraulic discharge reactor on the effectiveness of degradation
6. To establish the degradation mechanism of the reaction using immobilised nanocomposites and propose a kinetic model through kinetic study
7. To determine the scalability of the combined advanced oxidation system for treating effluents contaminated with PPCPs, EDCs and antiscalants

1.3 SCOPE AND LIMITATIONS

The scope of the degradation study was limited to a few selected pollutants by the reference group. Moreover, the scaling up of the DBD reactor could not be pursued due to limitations in funds granted, which was the advice from the reference group.

CHAPTER 2: CHEMICALS OF EMERGING CONCERN

2.1 INTRODUCTION

Emerging micropollutants or chemicals of emerging concern have no clear definition and no comprehensive list. Due to misconception among researchers the term has been used interchangeably. The US EPA (United States Environmental Protection Agency (2007) categorised emerging contaminants as new chemicals without regulatory status, of which the impact on the environment and human health is poorly understood or remains unknown.

Houtman (2010) opined that emerging contaminants do not only mean the newly developed and detected compounds in the environment but rather divided them into three different classes. The first class consists of chemical compounds recently released into the environment. The second class involves compounds that have been in the environment for a longer time but have recently been detected due to advances in analytical techniques. The third class refers to compounds whose associated adverse health effects is just now manifesting.

Kümmerer (2011) defined emerging contaminants as a more or less loosely defined sub-group of micro-pollutants present in the environment at low concentration with strongly variable chemical structures, properties, application ranges and effects. According to the United States Geological Survey (USGS, 2014), emerging micropollutants are any synthetic or naturally occurring chemicals or microbial constituents that have not historically been considered to be contaminants.

The emerging contaminants include persistent organic pollutants, micro-constituents, cyanotoxins, pesticides and herbicides, disinfection by-products (DBPs), endocrine disrupting chemicals (EDCs), pharmaceuticals and personal care products (PPCPs) and a host of other compounds. Presently, more than 80,000 chemicals have been identified as potential endocrine disrupting pharmaceuticals and the number of these emerging contaminants is still expected to increase in treated wastewater due to higher population density. This has resulted in growing public health risks in developing countries such as endocrine conduit disturbance in aquatic organisms, brain damage, convulsion, carcinogenic diseases, reproductive or behavioural disorder, cardiovascular disease, liver damage, and lung defects as well as disturbances in gene expression resulting in feminisation of aquatic organisms (Diamanti-Kandarakis et al., 2009).

The current scenario has become worse due to the lack of adequate and efficient water treatment facilities capable of effectively eliminating and degrading the toxic and recalcitrant compounds to harmless substances. The deterioration of water quality seriously affects the economic progress and impacts negatively on the sustainable development of a nation (Rahman et al., 2009). Therefore, in order to have a healthy population and better society with a consequential effect on the economy growth and sustainability, access to safe drinking water and functional wastewater treatment facilities should not be compromised. Different categories of chemicals of emerging concern are explained below

2.2 CLASSES OF EMERGING CONTAMINANTS

Different types of chemical containing products are currently manufactured to meet human basic needs in life ranging from cleansing agents, pharmaceuticals (prescribed and over the counter drugs), cosmetics, fragrances, and personal care products to mention but a few which are widely used globally. Basically, emerging contaminants are categorised into pharmaceuticals, personal care products, industrial chemicals, agricultural chemicals, disinfection by-products, etc. Most of these chemical compounds such as bisphenol-A, or 2-nitrophenol amongst others, possess endocrine activities that have generated public health concerns. Today, thousands of emerging micropollutants have been identified and detected in virtually all environmental samples such as water, soil and even in human food. Due to the recalcitrant nature of these compounds, they may bio-accumulate in living cells via the lipid layer and may be toxic to the organisms depending on the concentration and duration of exposure. It is predicted that these compounds may reach humans via food chain bio-magnification.

2.2.1 Pharmaceuticals

Pharmaceuticals are any synthesized or natural chemical compounds designed to cure and prevent the spread of diseases as well as adding value to human and animal life (Maletz et al., 2013). Pharmaceuticals have different chemical structures, thus their behaviour, applications and metabolism in the human and animal body and hence the environment will vary (Fawell and Ong, 2012; Jiang et al., 2013). Pharmaceuticals are classified based on their therapeutic uses into the followings: antibiotics (ciprofloxacin), anti-diabetics (sulfonylurea), anti-epileptic (carbamazepine), antimicrobials (penicillins), anti-inflammatories and analgesics (ketoprofen, diclofenac), antiulcer and antihistamine drugs (ranitidine and famotidine), anti-anxiety/hypnotic agents (diazepam), lipid regulators (Clofibrate) to mention but a few (Rivera-Utrilla et al., 2013). Van Doorslaer et al. (2014) reported that more than 5000 pharmaceuticals were synthesised and made available in the market for human and animal consumption.

Currently, the global annual drug consumption figures are in the range of 100,000-200,000 tons with countries such as Brazil, Russia, India, China, and South Africa having the greater proportion. Most of these drugs can be administered orally or by injection but due to their incomplete metabolism in humans and animals, part of the drugs may be excreted in urine or faeces and eventually end up in wastewater treatment plants. Due to growing utilisation of pharmaceuticals by humans and animals, coupled with incomplete assimilation in the body, the original or partially metabolised drugs have been identified in the environment. These contaminants are stable and difficult to degrade by conventional wastewater treatment plants, thus escape the wastewater treatment plants into the environment (Baker and Kasprzyk-Hordern, 2013). Ever since the early 2000s, extensive research has focused on the detection of pharmaceuticals and pharmaceutical residues in water sources (Kanakaraju et al., 2014). Kleywegt et al. (2011) reported the detection of over 30 different pharmaceuticals in finished drinking water across the world. Exposure to pharmaceuticals and its metabolites via food or water may have short and long-term health impacts on human and aquatic species depending on the dose and the duration of exposure (Daghrir and Drogui, 2013). Some of the adverse effects on humans and other ecological species include disruptions of the endocrine system, chronic toxicity and increased drug-

resistant bacterial strains. For instance, Daghgir and Drogui (2013) reported that the exposure to tetracycline residues resulted in the slow growth of terrestrial and aquatic species, signifying that tetracycline antibiotics possessed endocrine disrupting properties. Thus, excessive consumption of tetracycline should be avoided.

The main concern of the environmentalist is not about the acute toxic nature of the pharmaceuticals but rather their chronic toxicity on exposed organisms (Jiang et al., 2013).These pharmaceutically active compounds have furthermore been identified in different environmental water samples such as surface, ground or wastewaters in China, United States, Holland, Spain, Germany, Canada, Brazil and even in South Africa (Yan et al., 2014). In a related study, Matongo et al. (2015) investigated the presence of pharmaceuticals such as sulfamethazine, sulfamethoxazole, erythromycin, metronidazole, trimethoprim, acetaminophen, caffeine, carbamazepine, clozapine and ibuprofen in the Umgeni River, in the city of Durban in KwaZulu-Natal, South Africa. The authors found that clozapine had the highest concentration of 78.33 µg/L in the surface waters of the Umgeni River, while ibuprofen was found most in the sediment with a concentration of 62.0 µg/L. The authors ascribed the high level of these compounds to inefficiency on the part of the wastewater treatment processes as well as human activities.

According to Hughes et al. (2013), over 200 pharmaceutically active substances have been identified in river waters with ciprofloxacin having maximum concentration of 6.5 mg/L. The concentration of detected pharmaceuticals in water is conspicuous; nevertheless the quantified amounts differ from country to country depending on a number of critical factors such as the consumption pattern, or population size to mention but two. The fate and behaviour of most pharmaceuticals in the environment are also diverse and complex, and at the moment there is limited knowledge in the literature in this regard. Some pharmaceutical products are hydrophilic in nature, soluble in water, easily break down and have a short life span (Fent, 2006; 2008). While some pharmaceuticals such as naproxen, or sulfamethoxazole can remain in the environment without degradation for more than a year. Clofibric acid on the other hand takes several years to decompose depending on the environmental media.

2.2.2 Personal care products

Personal care products are made up of a large group of active and inert substances including prescribed and non-prescribed pharmaceuticals utilized by people and animals (Jiang et al., 2013). They include analgesics, synthetic hormones, sun screens, insect repellent, cosmetics, fragrances, preservatives, shampoos and toiletries. Unlike pharmaceuticals that are ingested, personal care products are applied directly on the human body to change appearance, taste and odour. Personal care products are may contain polycylic musks and parabenes used to inhibit bacterial decay (Fawell and Ong, 2012). Furthermore, disinfectants such as triclosan and chloroprene have been used industrially in the manufacture of consumer products such as air-fresheners, hand soap, toothpaste, sportswear, plastics, toys, lotions, medical disinfectants and mouthwash (Fawell and Ong, 2012). In the same vein, benzophenone and alkylated siloxanes are incorporated in sun-screen lotions and hair-care products. The micropollutants enter the aquatic environments including surface water through recreational activities such as swimming and also via showering and bathing as well as other technological process (Kasprzyk-Horden et al., 2009).

Over the years, a substantial number of personal care products and their transformed products have been identified in wastewater. Some of these metabolites get converted into harmless inorganic compounds such as carbon dioxide and water within a wastewater treatment plant or are partially adsorbed onto sedimentation sludge due to their lipophilic nature and non-biodegradability or adhere to other hydrophilic components (Jiang et al., 2013). Others escape the wastewater treatment plants and are more persistent in the environment either in their original or metabolised form. Houtman et al. (2010) reported that triclosan and chloroprene accumulate in the bile from bream in the Dutch River Dommel, Netherlands. Lastly, most endocrine disrupting compounds, pharmaceuticals and personal care products have been shown to disrupt endocrine systems, yet they are still unregulated and are carelessly discharged into the immediate environment, especially in developing countries where there is no stringent regulatory frame work

2.2.3 Endocrine disrupting compounds (EDCs)

Endocrine systems comprise the endocrine glands, hormones and receptors that regulate the body's physiological activities such as reproductive processes including embryonic development, sex differentiation and metabolic development (Flint et al., 2012). Endocrine glands secrete hormones which circulate within the body through the blood stream. However it has been found that a certain group of compounds mimic or disrupt endocrine glands from functioning properly. These compounds have been called endocrine-disrupting compounds and are also known as endocrine disrupting chemicals, or endocrine disruptors, or endocrine modulators. Endocrine disrupting compounds can be natural or artificial chemicals, however they interact with the estrogenic receptors and enhance or inhibit the hormones from functioning properly (Jackson and Sutton, 2008). Diamanti-Kandarakis et al. (2009) defined endocrine disruptors as compounds that interfere with the synthesis, secretion, transport, binding, action, or elimination of natural hormones in the body that are responsible for development, behaviour, fertility, and maintenance of homeostasis (normal cell metabolism).

These xenobiotics are present in most manufactured consumer products ranging from plastic bottles, children toys, cosmetics, toothpaste, detergent, polyvinylchloride pipes among others. Endocrine disrupting compounds cause adverse effects on aquatic organisms or their progeny via alteration of chemical messengers of the body or binding to receptors of the endocrine system at exposure levels up to a million times lower than carcinogen exposure levels of concern (Olujimi et al., 2010). Cases of intersex alteration among alligators, frogs and fish upon exposure to endocrine disrupting chemicals are no longer disputable facts (Aneck-Hahn et al., 2009). Among the endocrine disrupting compounds that have attracted recent scientific attention due to their production output and consumption pattern include phthalates, phenolic compounds (bisphenol A, nitrophenol, nonylphenol, alkylphenol, and chlorophenols), triclosan, ethinylestradiol, diethylstilbestrol, 17β-estradiol. More chemicals may be recognized as endocrine disrupters as the list of compounds increases due to unanticipated effects (Fatoki and Opeolu, 2009).

There are concerted efforts in the western world to provide an up to date list and regulation of persistent emerging contaminants (Pomiés et al., 2013). Despite the fact that there is little epidemiological data regarding the impact of endocrine disruptors exposure on human health, there are increasing incidences of adverse effects such as abnormal sperm count among males, as well as high rates of infertility, accelerated ovarian,

prostate, testicular and breast cancer amongst humans. Exposure to endocrine disrupting compounds has been reported to cause immune deficiency, neurological effects, impairment of intellectual and childhood development and psychological effects. The absence of a precautionary principle and regulated monitoring is responsible for the increasing concentration of micro-pollutants in the environment and has given rise to increasing public concern over the presence of endocrine disrupting compounds in drinking water. Proper identification, quantification as well as effective treatment strategies will be needed to remove these compounds from the water system.

2.2.3.1 *Sources of endocrine disrupting compounds*

Endocrine disrupting compounds enter the receiving waters via different point and non-point sources such as agricultural, household discharge, industrial, sewage and municipal wastewater as shown in Figure 2.10. Most researchers have demonstrated that wastewater treatment plants are not designed to effectively degrade emerging contaminants due to their complex molecular structure and low concentration in the aqueous matrix (Fawell and Ong, 2012). Subsequently, while many of these chemicals pass through the WWTPs based on their hydrophobic nature, the remainder get absorbed onto the particulate matter and settle with bottom sediments and are accumulated continuously through electrostatic interaction (Michałowicz et al., 2014) thus merely transfer from one phase to the other, from where they may leach. Besides WWTP discharges, other identifiable sources include animal husbandry operations, recreational activities, transportation or wash-off from roadways, and atmospheric deposition (Rogers et al., 2013). Most of these contaminants are mobile, highly stable, and recalcitrant and partly decompose or persist throughout conventional wastewater treatment, thus escape, bio-accumulate and metabolise in living tissues causing considerable adverse effects on aquatic species or humans (Bell et al., 2011).

Despite the fact that there is little epidemiological data regarding the impact of exposure to emerging contaminants on human health, there are increasing incidences of feminisation, immune deficiency, neurological effects, bacterial resistance and cases of intersex alteration among alligators, frogs and fish upon exposure to endocrine disrupting chemicals (EDCs). With advances in qualitative and quantitative analytical and standardized detection techniques, endocrine disrupting compounds such as bisphenol-A and 2-nitrophenol have been identified in water, soil and even human food. This has attracted public attention due to their potential negative impacts on natural ecosystems and humans (Fawell and Ong, 2012). These chemicals compounds have been established to disrupt endocrine systems, yet they are still unregulated and discharged carelessly into the immediate environment, especially in developing countries where there is no stringent regulatory and legal frame work. Although this problem has been known for more than a decade, little progress has been made to stem the tide of such pollutants from entering the global waterways. The main distribution pathway via WWTPs to drinking water is depicted in Figure 2.1. In this study, two compounds namely bisphenol-A and 2-nitrophenol were selected based on a literature survey, industrial use, consumption habits, production output, persistency level, poor biodegradability toxicity, bioaccumulation factor, frequent detection and prevalence in wastewater.

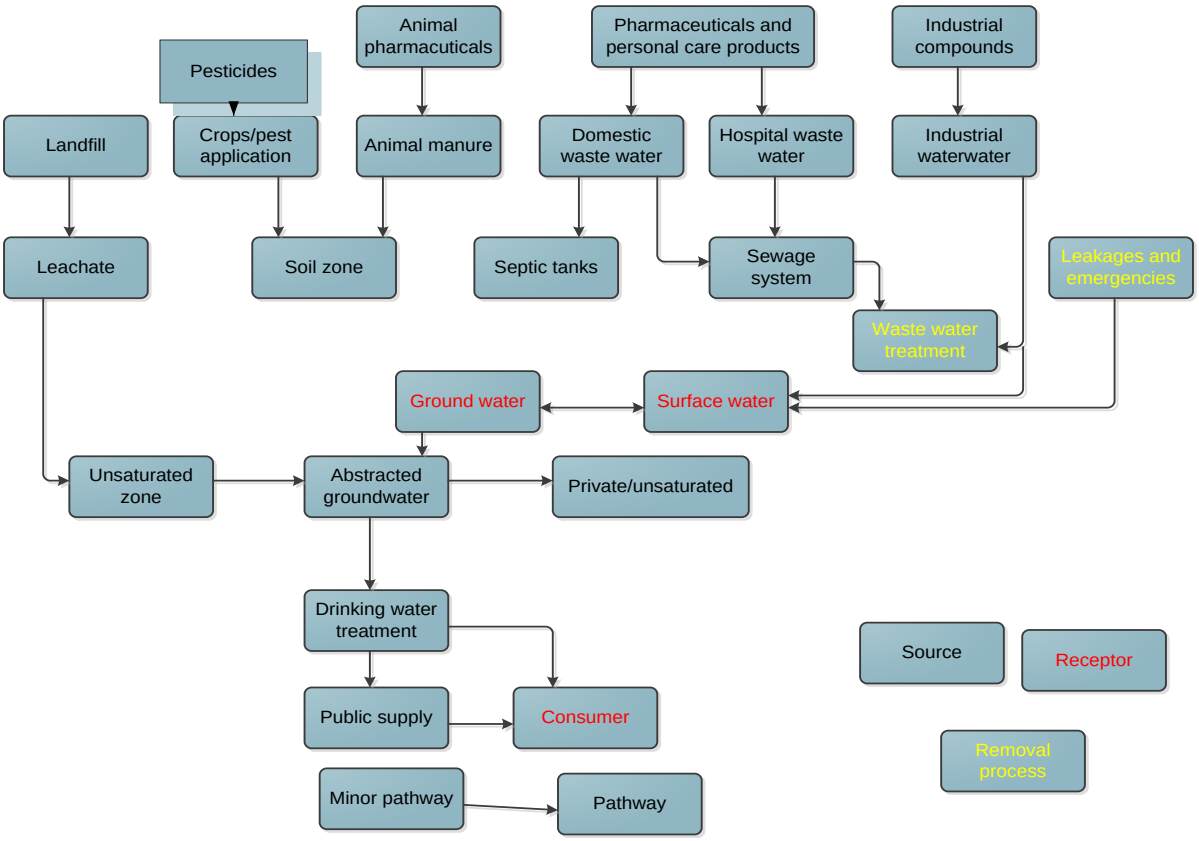

Figure 2-1: Potential sources and pathways of some emerging micropollutants to receptors and aquatic environment (Stuart et al., 2012).

2.2.3.2 *Mechanism of endocrine disruption compounds within the body system*

The mechanism of endocrine-disrupting compounds on the hormonal body system is a complex phenomenon and difficult to predict since compounds exist as mixtures. However, a review of various studies revealed that disruption can take place via multiple routes listed below:

- The contaminants can bind to the nuclear and hormonal receptor cells or sometimes block or mimic the chemical messengers in the body and cause considerable adverse ecological health effects. EDCs sometimes alter the response activity of genes. For instance, BPA can bind to oestrogen receptor β based on its lower affinity than estradiol (Rogers et al., 2013)
- The concentrations or level of the chemical messengers/hormones in the body may be affected via alteration of their metabolic or synthetic pathways (Olujimi et al., 2010)
- Interference with the hormonal-controlled physiological signals responsible for body homeostasis and development is often evident

- Lastly, by modification or modulation of certain chemical messenger receptors within the cells responsible for the immune system.

2.3 CHEMICALS OF EMERGING CONCERN IN SOUTH AFRICAN ENVIRONMENT

It is well established that persistent environmental pollutants with endocrine-disrupting and bio-magnification properties have been identified in South Africa water systems including drinking water (Aneck-Hahn et al., 2009). This has raised concerns regarding water quality in South Africa considering the current pollution status. Exposure to EDCs has adversely affected wildlife and aquatic species in South Africa. However, the reaction mechanism of these emerging contaminants on the human and animal endocrine glands are not yet understood and cannot be limited to activity in South Africa alone since water pollution transcends borders. Several researchers have focussed on the occurrence, detection, removal and even environmental impact assessment of EDCs in South Africa. For instance, a study had established that aquatic species such as fish and other amphibians were affected on exposure to 17β-estradiol (Burger and Moolman, 2006).

EDCs have also been detected in drinking water in South Africa; Olujimi et al. (2010) submitted that South Africa water contained high concentration of oestrogens such as 17β-estradiol. Similarly, Barnhoorn et al. (2004) revealed high concentrations of some EDCs in fat tissue of catfish in South Africa. These reports showed that EDCs are present in South African environments in different proportions depending on the use and consumption patterns. In an attempt to better understand the pollution status of EDCs in South Africa water sources, Burger and Moolman (2006) conducted a surveillance study of these sites; Makhatini flats, Vaal River Barage, Hartbeespoort and Rietvlei Dam in South Africa where significant EDCs activity was established. Fatoki et al. (2010) showed that the concentration of phthalates such as DBP in water samples ranged between 0.16 mg/L to 10.17 mg/L in rivers and dams in the Venda region. The latter value surpasses the 3 µg/L recommended by the United States Environmental Protection Agency (USEPA) for the survival of fish and other aquatic species.

Olujimi et al. (2012) investigated the presence of eleven priority phenols and six phthalate esters in five selected wastewater treatment plants and freshwater systems in Cape Town; their study showed that Zandvliet wastewater treatment plants accounted for the highest concentrations of phthalate esters compared to other WWTPs. Phenol, 2-chlorophenol and PCP were equally detected, though at low concentrations. Manickum and John (2014) quantified the level of steroid hormones such as 17-ß-estradiol (E2), estrone (E1), estriol (E3), synthetic estrogen (17-β-ethinylestradiol (EE2), testosterone and progesterone in Pietermaritzburg wastewater treatment using the non-analytical enzyme-linked immunosorbent assay (ELISA) technique. The authors reported that close to 92% of EDCs were eliminated by activated wastewater treatment plants while the residual 8% found their way into the environment. The authors ascribed different levels of pollutants to seasonal variation, different rainfall pattern, raw wastewater effluent flow rates, and activated sludge performance capacity among others. The authors recommended further treatment of the water and promulgation of effective legislation with respect to maximum allowable levels of these compounds in water matrices.

Very recently, Agunbiade and Moodley (2014) reported the presence of caffeine, nalidixic acid, atenolol and acetaminophen predominantly at very high concentration in the estuary mouth and blue lagoon of Umgeni River water in KwaZulu-Natal. The South Africa water system is exposed and acts as a sink for persistent environmental contaminants as well as their transformation products. And since these rivers serve for drinking purposes, there are anticipated concerns that continuous consumption of such water could lead to undesirable toxicological health effects among citizens in the near future, unless proactive measures are employed. Thus, these compounds must be quantitatively eliminated within treatment plants before ultimate discharge into rivers and lakes used for drinking water purposes. Because the wastewater is discharged into rivers or dams that are sources of drinking water, it constitutes indirect potable reuse. A gap analysis of literature reviewed showed that little information existed on the identification of intermediate compounds which are considered more toxic than the parent compounds, nor on the availability of treatment technologies for the decomposition and eventual elimination of these micropollutants from water. Equally, the eco-toxicity and chronic effect of the transformation products evolved during treatment including their mode of action on the target organisms have not been fully established.

2.4 POTENTIAL RISK FROM EXPOSURE TO CHEMICALS OF EMERGING CONCERN

There are concerns regarding the potential risk from exposure to pharmaceutically active agents in the environment (Fawell and Ong, 2012). Depending on their fate and behaviour in WWTPs and even in drinking water treatment plants, the probability of human exposure to these compounds is high. In order to conduct a thorough risk assessment of emerging micropollutants for humans, there is a need to assess the exposure rate and the actual dose; this will assist in determining the associated adverse health effects. Since the concentration of these compounds in water is low, the acute toxicity may be difficult to evaluate, but the precautionary principle should be kept in mind. Given also that long-term exposure data is not available, the risk assessment might be technically hard to calculate. Aquatic species have a greater risk of exposure to individual agents or combinations of these compounds. It has been established that feminisation of fish in freshwater systems is a result of exposure to certain endocrine disruptors. Further research is needed to find whether this exposure had a major impact on entire populations.

Strauch (2011) affirmed that the effects of exposure to pharmaceuticals and endocrine disruptors and human toxicity irrespective of their concentration in the water supply is yet to be ascertained but research carried out by Topp et al. (2008) revealed that estrogenic compounds have a very high bioaccumulation potential with considerable negative effects on aquatic organisms. This environmental bioaccumulation aggravates the abnormal hormonal control, reproductive impairments and persistent antibiotic resistance. Studies have shown that exposure to diclofenac and 17α-ethinylestradiol in the aquatic environment induced structural deformities of kidney and intestine as well as gene alteration which affect the body's metabolic activities (Kummerer, 2011). In addition to increasing occurrences of reproductive and developmental abnormalities in infants and children, recent reports of temporal downward trends in semen quality and testosterone levels as well as increased rates of testicular and thyroid cancers (Stuart, 2012) among adult male populations has generated concern regarding the potential risk of environmental endocrine disrupting chemicals (EDCs) to men's health.

Currently, it is difficult to link human health effects to exposure to emerging micropollutants due to the existence of background natural disease in the human body. It has been reported by Standford et al. (2010) that direct exposure to emerging contaminants in drinking water portends no danger because the concentrations of these compounds are too low to cause serious health effects, yet this study does not consider the synergistic effects nor the effects of long term, chronic exposure to diverse compound. According to Houtman (2010), the effect of exposure to low doses of chemicals of emerging concern in drinking water is estimated to begin to manifest after 80 years, yet once again this is based on acute toxicity levels. On the other hand, a series of abnormalities have been observed in the case of aquatic species, for instance, disruption of endocrine system of fish via exposure to low dose of estrogenic hormones leading to severe adverse effects (Kummerer, 2011).

The exposure rate is determined by comparing the exposure dose with the toxicity-based benchmarks. These toxicity-based benchmark standards vary and can be related to World Health Organization tolerable daily intake as well other standards. Very recently, Standford et al. (2010) conducted a comparative survey on the rate of exposure to oestrogenic activity and other compounds present in US drinking water, food, beverage, and air. The authors concluded that human beings are only exposed to a small fragment of pharmaceutically active compounds via consumption of municipal drinking water and there is no evidence of adverse human health effects due to exposure to US drinking water. Thus, the level of individual or mixtures of pharmaceutically active substances in drinking water was considered too low to cause a considerable chronic or acute health effects on humans (Bull et al., 2011). However, the extent and long term effects of exposure and synergistic effects still require further studies, and toxic levels for humans will not apply to other organisms.

2.5 CRITICAL APPRAISAL OF SELECTED ENDOCRINE-DISRUPTING CHEMICALS

2.5.1 Bisphenol-A

Bisphenol-A (BPA) or 2, 2-Bis (4-hydroxyphenyl) propane belongs to the class of phenolic chemical compounds containing two hydroxyphenyl groups. It is a white solid, poorly soluble in water but is readily soluble in organic solvents. It has a molecular weight and molecular formula of 228.1 g/mol and $C_{15}H_{16}O_2$ respectively. It has a melting and boiling point of 156ºC and 220ºC respectively, with water-octanol coefficient value of 3.32. The water-octanol coefficient value expressed in logarithm suggests that BPA is readily soluble in fat and poorly soluble in water. The molecular structure is represented in Figure 2.2. Historically, BPA was first synthesised by a Russian chemist (Alexander. P. Dianin) in 1891, via a condensation reaction of one molecule of acetone with two molecules of phenol, in the presence of hydrogen chloride as a catalyst. BPA is mostly utilized as an intermediate in the production of polycarbonate plastics, polyesters, plasticizers, pesticides, thermal printing paper and epoxy resins (Rogers et al., 2013). Other products containing BPA include baby bottles, drinking water bottles, medical equipment, microwave dishes, food can linings and dental sealants (Tsai et al., 2009). An increase in the global consumption of plastics products has caused the production of BPA to rise by 6-8% annually (Huang et al., 2012). According to the US Environmental Protection Agency (2010), over 1266 metric tons of BPA were discharged into the environment via manufacturing, incineration activities and wastewater treatment plants in 2008 alone. In 2012, the global production was

around 2.7 million tons and Global Industry Analysts had projected global production rate to rise to 6 million tons by the end of 2015. Currently, the USA, Taiwan, South Korea, China and Japan remain the highest producers of BPA in the world. With this geometrical increase and widespread use of plastics, BPA has been recognised globally, and its removal from wastewater has become a fundamental component of applied research.

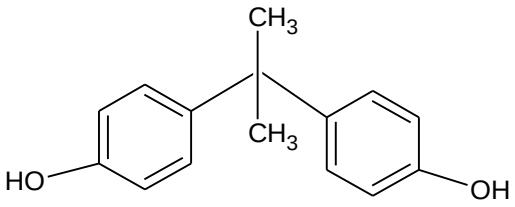

Figure 2-2: Structure of bisphenol-A

BPA is a well-known antioxidant and ubiquitous synthetic xeno-oestrogen in the environment for modulating the activity of endocrine glands in humans, wildlife and aquatic species (Rocha et al., 2013). Apart from its known estrogenic activities on cells, bisphenol-A also is suspected to alter the immune responses in humans by acting as agonists or antagonists to nuclear-hormone receptors without significant toxicity (Rogers et al., 2013). BPA can bind to different types of receptors such as estrogen, androgen, aryl hydrocarbon, peroxisome proliferator that mostly relate to endocrine hormones in the body (Michałowicz et al., 2014). BPA as an endocrine-disruptors possesses oxidative, mutagenic and hypomethylation properties and thus exerts different harmful effects on animals and humans (Ziv-Gal et al., 2013). As a result of the multidirectional effect of BPA on different receptors, the importation of infant food cans containing BPA such as baby feeding bottles have been strictly restricted in countries including China, North America, and Europe.

Similarly, the South African Ministry of Health has also proposed draft regulations that will restrain the manufacture, sale, import and export of polycarbonate baby bottles containing BPA. Due to the absence of strong covalent bonds between the chemical plastic components and BPA, fragmentation and leaching of BPA from the plastic products occur (Rocha et al., 2013). Exposure to BPA of humans, wildlife and aquatic species could vary. According to United State Environmental Protection Agency, bisphenol-A is a known endocrine disruptor. A number of studies have identified drinking water, manufacturing effluents, dust inhalation, agricultural run-off, food, drinking, and beverage containers as possible exposure routes to this chemical (Michalowicz et al., 2014). At the moment, the main exposure route to BPA is via inhalation or oral ingestion (Geens et al., 2012). However recently, transdermal exposure has become a source of concern (Geens et al., 2012). Thermal paper coated with BPA is used for till slips which are daily touched and handled by millions of people. BPA is regularly detected in municipal and industrial wastewater and its presence has been widely documented. With the geometrical increase and widespread use of plastics, BPA has turned out to be ubiquitously present in wastewater streams. The presence of BPA in the various water sources and other consumer products raises serious concerns regarding public health.

2.5.1.1 *Effect of BPA exposure*

Reliable evidence from literature regarding associated adverse environmental and health effects of BPA on human beings has been limited. Recently, epidemiological studies conducted by Vandenberg et al. (2007) linked abnormalities namely polycystic ovarian syndrome, obesity, endometrial hyperplasia, heart diseases, repeated miscarriages, prostate and breast cancer, attention-deficit hyperactivity disorder, and infertility to human exposure to BPA (Teppala et al., 2012; Wang et al., 2012). Moreover, there have been documented health effects from exposure of aquatic species to BPA. Currently, it has been established that long term exposure to BPA might lead to transgenerational health effects on humans and wildlife (Dmitruk et al., 2008). BPA possesses estrogenic activity, alters metabolic kinetics and promotes DNA damage including chromosomal abnormalities. BPA is suspected to alter the immune responses in humans by acting as agonists or antagonists to nuclear-hormone receptors without significant toxicity (Rogers et al., 2013). BPA also prevents the endocrine hormones such as sex hormones, thyroxin, insulins and leptins from functioning properly and may result in immunotoxic, heptatoxic, carcinogenic and sometimes mutagenic effects (Michalowicz et al., 2014; Wang et al., 2015). It has also being established that exposure to BPA by aquatic species have led to a high predominance of early puberty, heart disease, obesity, low fertility, low sperm count, breast, ovarian and testicular cancer (Geens et al., 2012). Exposure to BPA during pregnancy has been found to overshadow some critical genes in the womb, thus retarding growth. In the same vein, the decline in fish populations is attributed to exposure to BPA (Deborde et al., 2008). Considering the exposure rate to BPA, a precautionary approach involving elimination and decomposition of BPA from contaminated water is considered necessary in order to safeguard potable water supplies as well as reduce potential threats.

2.5.1.2 *Fate of bisphenol-A in the environment*

After the discharge and escape of persistent environmental pollutants from wastewater treatment plants (Swartz et al., 2016), a better understanding of their fate and impacts on the environment is imperative. BPA enters the environment during manufacturing activities, transportation, processing, handling among others. In fact, few places in the world are free of BPA (Rogers et al., 2013). The pathways of entrance into the environment could be air, water or sediment. However the most recognised source of entrance into the environment is via discharge of plastic products and household wastewater. Thus, the physico-chemical degradation of plastics causes leaching and volatilisation of BPA, which prompts the release of a substantial amount into the soil and lesser amounts into water and air respectively. BPA does not hydrolyse in water because of its chemical structure and as such more than 50% BPA gets adsorbed or binds onto sludge/sediment, however it undergoes reasonably rapid photo-degradation in wastewater treatment plants and receiving waters. BPA is readily decomposed by bacteria under both aerobic and anaerobic conditions. BPA is therefore regarded as a pseudo-persistent pollutant with a short half-life between 2.5 to 4 days, though other conjugates or residual by-products are associated with longer half-lives of up to a month (Geens et al., 2012), but because of high volumes that are constantly being discharged, is ubiquitous. The concentrations of BPA differ appreciably in wastewater treatment plants depending on their location, plastic use patterns and sampling period (Swartz et al., 2016). The fate and behaviour of the individual xenobiotic does not only depend

on its hydrophobic-hydrophilic properties but also on environmental conditions such as water solubility, pH, adsorption coefficient, redox conditions, temperature and bioaccumulation potential (Rahman et al., 2009). The quantity of residual pharmaceuticals and endocrine-disruptors in aquatic environments are frequently influenced by factors such as the amount of wastewater produced, the consumption patterns, geographical locations, lifestyle, appropriate treatment techniques, regulations and so on (Rogers et al., 2013).

2.5.2 2-Nitrophenol

2-nitrophenol (NP) is categorised as one of the three nitrated phenols with molecular weight and molecular formula 139.10 g/mol and $C_6H_5NO_2$ respectively. It is a yellow crystalline solid, readily soluble in water and moderately acidic upon dissociation in water. 2-nitrophenol is not naturally occurring in the environment. However it remains an integral component of industrial effluents, and has been identified in different urban and agricultural waste. It is mostly utilized in various industries as a reagent to manufacture organophosphate pesticides, herbicides, and explosives and as intermediate during the synthesis of dye (Ammar et al., 2007). The structure of 2-nitrophenol is shown in Figure 2.3.

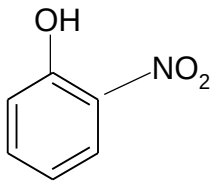

Figure 2-3: Structure of 2-nitrophenol

Due to the absence of stringent environmental regulatory frameworks, most phenolic compounds especially 2-nitrophenol (2-NP) have become an environmental pollutant commonly detected in water sources, soil and industrial effluents (Ahmed et al., 2015). United State Environmental Protection Agency (USEPA, 2007) categorised 2-NP as a toxic and recalcitrant organic pollutant with considerable endocrine disrupting properties. The compound is a highly stable, non-biodegradable chemical compound which bio-accumulates over a long period of time in the environment. 2-nitrophenol is difficult to degrade in soil or water by conventional biological wastewater treatment processes and other treatment options (Ribeiro et al., 2008). Also, 2-NP affects the hormonal reproductive functions of both male and female organisms (Ahmed et al., 2015).

With their high level of persistency in the environment and the associated health risks due to exposure, USEPA recommended the tolerable level of this compound in natural water to be below 4.8 µg/L. So far, there are no identifiable natural sources of 2-NP in the environment. The presence of 2-NP in water also introduces an unpleasant odour and taste to available drinking water with a resultant adverse health impact on downstream users. The rate of toxicity of 2-NP in water is measured based on its dissociation mechanism in aqueous media at a specific solution pH. The dissociation mechanism is linked to its toxicity level, thus a decrease in solution pH causes an increase in toxicity and promotes dissociation of the compound.

2.5.2.1 *Environmental effect of 2-nitrophenol*

The short-term effect of exposure to 2-NP can cause skin irritation while continuous exposure can lead to severe skin disorders (Boehncke et al., 2000). Inhalation of 2-NP can lead to headaches, dizziness, etc. Additionally, 2-NP has carcinogenic and mutagenicity effects on the target organisms. Although there is limited or lack of reliable data regarding the genotoxicity effect of 2-nitrophenol on humans, exposure to 2-NP can influence catabolic metabolites in the body. For instance, the exposure of female rats and male rats to 2-NP can causes estrogenic and anti-androgen effects.

2.5.2.2 *Fate of 2-nitrophenol in the environment*

The fate and behaviour of recalcitrant pollutants are quite diverse and complex depending on certain environmental factors, which complexity is partly responsible for the limited knowledge of their environmental fate. 2-nitrophenol may enter the environment via wastewater treatment plants. Other sources include industrial fugitive emissions, vehicular exhaust emissions, and atmospheric photochemical reactions. In the environment, 2-NP evaporates from the topsoil within 10 days while less than 10% decomposes slowly under aerobic conditions within 30 days inferring that 2-NP undergoes slow biodegradation (Ribeiro et al., 2008). In the terrestrial environment, the trio of photolysis, evaporation and biodegradation occurs while adsorption onto the particulate matter is not well defined. Because the pollutant does not adsorb onto soil, there is the possibility of leaching which may contaminate groundwater, although no monitoring studies have confirmed the presence of 2-NP in groundwater. Similarly, in the aquatic system, as a result of the low value of sorption constant characteristics (Koc) the pollutant did not adsorb onto particulate matter, instead certain fragments escaped during evaporation, photolysis and aerobic degradation (Boehncke et al., 2000).

The fate of 2-NP in the aquatic environment depends on the intensity of sunlight, solution pH, nature of particulate matter, aerobic conditions, amongst others. While the atmospheric half-life of 2-NP remains relatively unknown, the half-life under photolytic and aerobic conditions varies depending on the nature of water. For instance, in a fresh water systems, the half-life ranged between 1-8 days, in sea water it was between 13-21 days, whereas in top soil, the half-life of 2-NP under aerobic conditions is close to 12 days. This means that 2-NP undergoes slow photolysis under aerobic conditions. Finally, it is an indisputable fact that these compounds (BPA and 2-NP) are toxic in the environment and that it is only a matter of time before the levels build up to a point where human toxicity will be evident as loads increase. Therefore, the precautionary principle may be a better route and it is suggested that South Africa follow the lead of other advanced countries and regulate the products containing these persistent organic compounds especially bisphenol-A and 2-nitrophenol until further notice as there is not enough capacity for continuously monitoring new compounds before their release into the market place and from there into the receiving environment.

CHAPTER 3: ADVANCED OXIDATION TECHNOLOGIES

3.1 INTRODUCTION

There are increasing concerns about the presence of emerging micropollutants in the environment. The presence of emerging micropollutants has attracted attention from research institutions, government organisations and the public community worldwide, owing to their potential deleterious impacts on human beings and natural ecosystems. Contaminants such as pharmaceuticals and endocrine disrupting compounds enter surface waters through anthropogenic activities. Anthropogenic activities have continued to increase in most developing and developed nations around the world today due to very rapid industrialisation, urbanisation, population growth, associated changes in agricultural and other land-use practices which have caused a number of environmental problems. These contaminants are contained in large quantities in products used every day.

The continuous release of these contaminants into the environment raises the question of their individual and synergic effects on humans and biota. The behaviour of these compounds in wastewater is the key issue with regard to water reclamation and reuse. However, with the growing concern and recent discoveries about the high toxicity of emerging pollutants even at trace levels, their removal is increasingly becoming an issue relevant to the water industry and regulatory agencies, thus there is a need to find effective tools for the management of water contaminated by these emerging contaminants. Advanced oxidation techniques (AOTs) have been reported to have widespread application of treating organic pollutants presence in wastewater (Shannon et al., 2008). This process oxidises the complex organic matter found to be difficult to degrade biologically into simpler end products or mineralises it completely. In the last fifteen years, AOTs have been effectively utilised as an option to decrease the concentration of toxic pollutants in wastewater (Stasinakis, 2008). This chapter presents the review of literature on different advanced oxidation technologies (AOTs), photocatalytic process involving oxidation of organic pollutant in aqueous solution, as well as the synthesis and application of photocatalytic nanoparticles in the treatment of water.

3.2 DEGRADATION OF ORGANIC CONTAMINANTS USING AOTs

3.2.1 Classification of the different advanced oxidation techniques

The classification of these different advanced oxidation techniques is represented in Figure 3.1. The combination of strong oxidising agents such as $H_2O_2/O_3/Fe^{2+}/UV$ is often used to degrade the pollutants, but among the different available techniques of AOTs producing hydroxyl radicals, the Fenton process (Fe^{2+}/H_2O_2; $H_2O_2/Fe^{2+}/UV$) seems to be the most popular technology for wastewater treatment as revealed by the greater proportion of available data in the literature, because of its low investment cost and high efficiency (Ting et al.,

2008; Wang et al., 2009). The literature revealed that over 1000 papers have been published using some of these methods in wastewater treatment during the last decade. However, only a certain fraction of the H_2O_2 is converted into oxidants that are capable of transforming recalcitrant contaminants (Huang et al., 2001; Yeh et al., 2004), resulting in a large consumption of H_2O_2 and Fe^{2+} used that sometimes is difficult to recycle. There is also a high consumption of chemical reagents, limited pH range, deactivation by some ion complexing agents such as phosphate anions, and voluminous iron sludge production (Cheng et al., 2004; Georgi et al., 2007). These are some of the disadvantages of using the homogeneous Fenton process (Kasiri et al., 2008). Some of the other available advanced oxidation processes reported in the literature are combinations such as H_2O_2/UV light, O_3/TiO_2, H_2O_2/O_3, Fenton's reactions (Fe^{2+}/H_2O_2 or H_2O_2/Fe^{2+}/UV), TiO_2/UV, sonolysis, O_3/UV, O_3/sonolysis, $O_3/UV/H_2O_2$, catalytic oxidation, $O_3/TiO_2/H_2O_2$ and supercritical water oxidation.

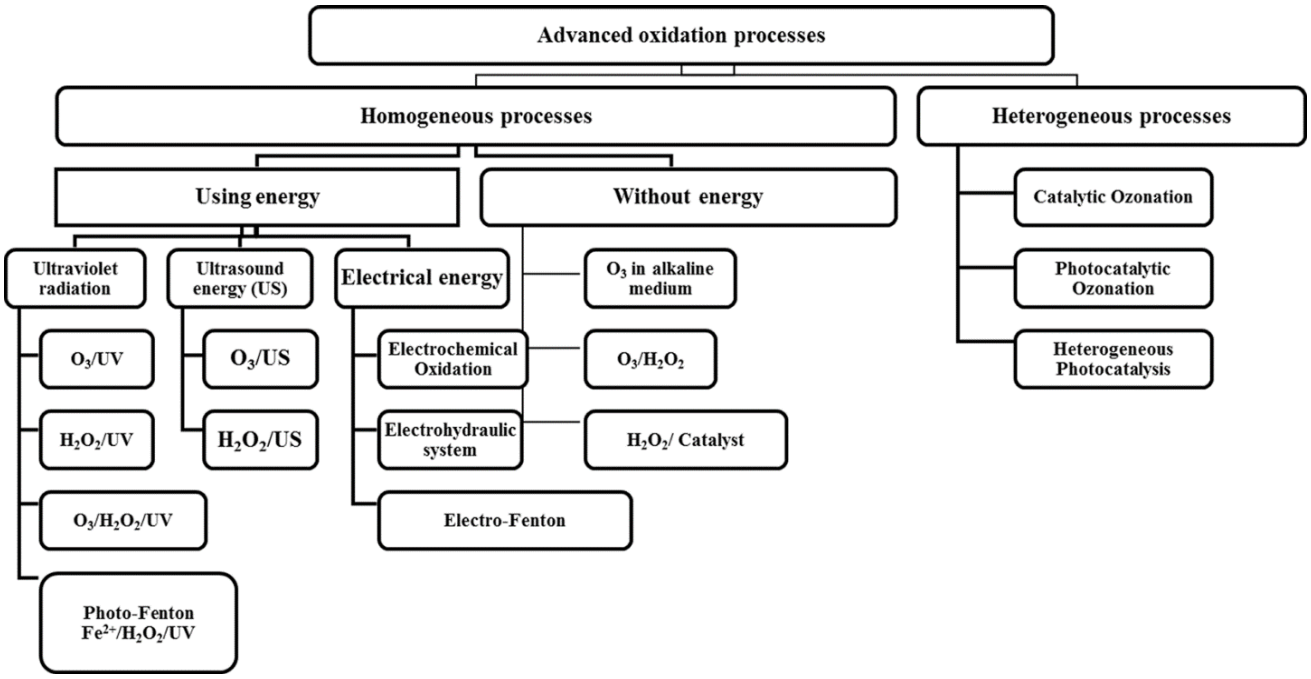

Figure 3-1: Various AOTs based on wastewater treatment technologies (sourced from Sharma et al. (2011)

The formed hydroxyl radical's interaction with the pollutants is the mechanism behind the combined effects of either one or two of the following: hydrogen peroxide (H_2O_2), titanium dioxide (TiO_2), or ozone (O_3) for the organics pollutant degradation wastewater. Among different AOTs, Fenton and Photo-Fenton for the removal of organics from wastewater have been extensively reviewed and thus have received greater attention than any other AOTs in recent years (Gogate and Pandit, 2004). This was substantiated by Maletz et al. (2013) in the survey of articles and abstract available online from more than 15475 international journals and other science scholar data bases. It is on this basis that other AOTs such as the dielectric barrier discharge process, and heterogeneous photocatalysis were considered and reviewed accordingly.

3.2.2 Degradation mechanism

One of the specific features of this technique is the ability to completely mineralise organic contaminant without any trace of more harmful residues. This reported complete degradation and mineralisation potential may be due to the generation of very reactive hydroxyl radicals. The hydroxyl radical is non-selective and highly reactive to degrade a wide range of organic pollutants due to due to its higher oxidation potential of 2.33 V when compared to other conventional oxidising agents such as H_2O_2 or $KMnO_4$ (Gogate and Pandit, 2004). The main mechanism of AOTs is centred on the generation of highly reactive free species. The reaction proceeds either by hydrogen abstraction or by forming a double bond with the organic compounds. The scheme is presented below. The hydroxyl radical attacks the organic chemicals (eq.1), hydrogen abstraction (eq.2) and lastly electron transfer (eq.3). In the reactions, organic compound is denoted with R.

$$R + HO\bullet \rightarrow ROH \quad (1)$$

$$R + HO\bullet \rightarrow R\bullet + H_2O \quad (2)$$

$$R_n + HO\bullet \rightarrow R_{n-1} + OH^- \quad (3)$$

3.2.3 Quantification of free reactive species

Molecular and radical species such as H_2O_2, O_3, $H^\bullet$ and $OH^\bullet$ obtained via heterogeneous photocatalysis, cavitation, and dielectric barrier discharge are powerful oxidants responsible for the physicochemical decomposition of organic contaminants. Over the years, the quantification of these active species has generated diverse interest and has become the subject of considerable investigation among experts in the field of advanced oxidation technologies due to their high selectivity and oxidation potentials. Different techniques such as electron spin resonance-spin trap, emission spectroscopy, chromatographic methods, chemical probes among others have been applied to quantify these species. However, most of these techniques are associated with one problem or the other. For instance, electron paramagnetic resonance (ESPR) technique which measures the spin adduct derivative after trapping is not sensitive and aside from that, the instrument is expensive and requires skilled personnel. This hinders its suitability for routine analysis. The measurement of aromatic hydroxylated derivatives based on the HPLC method is pH dependent due to the low concentration of OH radicals (Jen et al., 1998). In the case of Fenton and photo-Fenton process, solution pH is adjusted to 3-4. It is therefore imperative to identify suitable chemical or physical methods to quantify the generated free reactive species.

3.2.3.1 *Hydroxyl radicals*

Hydroxyl radicals are non-selective but highly reactive species with high oxidation potentials which are mostly responsible for the effective mineralisation of organic pollutants. In the case of DBD systems, the electrical discharge in water causes water ionization and in-situ production of O_3, H_2O_2 and OH radicals inside the streamer channel in a few hundred nanoseconds (Kirkpatrick and Locke, 2005). Procedures for quantifying

the hydroxyl radicals have been widely reported in the literature, including salicylic acid dosimetry based on high performance liquid chromatography (HPLC), disodium of terephthalic acid dosimetry (fluorescence spectroscopy), formaldehyde dosimetry (HPLC), and dimethylsulfoxide (HPLC). The quantitative determination of the actual yield of hydroxyl radicals in the aqueous media is important but never an easy task due to its transitory lifetime (Wang et al., 2009). The use of chemical probes has become a subject of debate simply because most chemical probes react with hydroxyl radicals and generate multiple products. The aromatic hydroxylation method involving chemical dosimetry probes such as salicylic acid, benzoic acid, para-chlorobenzoic acid, and coumarin-3-carboxylic acid based on gas-chromatography or liquid chromatography techniques is sensitive and convenient. Nevertheless, the method is associated with shortcomings such as poor solubility in water, formation of multiple reaction products, secondary formation of superoxide, thus making it difficult to prepare higher concentrations. In most cases, the concentration of the OH radicals in the discharge channel may be higher than the concentration of the chemical probes, thus making quantification challenging.

In the late 1990s, OH radical generation rate was determined by following a pseudo steady-state approach based on liquid or gas-liquid pulsed corona discharge in the presence of phenol as a chemical probe and carbonate ion as a scavenger (Hoeben et al., 1997). Hoeben et al. (1997) utilized 5,5-dimethyl-1-pyrroline N-oxide (DMPO) to trap OH produced by pulsed corona discharge. However, the spin-adduct DMPO-OH could not be detected by ESR due to decomposition by the pulsed corona reactor. Fluorescence spectrophotometry based on coumarin-3-carboxylic acid (CCA) dosimetry was further utilized, nevertheless the generation of a large background signal in bulk solution relative to the prepared standards made OH quantification problematic (Sahn and Locke, 2006). Aside from that, there was the formation of multiple by-products, thus making it extremely difficult to distinguish between the fluorescence compound and the dye molecules. The physical and chemical properties of some chemical probes are indicated in Table 3.1.

Table 3.1: The physical and chemical properties of different chemical probes used for OH radical detection

Physical Parameters	**Coumarine-3-carboxylic acid**	**4-Chlorobenzoic acid (pCBA)**	**Disodium salt of terephthalic acid**	**Dimethylsulfoxide (DMSO)**
Chemical Formula	$C_{10}H_6O_4$	$C_7H_5ClO_2$	$C_6H_4(COONa)_2$	C_2H_6OS
Melting point	109.15524	240-243	-	19°C
Boiling point	-	274-276	-	189°C
Solubility	Poor	Poor	Very good	Highly water soluble
Reaction rate constant with OH radical	$5 \times 10^9\ M^{-1}s^{-1}$	$5 \times 10^9\ M^{-1}s^{-1}$	$3.3 \times 10^9\ M^{-1}s^{-1}$	$4.5 \sim 7.1 \times 10^9\ M^{-1}s^{-1}$

Source: (Gupta, 2007)

Dimethyl sulfoxide is relatively water soluble and non-toxic even at higher concentration. It reacts with the hydroxyl radicals forming methanesulfinic acid (MSA), methyl radicals and formaldehyde as indicated in the equations below (Tai et al., 2004).

$$OH^{\bullet} + (CH_3)_2SO \longrightarrow CH_3SO_2H + {}^{\bullet}CH_3 \quad (4)$$

$$^{\bullet}CH_3 + H\text{-}R \longrightarrow CH_4 + R \quad (5)$$

$$^{\bullet}CH_3 + O_2 \longrightarrow CH_3COO^{\bullet} \quad (6)$$

$$2\ CH_3COO^{\bullet} \longrightarrow HCHO + CH_3OH + O_2 \quad (7)$$

Previously, spectrophotometric and HPLC measurement of the concentration of methanesulfinic acid was considered equivalent to generated hydroxyl radicals. Very recently, studies have shown that methane sulfinic acid is only an intermediate product which can still react with more hydroxyl radicals to form methane sulfonic acid and sulfate (Gupta, 2007). Thus, the quantitative determination of the generated formaldehyde via DMSO/$^{\bullet}$OH reaction can be considered equivalent to the hydroxyl radical. In this study, the disodium salt of terephthalic acid (NaTA) was used as a chemical probe to trap and quantify the hydroxyl radicals produced by the dielectric barrier discharge system due to its high reaction rate constant (NaTA). Terephthalic acid (TA) is readily soluble in water containing NaOH, but its higher conductivity value impedes the streamer properties. However, the reaction between NaTA and the OH radical is not affected by the presence of other active species such as H_2O_2, $HO_2^{\bullet}$, $O_2^{\bullet}$. The reaction between the disodium salt terephthalic acid (NaTA) (non-fluorescent) and hydroxyl radical in the treated water produces a stable 2-hydroxylterephthalic acid (HTA) which is fluorescent at 425 nm in a typical fluorescence spectrophotometer (Fang et al., 1996). The quantified peak intensity of the fluorescent compound (HTA) correspond to HTA concentration and is directly proportional to OH radicals in the solution. The reaction between NaTA and hydroxyl radical is represented in Figure 3.2.

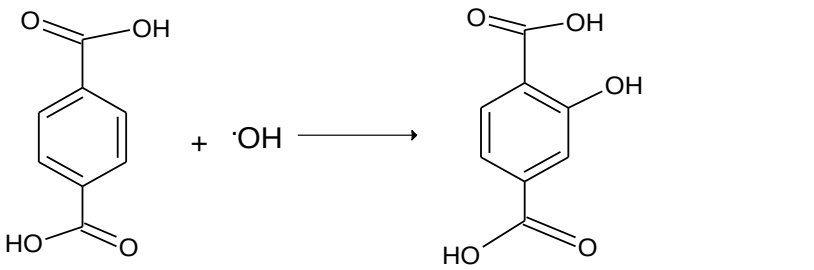

Terephthalic acid (non-fluorescent)

2-hydroxylterephthalic acid (fluorescent)

Figure 3-2: The formation of hydroxyterephthalic acid (HTA)

Sahni and Locke (2006) quantified OH radicals in a pulsed corona discharge system using chemical dosimetry, dimethyl sulfoxide (DMSO) and NaTA. It was found that the rate of formation of the OH radicals followed zero-order law irrespective of the applied voltage or the probes concentration. At 45 kV, the rate of formation of OH radical via DMSO and NaTA dosimetry were 1.2×10^{-7} Ms^{-1} and 1.67×10^{-8} Ms^{-1} respectively. The authors established a linear relationship between the OH radical and applied voltage over time. Sahni and Locke (2006) concluded that the concentration of hydroxyl radical produced by a pulsed corona discharge depends on a plethora of factors such as chemical probe concentration, reactor configuration, electrode materials, solution pH, conductivity, applied voltage, air flow rate, additives amongst others. Jo and Mok (2009) reported that the concentration of hydroxyl radicals produced by a dielectric barrier discharge system depended on the concentration of the electrolyte in the aqueous electrode, the applied voltage, the discharge power, and solution pH. Tahara and Okubo (2012) employed 5, 5-dimethyl-1-pyrroline N-oxide (DMPO) as OH radical trapping chemical probe followed by ESR measurement. Surprisingly, no hydroxyl radicals were detected due to their short lifetimes. Instead the formation of H_2O_2 was confirmed. Further addition of Fe^{2+} prior to plasma discharge in the presence of H_2O_2 liberated hydroxyl radicals although at low concentration.

3.2.3.2 *Hydrogen peroxide*

Hydrogen peroxide is one of the most relatively stable, abundant powerful oxidants produced by the DBD reactor and as such plays a dual role, including the decomposition of organic contaminants as well as the disinfection of water. It dissociates in the presence of ultra violet light into hydroxyl radicals ($OH^{\bullet}$), which in turn recombine with the bulk solution to form H_2O_2. Thus, quantification of the amount of H_2O_2 produced by the DBD is indirectly a determination of the amount of $OH^{\bullet}$. There are different methods for quantification of hydrogen peroxide. However, the colorimetric method is mostly reported in literature (Sahni and Locke, 2006). This involves the spectrophotometric measurement of the intense-yellow orange formed as a consequence of adding titanylsulphate to a solution containing hydrogen peroxide. The yellow colour is due to the formation of peroxotitanyl sulphonic acid shown in the reaction scheme below.

$$TiOSO_4 + H_2O_2 + H_2SO_4 \longrightarrow TiO_2(SO_4)_2^{2-} + H_2O + 2H^+ \quad (8)$$

The concentration of H_2O_2 produced by the DBD reactor is equivalent to the concentration of the peroxo titanyl sulphonic acid measured using UV-visible spectrophotometry at 410 nm. The substitution of the corresponding absorbance value at this wavelength into the Beer's Lambert formula allows calculation of the initial concentration of H_2O_2. Magureanu et al. (2013) quantified the amount of H_2O_2 generated by a pulsed corona discharge system and found that the concentration of H_2O_2 increased with an increase in the exposure time up to 200 mg/L in 30 minutes and thereafter decreased to 170 mg/L in the presence of methylene blue. The authors attributed the slight decrease to competition between the methylene blue and the intermediate compounds. Zhang et al. (2013) quantified the concentration of H_2O_2 produced by the dielectric barrier

discharge at 20 kV in distilled water and phenol solution in the presence or absence of TiO_2. It was found that about 7.02 mg/L H_2O_2 was produced by the system in distilled water compared to the phenol solution, which further increased to 10.7 mg/L upon addition of TiO_2. The increase in peroxide concentration was attributed to an increase in the OH radical yield and dimerisation of OH radicals in plasma and plasma/TiO_2 system. Whereas, in the phenol solution, there was suppression of OH radicals by both the phenol and other degradation products, which prevents OH radical recombination thus is responsible for lower H_2O_2 concentration. Lei et al. (2007) employed the colorimetric and indigo methods to quantify the amount of H_2O_2 and O_3 produced by a pulsed corona discharge system. They found that the concentration of H_2O_2 and O_3 produced by a pulsed corona discharge system increased with an increase in discharge time and reached 0.64 and 0.029 mM within 60 minutes respectively. The values reported were less than the concentration of oxygen bubbled into the reactor. The authors ascribed lower concentration of H_2O_2 relative to oxygen bubbling (2.02 Mm) to the reaction between the active electrons and nitrogen. Whereas, the low concentration of ozone compared to oxygen (0.032 mM) was attributed to the reaction between oxygen and nitrogen atoms in the bulk solution, forming nitrates.

3.3 PHOTOCATALYTIC PROCESS

3.3.1 Parameters influencing photocatalysis

The photocatalytic process involving oxidation of organic pollutant in aqueous solution is strongly dependent on a number of parameters which influence the solution kinetics. These parameters include solution pH, initial organic pollutant type and concentration, pH of the catalyst, catalyst loading, light wavelength and intensity, as well as the quantity of reactive oxygen species, calcination temperature used for catalyst preparation, radical scavengers and ionic profile of the polluted water. The next section provides detailed information on the influence of some of the aforementioned parameters related to the photocatalytic activity of TiO_2 nanoparticles.

3.3.1.1 *Solution pH*

The mineralisation efficiency of organic pollutants in a typical heterogeneous photocatalytic water system is mostly governed by solution pH, which impacts closely on the catalyst surface charge and the ionisation/dissociation state of the pollutant (Chong et al., 2010). The ionisation of organic pollutants in solution depends on the pollutant pKa value or isoelectric point of the catalyst. Thus, the effect of solution pH can be explained on the basis of electrostatic interaction between the charged TiO_2 species in solution and the pollutant. This can be illustrated using the point of zero charge (P_{ZC}) of TiO_2 (Chong et al., 2009b, c). Thus a change in solution pH affects the surface charge of most semiconductor metal oxides due to the fact that they are amphoteric in nature. Specifically, the point of zero charge of TiO_2 is 6.0-6.5. When the pH of the solution is equal to the point of zero charge of TiO_2 (6.5), there is little interaction between the TiO_2 nanoparticles and

the contaminant due to lack of electrostatic forces of attraction. In such a situation, hydrated neutral species such as titanol (TiOH) dominate.

When the pH value is less than 6.5 (under acidic conditions) the TiO_2 surface is highly protonated and becomes a net positively charged species ($TiOH^{2+}$) and exerts electrostatic forces of attraction upon the negatively charged organic contaminants in the solution. Such electrostatic attraction between the duo improves the photocatalytic reactions especially when the concentration of the anionic organic pollutant is low (Chong et al., 2010; Friedmann et al., 2012). At pH greater than the point of zero charge (under alkaline conditions), TiO_2 is deprotonated and becomes a negatively charged species (TiO^-) and thus exerts electrostatic repulsion upon the anionic organic compounds in solution. Thus, the interaction between the surface charge density of TiO_2 nanoparticles and the electronic properties of the organic compounds is pH dependent.

Additionally, at a pH less than P_{ZC} (<6.5) radical scavengers such as HCO_3^-, Cl^-, SO_4^{2-} that are mostly present in water react with the protonated species ($TiOH^{2+}$) and reduce its efficiency. Conversely, at high pH, radical scavengers exert little influence due to strong electrostatic repulsion between the scavengers and OH-. Nevertheless, the electrostatic repulsion is responsible for low generation of hydroxyl radicals. The photocatalytic efficiency is therefore a measure of the adsorption of the organic pollutants onto the surface of the catalyst and the solution pH influences the surface charge and ionic state of pollutants which in turn may alter the reaction mechanism. Whang et al. (2012) studied the influence of the solution pH over the range of 4-11 on the degradation of nitrobenzene by the semiconductor photocatalytic process. The authors reported that high degradation efficiency was obtained at low pH of 4, which was attributed to the generation of more hydroxyl radicals.

3.3.1.2 *TiO_2 dosage/loading*

The amount (or dosage) of powdered TiO_2 nanoparticles in the bulk of liquid within the photochemical reactor determines the overall oxidation rate of organic pollutants. The increase in the TiO_2 loading initially accelerates the photocatalytic mineralization reaction rate of organic pollutant and then decreases at high dosage values due to light scattering and screening effects of the particulates. In fact, there is a direct linear relationship between the amount of TiO_2 nanoparticles in solution and the overall photocatalytic reaction rate (Gaya and Abdullahi, 2008). This means the mineralisation rate of a pollutant increases with an increase in TiO_2 load up to an optimum loading. This linear relationship continues to exist until the oxidation rate is no longer proportional to the TiO_2 load. Beyond the optimum value, any further increase in the TiO_2 dose only causes screening of light without any significant improvement in the mineralisation rate. This is because the increase in the TiO_2 dose beyond the saturated level causes the solution to become highly turbid and leads to non-uniform distribution of light intensity. In such a situation, the particle-saturated solution obstructs light penetration and limits interaction with the pollutant, thus lowering the degradation efficiency.

Excessive addition of TiO_2 nanoparticles in the bulk solution promotes agglomeration/aggravation and light screening, which thus decreases the overall mineralisation rate. Establishing the optimum dose when using a powder form photocatalyst is crucial, but depends strictly on the solution pH and the nature of the pollutants.

The survey of literature revealed that catalyst dosage in the range of 0.2-1.0 g/L is sufficient for complete oxidation of organic pollutants. The influence of TiO_2 dosage on the extent of oxidation of organic pollutants using a photochemical reactor has been widely reported (Chong et al., 2010; Gaya and Abdullahi, 2008). The obtained results are however different, due to differences in the reactor configuration, UV lamp intensity, wavelength, wattage, organic compounds amongst other inconsistent parameters. In order to ensure sufficient light penetration and distribution that will guarantee effective activation of the catalyst and oxidation of the pollutants, excessive addition of powdered catalyst should be avoided. Thus, the optimum catalyst dose should be determined and added to the photochemical reactor during wastewater treatment. Supporting the photocatalyst on a suitable support would prevent the obscuring effect of particulates, and methods to durably support the photocatalyst is one of the aims of this study. Moreover, increasing the reactive surface of the supported photocatalyst is a further aim.

3.3.1.3 *Initial concentration of the pollutant*

The photocatalytic activity of TiO_2 nanoparticles often depends on the initial concentration of the pollutant. Under the optimised conditions of solution pH, TiO_2 dose, photocatalytic degradation of organic pollutants increases with an increase in the initial concentration of the pollutant until a certain level, where the reaction rate begins to decrease This observation has been widely reported in the literature by researchers (Pardeshi and Patil, 2008; Wei et al., 2009). This is because, as the initial concentration of the pollutant increases, the surface active sites of TiO_2 nanoparticles become saturated. The free, available hydroxyl radicals are thus limited, which affects catalytic performance, in turn reducing the mineralisation rate (Bahnemann et al., 2007). Additionally, photocatalytic degradation of higher concentration of organic pollutants generates a series of transformation products which remain in solution and may deactivate the catalyst surface via slow diffusion, thus reducing the degradation rate. On the contrary, the number of active binding site is not the rate determining step or limiting factor at low concentrations and as a matter of fact, a linear relationship exists between the reaction rate constant and the initial, low concentration of the pollutants. Therefore, the degradation reaction rate depends on both the concentration and nature of the organic contaminants being treated during the TiO_2 photocatalytic experiment. The concentration of both the particulate photocatalyst and organic pollutants must be optimised accordingly (Chong et al., 2010).

3.3.1.4 *Light wavelength*

The influence of ultraviolet light of different wavelengths on the heterogeneous photocatalytic reaction rate depends on the nature, phase and state of the TiO_2 nanoparticle. For instance, a light of wavelength $\lambda < 380$ nm is sufficient for the activation of the anatase phase of the commercial Degussa P-25 TiO_2 with a band gap of 3.2 eV while a light source of wavelength close to 400 nm is required to activate the rutile TiO_2 nanoparticle of band gap 3.02 eV. This shows that the catalyst with a smaller band gap requires a higher wavelength for activation than a catalyst with a high band gap. Thus, the reaction rate largely depends on the light wavelength and the band gap of the catalyst. Furthermore, ultraviolet light is categorised into three types, based on their

emitting wavelength and band gap, which includes UV-A, UV-B and UV-C (Chong et al., 2010). UV-A has a light wavelength ranging between 315-400 nm with a corresponding band gap of 3.10-3.94 eV. UV-B light wavelength ranges from 280 to 315 nm with a band gap of 3.94 and 4.43 eV. While the third category, UV-C mostly used to kill germs, has a light wavelength that ranges between 100-280 nm and a band gap of 4.43-12.4 eV. Among the three, UV-A remains the most widely used due to the availability of photon energy to activate the catalyst (Ochuma et al., 2007). Most reported laboratory scale experiments were conducted using UV-C lamp-driven photoreactor systems to activate the catalyst.

3.3.1.5 *Light intensity*

Aside from the previously mentioned factors, the extent of oxidation and conversion of organic contaminants in a typical photocatalytic reactor system is dependent on the distribution pattern of the light intensity within the photochemical reactor. The amount of light adsorbed by the semiconductor catalyst at a given wavelength is determined by the light intensity. The activation of the TiO_2 nanoparticle surface charge and the formation of electron-hole pairs is measured as a function of light intensity. The influence of light intensity on the oxidation reaction rate of organic pollutants has been widely reported (Ahmed et al., 2011). The increase in the light intensity is linearly proportional to the photocatalytic reaction rate. Finally, the influence of light intensity on the photocatalytic degradation rate must be investigated to guarantee effective utilisation of the photocatalytic oxidation reactor system.

3.3.1.6 *Interfering substances/radical scavengers*

The performance of a photochemical reactor and in particular, a heterogeneous photocatalyst, depends on the concentration of the inorganic species in the target water. Depending on the solution pH and the target surrogate organic compounds, radical scavengers influence the photocatalysis process via deactivation of the active sites on the catalyst. The photocatalytic deactivation is caused by inhibition between the anionic species on the TiO_2 surface and the anionic species in the target water (Chong et al., 2010). Additionally, the competition between the inorganic species and organic pollutants for the active sites on the catalyst also causes photocatalytic surface deactivation. The adsorption of the interfering substances onto the catalyst's active sites hinders the formation of hydroxyl radicals and decreases the photocatalytic degradation efficiency. Furthermore, radical scavengers such as nitrate, phosphate, sulphate, chloride, and carbonate destroy the hydroxyl radical by adsorbing the UV light and generating corresponding anionic radicals of lower oxidation potentials. Studies have shown that the photocatalytic degradation efficiency of organic pollutants is largely affected due to the presence of inorganic anionic species such as nitrates, carbonates, phosphates, sulphates, chloride, dissolved organic matter in water (Ahmed et al., 2011; Chong et al., 2010). Thus, a proper understanding of their roles and behaviours will assist in the design of an efficient photochemical reactor.

3.3.1.7 *Calcination temperature*

Depending on the photocatalyst synthetic routes employed, calcination temperature stimulates and controls the formation of nanostructured TiO_2. In fact, the structural phase transformation, degree of crystallinity, particle size and shapes are dependent on the calcination temperature applied during catalyst preparation. Calcination at lower temperatures may produce mixed phase of TiO_2. Whereas, calcination/annealing of TiO_2 gel/powder within the temperature range of 600-800ºC leads to structural phase change from a more thermodynamically and photochemically stable anatase phase to the condensed rutile phase. Furthermore, calcination/annealing at higher temperatures promotes the residual loss of water and volatile organic components, and hence may improve the crystallite growth. Additionally, calcination of TiO_2 gel at higher temperatures increases the colloidial thermal energy, and reduces the gel viscosity as well as the solvent dielectric constant. This further decreases the electrostatic barrier constant and suppresses particle agglomeration/aggregation. Studies have shown that photocatalytic activity of TiO_2 material synthesised at different calcination temperature varied but activity also depended on several other factors such as solution pH, nature of the surrogate model organic pollutants, interfering substances, light intensity amongst others (Ahmed et al., 2011, Chong et al., 2010).

3.3.2 Mechanism of heterogeneous photocatalysis

The basic mechanism of heterogeneous photocatalysis involves in-situ generation of powerful oxidants such as the hydroxyl radical under ambient conditions. In the heterogeneous photocatalysis process, the absorption of a photon of light either from sunlight or an illuminated light source by the semiconductor metal oxide such as titanium dioxide (TiO_2) causes the migration of a lone pair of electrons from the valence band to an empty conduction band, thus producing an electron (e^-)-hole (h^+) pair within the solid (Chong et al., 2010; Wankhade et al., 2013). These eventually break up into photoelectrons and photoholes in the conduction and valence band respectively. It should be noted that the photocatalytic reaction only becomes activated when the catalyst is able to absorb sufficient photon energy that is equal or greater than its band gap energy.

In a situation whereby the photons supplied have a lower energy than the catalyst band gap energy, energy degeneracy in the form of heat is usually evident. In the bulk solution, depending on the redox potential or energy level of the species (titanium and oxygen), the valence band becomes excited and oxidised while the conduction band of titanium dioxide accepts the transfer electron and is reduced. At this point, the semiconductor TiO_2 has become photo-excited (equation 9). Under irradiation from a highly energetic energy source, the positive hole (h^+) of the catalyst either oxidises the pollutant directly or oxidises water molecules into hydrogen gas and hydroxyl radicals. The negative electron hole combines with oxygen molecules and produces superoxide radicals (equation 10 and 11).

Photoexcitation: $TiO_2 + hv \rightarrow e^- + h^+$ (9)

Charge Carrier trapping of e-: $e\text{-}CB \rightarrow e^- TR$ (10)

Charge carrier trapping h+: $h^+VB \rightarrow h^+TR$ (11)

Electron-hole recombination: $e\text{-}TR + h^+VB(h^+TR) \rightarrow e\text{-}CB + heat$ (12)

Photoexcited e- scavenging: (O_2) ads + e- → O_2●- (13)

Oxidation of hydroxyls: HO- + H → HO● (14)

Photodegradation by HO●: R-H + HO● → R● + H_2O (15)

Direct photoholes: R + h+ → R+ → S(s) → final degradation products (16)

Protonation of superoxide: O_2●− +H+ → HOO- (17)

Co-scavenging of e-: HOO●+e-→HO_2- (18)

Formation of peroxide: HOO●+H+→H_2O_2 (19)

During the electron transfer and electron acceptor process, the hydroperoxyl radical is produced which extends the shelf life of photoholes (Wankhade et al., 2013). Furthermore, electron-hole recombination often occurs except if O_2 is available in the bulk to scavenge the electrons and produce the superoxide (O_2●-). Further reaction with protons (H^+) produces the hydroperoxyl radical (HO_2●-) and complete protonation gives hydrogen peroxide (H_2O_2). These reactive species react with organic pollutants via direct electron acceptors to give intermediates. Further oxidation produces CO_2 and H_2O. The step by step oxidation-reduction process leading to the formation and decomposition of organic pollutants by the free reactive species is shown in equation 6-13 (Chong et al., 2010; Wandkade et al., 2013).

The photocatalytic activity depends largely on the ability to prevent or reduce the electron-hole recombination rate on the catalyst surface. Literature surveys have shown that more than 90% of photogenerated electron-hole pairs recombined instantly after excitation, thus were responsible for the low quantum yield of most semiconductor photocatalytic reactions (Friedmann et al., 2010). The photocatalytic reaction occurs within a few femtoseconds (equation 10-15) and the cycle continues as long as energetic photo-light is available. In short, the decomposition of organic pollutants via the photocatalytic mechanism can both be facilitated by the hole and the hydroxyl radicals. The degradation pathways may not necessarily be the same but the same products in equal proportions are envisaged, thus making it extremely difficult to distinguish between the two. The photo-induced redox process of TiO_2 is shown in the equations below (Dalrymple et al., 2007).

From the above equations, the e^- denotes the conduction band while h^+ represents the valence band electrons respectively. e^-_{TR} and h^+_{TR} depict surface trapping valence band electrons and conduction band-holes respectively. While S represent the intermediate species. In fact, the mechanism of electron-hole pair formation on TiO_2 surfaces involves five key steps namely: photo-excitation, diffusion, trapping, recombination, oxidation (Figure 3.3) which steps eventually generate the powerful oxidants responsible for the degradation of target pollutants into carbon dioxide, water, and inorganic ions. The mechanism of generation of free reactive species such as OH, H_2O_2 depends on the nature of the pollutants and the photocatalyst (Friedmann et al., 2010). Lastly, the mineralisation of recalcitrant organics can be achieved via the combined efforts of the semiconductor metal oxides, intense ultraviolet light and hydroxyl radicals.

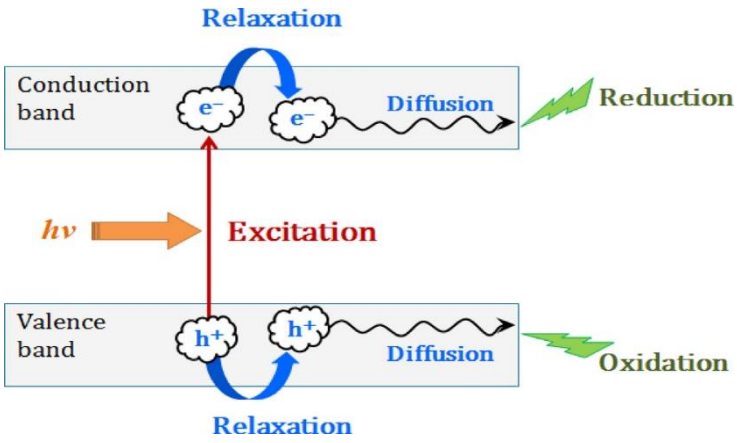

Figure 3-3: Schematic illustration of the formation of photoinduced charge carriers (e-/h+) on absorption of UV light (Lee and Park, 2013)

3.3.3 Application of TiO_2 for water treatment

Considering the significance of clean water to human life, it becomes imperative to preserve and sustain potable water including removal of toxic pollutants via adoption of a highly effective and eco-friendly alternative technology. Among the well-known advanced oxidation technologies is semiconductor-mediated photocatalytic oxidation technology, being one of the advanced oxidation technologies (AOT), used for water treatment. Heterogeneous photocatalysis involves acceleration of photo-light induced reactions in the presence of a catalyst (TiO_2). Novel nanomaterials are of great interest due to their high surface-to-volume ratio. TiO_2 is a photocatalyst which has attracted attention from fundamental research due to its strong oxidizing power and long-term stability (Chong et al., 2010; Suwarnkar et al., 2014).

Several studies have been conducted on the use of titania photocatalysts or immobilized forms of titania to degrade and mineralise organic compounds. On the other hand, immobilization of titania with either metals or non-metal oxides may not actually increase the photocatalytic activity of TiO_2 in the visible region. This is because in a photocatalytic reaction, two or more phases such as a light source and a semiconductor material are involved. While the photons initiate the photoreaction, the catalyst system is totally involved in the oxidation and reduction reactions of the pollutants using long wavelengths (Suwarnkar et al., 2014). Apart from that, only 7% of the visible light is utilised due to the band-gap. In order to increase the photocatalytic activity of TiO_2 using visible light, there is the need to maintain a stoichiometry between the catalyst and the mixed metal oxide. Despite this shortcoming, heterogeneous semiconductor TiO_2 processes appear as an alternative treatment design that could supplement existing technologies (Chong and Jin, 2012).

Heterogeneous photocatalysis is an environmentally friendly technique that makes use of sunlight or UV radiation and can be conveniently applied even in remote villages that lack access to electricity. The application of nano-titanium dioxide for water treatment is considered even more interesting for removing toxic organic pollutants in the aqueous matrix because the technology produces no sludge or residue of the pollutants.

Moreover, the catalyst itself remains unchanged throughout the process (Ibhadon and Fitzpatrick, 2013). Heterogeneous photocatalysis is currently in use in countries like Japan, USA, India and China for water and wastewater treatment. Apart from destroying bacteria and viruses, the increasing occurrence of algal bloom and subsequent formation of cyanobacterial microcystin toxins was reduced when TiO_2 in immobilized form was applied in fresh water treatment (Fukushima et al., 2000; Fujishima et al., 2008).

Studies have shown that thousands of non-degradable organic pollutants can be successfully decomposed by TiO_2 photocatalytic technology (Ahmed et al., 2011; Jiang et al., 2012). This section of the review will focus on a few applications of TiO_2 for the removal of organic pollutants in water. Yang et al. (2012) combined a novel functionalised nano-TiO_2 with an electrocatalytic membrane to treat oily wastewater and an increase in oil removal rate was observed with a corresponding decrease in the liquid hourly space velocity through an electrocatalytic membrane. The authors submitted that there was a synergy between the functionalised nano-particles and the membrane. The disinfection ability of Ag-TiO_2 composite films was linked to the electron trapping ability of Ag^+ which prevented the recombination of electron-hole pairs and enhanced the photodisinfection efficiency.

In another study, Domínguez-Espíndola et al. (2012) applied TiO_2 film and silver doped TiO_2 powders to disinfect municipal wastewaters containing gram-negative bacteria via monitoring of the microbiological inactivation under sunlight and UV irradiation. Their study showed that the maximum efficiency, and complete inactivation of faecal coliforms was achieved within fifteen minutes, and 4%-Ag impregnated on TiO_2 powders deactivated the bacteria more efficiently than ordinary TiO_2 powder. Dalrymple et al. (2007) confirmed complete photocatalytic degradation of estrogens without producing estrogenic intermediates in potable water. Hintsho et al. (2014) found that incorporation of 2% Ag onto carbon nanotubes containing 20% TiO_2 successfully removed 92% methylene blue in water. The observed increase was ascribed to the electron trapping ability of the silver which reduced electron-hole recombination rate.

Yang et al. (2006) demonstrated the synthesis of anatase TiO_2 nanoparticles for the degradation of methylorange using a sol-gel method. The effects of H_2O_2 addition, pH, TiO_2 phase composition and the recycled TiO_2 on the photocatalytic degradation of methyl orange (MeO) in TiO_2 suspensions under ultraviolet (UV) illumination were monitored. The authors confirmed that low pH value, and H_2O_2/TiO_2 addition were responsible for the photocatalytic oxidation of the MeO solution. The photodegradation rate decreased with an increase in pH value of the solution and varied with different amounts of H_2O_2. The obtained pure anatase TiO_2 showed better photocatalytic activity towards MeO decolouration than biphase TiO_2.

Austin et al. (2012) compared the decomposition rate of methaldehyde using UV/H_2O_2 and UV/TiO_2 treatment and argued that both treatment processes under the same optimised conditions could degrade the model compounds at an equal rate, but for a natural wastewater, the UV/TiO_2 treatment efficiency was reduced due to interference and blockage of hydroxyl radicals by background ions and organic matter. Chen et al. (2007) employed photocatalysis with nanosized TiO_2 powder to degrade dimethoate. It was observed that there was no correlation in the dimethoate and TiO_2 concentration increment and as such low degradation of the pollutants was observed. On the other hand, $H_2O_2/K_2S_2O_8$ incorporation with photocatalysis followed by sonication enhanced the decomposition efficiency. Chong and Jin (2012) investigated the photocatalytic ability

of titanium dioxide (TiO_2) nanofibres as a pre-treatment technique to degrade carbamazepine (CBZ) in simulated hospital wastewater. The obtained results revealed that during the 4 hour reaction time, 78% of CBZ, 40% of COD and 23% of PO_4 concentrations from influent wastewater were removed. The results after 0.5 hour analysis by high performance size exclusion chromatography revealed a dramatic shift of molecular weight from higher fractions (>10-1000 kDa) to lower fractions (<10 kDa). The photodegradation data perfectly fitted the Langmuir-Hinshelwood kinetics model. Li et al. (2011) observed that with increasing Ag-loading, the wavelength of Ag-TiO_2 shifted but the band gap energy decreased. The photocatalytic activity of Ag-TiO_2 was found to increase with the molar ratio of Ag-doped from 0 to 0.8%, but however, declined despite a further increase of the molar ratio to 2.0%. The commendable visible photoactivities of the nanocomposites were attributed to the activity of Ag deposits that sometimes act as electron trapper helping in the MB adsorption. In another study, photodegradation assisted by a catalyst (TiO_2) was conducted for removing EDCs (estrone, 17β-estradiol) using sunlight and UV irradiation (Zhang and Zhou, 2008).

Despite considerable benefits that nanotechnology affords, there are certain specific questions concerning the toxicity of nanomaterials to humans as well as the impact on the immediate environment (Clemente et al., 2012; Keller et al., 2012; Tsoi et al., 2013). In order to reduce the toxicity levels arising from the release of TiO_2 particles in water, there is a need to develop nanoparticles on rigid supports as this appears promising and reduces post separation challenges. However, the immobilisation of TiO_2 nanoparticles on a rigid support should be done to favour the formation of the anatase phase, minimise the release of any particles and guarantee minimal leaching rate. The theoretical understanding of a photocatalytic reactor design as well as parameter optimisation remains another technical task. Recently, a lot has been done in terms of addressing some challenges associated with heterogeneous photocatalysis, such as doping /immobilisation of the semiconductor catalyst with non-metal or metal dopants (Zhu et al., 2008; Tryba et al., 2009). Plasmonic elements are sometimes used to trap the charges on TiO_2 thus improving the responsiveness of the catalyst to visible light. Thus, heterogeneous photocatalysts developed on a support could be integrated with dielectic barrier discharge systems in order to accelerate the degradation rate of recalcitrant toxic pollutants present while minimising cost and the same time reducing the reaction time. This was the approach taken in this study.

3.3.4 Choice of TiO_2 support materials

In spite of several unique characteristics of TiO_2 nanoparticles, the photosensitivity and photocatalytic activity of TiO_2 is limited due to high band gap energy, electron-hole recombination rate from valence band to conduction band, and particle agglomeration that reduced the photocatalytic efficiency. Besides the aforementioned, post-separation and recovery from wastewater after utilization constitute major impediments to its full scale industrial applications. Based on the inherent shortcomings associated with the powder TiO_2 nanoparticles, immobilisation of TiO_2 nanoparticles on suitable substrates such as glass, ceramic, polymers, activated carbon, wooden fibre cloth, carbon fibre, stainless steel mesh amongst others has received attention in the field of heterogeneous photocatalysis. Several researchers have synthesised different supported TiO_2 nanoparticles. For instance, Hänel et al. (2010) employed the sol-gel method followed by a dip-coating technique to prepare pure and boron-doped TiO_2 nanoparticles supported on glass beads. The authors found

that the supported catalysts were stable and removed 33% phenol after three consecutive cycles, which suggests that the catalysts were re-usable. Shen et al. (2012) synthesised pure anatase TiO_2 nanoparticles supported on porous glass beads using an in-situ ion exchange process. The prepared supported photocatalysts were found to exhibit excellent photocatalytic activity and successfully removed 65% methyl orange within 30 minutes. Habibi et al. (2012) prepared alumina supported TiO_2 nanoparticles using the sol-gel method and found that under the optimum catalyst preparation conditions of calcination temperature (550ºC), refluxing temperature (66ºC) and calcination time (2 h), 61% degradation of acetaldehyde was achieved after 250 min. Wang et al. (2015) synthesized Cr-doped TiO_2 nanoparticles supported on a natural zeolite and found that 10% mol Cr-immobilized TiO_2/zeolite annealed at 400ºC removed 41.73% methyl orange compared to undoped TiO_2/zeolite which only removed 17.9%. The authors attributed the improved removal efficiency to the doping effect of Cr, which prevented electron-hole recombination rate.

Among the support materials upon which the TiO_2 catalyst is developed, stainless steel mesh possesses unique qualities when compared to other supports, which include maintenance of structural integrity under the high heat treatment (during calcination of TiO_2) whereas other materials such as quartz glass may deform and melt depending on the glass transition temperature. Also, stainless steel mesh is not susceptible to attack during the coating process unlike other supports. For instance, Nam et al. (2004) reported that diffusion of sodium from soda-lime glass into the TiO_2 film decreased the photocatalytic efficiency. Apart from the aforementioned, stainless steel mesh can be utilized in the electrochemical process while quartz and ceramics cannot be used due to their dielectric properties. Finally, it can be easily used in complex shapes and has excellent mechanical properties (Balasubramanian et al., 2004b). These prior studies informed our choice of stainless steel mesh as support in this study.

3.4 THE DIELECTRIC BARRIER DISCHARGE (DBD) TREATMENT SYSTEM

3.4.1 Overview

Dielectric-barrier discharges combine the advantages of non-equilibrium plasma properties with the ease of atmospheric-pressure operation. The advantage of using DBD to treat wastewater cannot be overemphasized; some of these benefits are summarized as follows:

- There is a direct multiple production of highly reactive chemical species in-situ without chemical dosing thereby eliminating the need for supplying sources of hydrogen peroxide, ozone and other highly reactive compounds externally (Malik, 2010; Jiang et al., 2014).
- There is a high rate of liquid-phase reactions which enhance and facilitate transfer into the gas phase (Locke et al., 2006)
- There is production of UV light, shock waves and putative supercritical conditions localized in the non-homogenous discharge channel of the transfer (Bruggeman and Locke, 2013).
- There is also control of relative amount of reactive species through the adjustment of applied electric fields and liquid flow rates.

However, this is not to say that DBD does not has its drawbacks, for instance the complexity of liquid reactions due to involvement of a wide range of closely coupled physical and chemical factors. The present state of knowledge is also not sufficient for predictive and accurate reactor design and analysis, although significant advances have been made. One of the general issues and questions concerning the role of electrical discharge processes for wastewater treatment is its ability to combine with other AOTs or conventional methods.

3.4.2 Combined dielectric barrier discharge system and heterogeneous photocatalysis

To date, studies still uphold advanced oxidation techniques (AOTs) involving the combination of corona discharge and heterogenous photocatalysis as the most promising method for the removal of PPCPs/EDCs from hospital wastewater and surface water (Kathryn et al., 2009; Fabiola et al., 2010). Corona discharge reactors incorporating nanocomposites is one of the fastest growing areas in environmental and nanotechnology being a promising tool for treating wastewater; although not intended to replace conventional methods but to augment these processes for higher-quality water. The term electrohydraulic discharge (ED) is used in general expression used to describe all non-thermal plasma systems using electrical discharge (current). While dielectric barrier discharge (DBD) is one particular configuration of the ED system. DBD plasma discharge is a novel water cleaning technology which has recently gained research interest, mainly due to its high efficiency, high speed, and zero or less chemicals needed (Santiago et al., 2007).

This non-thermal treatment technology injects a high-current/high-voltage electrical discharge between two submerged electrodes into an aqueous solution to form plasma (Jiang et al., 2014). The breakdown of this plasma generates chemically active species such as free radicals (OH), ions, atoms, meta-stables, O_3, and H_2O_2, etc. When combined with photocatalysis systems, a semiconductor (such as TiO_2) and UV or visible light combinations are used. When the UV light reacts with TiO_2, hydroxyl radicals are formed and mineralise organics pollutants into harmless inorganic pollutants such as carbon dioxide and water (Malik, 2010). The dielectric barrier discharge system for instance can be coupled with catalyst, carbon material, metal oxide, metal ions and other catalyst in order to improve the overall process efficiency. The high electric field generated as a consequence of high voltage electrical discharge, coupled with the photocatalyst that reduces the recombination rate of electron-hole pairs on the surface of TiO_2 can enhance the system's performance.

In addition, the electric field, ultrasonic irradiation and shock waves generated within the reactor also aids in the cleaning of the TiO_2 surface. This eventually hastens the mass transfer of the pollutants onto the solid catalyst surface. Thus, integration of plasma technologies with photochemical oxidation may improve their treatment performance and at the same time overcome some of their individual shortcomings (Jiang et al., 2014). However, the degradation efficiency of combined system depends on the nature of treated wastewater in question. Scott and Ollis (1995) highlighted four categories of wastewater contaminants namely; recalcitrant compounds, largely biodegradable compounds, inhibitory compounds and intermediate by-products. Thus, the performance of integrated processes may be dramatic, modest, negligible or adverse depending on the reaction conditions.

Dobrin et al. (2013) utilized pulsed corona discharge generated above liquid to degrade diclofenac in water. The results as presented indicated that complete removal of diclofenac occurred within 15 minutes. However, only 50% of the compound decomposed after 30 minutes of exposure to plasma. In the same vein, Zhang et al. (2012) utilized a pulsed high voltage discharge system to eliminate 2, 4-dichorophenol (2, 4-DCP) from aqueous solution. The study showed that a rise in peak voltage from 18 kV to 26 kV with a corresponding energy input from 0.0057 to 0.0397 kWh was responsible for the increase in degradation efficiency from 58% to 99% within 42 min. Low pH value and salt content of the solution were recognized as the possible factors thwarting the degradation of the modelled pollutant.

Bian et al. (2011) applied pulsed high voltage discharge to decompose 4-chlorophenol in water. The degradation process was accompanied with the formation of intermediate products such as hydroquinone, 4-chlororesorcinol and 4-chlorocatechol. Other intermediates identified included formic, acetic, oxalic, malonate, maleic and malic acid. In general, more of the intermediate 4-chlorocatechol was formed than hydroquinone or 4-chlororesorcinol. The possible degradation pathways for the intermediates and other ring-opening compounds were proposed. The initial degradation step was hydroxylation despite direct cleavage products observed at C(1)-C(2) or C(5)-C(6) bond. Within 36 minutes of the discharge, more than 50% mineralisation of the carbon compounds obtained from organic acids were observed while less than 20% of the carbon from aromatic products (equivalent to about 94% of initial carbon) was removed. However, after 60 min of discharge, 4-chlorophenol and its aromatic intermediates were removed completely leaving behind organic acids such as acetic and oxalic acid. With prolonged discharge to 120 min, 86% degradation was achieved leaving behind 14% of the initial carbon.

Wahyudiono et al. (2013) utilized pulsed discharge plasma over water to decolourise orange G, orange II, congo II and naphthol blue black. The results presented revealed that the rate of decolourisation of the dyes increased with a rise in the peak pulse voltage and pulse number. The maximum mineralisation rate of 50.05%, 41.64%, 44.98%, 53.25% was achieved corresponding to orange G, orange II, congo II and naphthol blue black. Zhu et al. (2013) found that an increase in the discharge voltage or pulse frequency is directly proportional to the removal rate of phenol. Equally, an increase in the oxygen flow rate was proportional to the rate of phenol removal from water. The energy efficiency and minimisation of economic cost of the electrohydraulic discharge system depends on its combinatory role with other AOTs, particularly photocatalysis. To buttress this fact, Scott and Ollis (1995) submitted that process integration is more beneficial and economical than a single AOT for wastewater treatment. The authors further found that biological pretreatment of the wastewater improved the overall efficiency of the integrated process. The authors admitted that coupling of the chemical and biological process is a difficult task during investigations and even when operated at full scale.

Jiang et al. (2014) also affirmed that the improvement of energy efficiency with minimal economic constraint lies in the coupling of plasma technology with heterogeneous photocatalysis. Thus, the integration of a dielectric barrier discharge (DBD) reactor with heterogeneous photocatalysts will enhance the degradation efficiency compared to single advanced treatment options (Li et al., 2007; Wang et al., 2008). The semiconductor photocatalyst utilises the ultraviolet produced during plasma discharge. The incorporation of

TiO_2 nanocomposites into such electrohydraulic discharge systems were found to enhance the photocatalytic activity of semiconductor metal oxides via a dramatic shift in the electron distribution (Wang et al., 2008).

Zhang et al. (2013) found that the degradation efficiency of indigo carmine solution was enhanced when bipolar pulsed discharge plasma was combined with TiO_2 photocatalysts. In fact, complete decolouration occurs within the first three minutes. Also, according to Chavadey et al. (2007) the integration of corona discharge with heterogeneous semiconductor metal oxides contributed to the generation of the superoxide radical anion (O^{2-}) responsible for the degradation of the pollutant. The performance of the electrohydraulic (or di-electric barrier) discharge system alone either in the laboratory or semi-pilot plants has been satisfactory. Therefore, its combination with other AOTs especially with the synthesized supported heterogeneous photocatalysis offer hope for real applications in the near future.

3.4.3 Single and combined advanced oxidation technologies based on dielectric barrier discharge system

Studies have shown that DBD systems can remove and degrade priority pollutants (Magureanu et al., 2011). Available information from literature indicates that no single advanced oxidation technology on its own is efficient to remove all contaminants, and the current practice requires a combined approach (Bruggeman and Locke, 2013). In trying to couple treatment processes, economic feasibility, system compatibility, and energy cost should be taken into consideration and comparative studies are needed with existing conventional methods. The DBD system can be coupled with catalysts, such as metal oxides, metal films and other catalysts to enhance free radical production and ultimately improve the overall process efficiency at a shorter time to overcome the shortcomings of individual processes (Jiang et al., 2014). However, the degradation efficiency of combined systems depends on the nature of the wastewater to be treated.

Wang et al. (2008) applied glow discharge plasma to degrade bisphenol-A (BPA) in aqueous solution. They observed that the BPA elimination rate as well as the rate of formation of H_2O_2 reduced in the presence of electrolytes such as sodium sulphate and phosphate solution, but increased in sodium chloride solution. Dobrin et al. (2013) utilized pulsed corona discharge generated above liquid to degrade diclofenac in water. The results as presented indicated that only 50% of the compound decomposed after 30 min of exposure to plasma. Magureanu et al. (2010) applied dielectric barrier discharge to decompose pentoxifylline in water. The influence of pulse repetition rate and initial concentration of the pollutant on the pollutant degradation rate and degradation yield were explored. It was found that pentoxifylline degradation rate depended on both parameters, and 92.5% conversion rate with a corresponding degradation yield of 16 g/kWh was achieved after 60 minutes.

In the same vein, Rong et al. (2014) demonstrated sulfadiazine degradation via water falling film dielectric barrier discharge system. The influence of solution pH, initial pollutant concentration, radical scavengers, and dosage of Fe^{2+} were explored. The authors observed 98% conversion rate for a 10 mg/L solution within 30 minutes at pH 9.10 in the presence of 1.0 mmol/L Fe^{2+} compared to 85% in the absence of Fe^{2+}. It was found that the presence of Fe^{2+} in the plasma zone enhanced the OH radicals and increased the mineralisation rate.

Liu et al. (2012) utilised dielectric barrier discharge alone to degrade carbamazepine in water. The authors achieved 100% pollutant removal rate via ex-situ discharge within 3 min. However, the degradation efficiency was affected by the formation of NOx, which consumed oxygen and reduced the solution pH.

Furthermore, Lesage et al. (2013) applied both dielectric barrier discharge and gliding arc discharge to decompose 4-chlorobenzoic acid in water. The authors found that DBD exhibited greater degradation efficiency than gliding arc discharge with respect to the pollutant. The formation of NOx and corrosion of the brass plate reduced the pollutant removal rate. Lesage and colleague (2013) revealed that gliding arc discharge generated a high concentration of NOx, which affected the solution pH and O_3 concentration more than in the case of DBD.

Zhang et al. (2013) demonstrated that combined pulsed plasma and TiO_2 nanotubes removed 98% phenol in water within 60 minutes with 20 kV discharge voltage compared to 60% removal rate by pulsed plasma alone. The authors ascribed the high removal rate to the existence of a synergistic effect between the pulsed plasma and the photocatalysts. Qu et al. (2013) investigated the decomposition of phenol in water using combined plasma/TiO_2 photocatalysis. They found that the combined system with a discharge voltage of 24 kV removed 91.4% phenol within 50 minutes compared to 60% removed by the plasma system alone. They linked the high removal rate to the production of more hydroxyl radicals by the combined system than in a single plasma system.

Wang et al. (2007) reported that pulsed corona discharge with a discharge voltage of 21 kV combined with TiO_2 supported on glass beads achieved 65% phenol removal within 60 minutes compared to 57% with pulsed corona discharge alone. The increase in the mineralisation rate of phenol was ascribed to the existence of a synergistic effect between the two processes, which possibly increased the amount of OH radicals, thus contributed to high degradation efficiency. The concentration of H_2O_2 produced by the combined system was 1.5 mmol/L compared to 1.0 mmol/L produced by pulsed corona discharge alone. The experiment was conducted as a function of gas bubbling type, solution pH and radical scavengers. In addition, Tang et al. (2013) utilised a combination of dielectric barrier discharge plasma and granular activated carbon (GAC) immobilised TiO_2 nanocomposites to decompose phenol in water.

Tang and co-workers (2013) found that combined DBD with TiO_2-GAC with input discharge voltage of 30 kV removed 88% phenol after 120 minutes compared to 69% obtained via DBD with GAC only. The 19% phenol removal rate was attributed to additional OH radicals provided by TiO_2. It should be noted that the difference in the removal efficiency reported by various authors can be attributed to several factors such as reactor configurations, applied voltage, initial concentration and type of pollutants, volume of aqueous solution, applied current, etc. None of the individual systems on their own were able to achieve complete degradation, but with an integrated system, degradation of the target pollutants was possible over time. Complete elimination is not achieved in all cases but the addition of a photocatalyst enhanced the observed removal. Therefore, the combination of the DBD system and heterogeneous photocatalysis offer hope for real applications in the near future.

3.5 INDICATOR PARAMETERS USED IN WATER TREATMENT

Wastewater comprises different constituents such as organic contaminants, inorganic species, and pathogenic agents amongst others. The organic species mostly identified in different water sources consist of pharmaceuticals, EDCs, pesticides, disinfection by-products (DBPs), metabolites, algae, and nutrients (Lessage et al., 2013). While the inorganic species include toxic metals, trace metals, radioactive elements and salts. These constituents are further classified into biodegradable and non-biodegradable species. The quality of potable drinking water or reused water is measured based on the reduction of these constituents to tolerable, permissible or acceptable limits using different indicator parameters (Rocha et al., 2013). These indicator parameters include, total organic carbon (TOC), chemical oxygen demand (COD), biochemical oxygen demand (BOD), biodegradable dissolved organic carbon (BDOC), colour, turbidity, alkalinity, pH, hardness, total dissolved solid (TDS), nitrogen and phosphorus content, chloride, and faecal coliforms. Apart from chemical analysis, biological assays involving the use of different toxicity kits or cell lines can also be conducted on the treated water to further confirm the purity level of such water (Oller et al., 2011; Makene et al., 2016).

Bioassay tests would provide information on the toxicity level of the water. Different types of toxicity assays such as anti-inflammatories test, nitrous test, daphnia test, interleukin 6 (IL-6) assays have been conducted on treated water (Oller et al., 2011). Therefore, the overall water quality can be measured using both chemical analysis as well as toxicity assays. In this study, the extent of mineralization of BPA or 2-NP was measured in terms of reduction in the total organic carbon.

Total organic carbon (TOC) is a measurement of the total, non-purgeable, chemically bonded organic carbon that is converted to CO_2. TOC includes the particulate organic carbon (POC) and dissolved organic carbon (DOC). It is an important indicator parameter mostly applied to measure the quality of water and performance of drinking water purification processes with regards to the presence of volatile and non-volatile organic compounds (Oller et al., 2011). The determination of TOC value involves basically two stages. The first stage deals with the conversion of the organic carbon to simple molecules such as CO_2. This can be achieved using any of the following processes: photodecomposition, thermal combustion, wet oxidation and pyrolysis methods (Fung et al., 1996). However, each of these methods has limitations. In the case of photodecomposition, the TOC value of water that contains recalcitrant non-purgeable organic compounds cannot be determined.

In addition, wet oxidation is limited to non-volatile organic compounds while the pyrolysis method cannot be used to determine low TOC values (1 mg/L) in a large volume of water. Whereas, the thermal method can decompose recalcitrant volatile and non-volatile organic compounds and can even be used for large volumes of water containing low TOC values (Anouzla et al., 2009). The second stage involves quantitative measurement of the CO_2 formed during the conversion of the organic bound carbon. The CO_2 measurement can be done using any of the following methods: nondispersive infrared (NDIR) absorption spectroscopy, thermal conductivity detector, ion exclusion chromatography (IC), non-suppressed ion chromatography, acid/base titration, gravimetry amongst others (Fung et al., 1996). The first three techniques require the use of analytical equipment while the last two do not. The extent of degradation of organic pollutants via DBD or

jet loop reactor can be measured either by measuring TOC or biological dissolved organic carbon (BDOC). It also involves determining the differences between the inorganic carbon and the total carbon content in the mixture. TOC cannot be conveniently used to distinguish between the biologically oxidisable constituents and inert organic matter. In this study, the extent of degradation of the modelled pollutants was measured using TOC as indicator parameter. The step by step conversion of the organic pollutant to CO_2 is shown in the equations below

$$R + O_2 \longrightarrow CO_2 + H_2O \quad (20)$$

$$R\text{-}N + O_2 \longrightarrow NO + CO_2 + H_2O \quad (21)$$

$$R\text{-}Cl + O_2 \longrightarrow HCl + CO_2 + H_2O \quad (22)$$

Where R represents carbonic substance.

3.6 SUMMARY

Advanced oxidation techniques have been shown to be highly effective for removing problematic, residual emerging contaminants from primary or secondary treated effluents. Especially, research has proved that combined advanced oxidation technologies worked better than single approaches. Photocatalysis is widely seen as a promising advanced oxidation technique for organics degradation, especially when doped with plasmon metals, but unless the photocatalyst is supported, the particulate form causes issues such as light penetration and post treatment separation. Dielectric barrier discharge, one of the forms of electrohydraulic discharge, has been studied extensively as a suitable advanced oxidation water treatment route that generates active free radical species in solution and proved to be suitable for organics decontamination of wastewater. Various studies were found in which photocatalysts were used in combined form with other advanced oxidation treatment options, but few studies exist on the integration of the photocatalyst in a dielectric barrier discharge system.

Moreover, the literature review detailed the various analytical procedures that can be applied to detect and quantify the type and concentration of free radical species generated in solution. In this study the research gaps identified showed that a significant challenge to integrating photocatalysis in a combined advanced oxidation system such as the dielectric barrier discharge system would be to support the photocatalyst on a suitable support whilst retaining the highly active anatase phase as well as maintaining a high surface area. The most feasible route to plasmon doping of the supported catalyst was identified based on prior knowledge. The photocatalyst will be integrated into a dielectric barrier discharge system for a combined advanced oxidation system in which no chemicals need to be added. Moreover the mechanisms and degradation pathways of endocrine disrupting compounds in a combined TiO_2/DBD system and the reactive species are to be determined.

CHAPTER 4: DEGRADATION OF ORGANIC POLLUTANTS USING TiO_2 COMPOSITES

4.1 INTRODUCTION

This chapter deals with the synthesis and characterization of photocatalytic nano-composites used in this study. The experimental protocols for the synthesis of supported TiO_2 nanocrystals, plasmon doping of TiO_2 nanocomposites, as well as the analytical techniques used in characterization of the nanocomposites are also detailed. Finally, results of the characterisation of the fused silica supported (Au, Cu and Ag) TiO_2 films as well as the stainless steel supported Ag/TiO_2 composite materials are discussed. The photocatalytic experimental details are presented firstly, then the results of photocatalysis are presented, firstly of the fused silica supported films and then the stainless steel supported samples. The degradation pathways of BPA and 2-NP pollutants in the DBD advanced oxidation system are presented at the end of this chapter.

4.2 METHODS FOR THE SYNTHESIS OF TiO_2 COMPOSITES

4.2.1 Overview

Nano TiO_2 can be synthesised via different techniques such as the sol-gel method, solvo-thermal method, hydrothermal treatment, chemical vapour deposition, chemical precipitation methods, sonochemical method, microwave method, electrodeposition amongst others (Karami, 2010). The synthesised TiO_2 material can be in the form of powder, crystals, or thin-films. Extensive reviews on most of these techniques, as well as the basic principles of heterogeneous photocatalysis particularly semiconductor TiO_2 have been widely reported in literature (Ahmed et al., 2011; Chong et al., 2010; Friedmann et al., 2012; Gaya and Abdullah, 2008; Nainani et al., 2012). Some of the commonly adopted procedures for the synthesis of TiO_2 nanoparticles are briefly explained below.

4.2.1.1 *Sol gel method*

A sol-gel method involves the formation of a colloidal suspension or sol through inorganic polymerisation reactions of titanium precursors in the presence of a solvent (Gupta and Tripathi, 2012). The titanium precursors can be inorganic metal salts ($TiCl_4$) or metal organic compounds {$(Ti(OCH(CH_3)_2)_4$}. In a typical sol-gel process, four basic stages are involved, specifically hydrolysis, polycondensation, drying and calcination/annealing. The hydrolysis step basically involves the dissolution of the titanium precursor in water or alcohol to form the colloidal solution or sol as shown in equation 23.

$$Ti(OR)_4 + 4H_2O \longrightarrow Ti(OH)_4 + 4\,ROH \quad (23)$$

where R represent alkyl group.

Instead of using alcohol and water, TiO_2 nanoparticles can be prepared via acid-catalysed hydrolysis of the titanium precursor followed by condensation leading to the formation of a gel. Under the conditions of low water content and hydrolysis rate, with excess titanium precursor, the Ti-O-Ti bond is favoured. Under high hydrolysis rate and medium water content, $Ti(OH)_4$ is favoured. With excess water content, the polymeric Ti-O-Ti chain is favoured. Thus, TiO_2 nanocrystals or thin-films can be obtained via dip or spin coating of the gel on a substrate (equation 24)

$$Ti(OH)_4 \longrightarrow TiO_2 + 2\,H_2O \quad (24)$$

The obtained TiO_2 is dried temporarily in the oven and further subjected to calcination at higher temperatures to remove the organic components. The schematic illustration of a typical sol-gel process is shown in Figure 4.1.

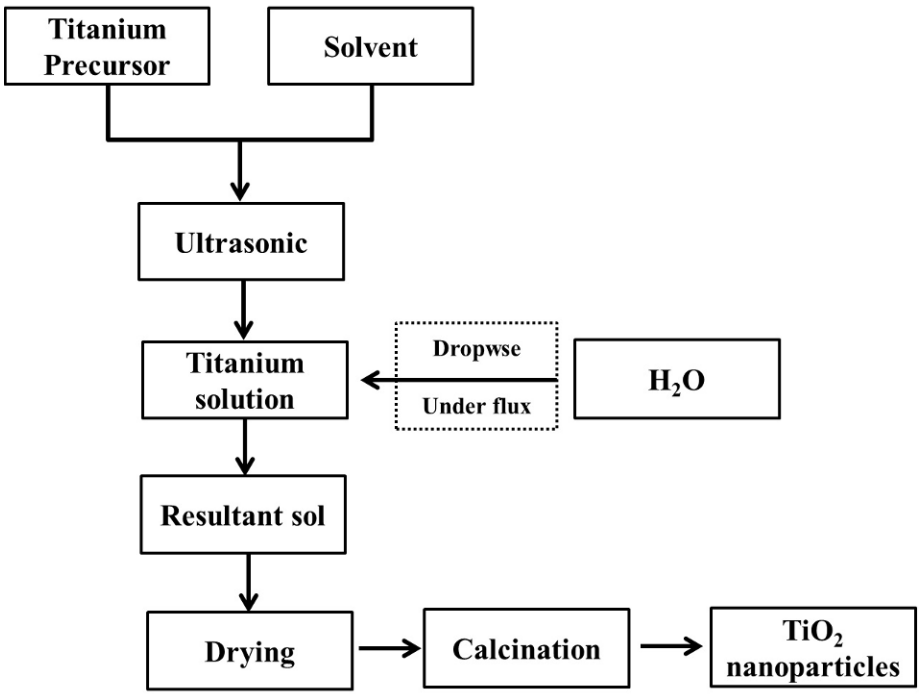

Figure 4-1: Scheme of the preparation of TiO_2 nanoparticles by sol-gel (Behnajady et al., 2013)

The particle size of the synthesised TiO_2 nanoparticles can be altered by controlling the solution pH, temperature and solution composition. Of all, the sol-gel technique appeared most promising due to production of nanoparticles with good homogeneity and high surface area at a relatively low cost (Monreal et al., 2009). TiO_2 in mesoporous, thin-films, nanotubes, nanorods, or dendrimer formats have been synthesised via the sol-gel method. Aside from that, the sol-gel technique has been used for the synthesis of doped nanomaterials with high surface areas. The advantages of the sol-gel deposition method are numerous and briefly outlined by Bestetti et al. (2010) as follows: (i) application of sol-gel technique on different substrate materials; (ii) easily conducted with ordinary laboratory equipment; (iii) it permits uniform coating of high contact areas and complex shapes; (iv) the properties of the resulting film can be easily manipulated and controlled via changing some parameters; and (v) dopants can be easily co-deposited. Because of these advantages, an interesting synthetic technique that could be used to control the size and the nature of the surface of TiO_2 nanoparticles obtained via calcination is utilising a polymeric precursor method which is further explored in this study.

4.2.1.2 *Hydrothermal method*

The hydrothermal technique involves the synthesis of TiO_2 in an autoclave with or without Teflon liners under controlled conditions of temperature and pressure, where water acts as a catalyst and as a constituent of the solid phases. The temperature can increase above the boiling point of water until it reaches the vapour saturation pressure. The internal pressure of the autoclave depends on the temperature and the quantity of the solution. It is a versatile technique widely employed in the ceramic industry for the synthesis of mono-dispersed and homogeneous nanoparticles and, in most cases, to process nanocomposite materials. Studies have shown that the size and shape of the synthesised TiO_2 made via the hydrothermal method are dependent on temperature, time duration, pressure, solvent type, medium pH (Gupta and Tripathi, 2012). The hydrothermal technique is suitable for the synthesis of TiO_2 nanotubes, nanorods, nanowires and nanofibers.

4.2.1.3 *Solvo-thermal technique*

The solvo-thermal technique is closely related to the hydrothermal treatment method except that the former uses a non-aqueous solvent. Unlike in the case of hydrothermal treatment, the applied temperature is much higher due to the flexibility of the chosen organic solvent. There is a greater control of particle size, shapes and crystallinity of TiO_2 nanoparticles than what can be obtained with the hydrothermal process. The technique is most versatile for the synthesis of nanorods, nanowires, nanotubes and nanocrystals of uniform but narrow size distribution and dispersion (Byranvand et al., 2013).

4.2.1.4 *Chemical vapour deposition method*

This involves the condensation of material in the vapour state usually in a vacuum to form a solid-phase material. The technique is usually used to form a thin layer on a substrate so as to improve its mechanical,

corrosion resistance, electrical, thermal, optical, etc. In a typical CVD process, the gases in the coating chamber are heated by thermal energy which induces the deposition (Byranvand et al., 2013). To achieve uniform deposition, process parameters such as flow rate, gas composition, deposition chamber geometry, deposition temperature and pressure need to be properly optimised. Typical examples of CVD are: electrostatic spray hydrolysis, diffusion flame pyrolysis, thermal plasma pyrolysis, ultrasonic spray pyrolysis, laser-induced pyrolysis amongst others. Highly active photocatalysts made by this technique were prepared by Hintsho et al. (2015).

4.2.1.5 *Precipitation method*

This is a reaction between two homogeneous liquid phases which prompts physico-chemical transformation processes to form a precipitate under the influence of temperature, solution pH, reactant concentration, solvent evaporation (Gupta and Tripathi, 2012). In a typical precipitation process, two basic elementary steps such as nucleation and agglomeration occur concurrently within the liquid medium leading to the formation of a solid phase. The rate of nucleation and agglomeration of particles in the homogeneous liquid phase medium can be regulated via slow addition of the anions and cations. This step promotes the precipitation of mono-dispersed particles. Not only that, careful adjustment or optimisation of the solution pH, reactant concentration, or solution temperature often produces a narrow size range and uniformly dispersed nanoparticles. However, in the case of heterogeneous liquid phase reactions, co-precipitation of oxides which are amorphous in nature often occur due to poor mixing within the liquid medium or slow precipitation rate.

Further application of the hydrothermal treatment method promotes transformation of the amorphous precipitates to highly crystalline materials. The precipitation and co-precipitation method are limited due to difficulty in controlling particle size and size distribution, occasioned by lack of suitable control mechanisms during nucleation, which makes the particles bigger instead of within the nano range. In spite of this, several researchers have used precipitation methods to synthesis TiO_2 nanoparticles (Chong et al., 2010; Kostedt et al., 2008).

4.2.2 Synthetic procedure for synthesising TiO_2 nanocomposites

8 g of powder polyacrylonitrile (PAN) was weighed and added to 92 g of dimethylformamide (DMF) making up 100 g of PAN and DMF. The mixture was thereafter stirred at room temperature (25 ^{0}C) for 12 hours in a capped bottle. At the end of 12 hours stirring, a slightly transparent 8% PAN/DMF viscous solution was obtained. Out of which, 50 mL of the mixture was taken and put in a separate bottle and subsequently followed by drop-wise addition of 6 g of 99% concentrated $TiCl_4$ with continuous stirring at 25°C using magnetic stirring at 150 rpm. This step was carried out in the fume cupboard. During the addition of the concentrated $TiCl_4$, there was a sudden disappearance of the transparent solution and appearance of a highly viscous brownish yellow colour (Figure 4.2). Besides, the addition of $TiCl_4$ was accompanied with the release of white fumes of hydrochloric acid and so the reaction was purely exothermic. The gel solution was stirred until the white fumes disappeared.

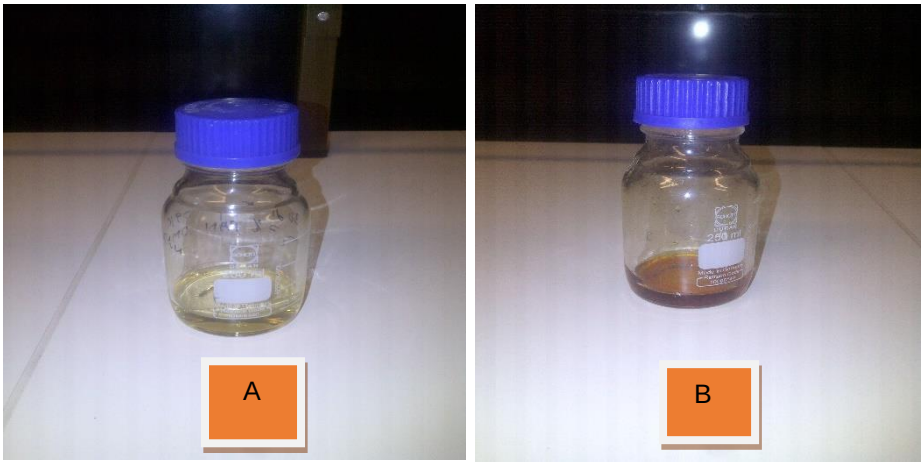

Figure 4-2: [A] = 8% slightly viscous PAN/DMF solution and [B] = highly viscous 8%PAN/DMF/TiO_2 sol gel solution

4.2.3 Procedure for coating stainless steel mesh substrate with the 8% PAN/DMF/TiO_2 sol gel solution

Prior to manual coating, the 4 cm by 4 cm stainless steel mesh sample was washed with acetone, ethanol and water, and then dried in the oven at 140°C. The clean stainless steel mesh was coated manually with the prepared sol gel formulation. 3 mL disposable plastic pipette was used to aspirate the sol gel solution which was then uniformly dispersed until the sol-gel completely covered the stainless steel mesh. Immediately after the coating, the brownish-yellow colour change to a violet colour. The coated mesh was air dried at room temperature in a fume cupboard for 10-15 minutes followed by calcination at 300°C, 350°C and 400°C in a Labfun tube furnace shown in Figure 4.3 below. The heating rate of 50 ^{0}C/min and a holding time of 1-4 hours was adopted based on prior work. The step by step experimental protocol is shown in Table 4.1 below. Nitrogen gas was flowed through the inner tube at 25 kPa in order to create an inert environment and to prevent side reactions such as hydrolysis and oxidation.

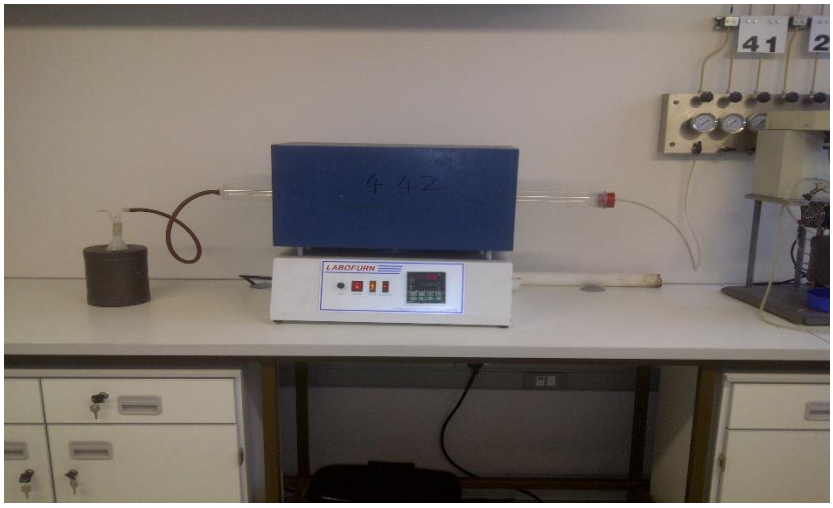

Figure 4-3: Labfun tube furnace used for calcination

Table 4.1: Experimental protocol for each synthesis

Synthesis code	Solution	Method	Calcination conditions	Results (HRSEM images)
MM300	8 g (PAN) + 92 g (DMF) + 6 g ($TiCl_4$) sol gel solution	Manual Coating	50°C/min to 300°C in air holding time = (1 h, 2 h, 3 h, 4 h)	Figure 4.1
MM350	8 g (PAN) + 92 g (DMF) + 6 g ($TiCl_4$) sol gel solution	Manual Coating	50°C/min to 350°C in air holding time = (1 h, 2 h, 3 h or 4 h)	Figure 4.2
MM400	8 g (PAN) + 92 g (DMF) + 6 g ($TiCl_4$) sol gel solution	Manual Coating	50°C/min to 400°C in air holding time = (1 h, 2 h, 3 h or 4 h)	Figure 4.3

4.2.4 Synthesis of Ag nanoparticles on TiO_2 coated stainless steel mesh using thermal evaporation procedure

The three steps involved in the thermal evaporation of plasmonic metal onto TiO_2 surface are described below.

4.2.4.1 *Step 1: Loading samples/starting vacuum system*

The vacuum chamber was vented by opening the vent valve for approximately ten minutes and the dome become loose. The dome was carefully placed on a black stand next to the machine. After this, the vent valve was closed and the samples (TiO_2 calcined at 400ºC for 2 h) was loaded and turned upside down on the sample holder while the source boat containing the plasmonic element (silver) was covered with a shutter or swing-arm shield. The dome was thereafter replaced and the mechanical vacuum pump was switched on for about 10 minutes. The Pirani Cold Cathode Gauge was also turned on to measure the pressure. This pressure was allowed to build-up for approximately 30 minutes until the desired value of 2.5×10^{-5} mbar was reached, while the water valve was opened for sensor cooling.

4.2.4.2 *Step 2: Evaporation/deposition*

Prior to the deposition of silver, the Qpod software on the laptop and the sensor crystal frequency reading was displayed properly. Subsequently, current was slowly applied until the metal begun to glow and evaporate and to achieve uniform deposition the evaporation rate of 0.5 Å/s was applied. The Qpod.exe. programme was

initiated and the shutter turned anticlockwise. The desired thickness of Ag (5 nm, 10 nm and 15 nm) were deposited onto TiO_2 composite surface by rotating the voltage variac. Once the desired thickness was achieved, the shutter was closed and the Qpod.exe. programme stopped and gradually the current reduced to zero. Thereafter, the vacuum pump and the cathode gauge were switched off and similarly the water valve for sensor cooling also closed. The system then rested until the vacuum turbo pump stopped.

4.2.4.3 *Step 3: After evaporation/unloading samples*

To remove the samples, the vent valve was switched on for 10 minutes for easy removal of the done. The dome was removed and the loaded samples carefully removed without touching the film surface. The thermal evaporator system is depicted in Figure 4.4.

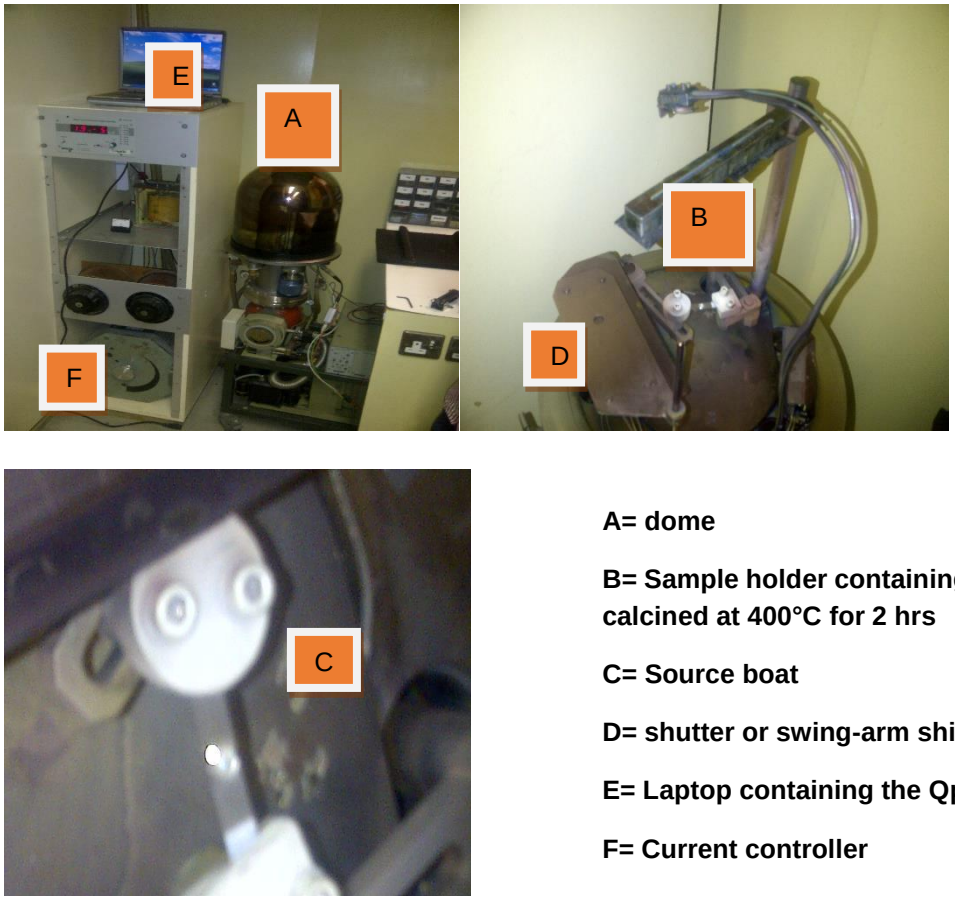

A= dome

B= Sample holder containing supported TiO_2 calcined at 400°C for 2 hrs

C= Source boat

D= shutter or swing-arm shield

E= Laptop containing the Qpod.exe.software

F= Current controller

Figure 4-4: Thermal evaporator used for depositing silver

4.2.5 Synthesis of thin films of Ag or Cu withTiO2 on fused silica support

Another series of photocatalysts were prepared on fused silica supports instead of stainless steel mesh as support in order to improve UV light access to photocatalysts and enhance their adhesion and activity. The protocol was as follows.

4.2.5.1 *Materials*

All chemicals were used as received without further purification and distilled water was used for all preparations. The chemicals used were 3-mercaptopropyltrimethoxysilane (MPTMS, Merck), hydrogen peroxide (ACE), ethanol (99%, MET-U-ED), 2-propanol, methyl orange (SAARCHEM SA), sulphuric acid (Merck), bromocresol purple (Associated Chemical Enterprises (Pty) Ltd), bisphenol A (MET-U-ED) and fused silica slides.

4.2.5.2 *Photocatalyst preparation*

Thin films of plasmon metal (Cu, Ag and/or Au) were deposited on the fused silica slides using a thermal evaporation technique which is shown in Figure 3.4A. To improve adhesion of the nanoparticles, the fused silica slides with dimensions of 2.5 cm by 3.5 cm were firstly etched with a 10% hydrofluoric acid solution to increase surface roughness. Adhesion promoter was then deposited by immersion in a solution of 3-mercaptopropyltrimethoxysilane (MPTMS) which was made up by mixing 20 mL of MPTMS, 20 mL of water and 60 mL of 2-propanol for 24 hours. Excess MPTMS was removed by dipping in 2-propanol briefly, followed by blowing a jet of nitrogen gas to dry the surface and then the slides were cured at 105°C for 7 minutes. For the deposition of copper, the copper source material was loaded onto a tungsten sample holder and placed in the centre of the equipment's dome. A desired vacuum was created using a vacuum pump. The current was then increased slowly until the copper source material started to melt and evaporate. The evaporated material was deposited on fused silica support that was placed above the copper.

This system was fitted with an acoustic crystal monitor for controlling the amount of metal deposit. When the desired thickness was achieved, the swing arm shield was closed to prevent more material from depositing onto the quartz substrates followed by switching off the vacuum pump and allowing air to get into the chamber to release the vacuum. The same procedure was repeated for the deposition of silver. Before, or after the plasmon metal (gold, silver or copper) was deposited as a thin film using the thermal evaporation technique (Figure 4.5A), the TiO_2 film (100 nm) was deposited on the fused silica slides using the sputter coating technique (Figure 4.5B). Experimental conditions used to prepare Cu and Ag thin films included: Vacuum Pressure: Copper 3.0 x 10^{-3} Pascal; Silver 3.2 x 10^{-3} Pascal. Current applied: Copper 95 Amps; Silver 100 Amps. Rate of deposition: Copper and Silver: Variable (0-1.2 nm/s). Frequency: Copper 591365.25Hz; Silver 591365.25 Hz. Different thicknesses of the plasmonic elements were prepared and QPod.exe software was used for the film thickness determination. Bimetallic films were also prepared using the same procedure. The metal films were deposited one at a time, layer by layer. The sample description and codes of the prepared samples are given in Table 4.2.

Table 4.2: Sample **description and codes**

Sample description	Sample Code
TiO_2 film with no metal film	T1
TiO_2 deposited on 5 nm Cu film	T5Cu
TiO_2 deposited on 10 nm Cu film	T10Cu
TiO_2 deposited on 20 nm Cu film	T20Cu
TiO_2 deposited on 25 nm Cu film	T25Cu
TiO_2 deposited on 5 nm Ag film	T5Ag
TiO_2 deposited on 10 nm Ag film	T10Ag
TiO_2 deposited on 20 nm Ag film	T20Ag
TiO_2 deposited on 25 nm Ag film	T25Ag
2 nm Ag film deposited on TiO_2 film	2AgT
5 nm Ag film deposited on TiO_2 film	5AgT
2 nm Cu film deposited on TiO_2 film	2CuT
5 nm Cu film deposited on TiO_2 film	5CuT

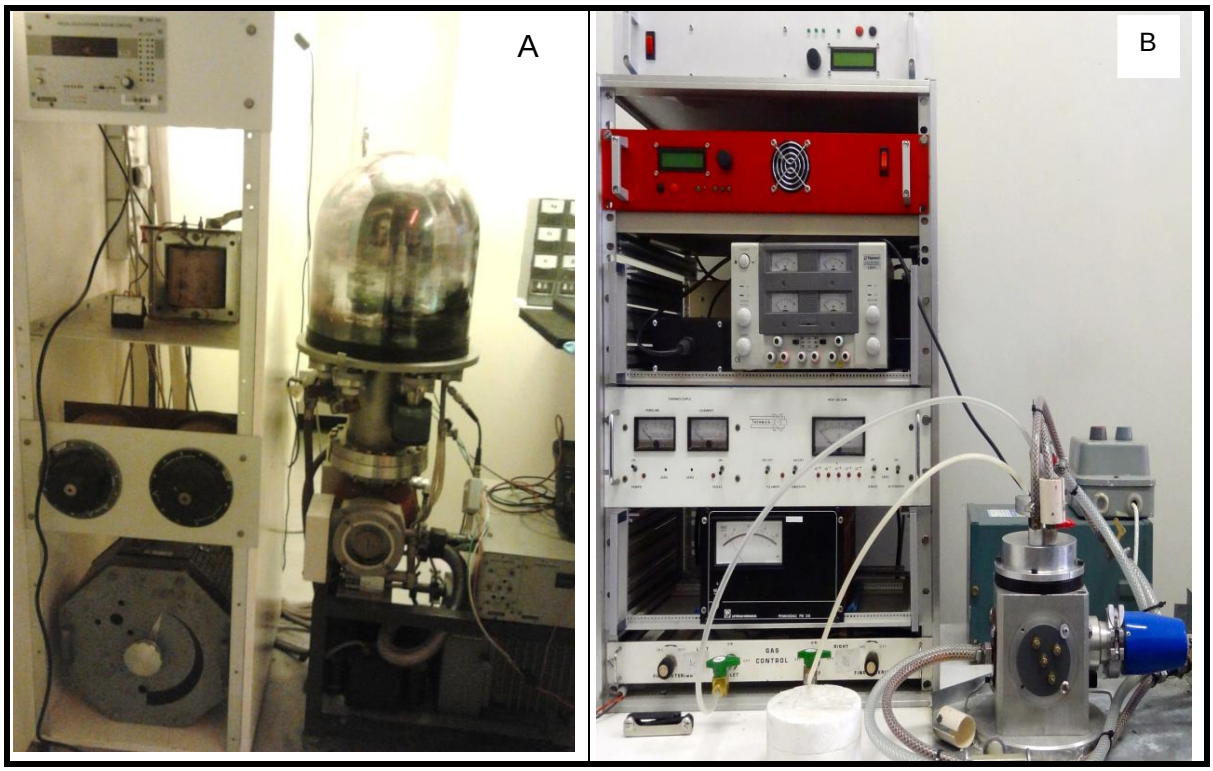

Figure 4-5: A photograph of (A) the complete thermal evaporation unit used for coating fused silica with gold, silver and copper thin films and (B) Sputter coating equipment for deposition of TiO2

4.2.5.3 *Photocatalyst characterisation*

The crystallographic properties of the prepared Ag/TiO_2 and Cu/TiO_2 thin films were obtained using X-ray diffraction from Bruker D8 Advance instrument with a Cu-Kα1 (λ – 1.54060 nm) X-ray tube and a LynxEye detector. The scanning range was from 2 theta value of 25° to 90°. The structure and morphology of the nanoparticles forming the thin films were analysed by HRSEM using a Zeiss Auriga Field Emission Scanning Electron Microscope where the SmartSem software was used to capture images and AZTEC program was used to do EDS (energy dispersive spectroscopy). The samples were sputter coated with carbon prior to HRSEM analysis. Rutherford Backscattering Spectrometry (RBS) measurements were performed with 2 MeV alpha ($4He^+$) particles using 6 MV Van de Graaff accelerator. The scattering angle was θ = 165° and the detector resolution was 20 KeV. The beam current was approximately 50 nA.

4.3 CHARACTERISTICS OF PLASMONIC METAL TITANIUM DIOXIDE THIN FILM ON FUSED SILICA

The results of the synthesis and characterization of the TiO_2 composites supported on fused silica are presented in this section. The prepared thin films on fused silica were fully characterized using high resolution scanning electron microscopy (HRSEM), UV-Vis diffuse reflectance spectroscopy, Rutherford backscattering spectrometry (RBS) and X-ray diffraction (XRD). The crystallographic properties of the prepared Ag/TiO_2 and Cu/TiO_2 thin films were obtained using X-ray diffraction from Bruker D8 Advance instrument with a Cu-Kα1 (λ – 1.54060 nm) X-ray tube and a LynxEye detector. The scanning range was from 2 theta value of 25° to 90°. The structure and morphology of the nanoparticles forming the thin films were analysed by HRSEM using a Zeiss Auriga Field Emission Scanning Electron Microscope where the SmartSem software was used to capture images and AZTEC program was used to do EDS (energy dispersive spectroscopy). The samples were sputter coated with carbon prior to HRSEM analysis. Rutherford Backscattering Spectrometry (RBS) measurements were performed with 2 MeV alpha (4He+) particles using 6 MV Van de Graaff accelerator. The scattering angle was θ = 165° and the detector resolution was 20 KeV. The beam current was approximately 50 nA.

4.3.1 Film Deposition

The rate of deposition of the metal films was difficult to control as it was fluctuating with time hence the graphs of a plot of rate of deposition against time were plotted to see the changes in deposition during the deposition process. The graphical representations of the experimental deposition rate and change of thickness with time for Ag films are shown in Figure 4.6. Although the rate of deposition varied, the resulting films were uniform. To study the effect of noble metal loading, different metal film thickness of 5 nm, 10 nm, 20 nm and 25 nm were deposited on fused silica. The 2 nm Ag film took only a minute to deposit and fluctuations in the rate of deposition were minimal when compared to other films. As the film thickness increased, the rate of deposition became more difficult to control and the fluctuations were higher, hence the deposition rates were constantly varied (increased and reduced) until the desired thickness was achieved.

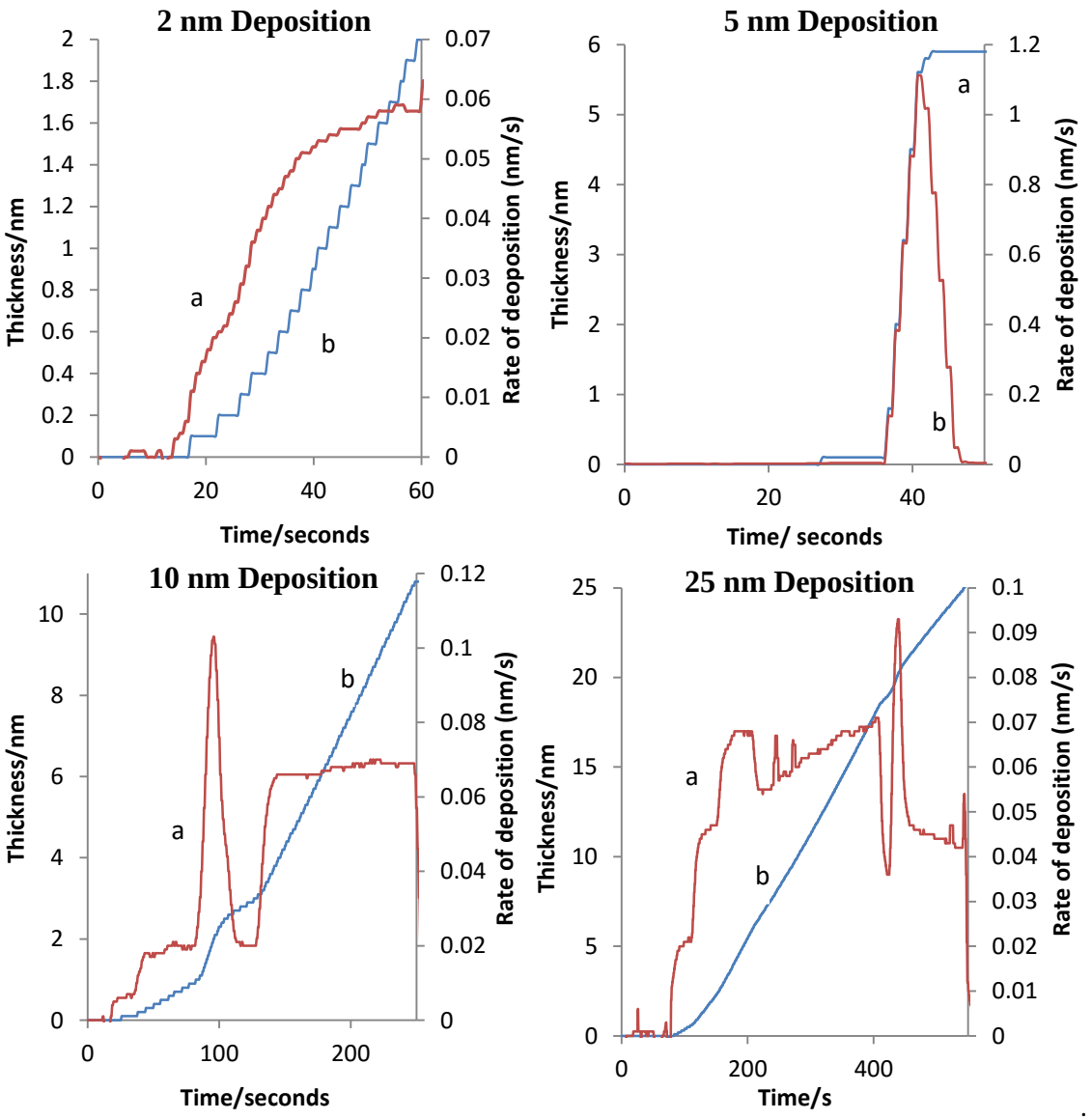

Figure 4-6: Graphs of (a) rate of deposition and (b) film thickness of 2 nm, 10 nm, 20 nm, and 25 nm Ag films.

4.3.2 HRSEM Analysis

The HRSEM of pure uncoated fused silica (Fig. 4.7A) shows that the surface was smooth and uniform. A comparison of the HRSEM image of pure uncoated fused silica and MPTMS surface treated fused silica (Fig. 4.7B) showed that the MPTMS layer was successfully formed on fused silica. The HRSEM images of the 10 nm monometallic Cu and Ag metal films film (Fig. 4.7C & 4.7D respectively) show that the nanoparticles were uniformly distributed on the surface of fused silica support. There were significant differences in the morphology between the Cu and Ag films due to the differences in the particle size.

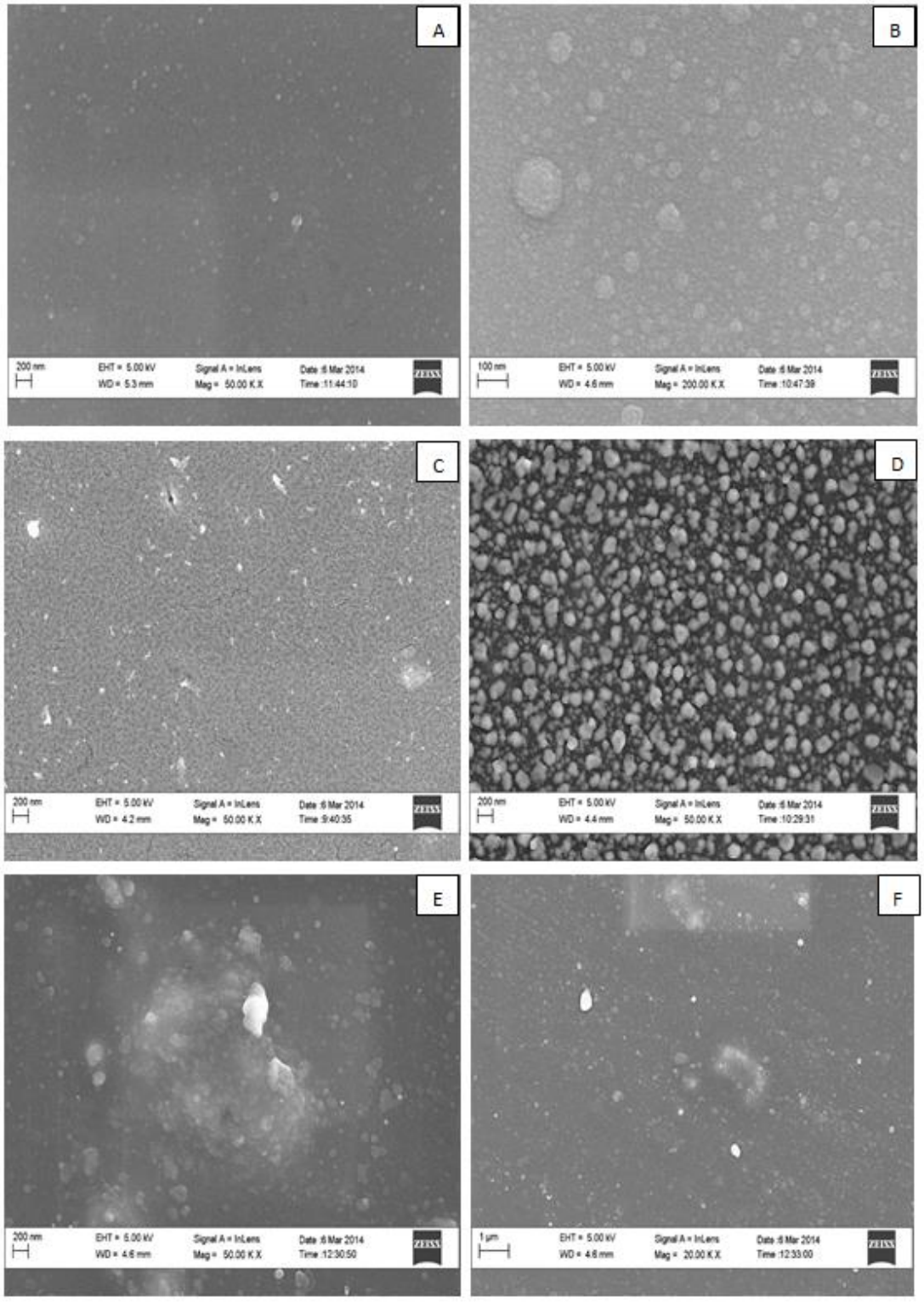

Figure 4-7: HRSEM of (A) pure fused silica (50 kX), (B) MPTMS treated fused silica (200 kX), (C) copper film (50 kX), (D) 10 nm silver film (50 kX) and (E & F) TiO_2 deposited on top of plasmonic silver films at 50.00 kX and 20 kX respectively.

The Ag particles were roughly spherical in shape and they did not have a uniform size but ranged from 68 to 200 nm whereas the copper nanoparticles were so small that their size could not be determined from the HRSEM images. The Ag film had smaller nanoparticles at the bottom than on top showing that as the thermal evaporation process continued, the size of the nanoparticles increased with an increase in film thickness due to coalescence resulting in a wide particle size distribution (polydispersed nanoparticles). The copper film did not show any variation of particle size with thickness and had a uniform particle size resulting in a smooth surface. TiO_2 film deposited on fused silica was agglomerated on some sections of fused silica (Fig. 4.7E).

4.3.3 Rutherford Backscattering Spectrometry (RBS) measurements

RBS analysis was performed to determine the elements in fused silica and the films. Fused silica in its pure form consists of only silicon and oxygen and RBS analysis of fused silica support showed that only those two elements were present and these were labelled in green (Fig. 4.8A). This shows that fused silica supports used in this study, were pure and had been cleaned thoroughly as no other elements were detected.

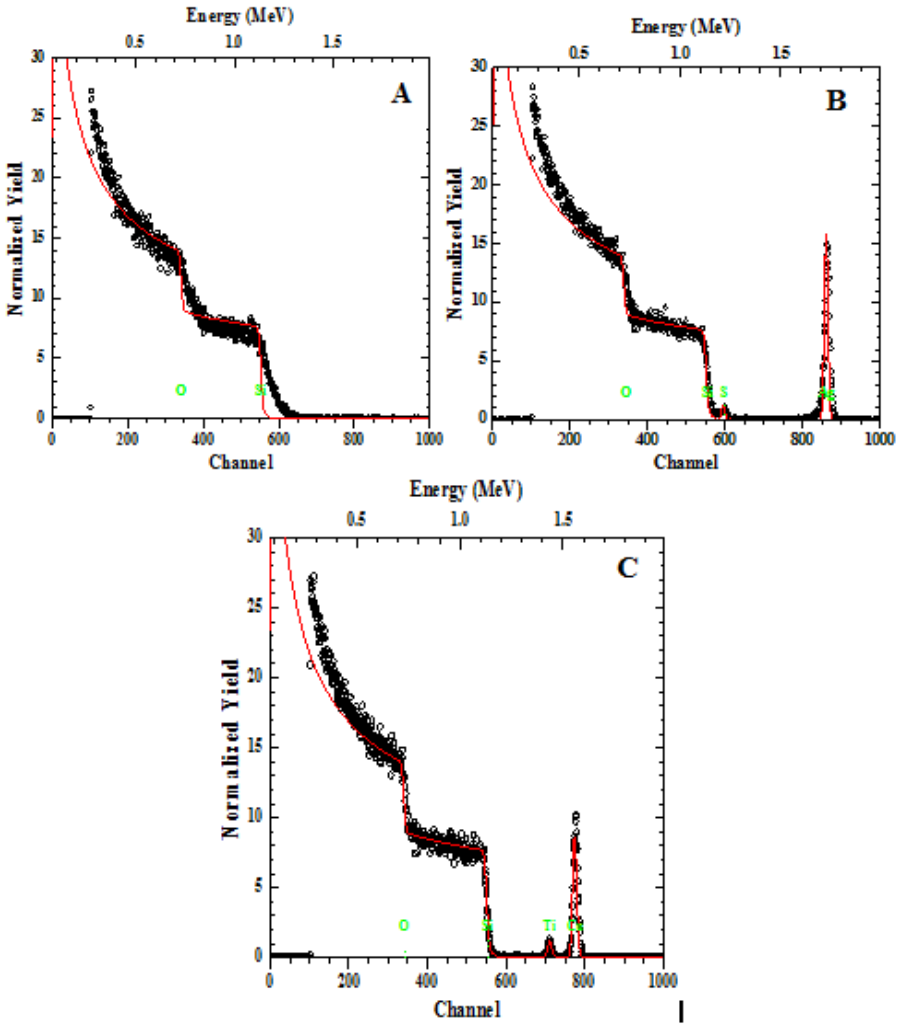

Figure 4-8: RBS analysis of (A) uncoated fused silica, (B) 10 nm Ag coated fused silica and (C) 10 nm Cu coated fused silica

The RBS analysis of 10 nm Ag coated fused silica (Fig. 4.8B) and 10 nm Cu coated fused silica (Fig 4.8C) confirmed the presence of copper and silver in their respective films as expected. The spectra show well-defined peaks at high energies, caused by Cu and Ag and onset of scattering at lower energies due to the various constituents of the fused silica substrate. In the Ag film, very small traces of sulphur were found and in the copper films some traces of titanium were also found. The detected oxygen in both the Cu and Ag films were ascribed to fused silica support.

4.3.4 XRD Analysis

The XRD analysis was done on plasmonic metal films of 25 nm and pure TiO_2 (100 nm) so as to see clearly the peaks due to plasmonic metals before the deposition of TiO_2 and peaks due to TiO_2. A thickness of 25 nm for plasmonic metals was chosen for XRD analysis so as to get clearer peaks. In the XRD pattern of pure TiO_2 (Fig. 4.9), the peaks at 2θ values of 27.53° and 55.21° indicated the presence of TiO_2 in the rutile phase while peaks at 2θ values of 26.31°, 37.89°, 48.87° and 64.33° indicated the presence of the anatase phase. The peaks at 2θ = 39.15°, 44.60°, 64.58° and 77.72° in the XRD pattern of the 25 nm Ag film were assigned to the diffraction from (111), (200), (220) and (311) lattice planes of pure face centred silver crystals respectively. This also indicated that the particles were crystalline in nature.

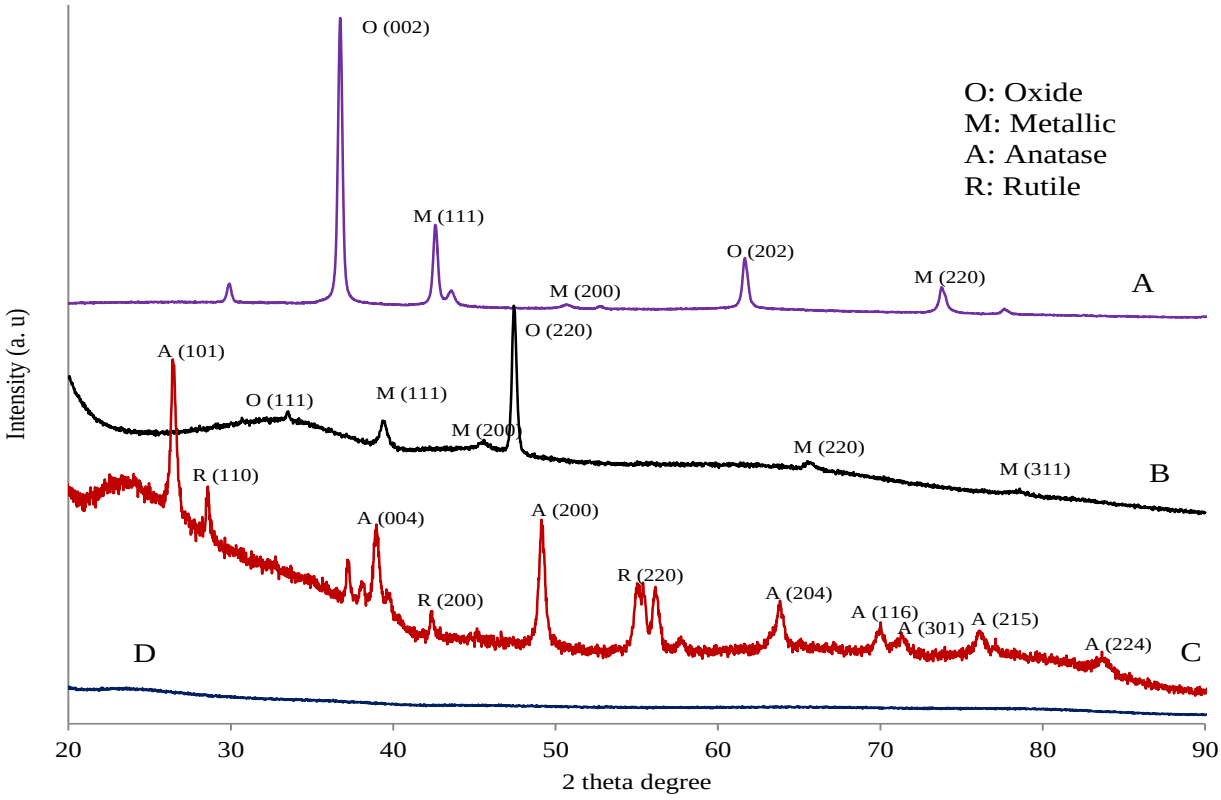

Figure 4-9: XRD patterns (A) 25 nm copper film, (B) 25 nm silver film, (C) 100 nm TiO2 film and (D) pure fused silica

No peaks were observed in the XRD pattern of MPTMS treated fused silica substrate. In the XRD pattern of 25 nm Cu film, the Bragg's reflections for copper nanoparticles were observed in the XRD pattern at 2θ values of 43.16°, 50.13° and 73.58° which corresponded to (111), (200) and (220) planes of face centred cubic (fcc) structure of copper. It can be seen that some traces of copper oxide were in the copper film as evidenced by the XRD peaks at 2 theta values of 36.58° and 61.52°. The sharp peaks in the diffraction pattern of copper indicated that the particles were crystalline.

4.4 CHARACTERIZATION OF STAINLESS STEEL MESH SUPPORTED AND AG DEPOSITED TiO_2 NANOCOMPOSITES

The characteristics of synthesized TiO_2 and Ag deposited TiO_2 nanocomposites, both supported on stainless steel mesh are presented in this section. Phase identity, crystal phase structure as well as the crystallite size was determined by powder X-ray diffraction (XRD) analysis performed on Bruker D8 Advance AXS with Cu-K α radiation. The sample was placed on a pre-greased glass slide and diffractograms were recorded between the angle of 20º and 80º. The morphological and structural identification of the prepared catalysts was investigated using the high resolution scanning electron microscope (HRSEM). The high resolution field emission gun scanning electron microscope (HRFEGSEM) was used for the characterization. Particle size was analysed by high resolution transmission electron microscope (HRTEM) technique. G2 F20 X-Twin MAT HRTEM model was used to analyse the particle surface morphology as well as particle distribution pattern.

Energy dispersive X-ray spectroscopy (EDS) was used to determine qualitative elemental composition while the selected area electron diffraction (SAED) helped to identify the samples' crystallographic structure and orientation. The chemical bonds present in the synthesized material were identified by Fourier transform infrared spectroscopy (FTIR) model Perkin Elmer 100 FT-IR spectrometer. UV-Vis diffuse reflectance was used to estimate the wavelength of TiO2 and Ag deposited TiO_2 nanocomposites recorded on samples diluted in $BaSO_4$ using a Harrick praying mantis diffuse reflectance accessory mounted in a Perkin Elmer Lambda 650 UV-Vis spectrophotometer. 25 mg of each photocatalyst was well ground with 0.5 g of $BaSO_4$ and spread onto the sampling plate prior to the measurement. The background reflectance of $BaSO_4$ (reference) was measured beforehand. The Kubelka-Munk function F(R8) was calculated as F(R8) = (1– R8)24/2R8, where R is the diffuse reflectance of the sample relative to the reflectance of a standard according to the Kubelka-Munk theory. The % diffuse reflectance was then plotted against the wavelength.

4.4.1 HRSEM, HRTEM and SAED of 8% (PAN/DMF/TiO2) sol gel solution coated stainless steel mesh

The HRSEM micrographs of synthesised TiO_2 particles prepared at different calcination temperatures are shown in Figures 4.10 TO 4.16. As shown in Figure 4.10 (A1), the morphology of the as-prepared catalyst calcined for 1 h at 300ºC was mainly in form of long nanorods and thereafter formed shorter nanorods as the holding time increased to 2 h. This suggests that the PAN is yet to fully decompose as the particles are still entrenched within it. The selected-area electron diffraction (SAED) pattern of the samples calcined at 300ºC

for 1 and 2 h confirmed the formation of nanorods. There was the appearance of agglomerated nanocrystals at 3 h holding time. The agglomerated nanocrystals were densely packed and became smaller as the holding time increased to 4 hrs (Figure 4.10 (A4)).

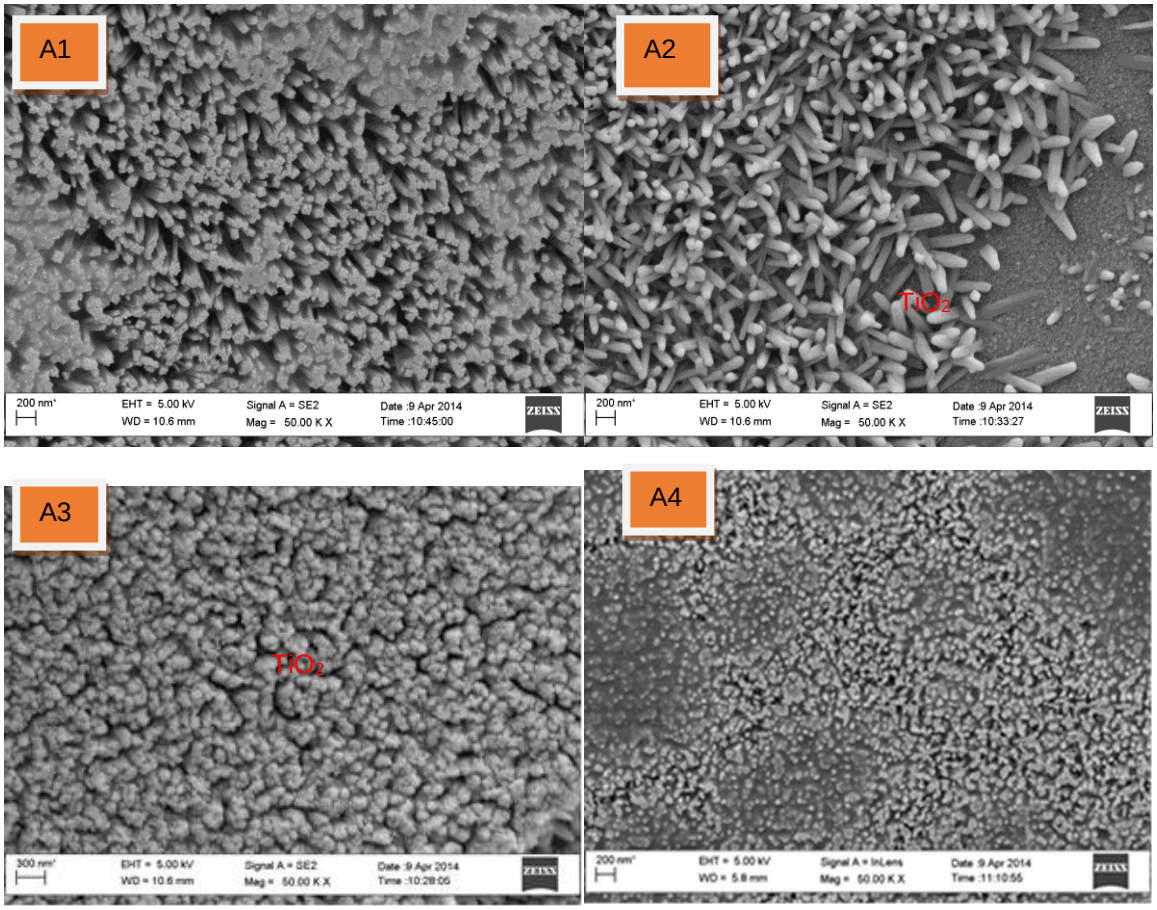

Figure 4-10: HRSEM of 8% (PAN/DMF/TiO_2) sol gel solution coated stainless steel mesh calcined at 300°C with heating rate of 50°C/min and holding times of [A1] = 1 h, [A2] = 2 h, [A3] = 3 h and [A4] = 4 h.

Figure 4.11 (B1 to B4) shows the HRSEM images of the prepared catalyst calcined at 350ºC at different holding time of 1-4 h. The SEM images show the surface and crystallite morphologies of supported TiO_2 nanocrystals on the stainless steel mesh. Aggregated particles of identical small crystallites were observed as the holding time increased except for image B2 where a different morphology of TiO_2 nanocrystals was observed. An increase in temperature from 300 to 350ºC shows that the crystals were still generally below 200 nm in size with an increase in calcination temperature. Apart from this, agglomeration became more evident as the calcination temperature increased, which suggests the impact of heat treatment on the particle size of TiO_2.

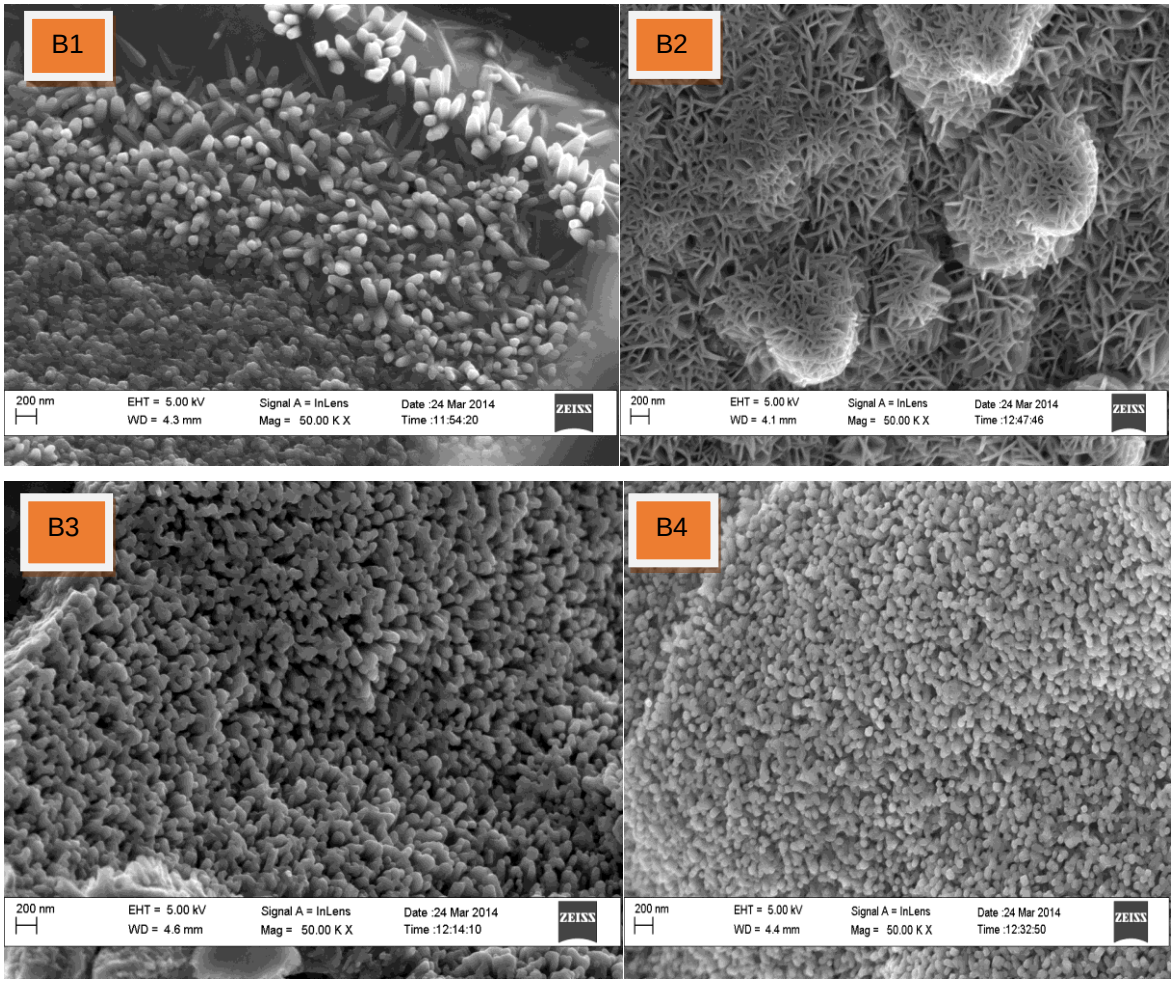

Figure 4-11: HRSEM of 8% (PAN/DMF/TiO2) sol gel solution coated stainless steel mesh calcined at 350°C with heating rate of 50°C/min and holding times of [B1] = 1 h, [B2] = 2 h, [B3] = 3 h and [B4] = 4 h.

Figure 4.12 (C1 to C4) shows the HRSEM images of supported TiO_2 calcined at 400ºC at the different holding times. Figure 3.12 (C1) shows a well-developed material having large, leaf-like crystal structure with a defined, micron sized morphology. As the holding time increased to 3 h, the size of the leaf-like structure reduced and agglomerated nanorods below 200 nm in size were formed.

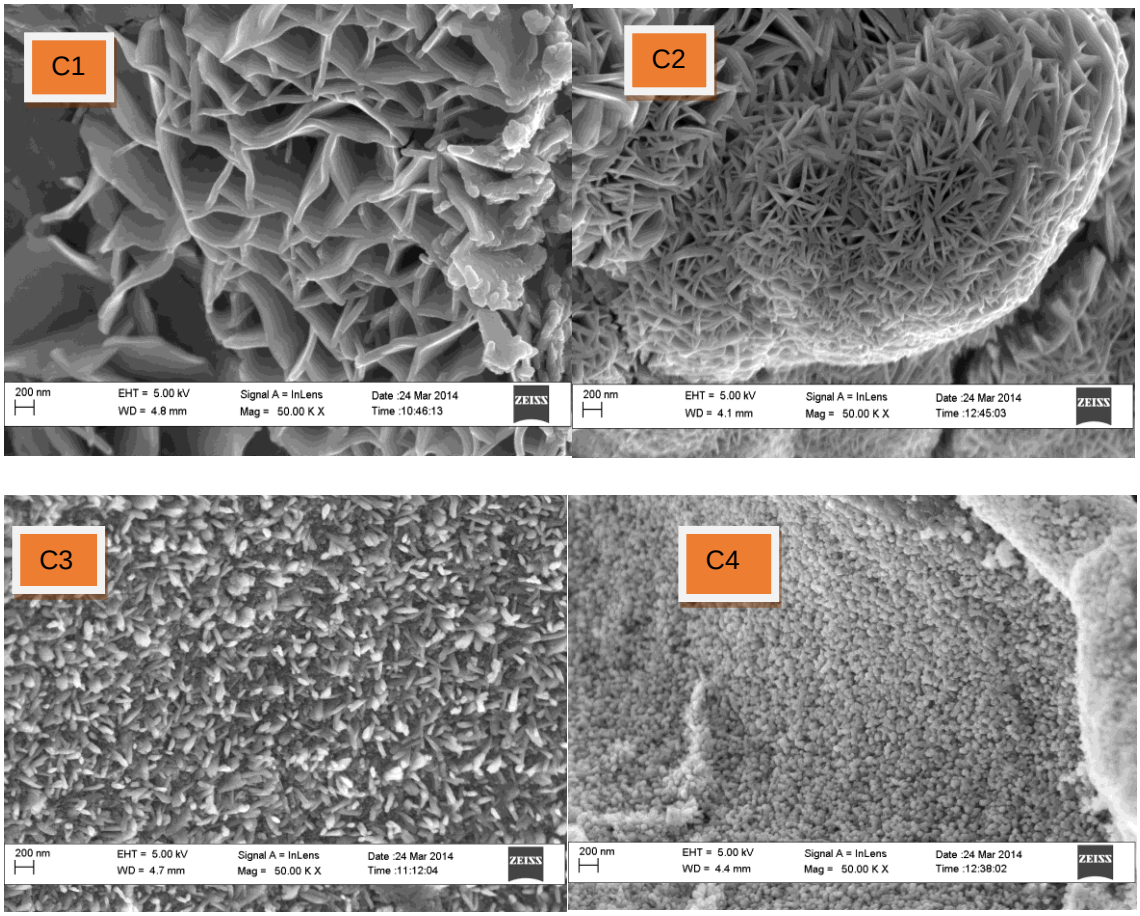

Figure 4-12: HRSEM of 8% (PAN/DMF/TiO_2) sol gel solution coated stainless steel mesh calcined at 400°C with heating rate of 50°C/min and holding times of [C1] = 1 h, [C2] = 2 h, [C3] = 3 h and [C4] = 4 h.

Figure 3.11 (C3) shows high homogeneity and high surface area as holding time was increased. At 400ºC for 4 h, crystalline TiO_2 material was produced although more agglomerated with irregular morphology. Generally, as the holding time increased, the size of the nanomaterial became smaller. The effect of the increase in the calcination temperature from 300ºC to 400 ºC, irrespective of the holding time, was shown in the size and the shape of the nanoparticles. High resolution transmission electron microscope (HRTEM) was applied to identify the crystalline nature as well as the particle size of the nanomaterial. From Figure 4.13 (D1-D3), the particles were held in a matrix of PAN. The shape of the nanocrystals was almost spherical and nearly equal in size. The TiO_2 nanocrystals are highly crystalline with pure anatase phase. The HRTEM image (D4) shows interplanar spacing that corresponds to the [101] plane of anatase TiO_2.

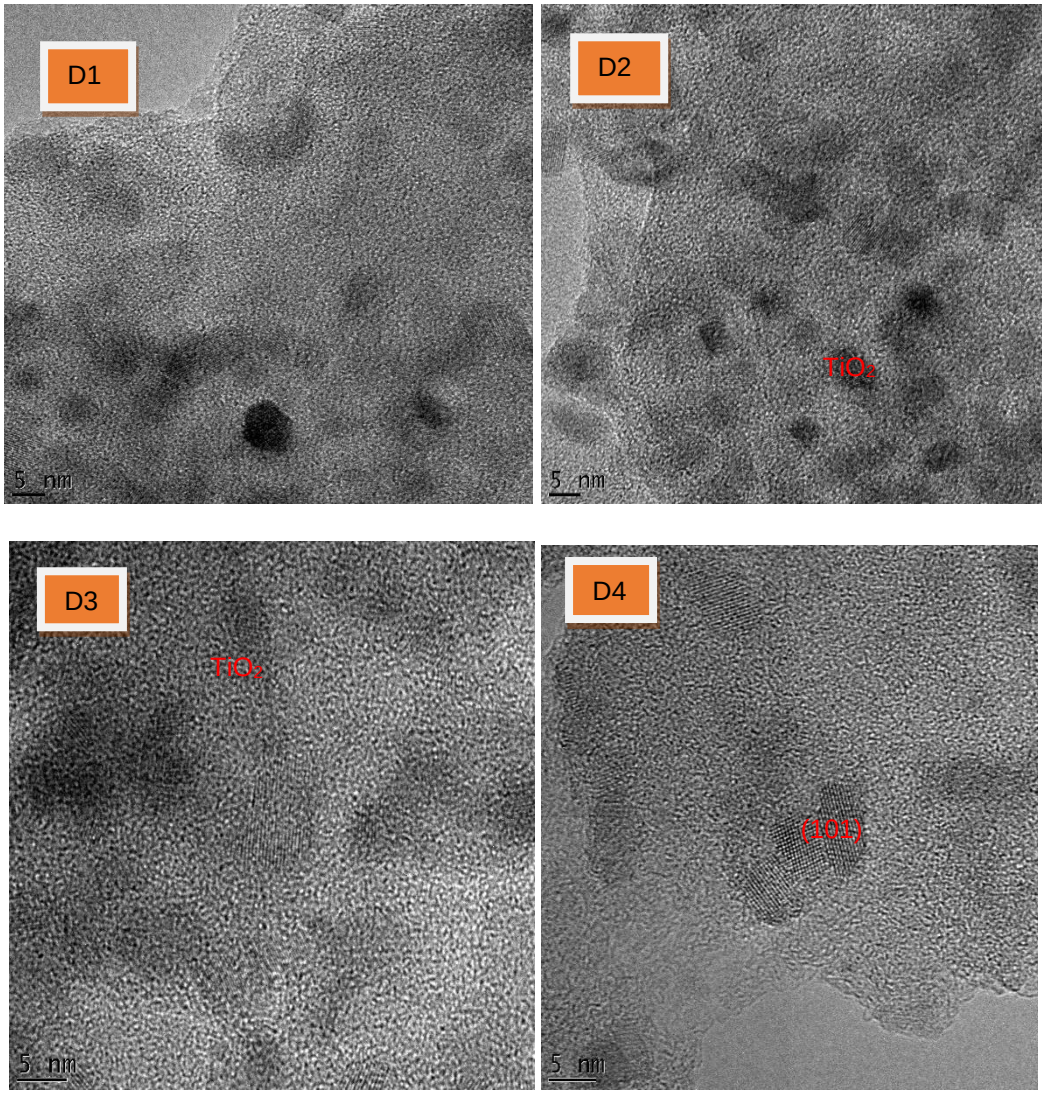

Figure 4-13: HRTEM of 8% (PAN/DMF/TiO2) sol gel solution coated stainless steel mesh calcined at 300°C with heating rate of 50°C/min and holding times of [A] = 1 h, [B] = 2 h, [C] = 3 h and [D] = 4 h.

The selected area electron diffraction (SAED) images in Figure 4.14 (D1 and D2) suggest a polycrystalline structure, composed of homogeneous diffraction maxima which are broadened and do not overlap each other. Thus, the polycrystalline diffraction ring index indicates that the supported TiO_2 catalyst is purely anatase phase which is in agreement with the XRD of these samples.

Figures 4.15 and 4.16 show the formation of roughly uniform particle structure, with some spherical-like fringes and highly polydisperse TiO_2 particles irrespective of the holding time. The titanium dioxide was anatase structure of (101) plane in Miller index as also revealed by XRD. The degree of crystallinity became more prominent at a holding time of 3 and 4 h in both cases. The selected area (electron) diffraction photograph shows an obvious electron diffraction ring, which suggests that the nanomaterials were composed of polycrystalline TiO_2.

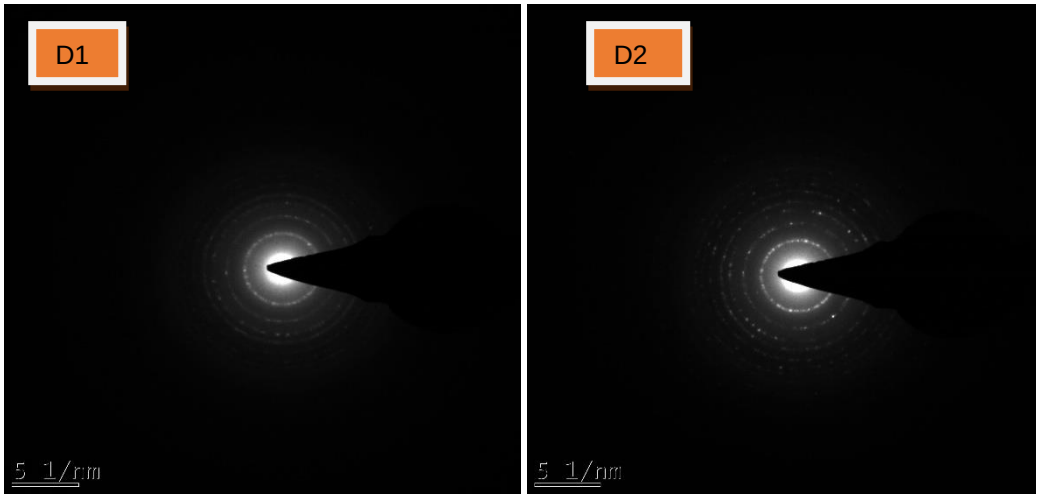

Figure 4-14: HRTEM-SAED of 8% (PAN/DMF/TiO_2) sol gel solution coated stainless steel mesh calcined at 300°C with heating rate of 50°C/min and holding times of [D1] = 1 h, [D2] = 2 h.

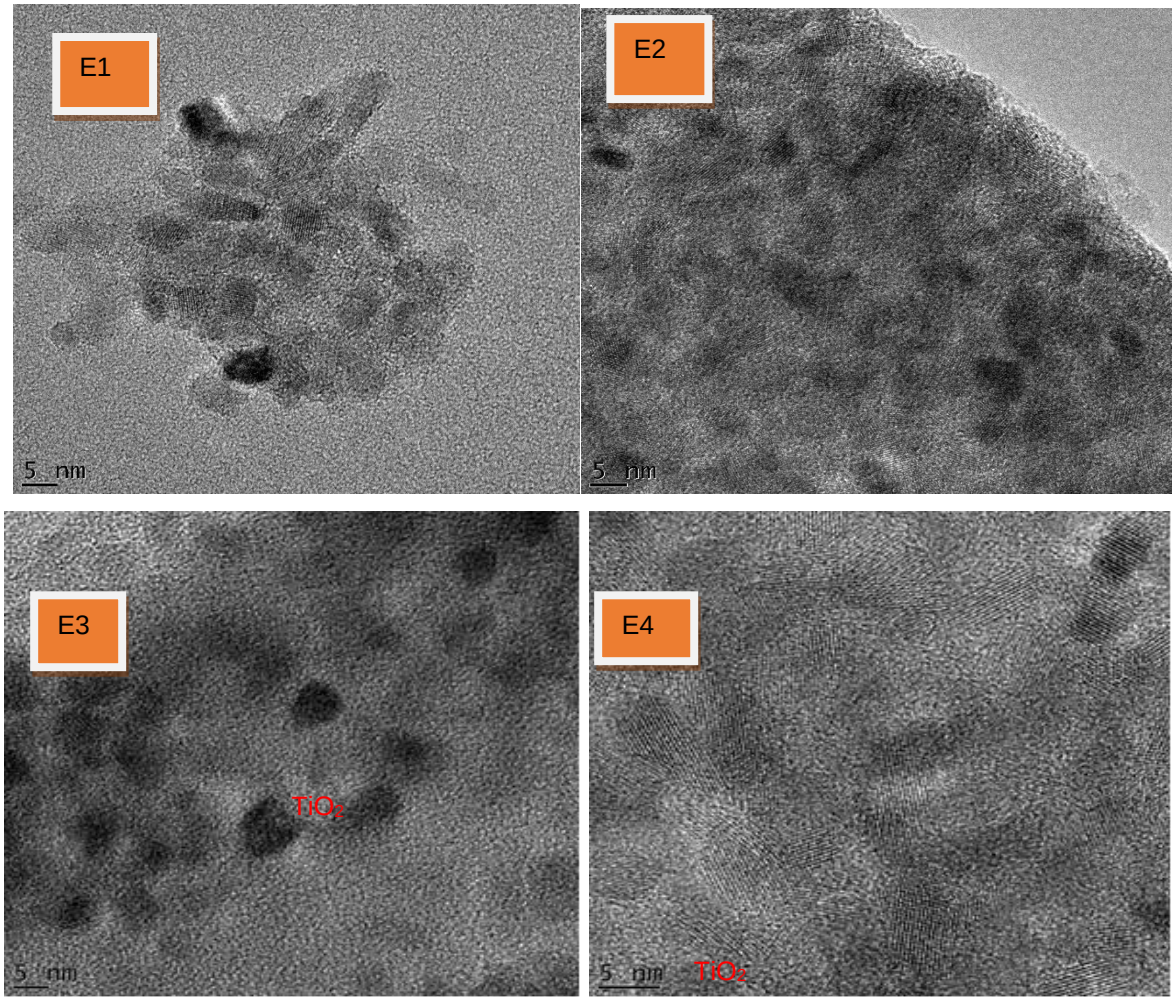

Figure 4-15: HRTEM of 8% (PAN/DMF/TiO2) sol gel solution coated stainless steel mesh calcined at 350°C with heating rate of 50°C/min and holding times of [E1] = 1 h, [E2] = 2 h, [E3] = 3 h and [E4] = 4 h.

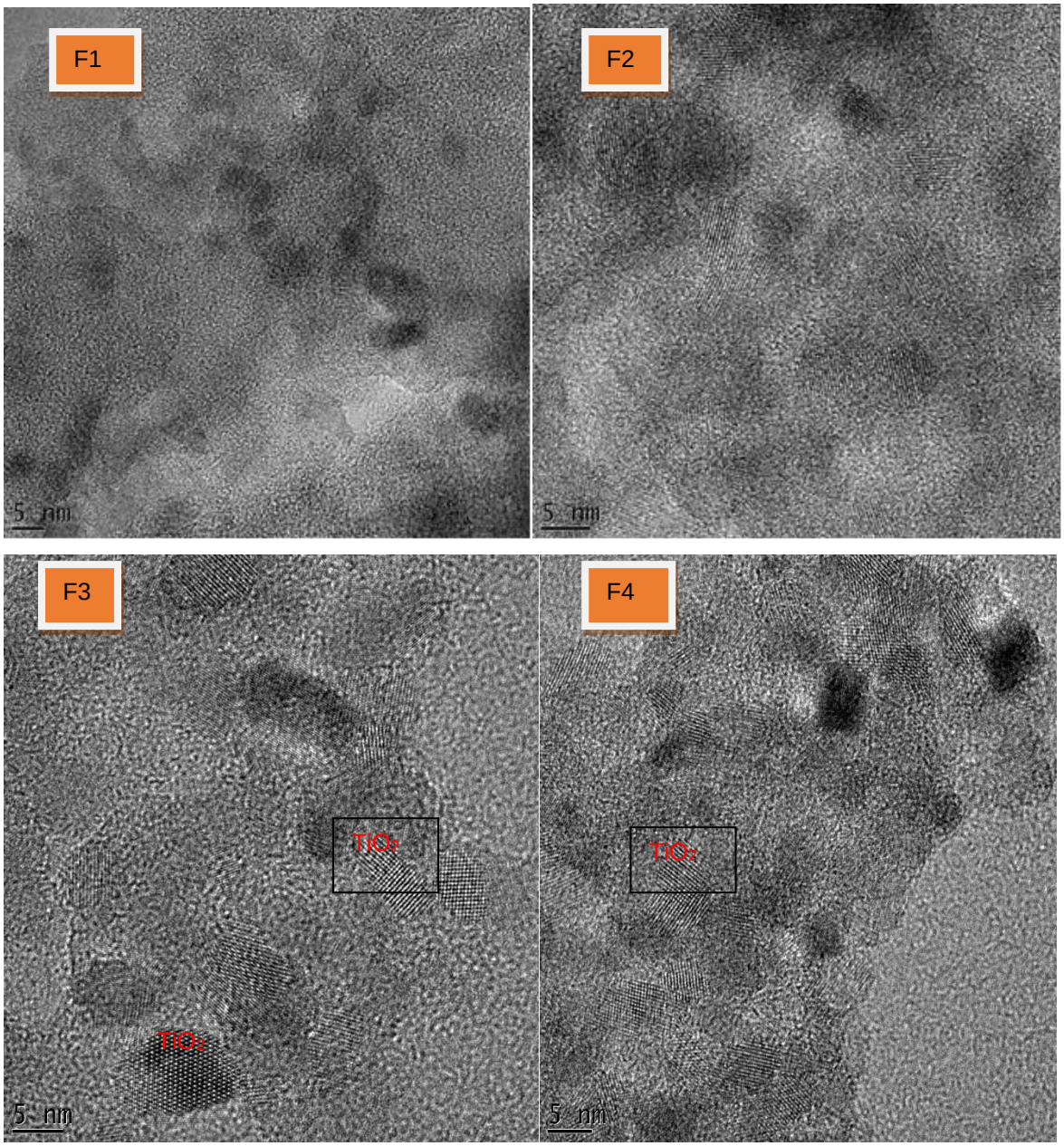

Figure 4-16: HRTEM of 10% (PAN/DMF/TiO2) sol gel solution coated stainless steel mesh calcined at 400°C with heating rate of 50°C/min and holding times of [F1] = 1 h, [F2] = 2 h, [F3] = 3 h and [F4] = 4 h.

4.4.2 X-Ray Diffraction

XRD was applied to establish the phase composition and purity of the synthesised, stainless steel supported TiO_2 catalyst. The XRD patterns of the catalysts are presented in Figures 4.17 to 4.19 and are similar. The HRTEM results presented above are in agreement with the XRD analysis (Figures 4.17 to 3.19). Figure 4.17 shows the XRD spectra of samples that were prepared at 300°C for various holding times (1-4 h).

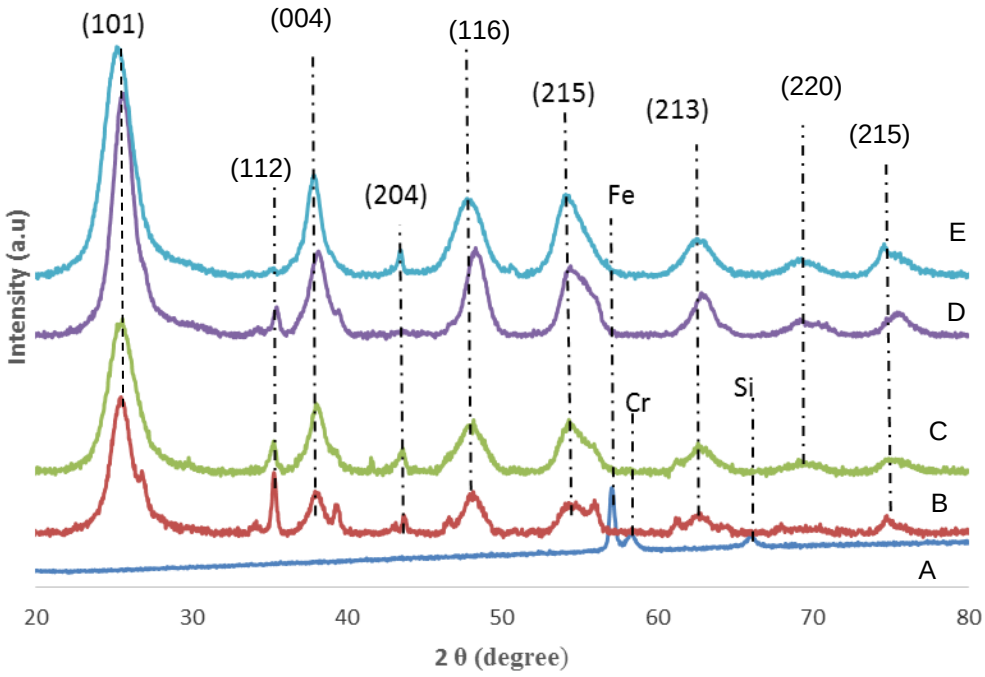

A= stainless steel mesh

B= 300^{0}C- 1 h

C=300^{0}C- 2 h

D=300^{0}C- 3 h

E=300^{0}C- 4 h

Figure 4-17: XRD pattern of stainless steel mesh supported and calcined TiO2 at 50°C /min up to 300°C at (1-4 h)

The peaks of the TiO_2 composites on stainless steel mesh, calcined 300°C at (1-4 h) correspond to anatase structure with good crystallinity. The high purity peaks at 2 θ values of 25.3, 37.9, 39.2, 45.1, 48.3, 53.7, 62.6, 68.8, 75.7 were observed in Figures 4.15 to 4.17 irrespective of holding time, and correspond to (112), (200), (220) and (215) planes of face centred cubic (FCC) anatase TiO_2, while other planes (101), (004), (204), (116) and (213) represent the anatase phase. The most intense peak at (101) which occurs at 2 θ = 25.3 in most of the XRD spectra represent a typical tetragonal anatase TiO_2. The most intense peak was observed at 25.31 2 θ value at a temperature of 400°C for 4 h while the lowest intensity of the 25.31 peak was achieved at a temperature of 300°C for 1 h. The intense and sharp peaks indicate the crystalline phase and purity of anatase TiO_2 nanocrystals. The intensity of the diffraction signal peak increased with an increase in calcination temperature and holding time. The average crystallite size of the synthesized TiO_2 nanomaterials was calculated using the Scherrer equation as shown in equation 25.

$$d = \frac{k\lambda}{\beta \cos\theta} \qquad (25)$$

Where d is crystallite size in nanometer, K= 0.89, λ is the wavelength of the X-ray which is 0.1541 nm, θ is the half-diffraction angle, β is the full width at half-maximum in radian. Using the above equation, the estimated crystalline size is given in Table 4.3. The information in Table 4.3 indicates that the increase in particle size of

the nanomaterial is directly related to the holding time at constant temperature and heating rate. The XRD peak at 101 revealed the crystallinity as well as the purity level of the synthesised supported anatase titanium dioxide nanomaterial. This exactly agrees with the Scherrer equation. The crystallite size (nm) increased as the synthesis holding time increased from 1 to 4 h.

Table 4.3: Crystallite size (d) of the supported TiO_2 calcined at 300°C for 1-4 h

Calcination temperature and holding time	2θ (degree)	β (radian)	Crystallite size (nm)
300ºC for 1 h	25.3	0.0277	4.9
300ºC for 2 h	25.3	0.0169	8.1
300ºC for 3 h	25.3	0.0151	9.1
300ºC for 4 h	25.3	0.0130	10.5

XRD patterns of stainless steel mesh and calcined TiO_2 at 50°C /min up to 350°C for 1-4 h are presented in Figure 4.18.

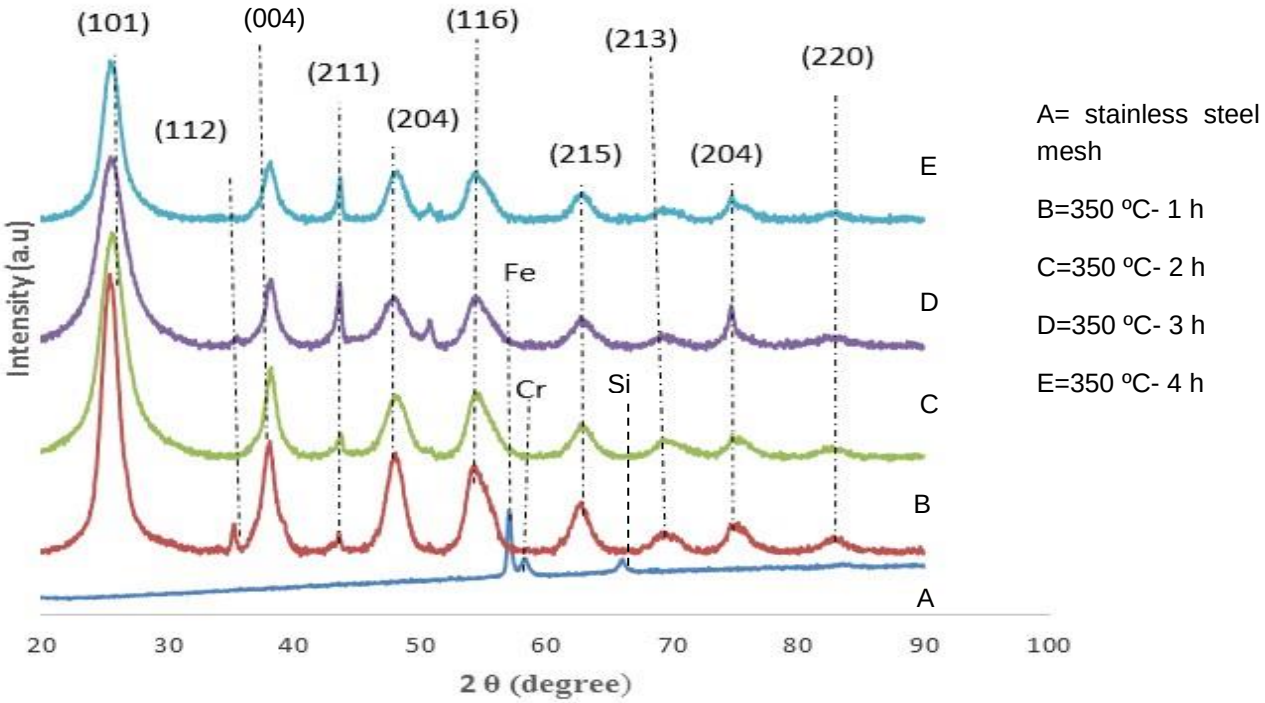

Figure 4-18: XRD pattern of stainless steel mesh supported and calcined TiO2 at 50°C /min up to 350°C at (1-4 h)

Table 4.4 again shows that the crystallite size (nm) increased as the synthesis holding time increased from 1 to 4 h at a temperature of 350ºC and crystallite size was somewhat larger than that obtained at 300 ºC. The XRD pattern of stainless steel mesh supported and calcined TiO_2 at 50°C /min up to 400°C at (1-4 h) is shown in Figure 4.19.

Table 4.4: Crystallite size (d) of the supported TiO_2 calcined at 350°C for holding time 1-4 hrs

Calcination temperature and holding time	2θ (degree)	β (radian)	Crystallite size (nm)
350ºC for 1 h	25.3	0.0122	11.2
350ºC for 2 h	25.3	0.0116	11.8
350ºC for 3 h	25.3	0.0109	12.6
350ºC for 4 h	25.3	0.0104	13.1

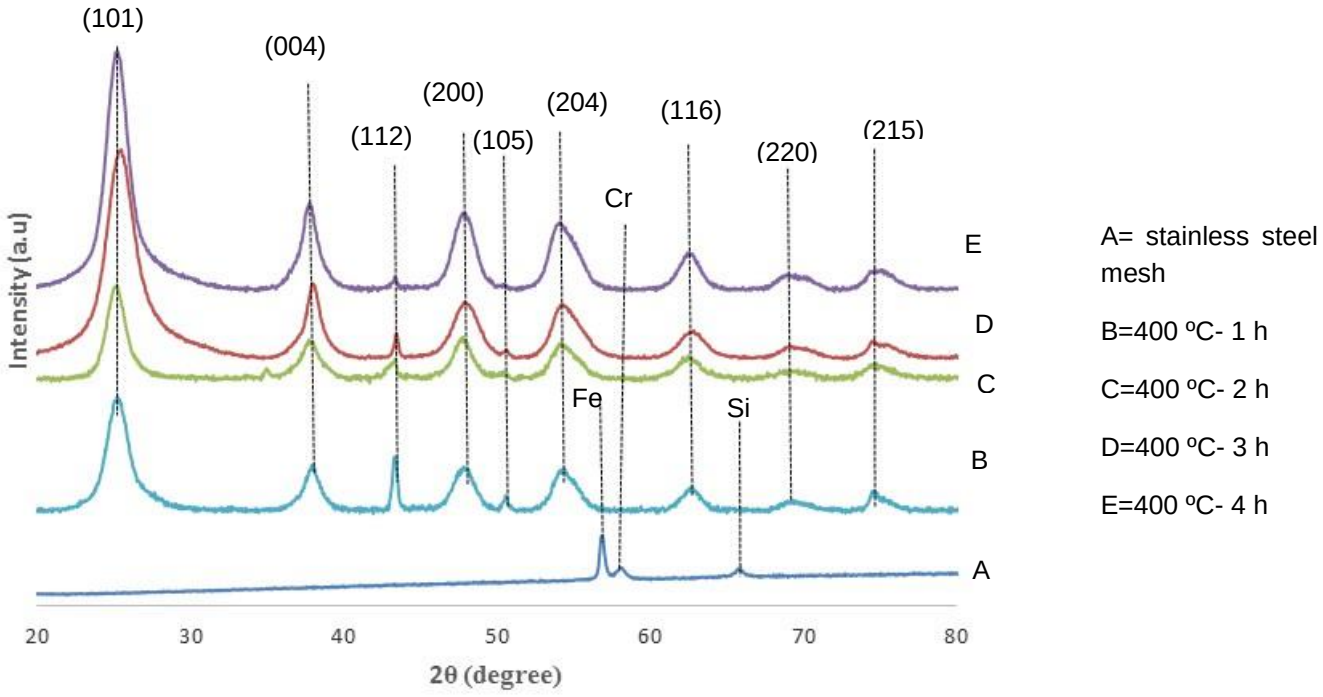

Figure 4-19: XRD pattern of stainless steel mesh supported and calcined TiO_2 at 50°C /min up to 400°C at (1-4 h)

Table 4.5: Crystallite size (d) of the supported TiO_2 calcined at 400°C for holding time 1-4 h

Calcination temperature and holding time	2θ (degree)	β (radian)	Crystallite size (nm)
400ºC for 1 h	25.3	0.0101	13.6
400ºC for 2 h	25.3	0.0095	14.4
400ºC for 3 h	25.3	0.0082	16.7
400ºC for 4 h	25.3	0.0069	19.8

Generally, as shown in Tables 4.3 to 4.5, the crystallite size (nm) increased as the calcination temperature and holding time increased from 300°C to 400°C for 1-4 h at constant heating rate of 50ºC per minute. The intensity of the diffraction peaks also increased with increasing calcination temperature and holding time. This was probably responsible for the increase in the crystallite size of the nano composite. The overall trend is better illustrated in Figure 4.20 which shows that the crystallite size range from 4.9 to 19.8 as the synthesis temperature increased from 300ºC to 400ºC. Clearly both calcination temperature and holding time affected the TiO_2 polycrystallite size, which is more accurately measured by the XRD peak broadening calculated using the Scherrer equation than from measuring agglomerated particles visible in HRSEM.

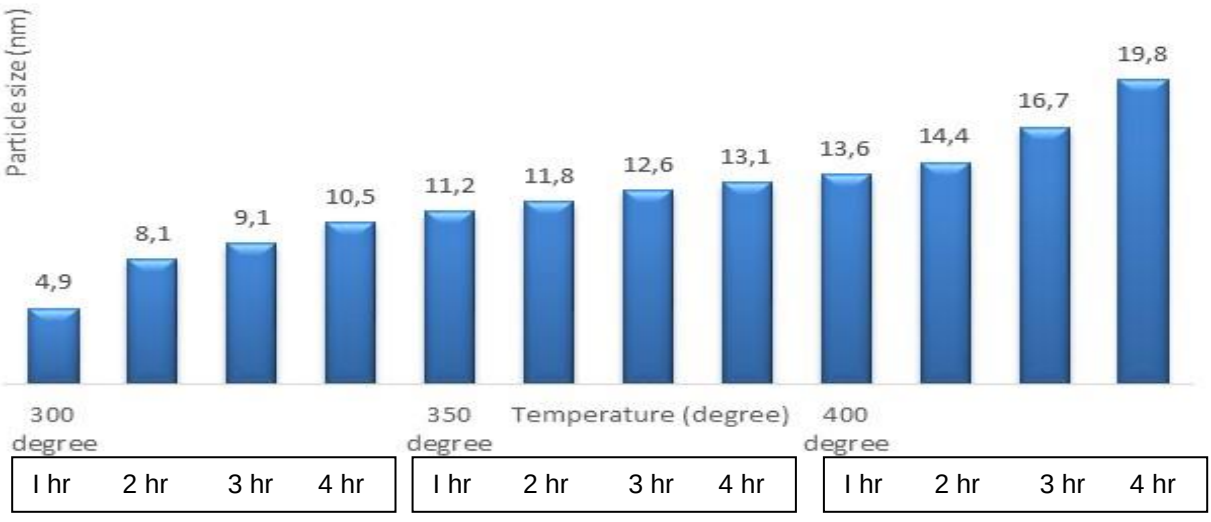

Figure 4-20: Particle size distribution as calcination temperature and holding time increased

4.4.3 Characterization of Ag deposited on stainless steel mesh supported TiO_2 nanocomposites

HRTEM and SAED pattern of the calcined TiO_2 at 400ºC for 2 hours, with 5 nm Ag/TiO_2 , or 10 nm Ag/TiO_2, or 15 nm Ag/TiO_2 nanocomposites, prepared using thermal evaporation for deposition of plasmonic metal onto TiO_2 surface (see Section 4.2.3) are shown in Figure 4.21. The TEM photos in Figure 4.21 show the morphology of Ag deposited onto TiO_2 surface. The dark spots within the composite material (P1-P3) depict the Ag-NP decorating TiO_2 nanocrystals. Thus, the presence and distribution of the spherical Ag NP can be observed clearly.

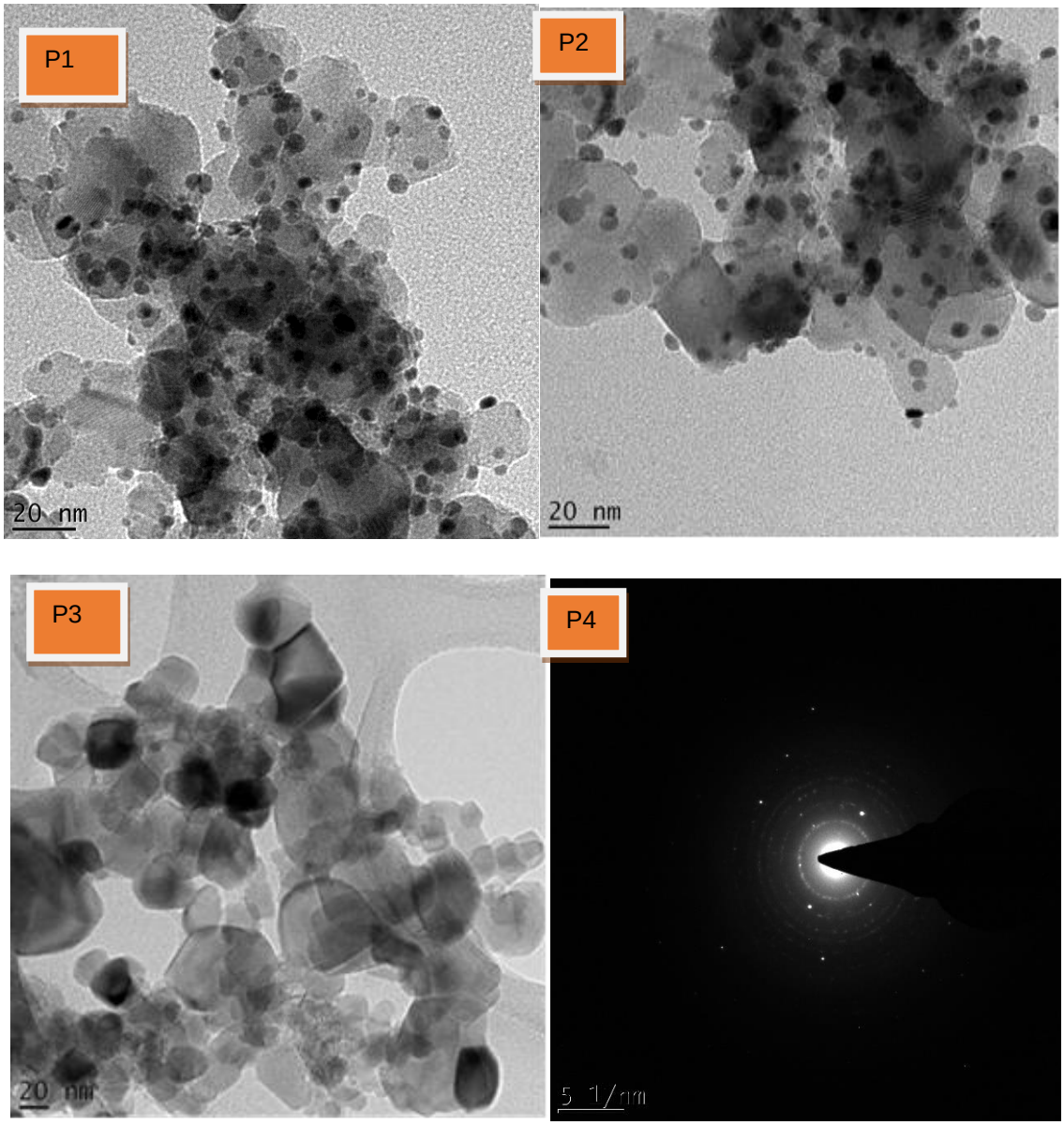

Figure 4-21: HRTEM of the calcined TiO_2 at 400ºC for 2 hours, with Ag layer thickness of 5 nm (P1), 10 nm (P2), 15 nm (P3) for Ag/TiO_2 nanocomposites and SAED pattern (P4)

In fact, the metallic silver appears widely distributed on the TiO_2 and are well scattered on the surface of TiO_2. But it did not form a thin film. This agrees with earlier studies that silver nanoparticles can be easily attached onto the surface of titania. This was attributed to its large radius (Sobana et al., 2006; Choi et al., 2009). The size of Ag nanoparticles were about 5-15 nm (Figure 4.22) (P1-P3)). The SAED revealed that the samples were made up of polycrystalline Ag nanoparticles and TiO_2 nanoparticles.

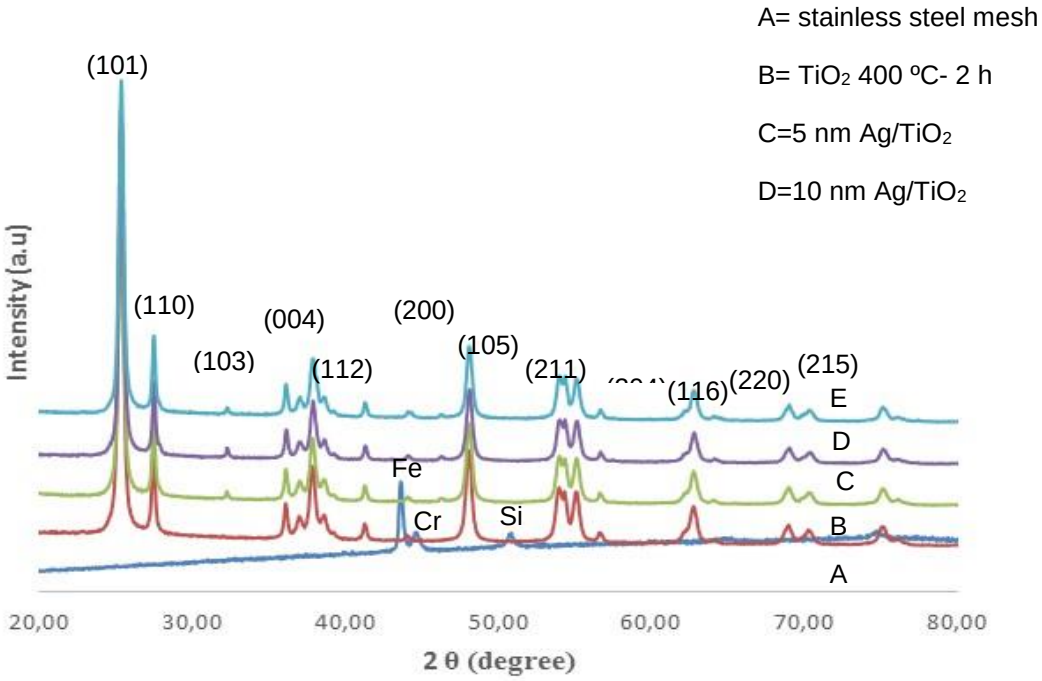

Figure 4-22: XRD pattern of stainless steel mesh support and calcined TiO_2, compared with 5 nm, 10 nm, or 15 nm Ag deposited TiO_2 nanocomposites

As shown in Figure 4.22, the XRD patterns of supported TiO_2 and Ag deposited TiO_2 nanocomposites almost coincide. The peak-match suggests that the Ag nanoparticles were actually embedded well into the TiO_2 crystals. The Ag peaks were not really discernible inferring that the crystallite size was smaller than XRD resolution. This could be attributed to the amount and size of Ag particle deposited, which made the peaks almost invisible by XRD as they are in the low nm range. The crystallite size of Ag only ranged between 5 and 15 nm according to HRTEM. Subsequently, the peak intensity of TiO_2 [101] remains the same and the diffraction angle hardly changed despite the deposition of different layer thickness of Ag. Therefore, the particle size of TiO_2 did not change as such with an increase in Ag content, suggesting that the crystallite size of photocatalysts remained more or less constant as measured prior to Ag deposition.

The diffused reflectance spectra of supported TiO_2 after being calcined at 400 C for 2 h and after thermal deposition of Ag upon the TiO_2 with thickness of Ag varying from 5 nm to 15 nm, are shown in Figure 4.23.

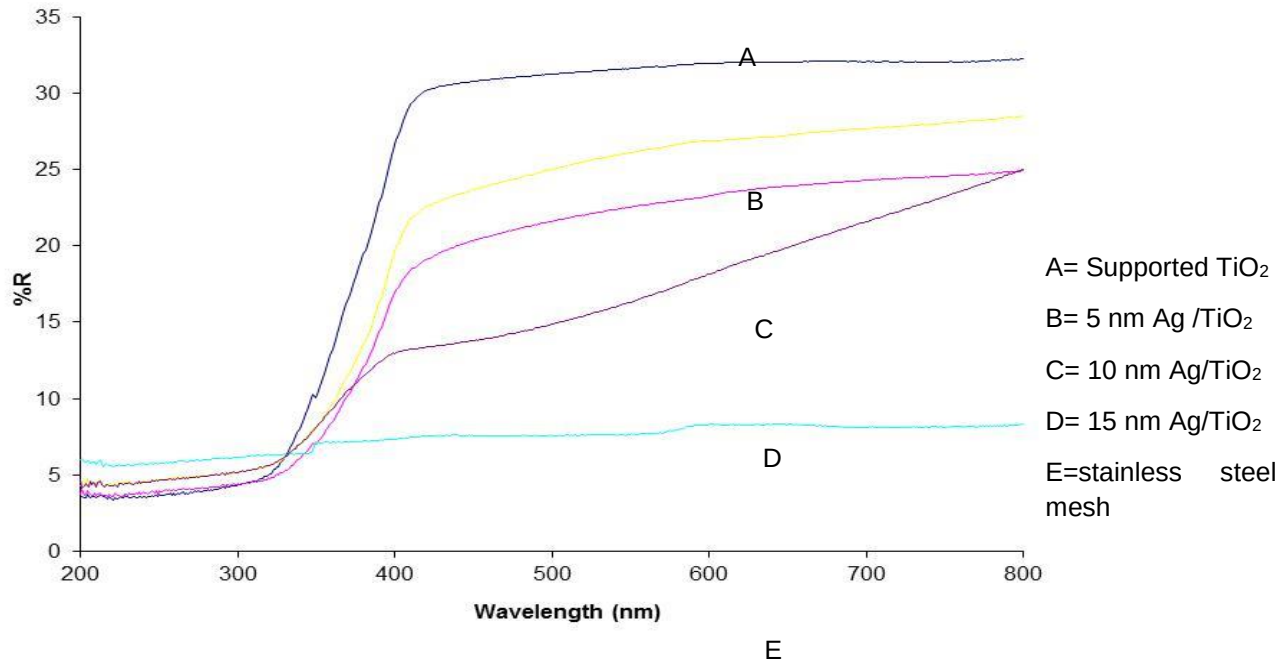

Figure 4-23: UV-Visible diffuse reflectance spectra of A) supported TiO_2 B) 5 nm Ag/TiO_2 C) 10 nm Ag/TiO_2, D) 15 nm Ag/TiO_2 and E) stainless steel mesh

In Figure 4.23 the Ag deposited TiO_2 samples actually exhibited a red-shift of an additional broad absorption band from 352-410 nm. The absorption band of Ag deposited TiO_2 slightly shifted towards the visible region. This was plausibly due to the surface plasmon absorption of metallic Ag that gives rise to localized energy in the band gap (Daniel et al., 2013). Similarly, it was possible for Ag to transfer electrons to the TiO_2 surface simply because the metallic band gap energy (*Eg*) has a lower Fermi level than that of TiO_2. The effect of incorporated silver towards extending the value of Ag to the visible region was ascribed to the electron donating character of the metallic silver. This improves the adsorption threshold in the electric field and at the same time reduces the recombination rate of the photo-generated electron-hole pairs in TiO_2. Also, the absorption band observed at 410 nm has been widely reported in the literature for metallic silver deposited on TiO_2 lattice (Suwarnkar et al., 2014). However, excessive deposition of metallic silver onto TiO_2 surface creates big silver clusters that may perhaps prevent light from reaching the TiO_2 surface as evidenced in HRSEM images for the 15 nm Ag sample. As a result of that, the band gap energy of 15 nm Ag was higher than 5 and 10 nm Ag. The band gap energy (Eg) of the supported TiO_2 as well as the Ag deposited TiO_2 nanocomposites were obtained using the equation below.

$$Eg = \frac{1240}{\lambda} \text{ ev} \qquad (26)$$

Where *Eg* stands for the band gap in electron volt (eV), and λ is the wavelength of the absorption edges in the spectrum in nanomater (nm).

As depicted in Figure 4.23, the integrated UV-Vis spectra from supported TiO_2, 5 nm Ag/TiO_2, 10 nm Ag/TiO_2, 15 nm Ag/TiO_2 and stainless steel mesh have the following wavelengths of 393 nm, 398 nm, 410 nm and 408 nm respectively. From the above equation, the estimated band gap energy of the synthesized TiO_2 and deposited different thickness of Ag onto TiO_2 surface are shown in Table 4.6 below. Thus, E_g values of the supported TiO_2 nanoparticle have been narrowed from 3.15 to 3.02 eV by deposition of Ag on TiO_2 matrix.

Table 4.6: Wavelength edge and the estimated band gap energies of supported TiO_2 with different thickness of Ag

Synthesised material	Wavelength edge (λmax)	Band gap (Eg) (ev)
Stainless steel mesh		
TiO_2	393	3.15
5 nm Ag/TiO_2	398	3.11
10 nm Ag/TiO_2	410	3.02
15 nm Ag/TiO_2	408	3.04

Figure 4.24 depicts the FTIR spectra of ordinary PAN used in synthesising the supported catalyst while Figure 4.25 presents the FTIR spectra of the supported photocatalyst and Ag deposited TiO_2 nanocomposites.

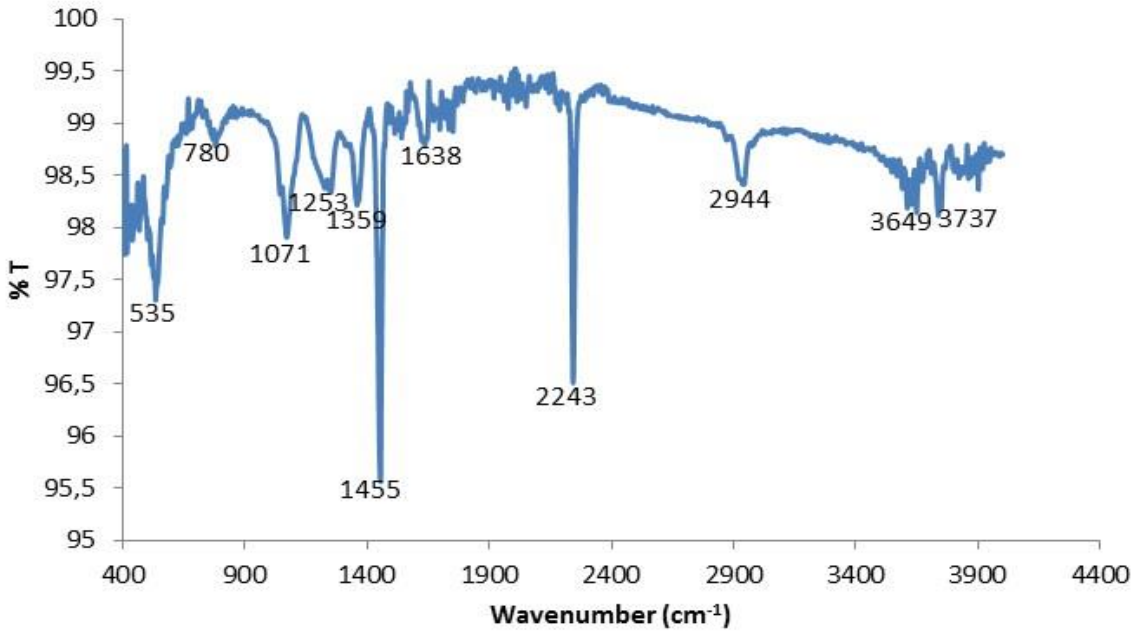

Figure 4-24: FTIR spectra of ordinary polyacrylonitrile

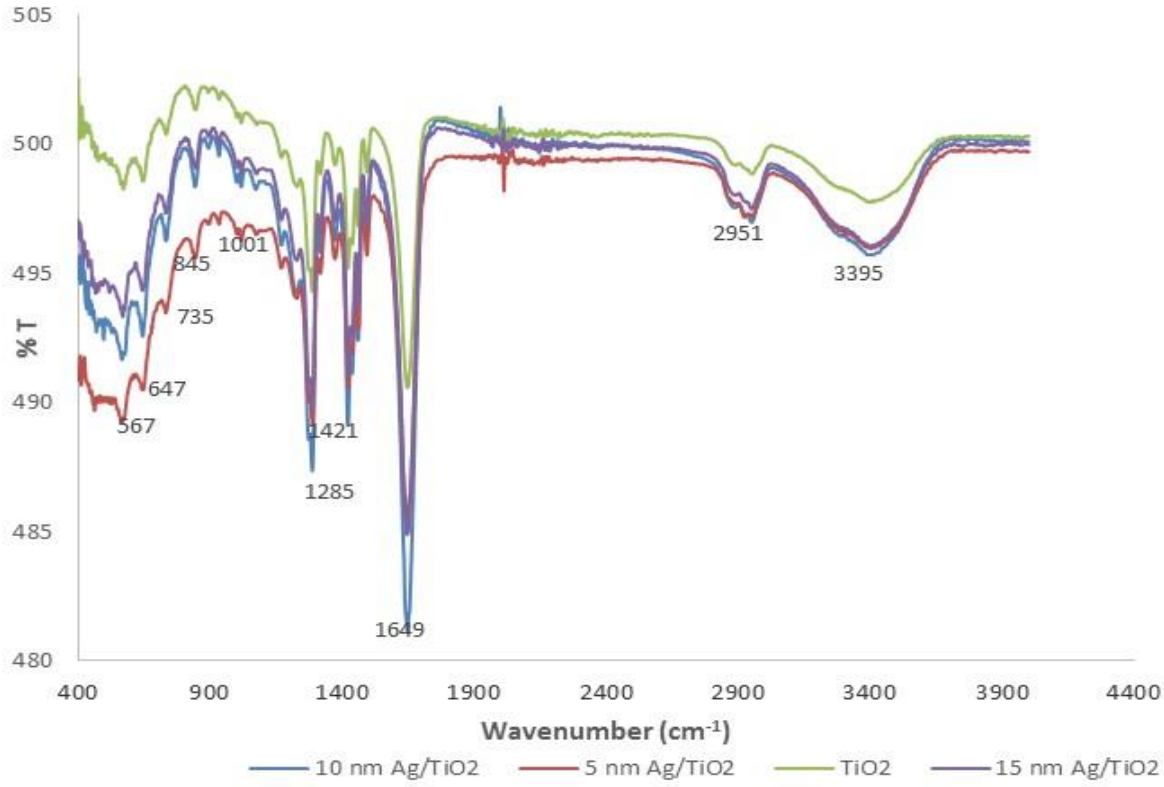

Figure 4-25: FTIR of PAN sol-gel supported TiO_2, compared to 5 nm Ag/TiO_2, 10 nm Ag/TiO_2, 15 nm Ag/TiO_2 nanocomposites

The FTIR spectra of ordinary PAN show peaks that relate to CH_2, C=N, C=O, C-O and C-H bonds of PAN. In Figure 4.25 the absorption peak at 2944 cm^{-1} corresponds to C-H bonds in CH, CH_2 and CH_3 whereas the peak observed at 2951 cm^{-1} is similarly related to C-H bonds. Another peak observed at 2243 cm^{-1} in Figure 4.25 was due to the presence of nitrile (C=N) bonds, and this confirms the existence of the nitrile group in the unmodified polyacrylonitrile chain. The absorption peaks in the range of 1455-1638 cm^{-1} and 1071 cm^{-1} are related to C=O, C=C, or C-O bonds.

After the carbonation and stabilization of 8% PAN/DMF/$TiCl_4$ at 400ºC for 2 hours, supported TiO_2 was formed after which different thickness of Ag was deposited (details in Section 4.2.3). The FTIR spectra of the synthesised material taking into cognisance the raw material (PAN) show that some PAN peaks disappeared due to carbonization depending on the applied calcination conditions, while other new noticeable peaks were identified (Figure 4.25). The peaks at 1455-1638 cm^{-1} and 1071 cm^{-1} that are related to C=O, C=C, or C-O bonds are still visible in the calcined samples and thus indicate the possible formation of a strong adhesive bond created by partial PAN decomposition between the TiO_2 and the stainless steel mesh.

The TiO_2 has absorption at 740, 725, 647, 568 and 560 cm^{-1} which are the characteristic peaks of TiO_2 that correspond to antisymmetric Ti-O-Ti mode of TiO_2, Ti-OH and Ti-O stretch. Peaks at 1289 cm^{-1} and a broad

band at 3395 cm^{-1} was assigned to mixed hydroxyl groups such as Ti-O-H. The sharp peak at 1649 cm^{-1} and broad peak at 3395 cm^{-1} were attributed to the stretching vibration of -OH and C-H vibration groups as well as surface adsorbed water (Jagadale et al., 2008; Suwanchawalit et al., 2011). This shows that -OH group adsorbed to the surface of TiO_2 and formed TiO_2-OH bonds that arose from the hydrolysis reaction in the preparing process. The adsorbed OH ions play a crucial role in photocatalysis by trapping the charge carriers, forming reactive OH radicals that actually promote the photocatalytic process.

The FTIR spectrum of titanium dioxide exhibiting a stretching vibration at 735 cm^{-1} ascribed to the presence of the CH_2 group. A stretchable vibration band at 2,951 cm^{-1} confirms the presence of C-H group. The FTIR spectra of the crystals show the Si-CH_3 bonds at 1285 cm^{-1}. The band 1421 cm^{-1} corresponds to a vibration of the Ti-Ligand bond. In most cases, the sharp bands around 1649 cm^{-1}, 1465 cm^{-1}, 1421 cm^{-1} can be assigned to OH modes (bending modes) of hydroxyl (OH) groups. The band at around 1001 cm^{-1} corresponds to the asymmetric stretching vibrations of SiO_2 tetrahedral. A shoulder at about 845 cm^{-1}, though not too broad, suggests bonds of the type Ti-O-Si arising from the interaction with the stainless steel mesh. The band between 567 and 647 cm^{-1} can be ascribed to Si-O and Fe-O bonds (bending vibrations). The silicon and iron are probably from the stainless steel mesh as indicated in XRD. The intensity of bands at 3395, 1649 and 735 cm^{-1} indicates the formation of Ag-TiO_2 composite (Suwarnkar et al., 2014).

4.5 PHOTOCATALYTIC ACTIVITY OF SUPPORTED TiO_2 NANOCRYSTALS

This section provides experimental information on the photocatalytic set up used to determine the activity of the various synthesised catalysts.

4.5.1 Fused silica supported materials

The effect of loading of the plasmonic elements on the photocatalytic activity of TiO_2 was investigated using different metal film thicknesses. This was done so as to find the optimum loading of each metal for better TiO_2 photocatalytic activity enhancement. All the elements (Cu and Ag) were investigated separately to find out which metal was better than the other. The use of a bilayer system and the effect of order of deposition were also investigated. These various experiments were conducted so as to come up with the best conditions for the enhancement of TiO_2 photocatalytic activity. The photocatalytic activities of the thin films were evaluated based upon the removal of methyl orange as a model pollutant. The Ag/TiO_2 and Cu/TiO_2 thin films on fused silica were immersed in a 10 ppm (30.6 µM) methyl orange solution. The methyl orange solution was prepared using distilled water. The solution was then irradiated with UV light of wavelength 254 nm. Aliquots were taken after every 30 minutes for UV-Vis analysis at a wavelength of 468 nm. The schematic representation of the experimental set up is shown in Figure 4.26.

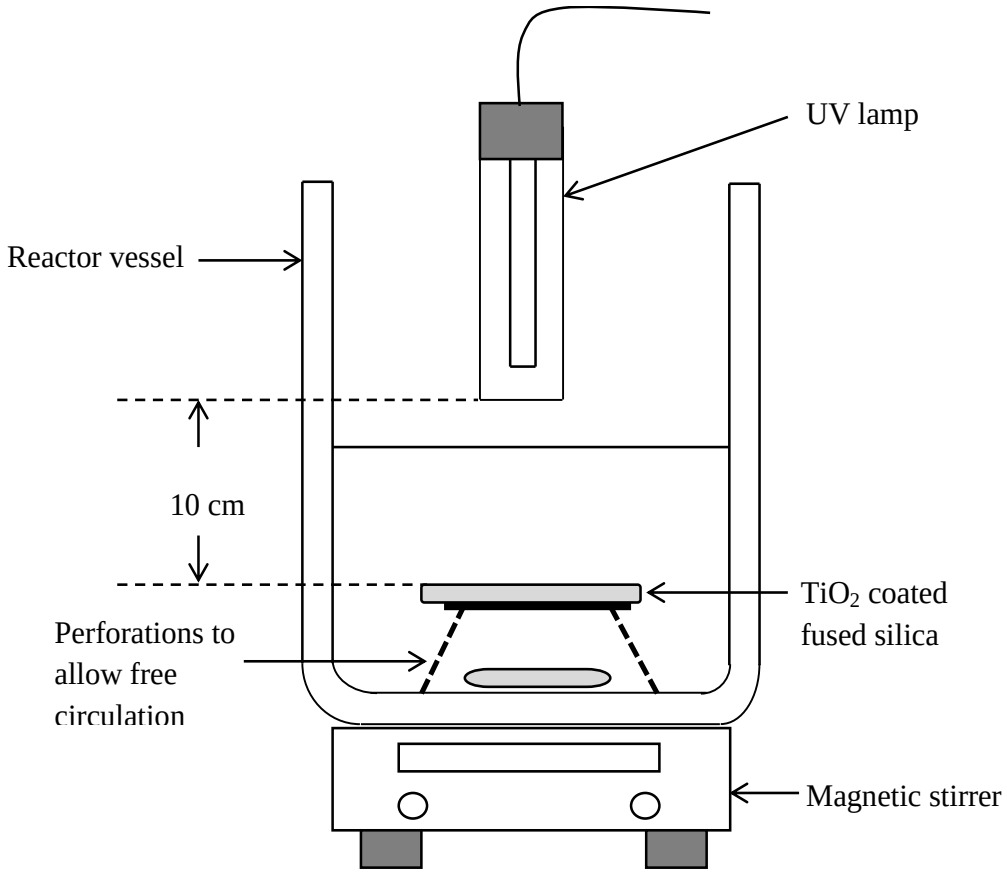

Figure 4-26: Schematic diagram showing the set-up for the photocatalytic activity experiment

The experiments were done in a dark room to exclude ambient light. A control experiment (CE) was done with no catalyst but with UV light irradiation. The best photocatalyst in photodegrading methyl orange was also tested for its photocatalytic activity towards bisphenol A (BPA) of concentration 43.8 µM using the same experimental conditions as those used for methyl orange. The change in concentration of BPA was also determined by UV-Vis analysis at a wavelength of 586 nm.

4.5.2 Stainless steel supported Ag/TiO_2 composite materials

The photocatalytic activity of both the supported TiO_2 nanocrystals calcined at (300º, 350º and 400ºC for 3 h holding time were evaluated using methylene blue (MB) (concentration of 10 ppm) as a modelled pollutant. MB was used as a model pollutant to rapidly evaluate the most active catalyst and its removal percentage as measured by decoloration was taken as a measure for comparing photocatalytic activity. The experiment was conducted in a self-designed 500 mL beaker photo reactor containing 50 mL of MB solution (10 ppm concentration), pH of 6.8 and 30 mg of the supported catalysts. 30 mg of the supported photocatalyst and 50 mL of MB aqueous solution were placed in a beaker with continuous magnetic stirring at ambient temperature. The MB solution was irradiated with a 9 W UV mercury vapour lamp of wavelength of 254 nm. The UV lamp was positioned at the centre at a distance of 1 cm between the UV lamp and surface of MB. The supported

catalyst was immersed in such a way that the incident light fell onto the surface of the catalyst. The photocatalytic experiment was conducted in darkness to avoid interference with normal light. Prior to photocatalytic activity, a control experiment involving 30-35 mg supported catalyst and 50 mL of MB (10 ppm) was conducted in the dark with continuous stirring for 6 h on a magnetic stirrer at 150 rpm. A 2 mL solution was sampled periodically at every 1 h and immediately analysed using a UV-Visible spectrophotometer. This was done to establish that removal of methylene blue by the supported catalyst did not occur via adsorption. Further control experiments were conducted by exposing the methylene blue to UV-light without catalysts. These were done to establish that the degradation of the target compound at ambient temperature was only due to the presence of the supported photocatalysts.

The supported catalyst immersed in MB solution was continuously stirred in the dark for 30 min to establish adsorption/desorption equilibrium. The concentration of the dye after adsorption saturation was taken as the initial concentration of the MB. Thereafter, the photo-reactor was closed; the UV lamp switched on for 30 minutes to provide constant light intensity during the experiment and photocatalytic decomposition of MB was continuously monitored. At specific time intervals, 2 mL samples were withdrawn from the photoreactor and centrifuged accordingly to separate any residual catalyst. The absorption intensity of the clear solution at 664 nm was then measured using a Nicolette-Evolution 100 Ultraviolet spectrophotometer (Thermal Electron Corporation, UK). The actual concentration of the MB was estimated from the calibration curve. The experiment was repeated twice and an average experimental value was determined. The effect of the solution pH (3, 6, 9, and 12) and initial concentration of MB (10, 20 and 30 ppm) were studied.

4.5.2.1 *Effect of the solution pH*

The effect of solution pH on the photocatalytic activity of the stainless steel supported catalyst was determined by varying the pH of the methylene blue from 3 to 12. The solution pH was adjusted by adding a few drops of 0.5 M NaOH or 0.5 M H_2SO_4. The experiment was conducted in a self-designed 500 mL beaker photo reactor containing 50 mL of MB solution (10 ppm concentration) and 30 mg of the supported catalysts. The mixture containing the supported catalysts was continuously stirred on a magnetic stirrer at 150 rpm for 5 h. At specific time intervals, 2 mL samples were withdrawn from the photoreactor and centrifuged to separate the residual catalyst. The absorption intensity of the clear solution at 664 nm was then measured using Nicolette-Evolution 100 Ultraviolet spectrometer. The experiment was repeated twice (n= 2) and average experimental values were determined.

4.5.2.2 *Effect of the initial concentration of methylene blue*

The effect of initial concentration of MB over time on the photocatalytic decomposition of modelled pollutants in the presence of stainless steel supported TiO_2 nanocrystals and Ag deposited TiO_2 nanocomposite was investigated in the concentration range of 10-30 ppm. The pH of the MB was regulated to 3 by adding drops of 0.5 M H_2SO_4. This experiment was also conducted in a self-designed 500 mL beaker photo reactor

containing 50 ml each of MB solution (10 to 30 ppm concentration) and 30 mg of the supported catalysts. The mixture containing the supported catalysts was continuously stirred on a magnetic stirrer at 150 rpm for 5 h. At specific time intervals, 2 mL samples were withdrawn from the photoreactor and centrifuged to separate the residual catalyst. The absorption intensity of the clear solution at 664 nm was then measured using Ultraviolet spectrometer mentioned earlier. The experiment was repeated twice and average experimental values were determined. After the experiment, the residual mass loss of the supported catalyst was estimated based on the differences between initial and final masses.

In further experiments of the photomineralisation of MB solution by stainless steel supported TiO_2 nanocrystals and Ag deposited TiO_2 nanocomposites the optimum solution pH and initial concentration of MB were applied. The concentration of the MB solution after the photocatalytic degradation experiment was calculated from the absorption intensity of the clear MB solution measured at 664 nm by Nicolette-Evolution 100 Ultraviolet spectrophotometer in line with calibration curve. The different concentration and the calibration curve are shown in Table 4.7 and Figure 4.27 respectively.

Table 4.7: Different concentrations of methylene blue used for the calibration curve

Concentration (ppm)	Absorbance
2	0.517
10	2.060
15	2.913
20	3.712
40	6.991

The residual concentration of each sample after the photocatalytic experiment was estimated from the calibration curve via extrapolation. Alternatively, the absorbance value was divided by the obtained slope from the calibration curve.

$$Residual\ concentration\ (in\ ppm) = \frac{Absorbance}{Slope\ of\ the\ calibration\ curve}$$

The degradation percentage of MB by the photocatalyst was calculated using the equation below.

$$Degradation\ percentage\ = \frac{Co - Ct}{Co} * 100$$

Where Co and Ct represent the initial and the final concentration of MB solution respectively.

MB was used as a model pollutant to rapidly evaluate the most active catalyst and its removal percentage was taken as a measure for comparing photocatalytic activity. The reader should note that percentage removal does not imply complete degradation as the decoloration of MB merely indicates the rate of conversion of the MB molecule into intermediate compounds, not its complete mineralisation.

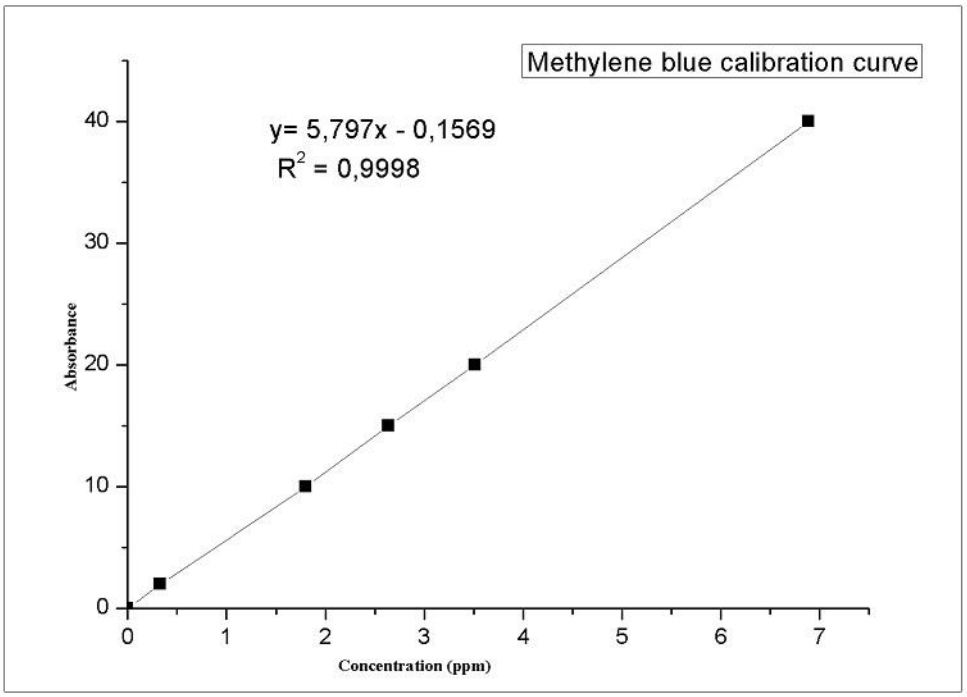

Figure 4-27: Calibration curve of the standard methylene blue solution.

4.6 RESULTS AND DISCUSSION

The extent to which Ag monolayer and bilayer systems enhanced the photocatalytic activity of TiO_2 photocatalyst is also presented. Thereafter the photocatalytic activity of the stainless steel mesh supported composites for MB decoloration are presented.

4.6.1 Photocatalytic degradation by fused silica supported thin films of TiO_2

Photocatalysis involves absorption of photo-light by catalysts to generate free reactive species. The photocatalytic efficiency depends on the ability of the catalyst to create electron-hole pair which in turn generates free radicals. The generation of the electron-hole pairs by the synthesised TiO_2 catalyst depends on TiO_2 dosage, initial concentration of the model pollutants, light intensity/wavelength, calcination temperature amongst others. However, several studies have demonstrated the effectiveness of heterogeneous photocatalyst such as TiO_2 on the mineralization of different organic pollutants (Barakat et al., 2013; Jia et al., 2012; Leong et al., 2014).

The effect of loading of the plasmonic elements on the photocatalytic activity of TiO_2 was investigated using different metal film thicknesses. This was done so as to find the optimum loading of each metal for better TiO_2 photocatalytic activity enhancement. All the elements (Cu and Ag) were investigated separately to find out which metal was better than the other. The use of a bilayer system and the effect of order of deposition were also investigated. These various experiments were conducted so as to come up with the best conditions for the enhancement of TiO_2 photocatalytic activity.

4.6.1.1 *Effect of film thickness using silver*

Generally all the four photocatalysts (T5Ag, T10Ag, T20Ag and T25Ag) showed higher photocatalytic activity than the pure TiO_2 photocatalyst under UV light (Fig. 4.28) which implies that all the Ag film thicknesses improved the photocatalytic activity of TiO_2 photocatalyst. The reason for the observed increase in photocatalytic activity of the metal coated TiO_2 photocatalyst is ascribed to the Schottky barriers formed between the TiO_2 and the Ag nanoparticles. These barriers may facilitate the transfer of electrons from TiO_2 nanoparticles with high Fermi level to silver nanoparticles which have a low Fermi level, resulting in reduced electron-hole recombination rates. These results are similar to those reported in literature on the production of hydrogen in a photocatalytic process using Ag/TiO_2, Au/TiO_2, and Pt/TiO_2 (Chiarello et al., 2010). In the study, it was found that hydrogen production was enhanced by the metals due to the formation of Schottky barriers which promoted photogenerated electron transfer.

There was a gradual increase in the photodegradation of methyl orange as the Ag metal film thickness was increased from 5 nm to 20 nm. Further increases in film thickness to 25 nm caused a decrease in TiO_2 photocatalytic activity by 16.89% implying that 20 nm was the optimum film thickness of Ag. The results are summarized in Table 4.8 and the general trend for the films in enhancing TiO_2 photocatalytic activity was T20Ag > T10Ag > T25Ag > T5Ag > T1. The reason for the observed trend was that the thicker the Ag metal film, the better the displacement of the electrons to lower layers of the metal film. This implies that there are more chances of the electrons to be far from the TiO_2 photocatalyst layer where electron holes are confined hence, the charge separation is better when compared with thin metal films. This would result in the surface of TiO_2 being enriched with holes which can directly degrade methyl orange and oxidize water to produce hydroxyl radicals that degrade organics effectively.

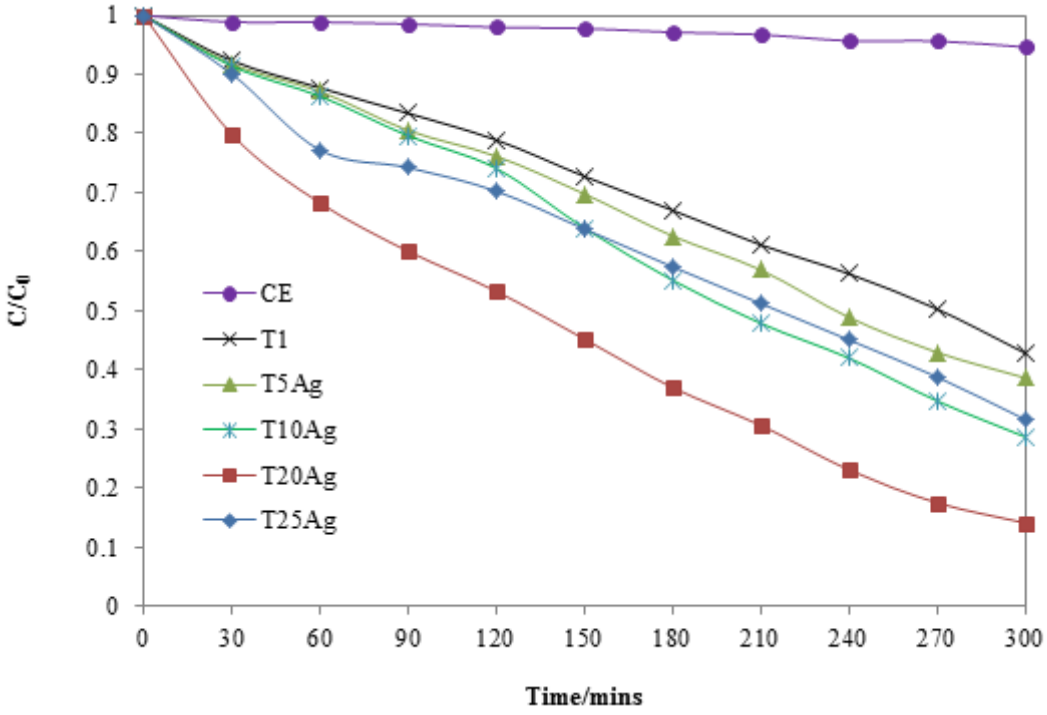

Figure 4-28: Photodegradation profiles of methyl orange (10 ppm) using fused silica coated TiO_2 photocatalyst deposited on Ag films of different thicknesses (5, 10, 20 and 25 nm) under UV light at 25°C and pH 7.

4.6.1.2 *Effect of film thickness using copper*

Fig. 4.29 shows the photodegradation curves of methyl orange using 100 nm TiO_2 photocatalyst film deposited on top of Cu films of different thicknesses on fused silica support that are T5Cu, T10Cu, T20Cu and T25Cu. A higher photodegradation rate of methyl orange was observed in the first 30 minutes when compared to later times and this was characteristic for all copper films underneath TiO_2 photocatalyst (Figure 4.29). The highest photocatalytic activity was achieved when TiO_2 was deposited on a 5 nm Cu film which was the thinnest and further increase in the metal film thickness above 5 nm had a detrimental effect on the photocatalytic activity. The photocatalytic activities of all the photocatalysts with Cu film thicknesses above 5 nm were below the photocatalytic activity of T1 (bare TiO_2). The relatively higher performance with a 5 nm Cu film under UV light when compared to pure TiO_2 is due to the fact that copper nanoparticles (CuNPs) trap electrons from TiO_2 thereby reducing electron-hole recombination rates and also the resulting increase in electron density in CuNPs gives rise to a shift in plasmon since the surface plasmon resonance band intensity and wavelength depends the electron charge density (Huang et al., 2010). The reason for the observed trend T5Cu > T1 > T10Cu > T25Cu > T20Cu could be due to the presence of Cu^{2+} ions in solution due to leaching.

These Cu^{2+} ions have been found to retard the photocatalytic activity of TiO_2 due to, (i) the short circuiting reaction which causes electron-hole recombination and (ii) the deposition of Cu metal which causes a reduction in the light reaching TiO_2 (Dhananjeyan et al., 1997). However, there is controversy in literature about the

effect of Cu^{2+} on the photodegradation rate. Some authors mention an increase in photodegradation rate until an optimum concentration (Brezova et al., 1995) while others mention a detrimental effect (Wei et al., 1992).

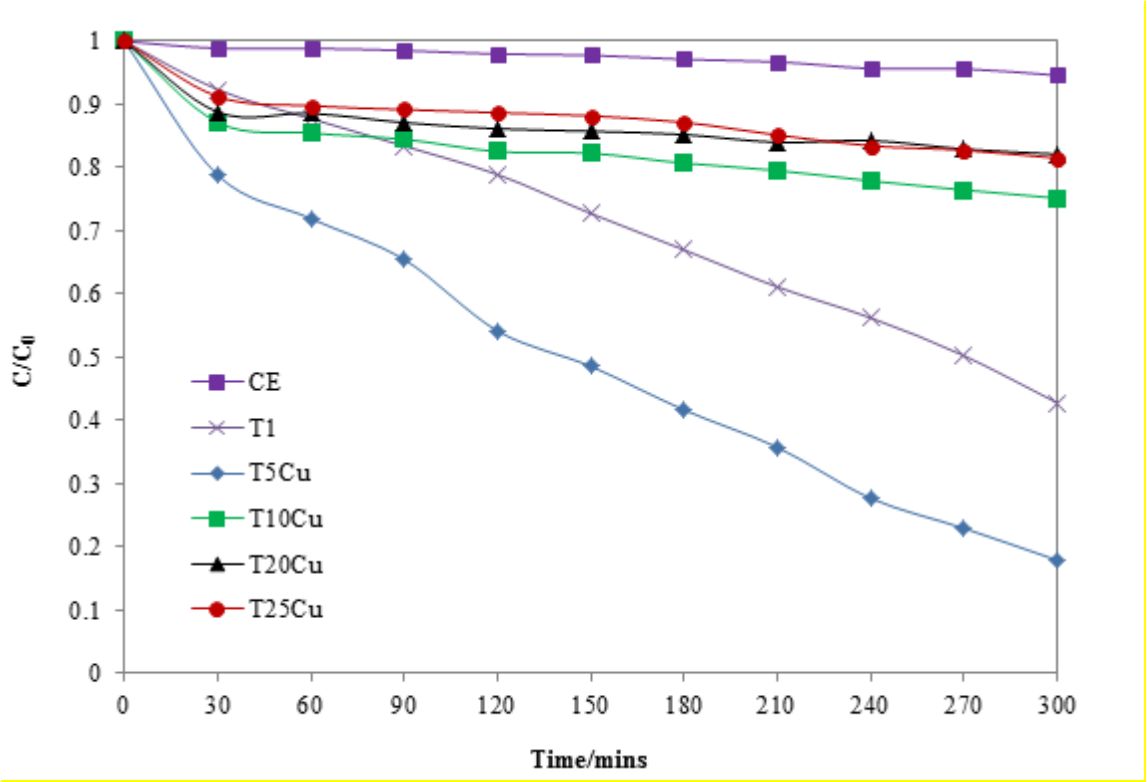

Figure 4-29: Photodegradation curves of methyl orange (10 ppm) using fused silica coated TiO_2 photocatalyst film deposited on top of Cu films of different thicknesses (5, 10, 20 and 25 nm) under UV light at 25°C and pH 7.

4.6.1.3 *Comparison of the effect of Cu and Ag on TiO_2 photocatalytic activity*

This section summarizes and makes a comparative evaluation of the effect of using different plasmonic metal thin films on fused silica on the photocatalytic activity of TiO_2 towards methyl orange solution. The control experiment used pure TiO_2 photocatalyst film on fused silica, the fixed parameter was the metal thickness, and the variable was the type of the plasmonic metal used. The percentage photodegradation of methyl orange at 25°C and pH 7 under UV light using TiO_2 photocatalyst on top of different plasmonic metal layers are shown in Table 4.8.

It can be seen from Table 4.8 that for a 5 nm metal film, the highest enhancement of 24.86% was achieved by copper whereas silver showed only 4.17% when TiO_2 was deposited on top of the metal. The 10 nm, 20 nm and 25 nm metal films of copper had a negative impact on the photocatalytic activity of TiO_2. They inactivated the photocatalyst and the resulting photodegradation of the methyl orange under UV light was reduced by 32.36%, 39.32% and 38.68% respectively when compared to pure TiO_2 photocatalyst with no metal film underneath. Unlike copper, all the film thicknesses of silver used in this study improved the photocatalytic activity of TiO_2 towards methyl orange when compared to the pure TiO_2 photocatalyst. The optimum film

thickness for Ag was 20 nm which gave the best overall TiO_2 photocatalytic activity enhancement, whereas for copper it was the 5 nm layer.

Table 4.8: Percentage degradation of methyl orange at 25°C and pH 7 under UV light using TiO_2 photocatalyst on different metal films of different thicknesses**.**

Photocatalyst	% of Methyl orange photodegraded after 300 minutes		% Increase relative to pure TiO_2 photocatalyst	
	Ag	Cu	Ag	Cu
TiO_2 on 0 nm	57.16	57.16	-	-
TiO_2 on 5 nm	61.33	**82.04**	+4.17	+24.86
TiO_2 on 10 nm	71.32	24.80	+14.16	-32.36
TiO_2 on 20 nm	**85.27**	17.84	+28.11	-39.32
TiO_2 on 25 nm	68.38	18.48	+11.22	-38.68

4.6.1.4 *Effect of order of deposition*

The evaluation of the effect of order of deposition of metal films relative to TiO_2 photocatalyst film was done to determine the best metal film position (top or bottom) on fused silica for the enhancement of photocatalytic activity of TiO_2 towards methyl orange (Figure 4.30). It was determined by depositing a thin film of noble metal on top of the fused silica supported TiO_2 photocatalyst and in the other case underneath the TiO_2 photocatalyst as reported previously. The control was pure TiO_2, the variable was the position of the plasmonic metal relative to TiO_2 photocatalyst film and the fixed parameters were the type of plasmonic metal and film thickness. Each plasmonic metal was evaluated separately.

The choice of using very thin films of 2 nm and 5 nm on top of TiO_2 was based on the view of trying to minimise leaching of the noble metal nanoparticles (MNP) into the water as they would be in direct contact with water. When TiO_2 was deposited on top of the metal film, there were two advantages that favoured photocatalysis and these were (i) reduced leaching of metal nanoparticles, and (ii) prevention of metal oxidation as TiO_2 acts as a protective layer for the metal nanoparticles.

When a 2 nm or 5 nm film of a noble metal element Ag was deposited either on top or underneath the TiO_2 photocatalyst film, there was better photocatalytic activity in both cases when compared to pure TiO_2. A 2 nm Ag film deposited on top of TiO_2 photocatalyst showed 85.85% degradation of methyl orange after 300 minutes (5 h) but when the same Ag film thickness was deposited underneath the TiO_2 photocatalyst film, there was a decrease in photocatalytic activity to 68.38% for the same degradation reaction time. The same trend was also

observed when the order of deposition was changed for the 5 nm Ag film but the change (6.12%) was insignificant as shown in Table 4.8.

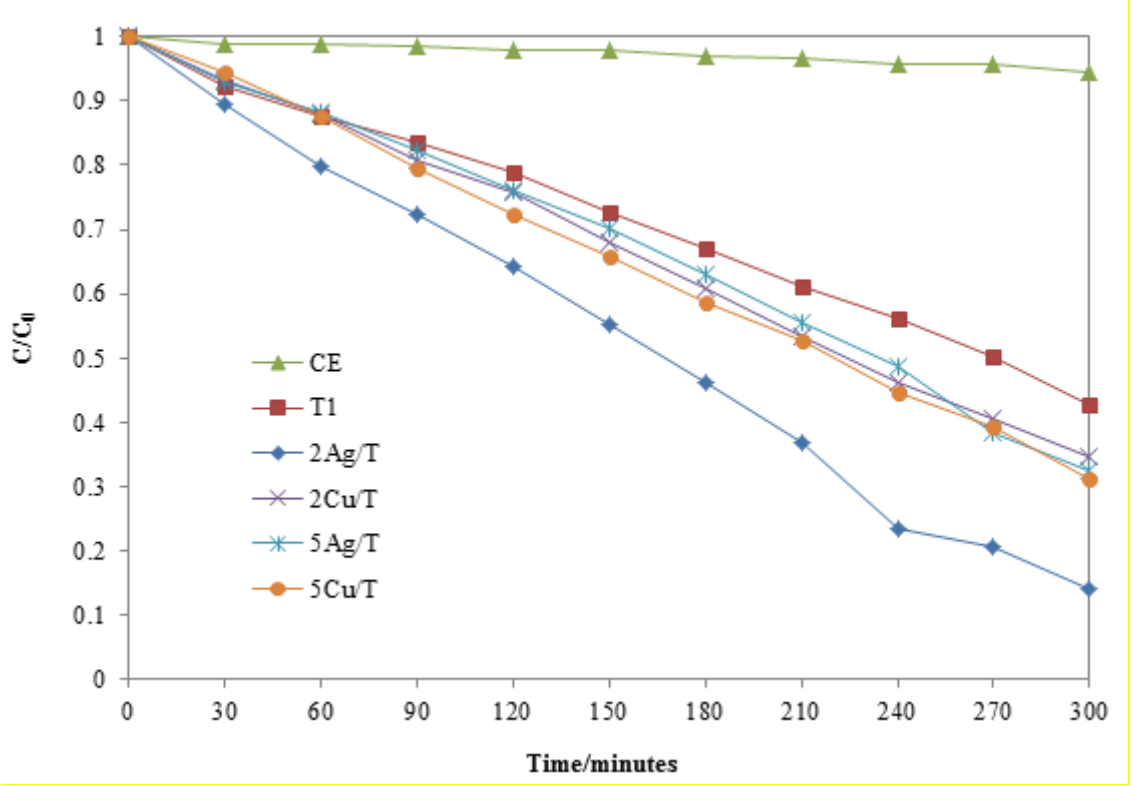

Figure 4-30: Photodegradation profiles of 100 mL of 10 ppm methyl orange solution under UV light at 25°C and pH 7 showing the effect of different metal thicknesses deposited on TiO_2 photocatalyst on fused silica.

The reasons for the better performance of Ag in enhancing TiO_2 photocatalytic activity when deposited on top for both the 2 nm and 5 nm films rather than when it is deposited underneath TiO_2 film could be: (i) Ag absorbs in the UV region hence it created localised surface plasmon resonance (LSPR) which boosted excitation of electrons in TiO_2 (Hedayati et al., 2014) and (ii) the oxidation of silver into silver oxide (silver slightly oxidizes to AgO) (Dang et al., 2011). The resulting oxide could participate in the photodegradation of methyl orange resulting in high efficiency of the photocatalytic system. The formation of the oxide is supported by the appearance of a minor peak at 2θ value of 33.4° which was assigned to the silver oxide (Ag_2O) in the XRD spectrum of the silver film implying that some part of the deposited Ag was oxidized but not to a great extent as can be observed from the intensity of the peak which was relatively lower.

When copper film (2 nm) was used, it also followed the same trend as silver. It increased TiO_2 photocatalytic activity more when it was deposited on top of TiO_2 (65.50%) than when it was deposited underneath the TiO_2 photocatalyst (60.85%). The reason for this could be that Cu can be easily oxidised when exposed to air forming its oxides which can participate in the photodegradation process. The Cu_2O and CuO are p-type

semiconductors with narrow band gaps of 1.2 eV and 2.2 eV respectively (Zeng et al., 2014). The formation of these oxides is evidenced by the appearance of three peaks arising from the oxides in the XRD spectrum.

When the 5 nm copper film was used, the trend was opposite to that of the 5 nm silver. The copper enhanced photocatalytic activity of TiO_2 better when the 5 nm film was deposited underneath TiO_2 film (82.04%) than when deposited on top of TiO_2 photocatalyst film (68.90%). The reason for this observation could be that, there was a reduction in surface area of TiO_2 when the 5 nm copper metal film was on top and some TiO_2 active sites were covered. This could have resulted in reduced contact between the pollutant and TiO_2 photocatalyst surface during photodegradation. The results of the above findings on the effect of the order of deposition for all the two plasmonic elements under study are summarized in Table 4.9.

Table 4.9: Percentage degradation of methyl orange under UV light using TiO_2/plasmonic MNP films with different orders of deposition**.**

Plasmonic element & thickness	% Degradation of MeO under UV light		% Change when metal film was on top instead of underneath TiO_2
	Metal film on top of TiO_2	Metal film underneath TiO_2	
2 nm Ag film	**85.85**	68.38	+17.47
5 nm Ag film	67.45	61.33	+6.12
2 nm Cu film	65.50	60.85	+4.65
5 nm Cu film	68.90	82.04	-13.14

Generally all the 2 nm and 5 nm plasmonic metal decorated TiO_2 photocatalyst showed higher photocatalytic activity than pure TiO_2 due to the creation of the Schottky barriers between the metal nanoparticles and the TiO_2 photocatalyst. This facilitated the movement of electrons resulting in reduced electron-hole recombination rates. The proposed mechanism of enhancement of the TiO_2 photocatalyst by the plasmonic metal is shown in Figure 4.31.

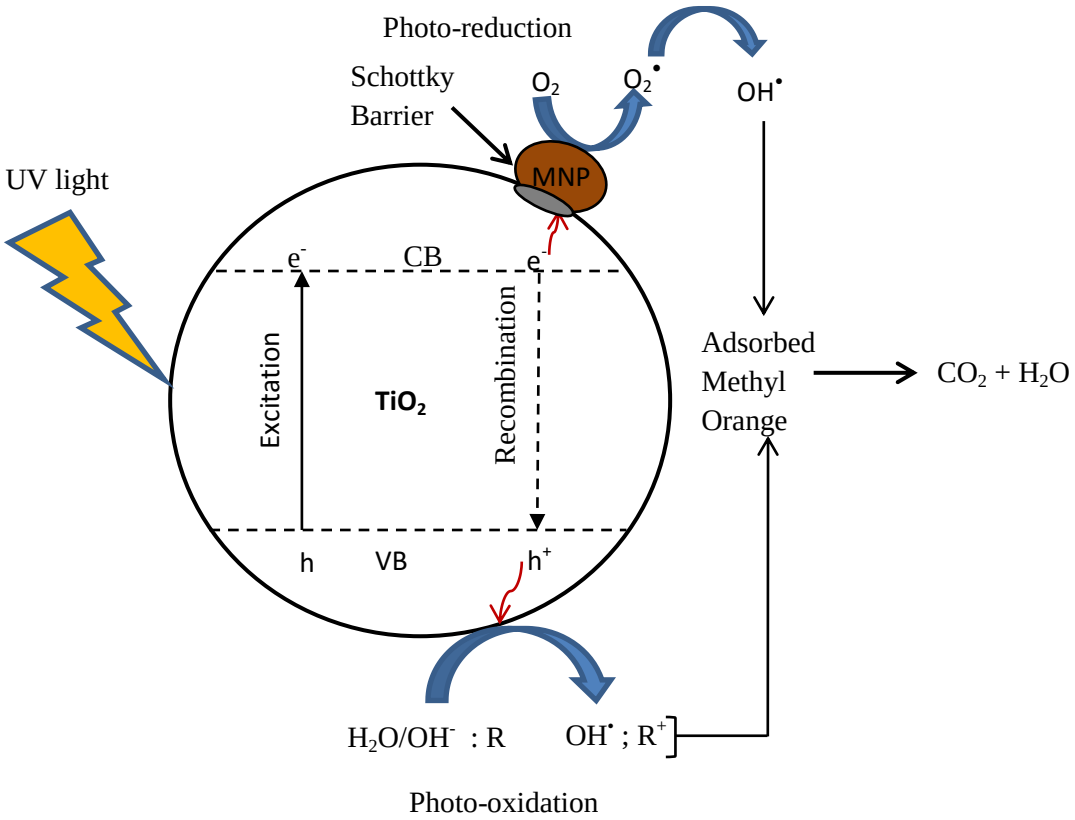

Figure 4-31: Schematic representation of the proposed mechanism of activation of TiO_2, electron trapping by metal nanoparticles (MNP) and photodegradation of MeO under UV light.

4.6.1.5 *Effect of using a bilayer metal film*

The use of a bilayer plasmon metal film was done so as to find out if it was better than using a monolayer of the metal film in enhancing TiO_2 photocatalytic activity. Instead of using one noble metal film, two different noble metal films (Cu & Ag) were deposited, layer by layer. In the bimetallic layers, each metal was 5 nm thick to give a total thickness of 10 nm for both metals underneath the TiO_2 photocatalyst. This was done so that the observed effect comes from different combinations and not the metal loading. The use of the bilayer/bimetallic metal films was compared to the monolayer of the same thickness. In this study the Ag film was in contact with TiO_2 film and the Cu film was in contact with fused silica support. Table 4.10 presents data on percentage degradation of methyl orange using TiO_2 photocatalyst on 10 nm metal films of Cu, Ag and mixed Ag/Cu. The photocatalytic activity of T10Cu and T10Ag towards methyl orange was 24.80% and 71.31% respectively but when TiO_2 was deposited on a bilayer of Cu and Ag (T1/Ag/Cu) of the same thickness, the photodegradation increased to 74.36% which was higher than TiO_2 on monometallic films. This showed that when two metals were combined, they worked synergistically and performed better than a single metal since the metals could augment one another.

Table 4.10**: Percentage degradation of methyl orange using TiO_2 photocatalyst on 10 nm metal films (monometallic and bimetallic layers) under UV light.**

Photocatalyst	Metal thickness	% Photodegradation after 300 minutes
T1	0 nm	57.16
T10Cu	10 nm	24.80
T10Ag	10 nm	71.32
T1/Ag/Cu	Ag (5 nm)/Cu (5 nm)	74.36

When two metals whose work functions are different are brought into contact, charge transfer occurs whereby electrons flow from the metal with higher Fermi energy to that with lower Fermi energy. In this case the order of the work functions was $\varphi_{Cu} > \varphi_{Ag} > \varphi_{TiO2}$, hence electrons were flowing to the metal from the semiconductor on contact. In a bilayer system, there are more than two contacts (TiO_2/metal, metal/metal and metal/ fused silica support) resulting in more than two Schottky barriers being formed which promote efficient electron transfer from the photocatalyst. This could have caused the observed enhanced photocatalytic activity of TiO_2 by bilayer metal film.

4.6.1.6 *BPA photodegradation*

The best plasmonic metal decorated TiO_2 photocatalytst (2 nm Ag on TiO_2) in the photodegradation of methyl orange was also tested for its photocatalytic activity towards BPA which is an endocrine disruptor (Figure 4.32). The photocatalyst degraded 61.86% of BPA after 300 minutes which was 23.99% lower when compared to methyl orange photodegradation (ca. 85.85%). The same trend was also observed using pure TiO_2 photocatalyst which degraded 47.10% of BPA after 300 minutes which was 10.06% lower than that of methyl orange (ca. 57.16%). These results (Figure 4.32) show that BPA is more difficult to degrade than methyl orange under the same conditions. There are three possible reasons why these two contaminants were not degraded to the same extent even when the same mass and volume were used and these are: (i) methyl orange has a higher molar absorption coefficient than BPA hence its rate of degradation will be higher, (ii) methyl orange could have been more adsorbed on the photocatalyst than BPA. It is known that a contaminant needs to be in contact with the catalyst for it to be degraded hence if it is adsorbed more readily then its degradation is promoted. It has been reported that organic substrates with electron withdrawing nature strongly adhere to the photocatalyst and are more susceptible to direct oxidation than those with electron donating groups (Bhatkhnade, 2004). In this study, methyl orange had more electron withdrawing groups than BPA, (iii) the azo bonds in the azo compounds are active and are easily degraded. It has also been reported that azo bonds are

the most active in azo-dye molecules hence would be susceptible to attack by positive holes and hydroxyl radicals (Saggioro et al., 2011).

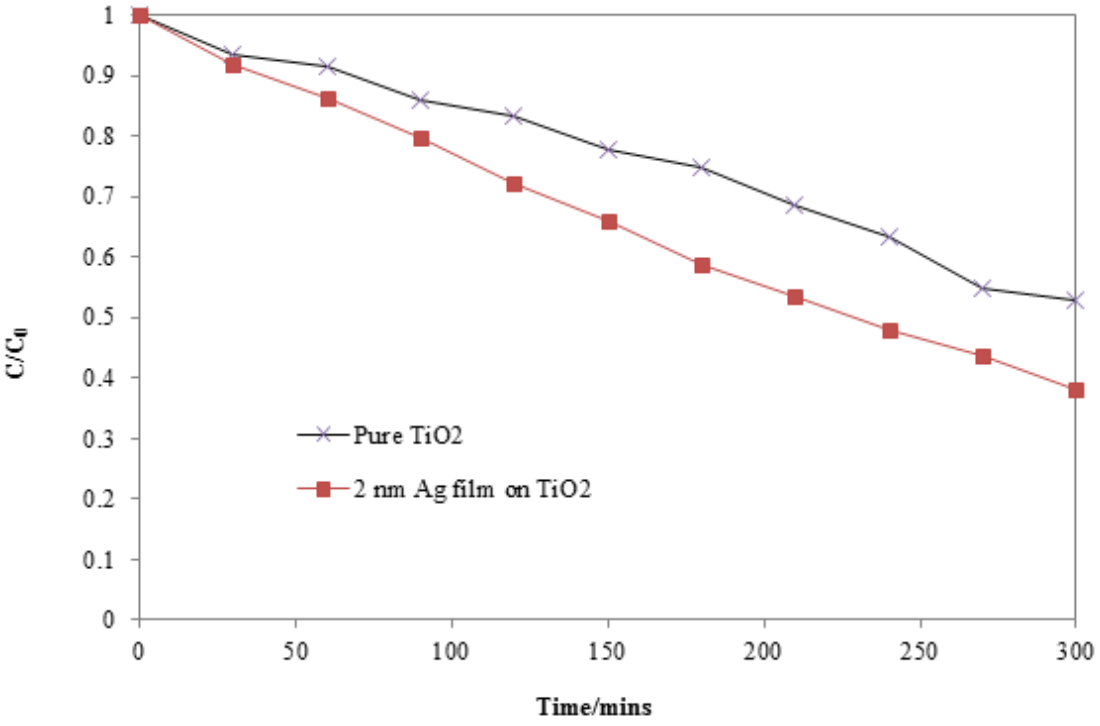

Figure 4-32: Photodegradation profiles of 100 mL of 10 ppm BPA solution under UV light at 25°C and pH 7 using pure TiO_2 and TiO_2 with 2 nm Ag on top.

4.6.1.7 *Plurimetallic metal films*

The percentage degradation of MeO after 5 hours for TiO_2 photocatalyst on different metals of different thicknesses is shown in Table 4.11. It should be noted that since the experiments were done under UV and all the metal in question absorb mostly in the visible region, then the mechanism of enhancement is mainly due to reduction of electron-hole recombination by acting as electron reservoirs rather than by boosting generation of electrons. All silver films used in the study showed an improvement in the photocatalytic activity of TiO_2 but there was a trend followed. The photocatalytic activity increased as the silver thickness was increased from 2 nm to 5 nm, 10 nm and 20 nm and then started decreasing when the thickness was 25 nm showing that 20 nm was the optimum thickness for enhancement. The optimum thickness for gold was 10 nm and for copper 5 nm. Beyond the optimum thickness, the photocatalytic activity was worse than even bare TiO_2 in case of Au and Cu samples as is shown in Table 4.11. The reason for the enhancement at the optimum thickness is the charge separation. When TiO_2 is excited by UV, electrons move to the surface and accumulate there and holes remain in the TiO_2. Since the TiO_2 is in direct contact with the metal nanoparticles, electrons will transfer to the metal.

Table 4.11**: Percentage degradation TiO_2 with different metal films of different thicknesses**

Photocatalyst	% of Methyl orange photodegraded after 300 minutes			% Increase relative to pure TiO_2 photocatalyst		
	Au	Ag	Cu	Au	Ag	Cu
TiO_2 on 0 nm	57.16	57.16	57.16	-	-	-
TiO_2 on 2 nm	64.16	60.38	60.85	+7.00	+3.22	+3.69
TiO_2 on 5 nm	85.13	61.33	82.04	+27.97	+4.17	+24.86
TiO_2 on 10 nm	84.69	71.32	24.80	+27.53	+14.16	-32.36
TiO_2 on 20 nm	24.74	85.27	17.84	-32.42	+28.11	-39.32
TiO_2 on 25 nm	24.30	68.38	18.48	-32.86	+11.22	-38.68

The accumulation of the holes in TiO_2 eventually results in production of hydroxyl radicals which degrade methyl orange. The reason for a decrease in photocatalytic activity of TiO_2 with metal thickness greater than the optimum thickness is that thicker films have more room to store electrons far away from TiO_2 and the electrons cannot be effectively consumed by methyl orange and this results in the elevation of the Fermi level and weakening of the internal electric field (Ren *et al*., 2015). The depression effect of Au (20 nm & 25 nm) and Cu (10, 20 & 25 nm) on the photocatalytic activity below that of bare TiO_2 needs further consideration. All combinations of metals used to modify the TiO_2 photocatalyst (Table 4.12) showed great improvement in the photodegradation of methyl orange under UV light and the enhancement was higher than the monolayer system of the same thickness and at least containing a common element.

Table 4.12: TiO_2 on monolayer, bilayer and a three layer system of the same thickness (10 nm).

Photocatalyst	% Degradation of MeO after 5 hours
TiO_2	57.16
TiO_2/(Au/Ag)	78.19
TiO_2/(Ag/Cu)	74.36
TiO_2/(Au/Cu)	84.74
TiO_2/(Ag/Au/Cu)	**86.26**
TiO_2/Au	76.34
TiO_2/Ag	71.32
TiO_2/ Cu	24.80

The highest photocatalytic activity was achieved using TiO_2 on a three layer system of all the three metal nanoparticles as shown in Table 4.12. The results show that two or three materials combined synergistically perform better than the use of a single metal since one material can compensate for the drawbacks of the other. In the three and four component systems for instance TiO_2/(Au/Ag) and TiO_2/(Ag/Au/Cu) respectively, more than one Schottky junctions are formed which reduce electron-hole recombination rates. Silver has the lowest work function among the three metals followed by copper and gold with the highest, i.e. $\varphi_{Ag} > \varphi_{Cu} > \varphi_{Au}$. There will be charge transfer across the interface between the metals which are in contact since they have different work functions. The charge flow from the low work function metal will stop when the Fermi levels become equal. The good conductivity of the metals allows easy flow of electrons from the region of contact with the TiO_2 ensuring good separation of electrons from the photogenerated holes.

4.6.1.8 *Photodegradation under UV light versus sunlight*

All the photocatalysts used in this study showed higher photocatalytic activity under UV light than under sunlight. All plasmon modified TiO_2 photocatalysts showed better activity than bare TiO_2 photocatalyst both under UV and sunlight due to the same reasons given in the previous sections. The photodegradation results are shown graphically in Figure 4.33. The photodegradation of MeO orange under sunlight is highest with a 2 nm film of Cu on TiO_2. The reasons for this could that, (i) Cu nanoparticles are on the surface TiO_2 hence are exposed to air and since they are unstable relative to its oxides, some of it will be oxidised to CuO and Cu_2O which both have a small band gap hence can easily absorb visible light. When initiated by light, there will be interparticle electron transfer from the oxide to the TiO_2 thereby coupling of TiO_2 with a low band gap semiconductor. (ii) The plasmon enhancement from the un-oxidised CuNP nanoparticles due to field enhanced light absorption and visible light sensitization makes the photocatalyst very active under visible light.

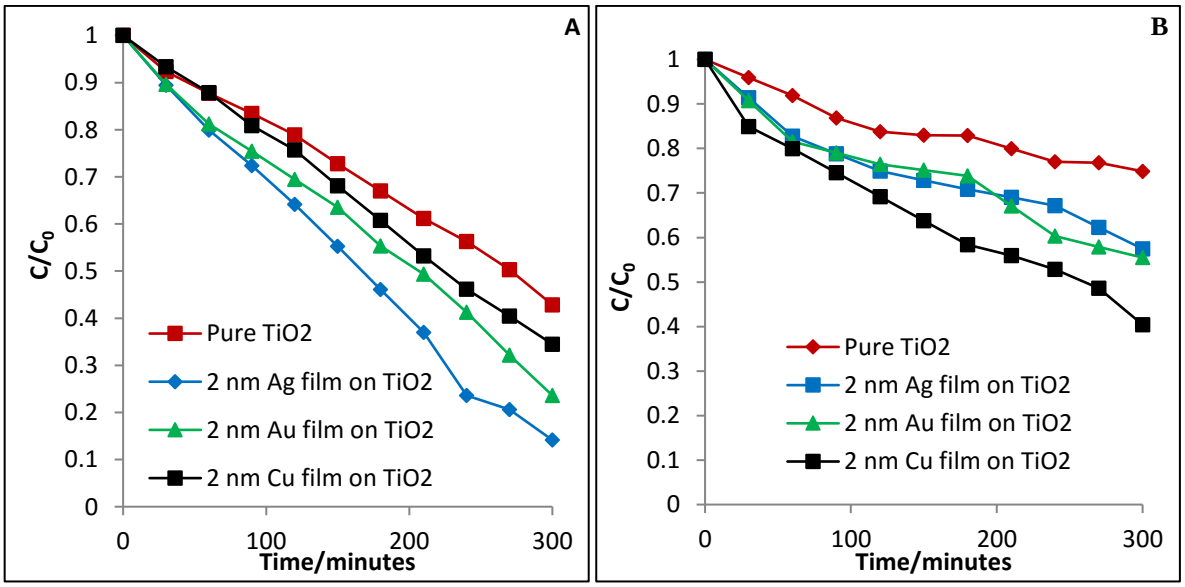

Figure 4-33: Photodegradation of methyl orange under (A) UV light and (B) sunlight.

For the same thickness of 2 nm, the activity of the same sample (Cu/TiO_2) is higher under visible light than UV since Cu and its oxides if present absorb in the visible region. The results are also shown in Table 4.13 for easy comparison of the extent of increase of the efficiency relative to bare TiO_2. When the photodegradation results of the same photocatalyst under UV are compared to sunlight results, CuNP showed the least decrease of 5.91% in sunlight followed by AuNP (26.88%) and lastly AgNP (43.3%). When the results are compared to bare TiO_2 both under UV and sunlight, Cu showed the highest improvement from 8.34% increase under UV to 34.47% increase under sunlight. AuNP showed an increase too but AgNP showed a decrease.

Table 4.13: Percent degradation under UV light and sunlight.

Photocatalyst	**% Degradation under UV light after 5 hours**	**% Degradation under sunlight after 5 hours**	**% Increase relative to bare TiO_2 under UV**	**% Increase relative to bare TiO_2 under sunlight**
Pure TiO_2	57.16	25.12	-	-
2 nm Au on TiO_2	71.39	44.51	14.23	19.39
2 nm Cu on TiO_2	65.50	59.59	8.34	34.47
2 nm Ag on TiO_2	85.85	42.55	28.69	17.43

The reason for the increase for both Au and Cu is that, both metals absorb in the visible region (Au λ=560 nm and can reach 700 nm or more depending on size and shape) and (Cu λ=570 nm) hence creating strong plasmonic electric fields which enhance light absorption and electron-hole generation. Ag absorbs close to UV hence it is expected that its activity is lower in sunlight than Au and Cu which absorb at low energy. The diffuse reflectance spectra and derivatives of fused silica supported TiO_2/Au composite and TiO_2/Ag composite material is shown in Figure 4.34. The band gaps were calculated using the formula:

$$Eg = \frac{1239}{\lambda edge}$$

where λedge is the wavelength of the optical absorption edge were 3.13 eV and 3.12 eV for TiO_2/Au and TiO_2/Ag composites respectively.

These values are very close to the band gap of unmodified TiO_2 of 3.2 eV meaning that the increase in photocatalytic activity of some composites when compared to bare TiO_2 is not mainly due to band gap reduction but other factors such as Schottky barriers formation, reduced electron-hole recombination and improved charge generation.

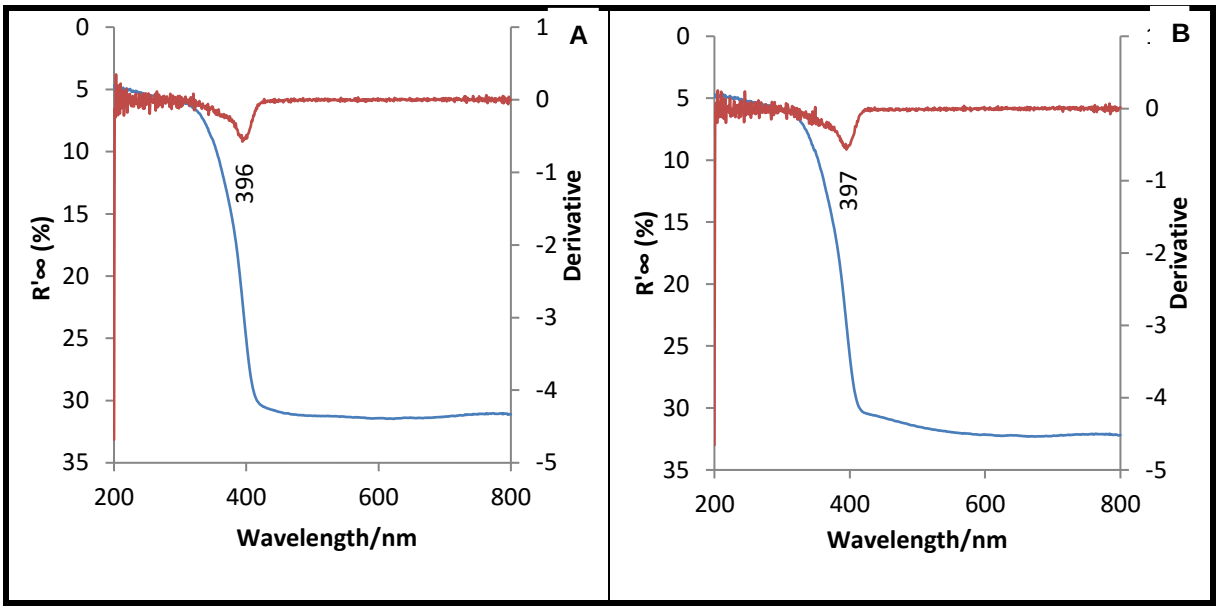

Figure 4-34: Diffuse reflectance spectra of (a) TiO_2/Au composite and its derivative, (b) TiO_2/Ag composite material and its derivative.

4.6.1.9 *Summary*

Copper, gold, and silver were successfully deposited on MPTMS treated fused silica using a thermal evaporation technique and TiO_2 films were deposited using the sputter coating technique. HRSEM showed that the plasmonic metal nanoparticles were uniformly distributed on the fused silica substrates. The highest photodegradation of methyl orange after 5 hours was achieved by TiO_2 photocatalyst under UV light with 2 nm Ag film on top. Ag nanoparticles were found to perform better in enhancing TiO_2 photocatalytic activity when they were deposited on top of the TiO_2 photocatalyst rather than underneath whereas copper performed better when it was deposited underneath TiO_2 film than on top. Overall, silver was better than copper in enhancing TiO_2 photocatalytic activity in UV light due to the localised surface plasmon resonance effect of Ag, whereas Cu performed better than Ag in sunlight. The use of bimetallic and trimetallic layers increased the photodegradation of methyl orange and percentage removal was higher than the use of equivalent monometallic layers, as a result of the synergistic effect of the two or three metal nanometres thick films.

4.6.2 Photocatalytic degradation by stainless steel supported TiO_2

The next subsections focus on the photocatalytic activity of the various synthesised, stainless steel mesh supported TiO_2 nanocrystals calcined at 300º, 350º and 400ºC for holding times between 1 to 4 h using MB as a model pollutant. MB was used as a model pollutant to rapidly evaluate the most active catalyst and its removal percentage was taken as a measure for comparing photocatalytic activity. The supported TiO_2 nanocrystals with the highest photocatalytic activity were selected and different thickness of metallic Ag were deposited thereon. The photocatalytic activity of the various Ag deposited TiO_2 nanocomposites in comparison

with the optimum supported TiO_2 nanocrystals were equally evaluated. The most active photocatalysts were then applied in the photocatalytic degradation of BPA and Nitrophenol in a dielectric barrier discharge system.

4.6.2.1 *Effect of calcination temperature on MB removal rate*

The results of the effect of calcination temperature on the photocatalytic activity of MB using various supported catalysts are presented as follows. Figures 4.35-4.37 revealed the MB removal rate profile using the supported TiO_2 nanocrystals calcined at 300º, 350º and 400º for 1-4 h. The experiment was conducted in a self-designed 500 mL beaker photoreactor containing 50 mL of MB solution (10 ppm concentration), pH of 6.8, and 30 mg of the supported catalysts. Prior to the photocatalytic measurement, the blank experiment was conducted on a MB solution containing the supported catalyst which was magnetically stirred in the dark for 6 h. Thereafter, for baseline purposes, the MB solution was exposed to direct UV irradiation alone without catalyst. Furthermore, each catalyst was then exposed to UV light with a 9 W UV mercury vapour lamp of wavelength of 254 nm and the MB removal rate was monitored for 6 h. The experiment was repeated twice (n= 2) and average experimental values were determined.

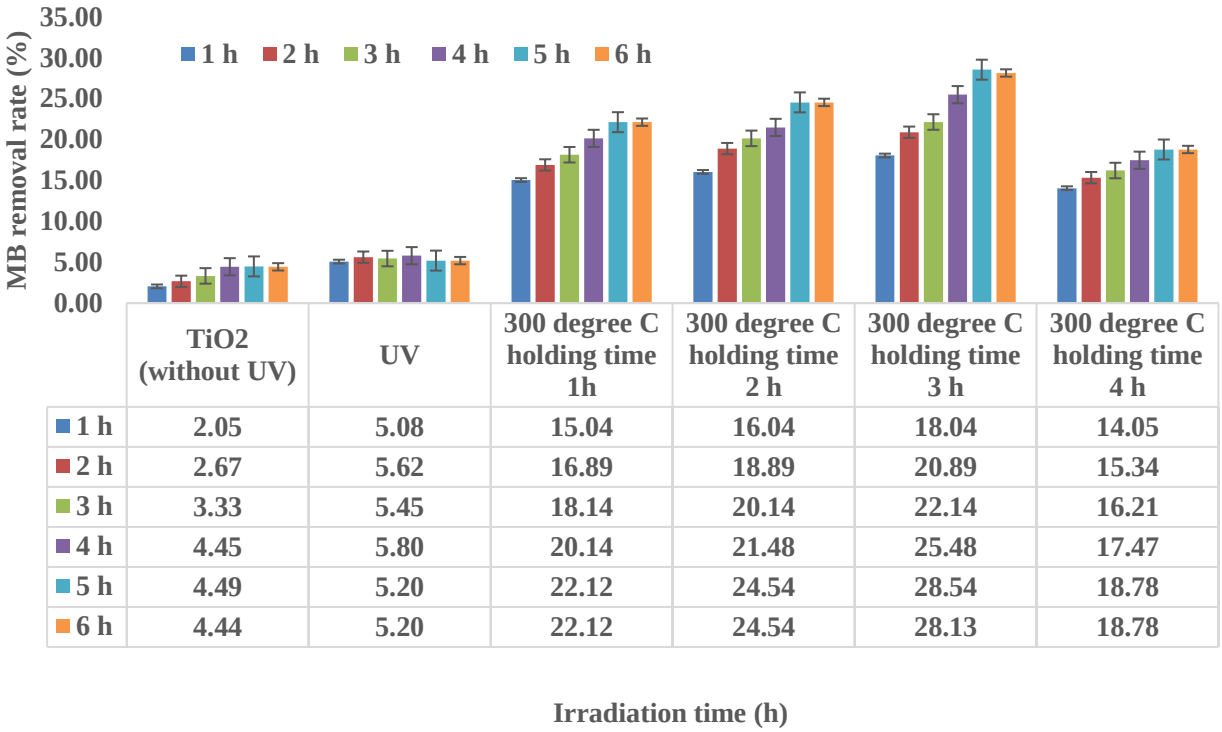

	TiO2 (without UV)	UV	300 degree C holding time 1h	300 degree C holding time 2 h	300 degree C holding time 3 h	300 degree C holding time 4 h
1 h	2.05	5.08	15.04	16.04	18.04	14.05
2 h	2.67	5.62	16.89	18.89	20.89	15.34
3 h	3.33	5.45	18.14	20.14	22.14	16.21
4 h	4.45	5.80	20.14	21.48	25.48	17.47
5 h	4.49	5.20	22.12	24.54	28.54	18.78
6 h	4.44	5.20	22.12	24.54	28.13	18.78

Figure 4-35: MB removal rate profile by supported TiO2 nanocrystals calcined at 300º C for 1-4 h. (MB concentration (10 mg/L), pH 6.8, catalyst dose 30 mg, UV lamp (9 W), solution volume (50 mL), irradiation time (6 h), stirring speed 150 rpm)

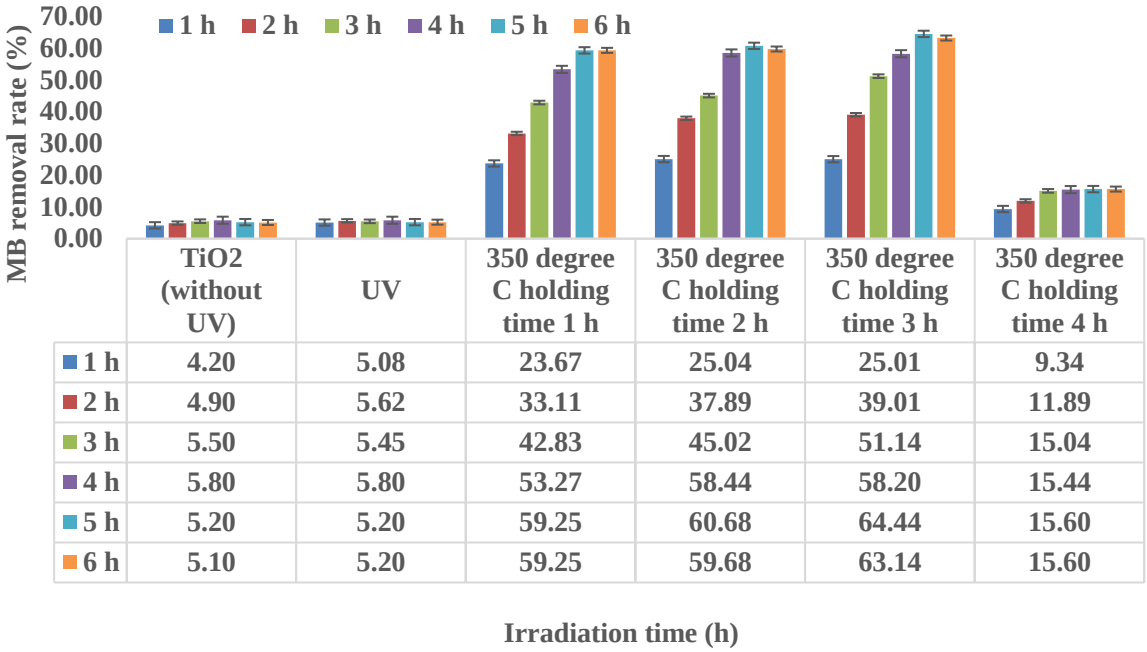

	TiO2 (without UV)	UV	350 degree C holding time 1 h	350 degree C holding time 2 h	350 degree C holding time 3 h	350 degree C holding time 4 h
1 h	4.20	5.08	23.67	25.04	25.01	9.34
2 h	4.90	5.62	33.11	37.89	39.01	11.89
3 h	5.50	5.45	42.83	45.02	51.14	15.04
4 h	5.80	5.80	53.27	58.44	58.20	15.44
5 h	5.20	5.20	59.25	60.68	64.44	15.60
6 h	5.10	5.20	59.25	59.68	63.14	15.60

Figure 4-36: MB removal rate profile by supported TiO2 nanocrystals calcined at 350º C for 1-4 h. MB concentration (10 mg/L), pH 6.8, catalyst dose 30 mg, UV lamp (9 W), solution volume (50 mL), irradiation time (6 h), stirring speed 150 rpm

Figure 4.35 represents both the control experiment and the photocatalytic activity of supported TiO_2 nanocrystals calcined at 300ºC for 1-4 h using MB as a modelled pollutant. The result in Figure 4.35 (TiO_2 without UV) demonstrates clearly that only 4.4% of the MB was removed in the dark for 6 h. Likewise in Figures 4.36 and 4.37, the MB adsorption onto the catalyst monitored in the dark never exceeds 5.2% of the initial concentration of MB. It is obvious that the elimination of MB was not based on adsorption phenomenon simply because the supported catalysts did not show strong absorption of the target compound. No significant changes were observed over time thus the adsorption can be considered negligible. It was difficult for the MB molecules to be transferred from the solution onto the catalyst surface by adsorption. In the same vein, the direct photo-mineralization of the MB solution in the absence of the supported catalysts (Figures 4.35-4.37) indicates that only 5.2% MB was removed at the end of 6 h, which was also insignificant compared to results obtained when MB was irradiated in the presence of the catalyst and can thus also be considered negligible.

The slight removal rate under UV without the catalyst is partially due to the interaction of the photonic energy with the carbon-carbon framework in the MB resulting in chromophore cleavage and mineralization (Carlucci et al., 2014). Jia et al. (2012) had earlier demonstrated that incident light of lower wavelength in the range of 253.7-289 nm possesses high photonic energy which is capable of decomposing the organic carbon framework. Additionally, organic dyes such as MB with two unsaturated benzene rings in their structure have strong absorption of short-wave UV light.

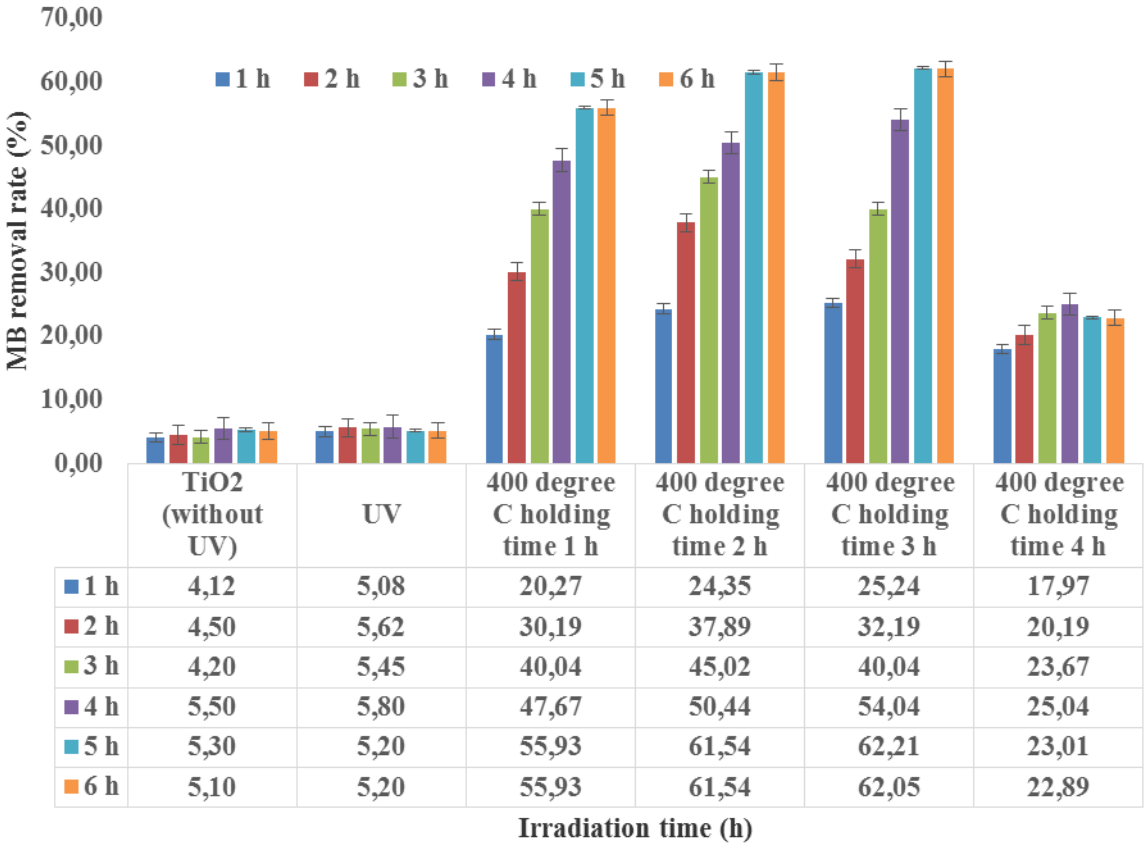

	TiO2 (without UV)	UV	400 degree C holding time 1 h	400 degree C holding time 2 h	400 degree C holding time 3 h	400 degree C holding time 4 h
1 h	4,12	5,08	20,27	24,35	25,24	17,97
2 h	4,50	5,62	30,19	37,89	32,19	20,19
3 h	4,20	5,45	40,04	45,02	40,04	23,67
4 h	5,50	5,80	47,67	50,44	54,04	25,04
5 h	5,30	5,20	55,93	61,54	62,21	23,01
6 h	5,10	5,20	55,93	61,54	62,05	22,89

Figure 4-37: MB removal rate profile by supported TiO2 nanocrystals calcined at 400º C for 1-4 h. MB concentration (10 mg/L), pH 6.8, catalyst dose 30 mg, UV lamp (9 W), solution volume (50 mL), irradiation time (6 h), stirring speed 150 rpm

Thus, exposure of MB to UV light of short wavelength obviously prompted the MB removal rate observed. However, the two control experiments showed that only limited MB removal occurred and the overall performance of the catalyst would thus not depend on adsorption alone.

Similar results have been reported in the literature on the performance of TiO_2 photocatalysts in the dark and under UV irradiation alone (Ba-Abbad et al., 2012; Leong et al., 2014). Furthermore, at 300ºC holding time 1-3 h, MB removal rate slightly increased with irradiation time especially when compared to UV light itself. The slight removal increment (between 25-30%) at this temperature and holding time can be attributed to incomplete decomposition of PAN. The low photocatalytic activity can also be ascribed to a low crystallisation process at that temperature together with particle agglomeration which may have prevented adequate UV light penetration. The supported catalyst calcined at 300ºC for 3 h had a higher MB removal rate and the lowest value was obtained at 4 h holding time. The lower MB removal rate at 4 h holding time can be attributed to weak intermolecular forces of attraction between the catalyst and the stainless steel mesh, which led to the loss of catalyst from the mesh.

Only a small quantity was retained which was thus possibly responsible for the low removal observed. According to Figure 4.10, the percentage MB removed increased to around 60% with irradiation time of 6 hr for the catalyst calcined for 3 h holding time at 350º. Not only that, the obtained MB removal values were similar as calcination temperature increased from 350º to 400ºC up to a calcination time of 3 hr. The higher percentage MB removal obtained as the calcination temperature was increased above 300ºC may be due to improved crystallisation of TiO_2 and reduced crystal defects (Leong et al., 2014). The high photocatalytic activity at 350º and 400ºC may be linked to the anatase phase of TiO_2. Studies have shown that anatase phase is the most active due to the presence of available oxygen vacancy sites which favour OH radical formation and improve the photomineralisation process (Leong et al., 2014; Sheikhnejad-Bishe et al., 2014).

The increase in the percentage MB removed can be ascribed to more complete decomposition of PAN, and the additional heat which promoted crystal growth. This result agrees with He et al. (2014) who ascribed the increased photocatalytic activity of the synthesised TiO_2 nanoparticles to an increased calcination temperature that enhanced the crystallisation process, and related low photocatalytic activity to low crystal formation. As presented in Figures 4.9-4.11, the photocatalytic activity of the synthesised catalysts towards MB increase with increasing UV irradiation time in the following order of 350 º > 400 º > 300 º C. It is also noteworthy mentioning that the optimum UV irradiation time was 5 h irrespective of the conditions applied to prepare the catalyst, as no significant increment was observed at 6 h. This may possibly be due to overloading of the TiO_2 active sites with MB or intermediate molecules after 5 h which could also prevent interaction of the UV light with the catalyst.

The differences in the photocatalytic activity of the catalyst could also be due to different particle sizes and surface areas. Thus the calcination temperature applied during gel decomposition played a crucial role in the photocatalytic activity of the prepared TiO_2 materials. Moreover, extending the calcination holding time beyond 3 h in all cases caused the delamination of the catalyst from the stainless steel support. This was deemed to be due to complete thermal degradation of PAN carbon, which until 3 h acted as an adhesive of the TiO_2 nanocrystals.

Figure 4.38 depicts the comparison of MB removal rate after 5 h irradiation time of the supported TiO_2 nanocrystals calcined at 300°C, 350°C, and 400°C for 3 h. Although the mechanism involved in the photodecomposition of MB remains unknown, it is believed that the mineralisation of MB molecules is based on the OH radicals generated via electron-hole pairs on the TiO_2 surface. It is obvious from Figure 4.38 that supported TiO_2 nanocrystals calcined at 300 for 3 h had the lowest photocatalytic activity. The low photocatalytic efficiency at 300ºC can also be associated with crystalline defects as shown in the XRD patterns and rapid photo electron-hole recombination rate for smaller particle size (usually less than 10 nm) on the TiO_2 surface. Thus, the rapid surface electron-hole recombination rate caused by smaller particle size could inhibit the generation of OH radicals and contribute to reduced photocatalytic activity (Leong et al., 2014). This finding was supported by Kavitha et al. (2013) who attributed the photocatalytic performance of TiO_2 to the particle morphology, calcination temperature and surface area.

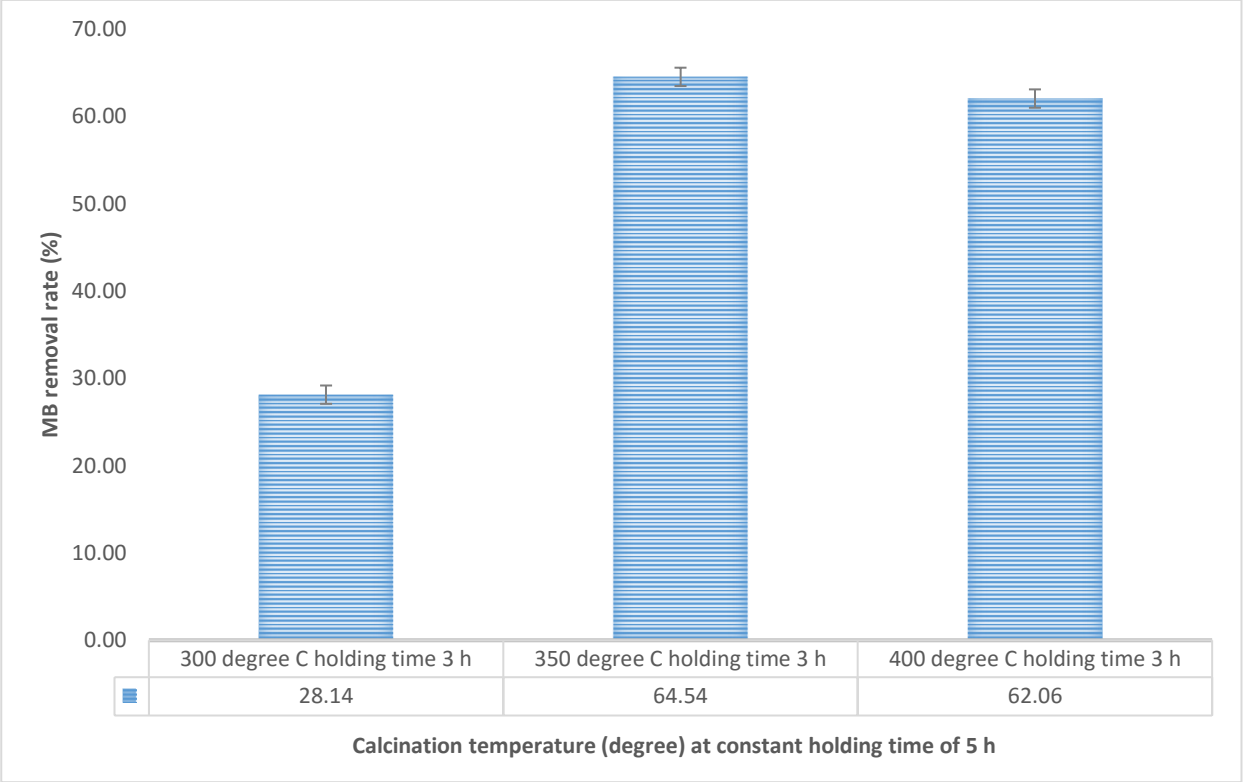

Figure 4-38: Comparison of MB removal rate after 5 h using supported TiO_2 nanocrystals calcined at 300°C, 350°C, 400°C for 3 h

In addition, the supported TiO_2 nanocrystals calcined at 350ºC and 400ºC showed better photocatalytic performance due to improved crystallinity as was demonstrated in the XRD results. The XRD crystallite size as determined by the Scherrer equation ranged between 4 and 10 nm for photocatalysts prepared at 300ºC but ranged between 11 and 13 for those calcined at 350ºC and between 13-19 nm for those calcined at 400 ºC. The percentage MB removed by the two catalysts within 5 h were closely related, this is due to the fact that the two materials had a similar particle size range and were purely anatase phase, which has been reported to be more thermodynamically and photocatalytically active than other phases (Ahmed et al., 2011). By and large, among the three catalysts, supported TiO_2 nanocrystals calcined at 350ºC had higher photocatalytic activity than the others, where over 64.54% MB removal was obtained within 5 h under the conditions applied.

The difference in the percentage MB removed was partially attributed to different surface areas as a result of different particle sizes. Zhao et al. (2009) ascribed a sharp decrease in the photocatalytic activity of TiO_2 nanoparticles to crystallite growth at higher calcination temperatures. According to the XRD results, the higher crystal size of catalysts calcined at 400ºC may be responsible for the slight decrease in the percentage MB removed. He et al. (2014) demonstrated that TiO_2 nanoparticles heat-treated at 250ºC exhibited a greater photocatalytic activity than at 400 ºC. He et al. (2014) attributed the observed high photocatalytic activity to improved crystallisation and reduced crystal defects. The catalyst with the highest photocatalytic activity was selected for the next set of experiments (350ºC for 3 h).

4.6.2.2 *Effect of solution pH*

Solution pH is one of the several parameters that influence the photocatalytic degradation of organic compounds including the surface charge and the size of aggregate of a photocatalyst. Several studies have been conducted on the influence of solution pH on the photocatalytic mineralization behaviour of organic pollutants using TiO_2 nanoparticles (Ahmed et al., 2011, Chong et al., 2010; Wu et al., 2009). In that regards, the effect of solution pH on MB removal by a photocatalyst was explored, the experiments were conducted at different pH value ranging from 3-12 and the desired pH value was adjusted using 0.5 M NaOH or 0.5 M H_2SO_4 solution. Figure 4.39 represents the results of the effect of solution pH on the photocatalytic activity of MB over supported TiO_2 nanocrystals calcined at 350ºC for 3 h.

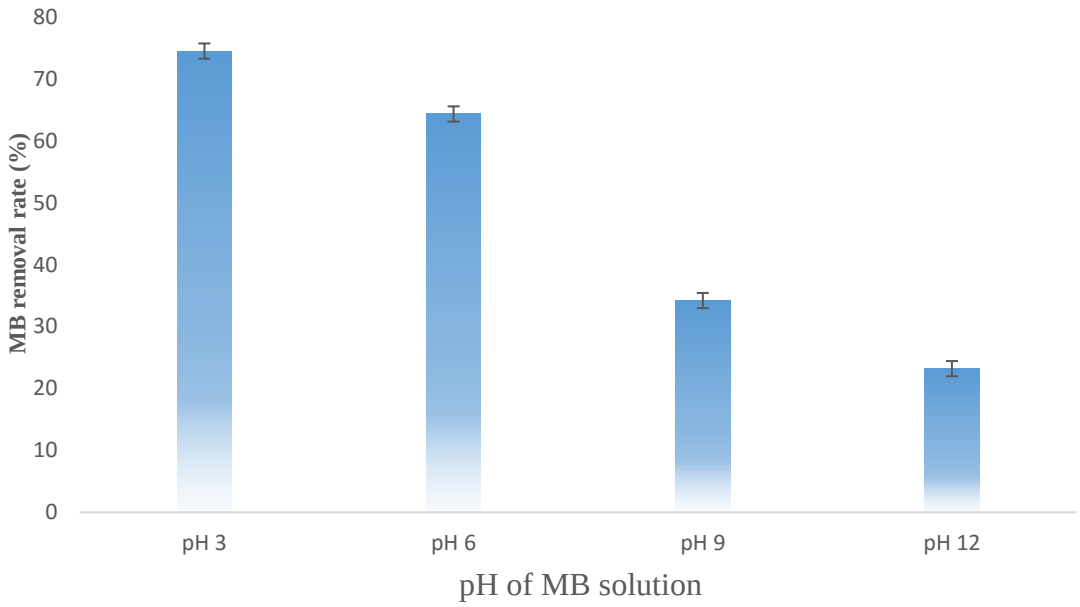

Figure 4-39: Effect of solution pH on the MB removal rate using supported TiO_2 calcined at 350ºC for 3 h. Solution volume (50 mL), irradiation time (5 h), MB concentration (10 mg/L)

It is clear from Figure 4.14 that the percentage MB removed decreased with an increasing solution pH. The maximum percentage MB removed after 5 h was obtained at pH 3 and the lowest removal was achieved at pH 12. Hence, MB removal was favoured in the acidic region more than the alkaline region which could be ascribed to enhanced surface adsorption of MB upon the catalyst at that pH. Thus, pH 3 was selected as the optimum value. Suwarnkar et al. (2014) reported that maximum photodecomposition of methyl orange was obtained in the acidic region precisely at pH 3. The increase in percentage MB removed at low pH value can be explained on the basis of amphoteric behaviour of charged TiO_2 nanocrystals in aqueous solutions containing organic pollutant. Specifically, the point of zero charge of TiO_2 is the range 6.0-6.5. At pH 3 below 6.5 (under acidic conditions), the TiO_2 surface is highly protonated and becomes a net positively charged species ($TiOH^{2+}$), while the MB molecules in aqueous solution are negatively charged. This prompts electrostatic interaction between the positively charged TiO_2 and anionic MB species.

Such electrostatic attraction enhances adsorption and generates more hydroxyl radicals which enhance the photocatalytic activity (Chong et al., 2010; Friedmann et al., 2012). Dai et al. (2007) reported that acidic conditions (low pH value of 2) favour oxidation of the methyl orange. Al-Shamali et al. (2013) also reported that maximum MB removal after 2 h solar irradiation of the TiO_2 catalyst occurred in the acidic region precisely at pH 4. At pH 9-12 which is greater than 6.8 (under alkaline conditions), the TiO_2 surface is completely deprotonated and becomes a negatively charged species (TiO-), and results in electrostatic repulsion of the anionic MB in solution. Therefore, the low photocatalytic activity at high pH was attributed to electrostatic repulsion. Besides, at high pH, the concentration of hydroxide ion is high; such a high amount of hydroxide ion prevents the UV light from adequately interacting with the catalyst surface and results in low MB removal rate. The other possibility for low MB removal rate involves formation of radical scavenger such as HCO_3- at high pH values. The scavenging effect of carbonates species on the available OH radicals can reduce the degradation rate. These results have shown that solution pH influences the surface charge of the catalyst and the ionic state of pollutants which in turn determine the reaction mechanism.

4.6.2.3 *Effect of initial concentration of MB on the removal rate*

The photocatalytic efficiency of TiO_2 nanocrystals is most influenced by the initial concentration of the pollutant. Thus, the effect of the initial concentration of MB on the photocatalytic efficiency of supported TiO_2 nanocrystals under 9 W UV lamp at pH 3 was investigated. The results of the photocatalytic activity of the supported TiO_2 nanocrystals on different concentration of MB in the range of 10-30 mg/L at constant irradiation time, solution pH and MB solution volume is presented in Figure 4.40.

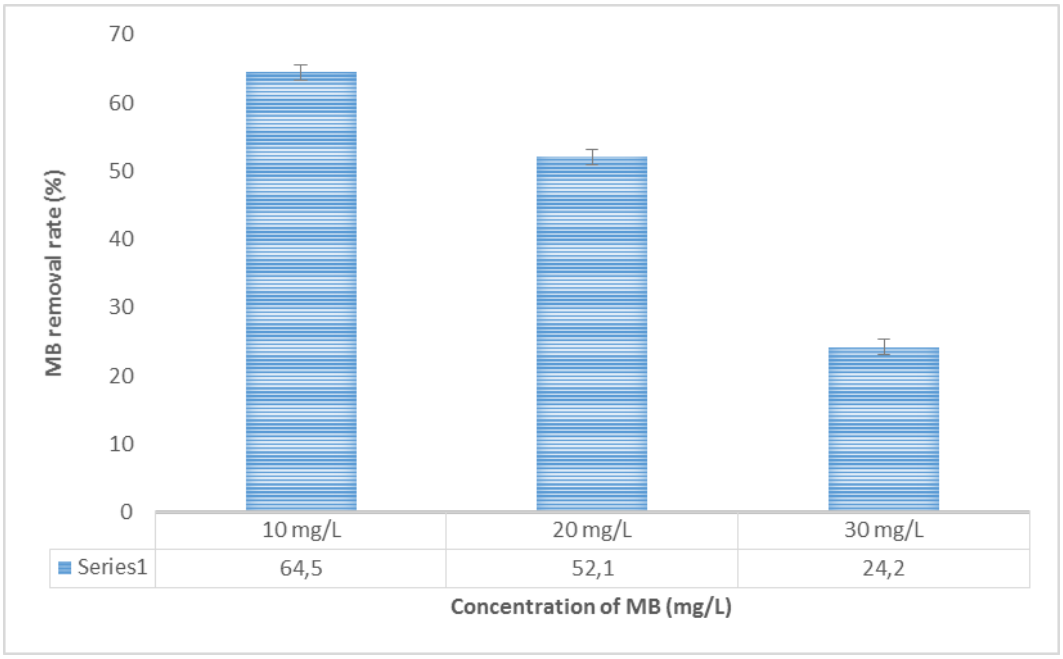

Figure 4-40: Effect of initial concentration of MB using supported TiO_2 calcined at 350ºC for 3 h. Solution volume (50 mL), irradiation time (5 h), solution pH (3)

It is apparent from the results that a high percentage MB removal was obtained at 10 mg/L (the lowest concentration of MB studied) and vice versa. This could be attributed to the availability of more active sites, OH radicals and efficient UV light absorption and interaction with the catalyst (Ahmed et al., 2011; Dai et al., 2007). Whereas, at high pollutant concentration, the number of free OH radicals did not correspond to the catalytic active sites in solution, as a matter of fact, an excess of MB or intermediate molecules may be absorbed upon the TiO_2 surface. The adsorption of more MB or intermediates onto TiO_2 surface could hinder the pollutant/OH radical ratio resulting in low photocatalytic activity (Ba-abbad et al., 2012). Furthermore, Bahmemann et al. (2007) linked low photocatalytic activity at high pollutant concentration to the formation of intermediates, which compete with the parent compound for the active sites. The competition with the intermediates, via slow diffusion onto TiO_2 surfaces, may cause deactivation of the catalytic active sites, which is in turn could be responsible for low MB removal. Additionally, the higher concentrations of MB in solution prevented the UV light from effectively interacting with the catalyst surface, thus decreased the generation of electron-hole pairs and formation of free reactive species. The cumulative effect was responsible for low MB removal rate. This observation is consistent with the previous literature on photocatalytic studies involving effect of initial pollutant concentration (Al-Shamali, 2013; Barakat et al., 2013; Dai et al., 2007).

4.6.2.4 *Photocatalytic Activity of Ag Deposited TiO_2 Nanocomposites*

The photocatalytic performance of stainless steel mesh supported TiO_2 nanocrystals and the different Ag deposited TiO_2 nanocomposites using MB as a model pollutant was monitored. The results of the photodecomposition of 10 mg/L MB by each sample is represented in Figures 4.41 and 4.42. Prior to the photocatalytic experiment, the supported TiO_2 nanocrystals was immersed in MB solution and magnetically stirred in the dark for 5 h. At the end of 5 h interaction between the catalyst and MB, about 3.3% MB was removed (Figure 4.41), which was attributed to the adsorption behaviour of the catalyst. In addition, in the absence of supported TiO_2 nanocrystals by direct ultra-violet irradiation of MB solution alone, only 5.9% MB removal rate was noticed within 5 h of treatment. The results of the blank experiments demonstrated that no catalytic activity took place; instead, the slight MB removal was ascribed to the adsorption behaviour of the catalyst and photolytic reaction. This observation has been reported by different workers on TiO_2 photocatalysts (Carlucci et al., 2014; Jia et al., 2012; Leong et al., 2014). Generally, the mechanism of photocatalytic efficiency of TiO_2 nanocrystals is based on the excitation of electrons from the valence to the conduction band upon UV-light irradiation. The photogenerated electrons may be utilised in the degradation of MB.

According to the results shown in Figures 4.41 and 4.42, it can be seen that all stainless steel mesh supported samples possessed photocatalytic activity in the removal of methylene blue compared to the blank experiments. It was obvious that the photocatalytic efficiency of supported TiO_2 nanocrystals increased with an increase in the amount of plasmonic Ag deposited up to an optimum of 10 nm layer thickness. However when Ag increased to 15 nm, the MB removal rate reduced.

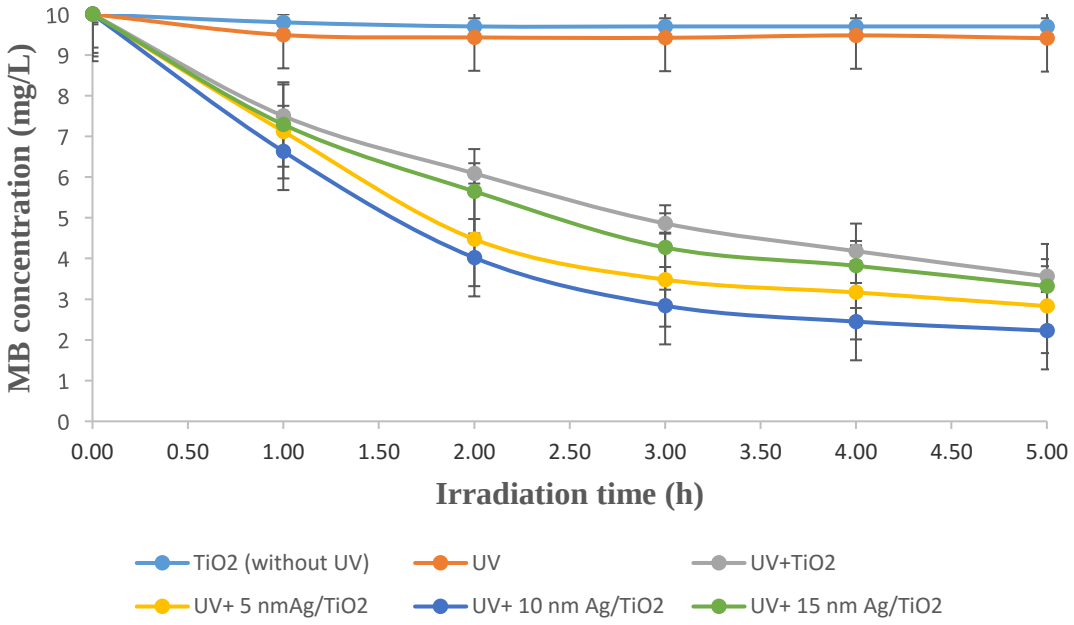

Figure 4-41: Photocatalytic activity of MB using various supported TiO_2 nanocrystals calcined at 350ºC for 3 h and Ag deposited TiO_2 nanocomposites. Experimental conditions: Concentration of MB (10 mg/L), Catalyst dose 0. 35 mg and volume of MB 50 mL

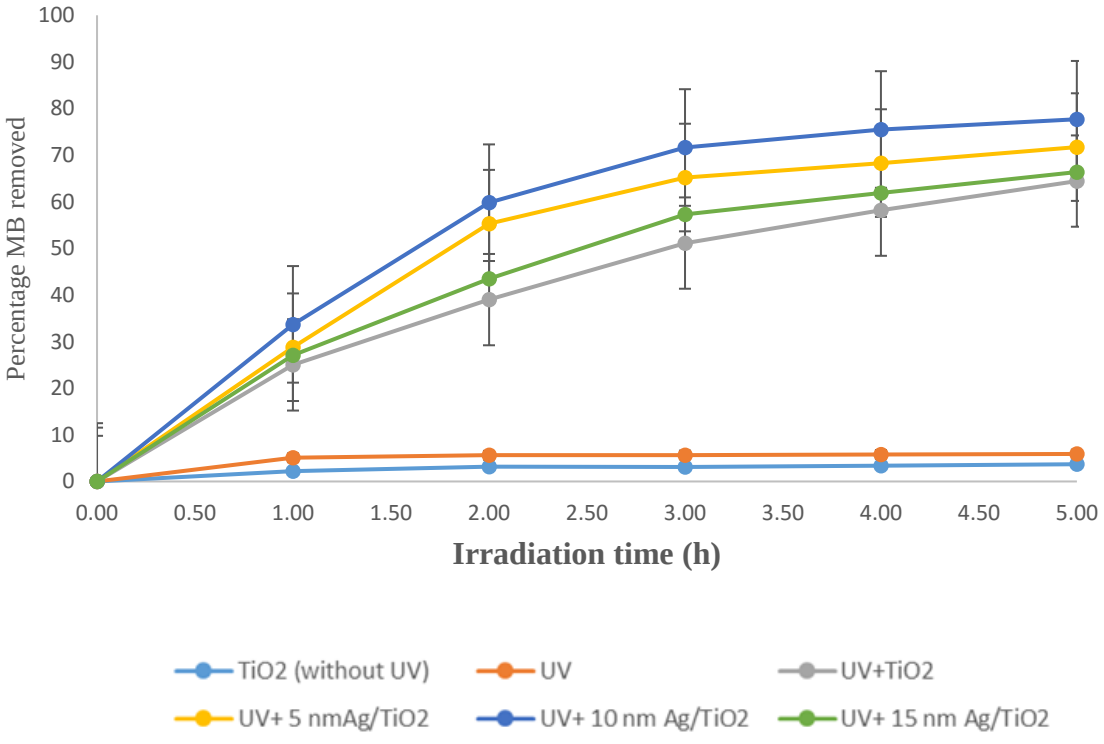

Figure 4-42: Percentage MB removed using various supported TiO_2 nanocrystals calcined at 350ºC for 3 h and Ag deposited TiO_2 nanocomposites. Experimental conditions: Concentration of MB (10 mg/L), Catalyst dose 0. 35 mg and volume of MB 50 mL, solution pH 3

Additionally, all the Ag deposited TiO_2 nanocomposites were more active than ordinary supported TiO_2 nanocomposites. Also in Figures 4.41 and 4.42, the concentration and percentage MB removed decreased with irradiation time in the following order: 10 nm Ag/TiO_2 > 5 nm Ag/TiO_2 > 15 nm Ag/TiO_2 > TiO_2. The addition of Ag enhanced the MB removal rate by 13.3%. The enhanced photocatalytic activity of 5 and 10 nm Ag/TiO_2 nanocomposites compared to 15 nm Ag/TiO_2, may be linked to the free electrons in metallic Ag which acted as electron trappers and supressed the electron-hole pair recombination rate (Chen and Lee, 2014; Subrahmanyam et al., 2012). Also, the improved MB removal rate of 10 nm Ag/TiO_2 over 5 nm Ag/TiO_2 may be attributed to differences in particle size and band gap. Among all the catalysts, the highest percentage MB removal of 77.7% was observed for 10 nm Ag/TiO_2 nanocomposites. This improved photocatalytic efficiency could be attributed to the fact that Ag on the TiO_2 surface trapped the photo-induced electrons and prevented the electron-hole recombination rate as a result of the Schottky barrier. The other possibility could be ascribed to the formation of more hydroxyl radicals responsible for mineralisation of MB. Furthermore, beyond the 10 nm Ag/TiO_2, the photocatalytic degradation of MB decreased from 77.7% to 66.3% as the thickness of Ag increased to 15 nm (Figures 4.41 and 4.42).

Furthermore, a higher amount of Ag on the TiO_2 surface may constitute a barrier and act as recombination centre for most photo-generated holes which could inhibit interaction between TiO_2 and MB. The higher photocatalytic activity of Ag/TiO_2 nanocomposites could be explained in terms of the differences in work function (Φ) value of Ag and TiO_2. The work function of TiO_2 was 4.2 eV whereas that of Ag was 4.6 eV. With the deposition of Ag, an interfacial layer was formed, which accelerated the transfer of electrons from TiO_2 to Ag. The transferred electrons were trapped by Ag to create more holes on the TiO_2 surface and eventually improved the photocatalytic activity (Chen and Lee, 2014). This result is in accordance with the findings and argument proposed by Ewa Kowalska et al. (2010) for Au deposited TiO_2 surface. Research had shown that the presence of Ag on the TiO_2 surface may form a Schottky energy barrier and create plasmonic effects, which promotes the photocatalytic process (Subrahmanyam et al., 2012).

Chen and Lee (2014) demonstrated that Ag doped TiO_2 nanoparticles had a higher photomineralisation rate constant of MB than ordinary TiO_2 nanoparticles. Chen and colleague (2014) ascribed the improved photocatalytic activity to the Schottky energy barrier created by Ag on TiO_2 surface, which decreased electron-hole recombination and enhanced catalytic efficiency. Suwarnkar et al. (2014) reported that addition of 0.25 mol % Ag onto TiO_2 lattice structure enhanced the photocatalytic degradation of methyl orange by 96%. The authors also found that excessive Ag beyond an optimum concentration could lead to complete coverage of TiO_2 surface, which prevented direct ultraviolet light from interacting with the catalysts and reduced the concentration of the photogenerated holes. This consequently reduced the number of available active sites and the photodecomposition efficiency of methyl orange.

Furthermore, excessive Ag often intensifies the diffusion distance which may affect the formation of hydroxyl radicals and subsequently decrease the photocatalytic activities (Cao et al., 2008). Studies have shown that higher content of Ag particles on TiO_2 surface may possibly accelerate the hole capture, create interfacial barriers, affect the charge separation and decrease the photocatalytic efficiency of TiO_2 (Subrahmanyam et al., 2012).

Figures 4.43 and 4.44 depict the variation of UV-visible adsorption spectra of MB by supported TiO_2 nanocrystals and 10 nm Ag/TiO_2 nanocomposites. As indicated in the two figures, there was a progressive decrease in the MB peak intensity at 665 nm with irradiation time. The decrease indicates the destruction of fused aromatic ring structures as well as the MB chromophores by the catalysts. The decomposition of MB chromophores was faster in the presence of 10 nm Ag/TiO_2 than ordinary supported TiO_2 nanocrystals without Ag. The results further demonstrated Ag as a good dopant. Daniel et al. (2013) had earlier observed that modification of TiO_2 surface with plasmonic Ag significantly improved the photodecomposition rate of organic dyes.

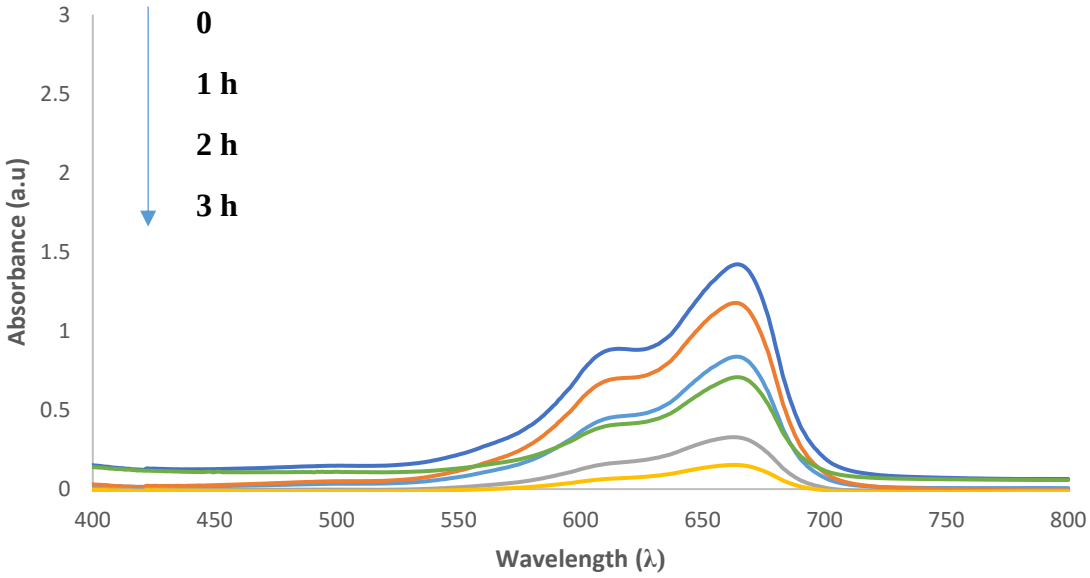

Figure 4-43: UV-visible absorption spectra of MB degradation under UV-light by supported TiO_2 nanocrystals

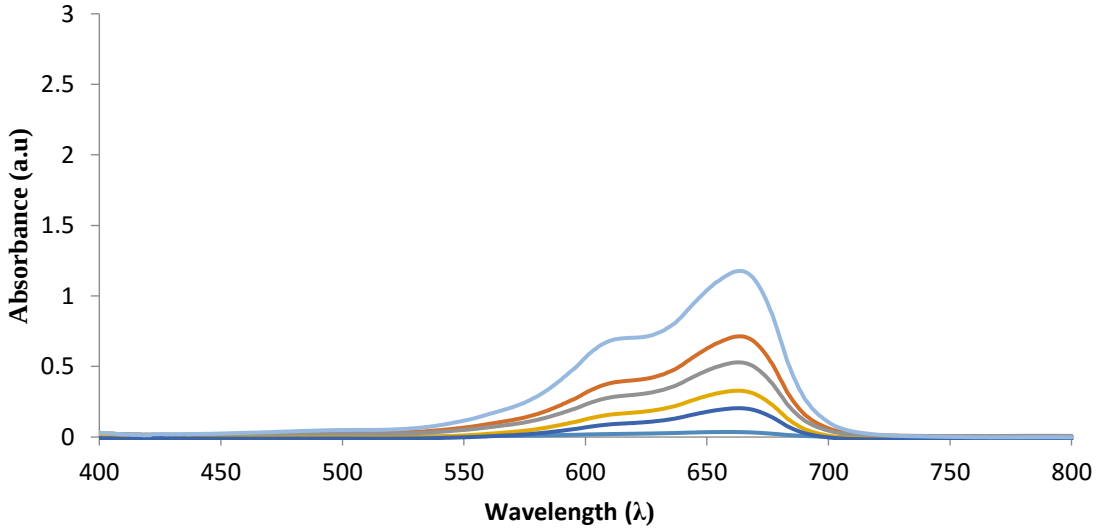

Figure 4-44: UV-visible absorption spectra of MB degradation under UV-light by 10 nm Ag deposited TiO_2 nanocomposites.

4.6.3 Degradation Kinetics of MB

The mineralisation kinetics of MB by stainless steel mesh supported TiO_2 nanocrystals and Ag deposited TiO_2 nanocomposites could be explained using the Langmuir-Hinshelwood first-order kinetics model. The obtained experimental values were fitted into the equation represented below.

$$-\ln\frac{C}{Co} = kt$$

Where Co represents the initial concentration of MB and C was the concentration at different time interval t, k represents the first-order reaction rate constant (min^{-1}). Figure 4.45 represents a graph of ln C/Co against the irradiation time.

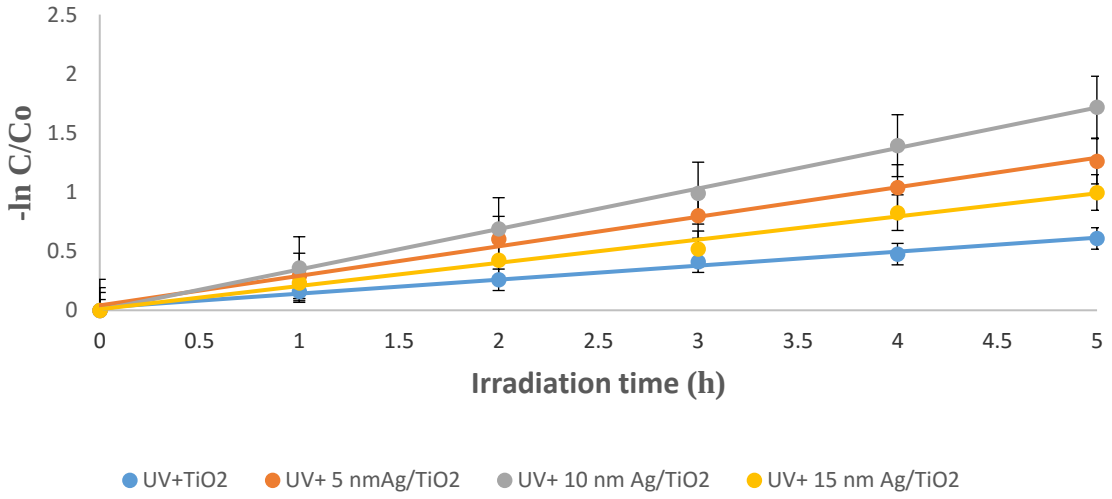

Figure 4-45: The kinetics of MB mineralization using supported TiO_2 nanocrystals and Ag deposited TiO_2 nanocomposites. (Experimental conditions: MB concentration (10 mg/L), solution pH 3, MB volume 50 mL, Catalyst dose 30-35 mg and irradiation time 5 h

The photodecomposition reaction of MB of all catalysts demonstrated a linear relationship between the MB concentration and irradiation time. The regression coefficient (R^2) value as indicated in Table 4.14 was closer to one signifying that the photooxidation reaction of MB fitted well to pseudo-first order. In addition, according to the information provided in Table 4.14, it is obvious that the photodegradation rate constant of Ag deposited TiO_2 nanocomposites were higher than ordinary TiO_2 nanocrystals without Ag. It is also noteworthy mentioning that the degradation half-life $t_{1/2}$ decreases with increasing Ag content. Similar observations were reported by Cao et al. (2008) on the photocatalytic degradation of aqueous acetamiprid by Ag-doped titania nanoparticles.

Table 4.14: The photocatalytic degradation rate constant and half-life of MB. Initial concentration of MB, 10 mg/L, solution pH 3, catalyst dosage 30 mg, irradiation time 5 h

Catalysts	**Rate constant (k)**	**Linear regression equation**	**Half-life ($t_{1/2}$) = ln2/k**	**Regression coefficient (R^2)**
Supported TiO_2 nanocrystals	0.1183	lnC/Co= -0.1183t	5.85	0.9878
5 nm Ag/TiO_2 nanocomposites	0.1960	lnC/Co= -0.1960t	3.53	0.9903
10 nm Ag/TiO_2 nanocomposites	0.2498	lnC/Co= -0.2498t	2.77	0.9940
15 nm Ag/TiO_2 nanocomposites	0.3423	lnC/Co= -0.3423t	2.02	0.9989

CHAPTER 5: REMOVAL AND DEGRADATION OF ORGANIC POLLUTANTS USING THE DIELECTRIC BARRIER DISCHARGE (DBD) SYSTEM

5.1 INTRODUCTION

This chapter presents the results obtained based on the experiments conducted on the removal and degradation of bisphenol-A (BPA) and 2-nitrophenol (2-NP) by dielectric barrier discharge (DBD) system and combined DBD/photocatalysis using the stainless steel mesh supported Ag/TiO_2 photocatalysts prepared at 350 C for 3 h.

5.2 EXPERIMENTAL

The experimental protocols for the removal and degradation of bisphenol-A (BPA) and 2-nitrophenol (2-NP) by dielectric barrier discharge (DBD) system and combined DBD/photocatalysis are presented in this section.

5.2.1 Design of the dielectric barrier discharge (DBD) reactor

As the purpose of this investigation was to establish whether dielectric barrier discharge is a viable alternative for the removal of organic compounds from wastewater, it is apparent that the methodology for the investigation is centred on the design and operation of the DBD reactor. In this section, the design, construction and operation of the DBD reactor will be discussed. The modular DBD reactor was designed at the ENS research group, University of the Western Cape, South Africa. The design is closely related to that of a 5 tube, single pass, heat exchanger. In this design, however, copper electrodes (held in place by specially designed disks referred to as electrode placement disks) are centred in each of the tubes. The design of the shell also contained 3 baffles to ensure proper fluid mixing in the shell and to reduce dead spots therein.

Figures 5.1 below shows the third angle projections of the reactor. These include the isometric, front, top and side views. Figure 5.2 shows a flow simulation done for the shell side flow to illustrate the effect of the baffles. The reactor should be assembled from individually fabricated parts that are bolted together, using 4 galvanised bolts, to make disassembly for cleaning possible. The tubes should be constructed from quartz glass (a dielectric material which does not absorb UV light), the shell should be constructed from Perspex, the end caps should be constructed from polypropylene (in the figures above they are transparent for better illustration of inside construction), and the shell flanges, baffles and electrode placement disks should be constructed from high temperature resistant Teflon.

A

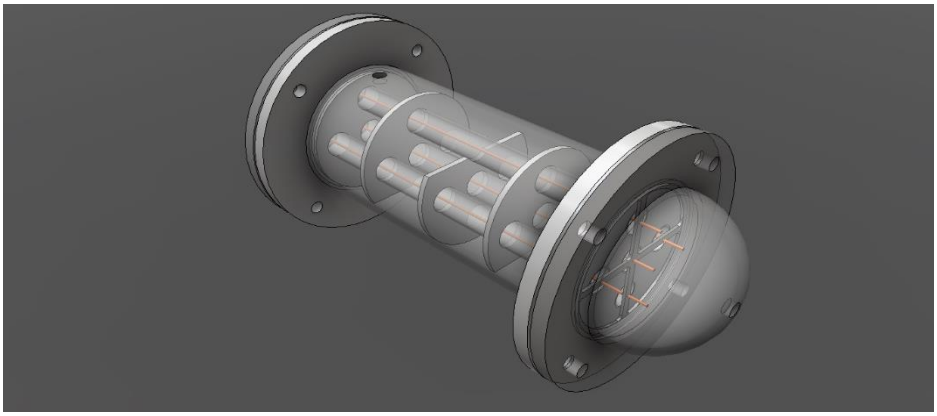

B

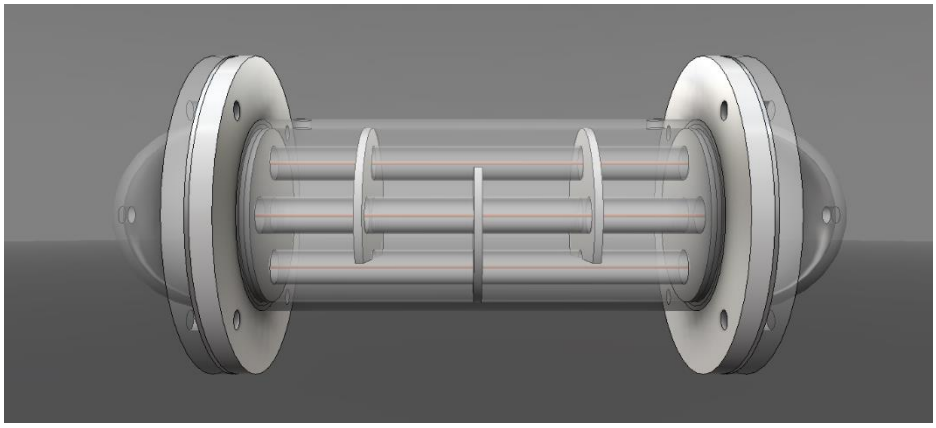

C

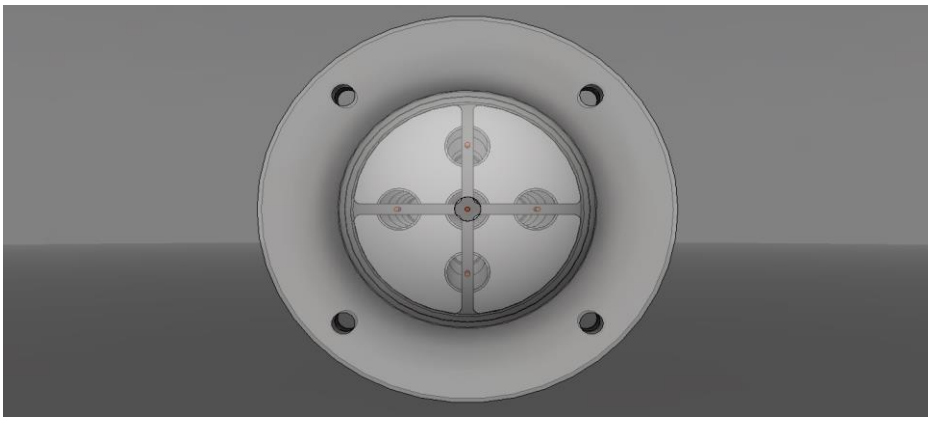

D

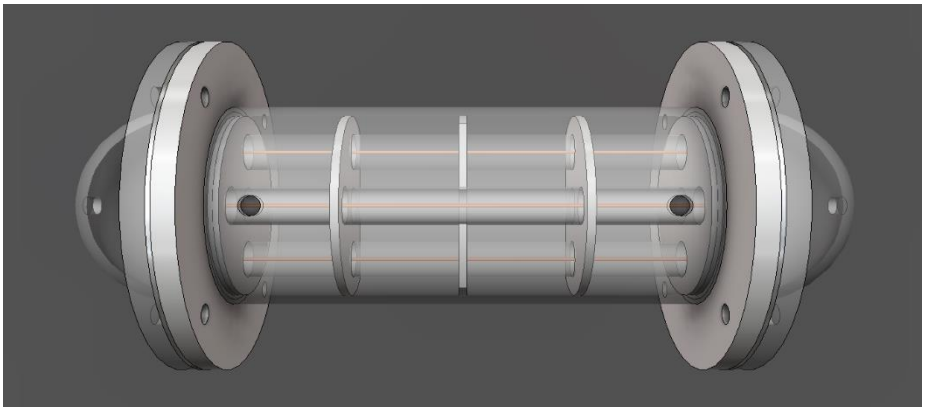

Figure 5-1: Isometric (A), front (B), top (C) and side view of reactor created in Autodesk Inventor Fusion

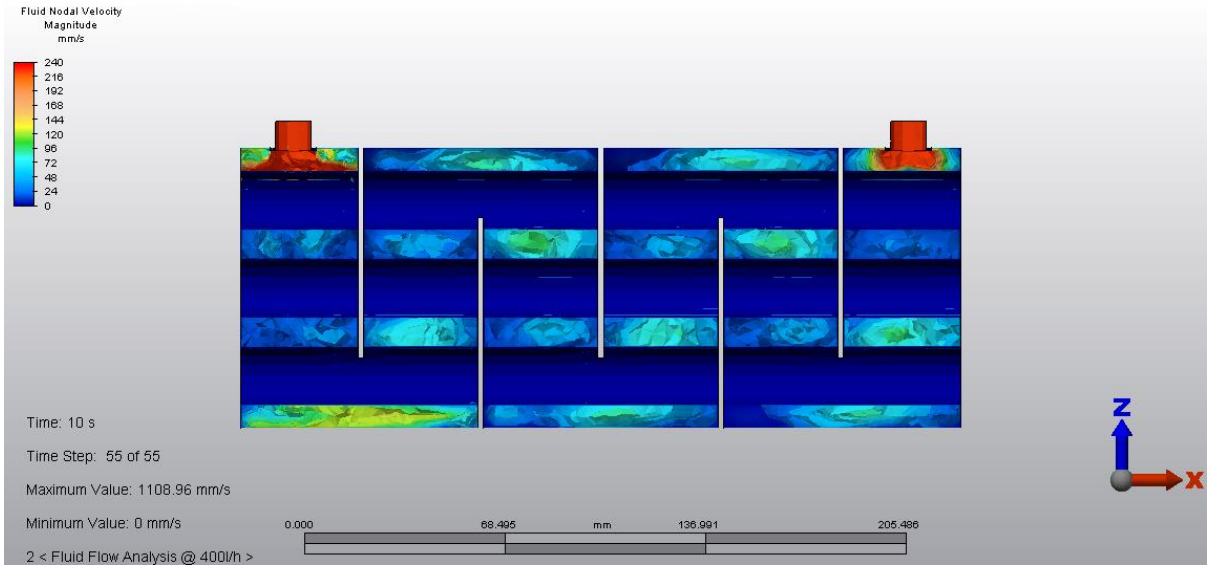

Figure 5-2: Flow simulation for baffles using Autodesk Simulation Multiphysics

This study will try to combine a single cell of the DBD with Ag immobilized titania composites. The overall treatment efficiency can be evaluated by the contribution made by both the DBD system and synthesised supported photocatalyst. In this study the design of the DBD was prepared (Liebenberg, 2013) but could not be realised due to budgetary constraints and a single DBD cell, optimised in the previous study and rebuilt according to the optimised criteria was used for laboratory scale experimentation in this study.

5.2.2 Dielectric barrier discharge: experimental set-up

This section presents the degradation procedure of BPA and 2-NP by the dielectric barrier discharge (DBD) system alone. This was followed by the integration of the supported synthesised photocatalysts with dielectric barrier discharge system to degrade BPA and 2-NP. In this section, the optimized DBD reactor was used as reported by Mouele (2014). Figure 5.3 represents the schematic diagram of DBD system used for the degradation of BPA or 2-NP in aqueous solution. The device comprised a DBD reactor that generated powerful oxidants such as hydroxyl radicals, hydrogen peroxide, ozone and ultraviolet light, using an AC high voltage power supply, step down transformer, air flow meter, air pump, ground electrode and a reactor vessel containing the model wastewater. The DBD reactor was a double quartz tube with a quartz inner tube and outer tube diameter of 1 mm and 7 mm respectively. The AC high voltage power supply was set at 25 V, delivering a current of 5 A and a power of 125 W, and was connected in series to a transformer and rectifier that steps the AC voltage up to a DC output voltage of ~8 kV. This potential was applied between the electrode in the DBD reactor and the electrode held in the systems' inner quartz tube shown in Figure 5.3.

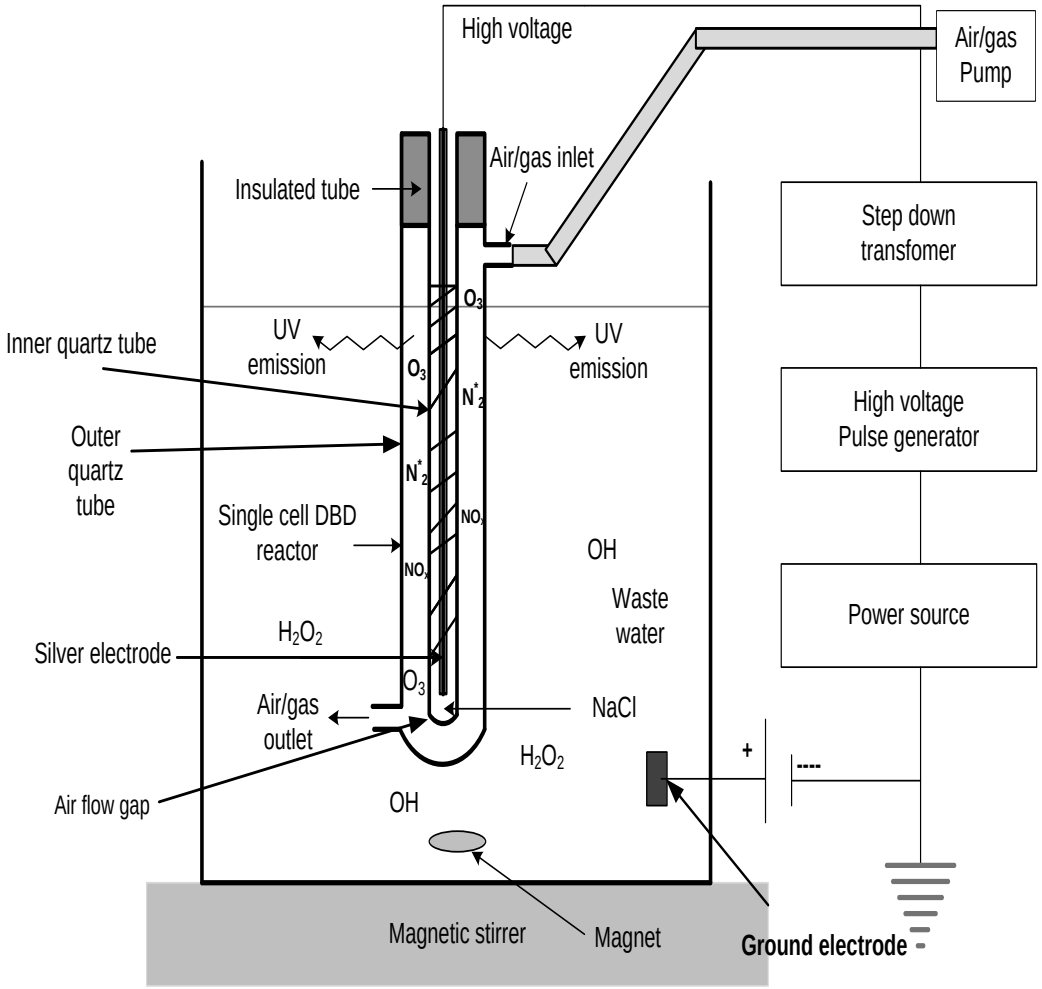

Figure 5-3: The schematic diagram of the dielectric discharge barrier system

The 0.5 mm silver electrode directly connected to the high voltage (output of the transformer) was immersed in a 50 g/L sodium chloride electrolyte placed in isolation within the inner quartz tube of the single cell DBD reactor. Air was provided in the space between the inner and outer quartz reactor tubes by an air pump with a high and low flow speed switch which was connected to both air flow meter and the space between the inner and outer quartz tubes forming an air flow gap. An air-flow rate of 3.0 L/min was used through the 2 mm air flow gap. The 0.5 mm thick silver electrode was placed inside the electrolyte isolated in the inner quartz tube of 1 mm diameter while the ground electrode was submerged into the reactor vessel to complete the circuit and was also grounded to the earth to avoid risk of electrocution. The DBD reactor was 23 cm long with an inlet and outlet for air circulation. All through the discharge, the powerful oxidants and UV/visible light produced acted simultaneously to decompose the target compounds. The ozone generated by the DBD reactor was continuously and uniformly dispersed within the solution compartment by sparging and magnetic stirring of the BPA or 2-NP solution being treated.

5.2.3 Degradation of BPA and 2-NP using the DBD system

The 10 ppm (4.4×10^{-5} M) solution of the prepared BPA or 2-NP was used. 1.5 L of the simulated wastewater was measured and placed in a 2 L beaker. The original depth of the simulated organic wastewater in the reactor vessel was about 130 mm and later rose to about 135 mm due to the introduction of air which produced bubbles in the solution compartment. The electrical conductivity of the aqueous solution of BPA and 2-NP were measured to be 20.1 and 51.3 µS/cm with the aid of multi-parameter analyser C3010. The DBD experiment was conducted for 120 minutes at room temperature (20ºC) and sampling was done at time intervals of ten minutes. The efficiency of the DBD process was determined by measuring the residual concentration of BPA or 2-NP using detailed HPLC methodology provided in Table 5.1.

Table 5.1: Chromatographic parameters used for analysis of BPA and 2-NP

HPLC parameters	**Conditions**		
Chromatograph	Waters		
Detector	UV		
Column	Spherisorb C_{18} (15mm, 3.9mm 5µ)		
Injection volume	20 mL		
Mobile phase	A: water,	B: Acetonitrile	
Flow-rate	1 mL/min		
Gradient elution	Time	%A	%B
	0	85	15
	25	0	100
	28	0	100
	30	85	15
Temperature	26ºC		
Data Collection	Breeze software version 2		

5.2.3.1 *HPLC instrumentation and chromatographic conditions*

The residual concentrations of BPA and 2-NP were determined using a Waters high performance liquid chromatographic chromatograph equipped with a Waters 1525 binary HPLC pump, Waters 2487 dual λ absorbance detector, and Waters 2707 auto-sampler and running on the Breeze software. Separation was done with the aid of a Spherisorb C_{18} reversed-phase column and a gradient elution method involving two mobile phases was used. The optimized gradient program used for elution and quantification the target compounds is shown in Table 5.1.

5.2.3.2 *Calibration curve of BPA and 2-NP*

Standard solutions of BPA and 2-NP were prepared by diluting a 1000 ppm stock solution and a standard working curve based on mean HPLC peak areas was constructed for a concentration range of 10-80 ppm. The temperature was maintained at 26°C throughout the analysis. Evaluation and quantification were made using a chromatography data system. The retention time for 2-NP and BPA was 8.2 and 13.3 min respectively obtained at 280 and 278 nm respectively. A calibration curve of standard solution against the peak area was plotted. The HPLC chromatograph of BPA and 2-NP at a retention time of 8.2 and 13.3 min is shown in Figure 5.4 and 5.5. The calibration curve of both 2-NP and BPA are shown in Figure 5.6 and 5.7 respectively.

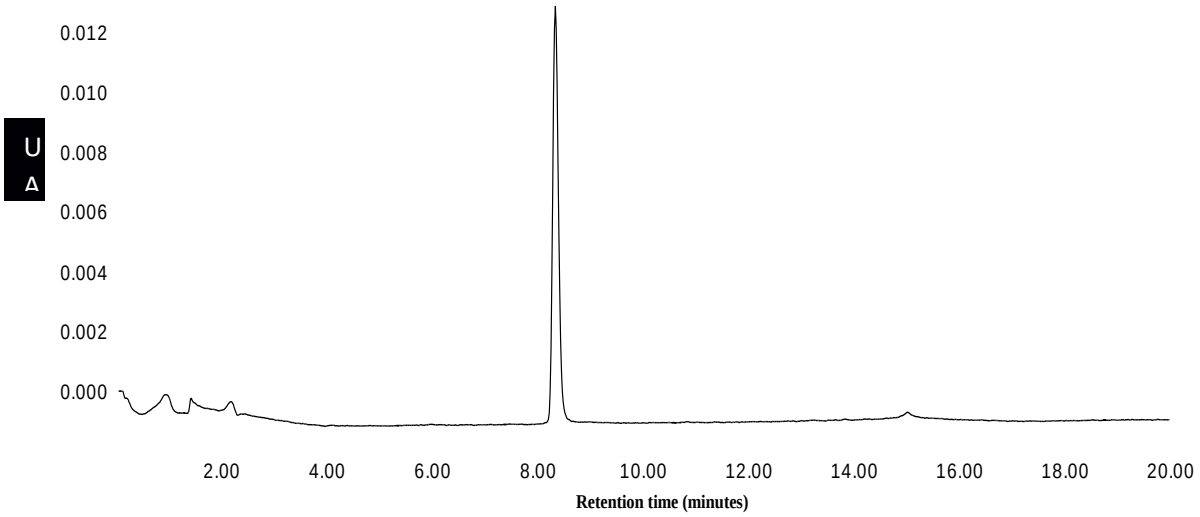

Figure 5-4: HPLC chromatogram of 2-nitrophenol

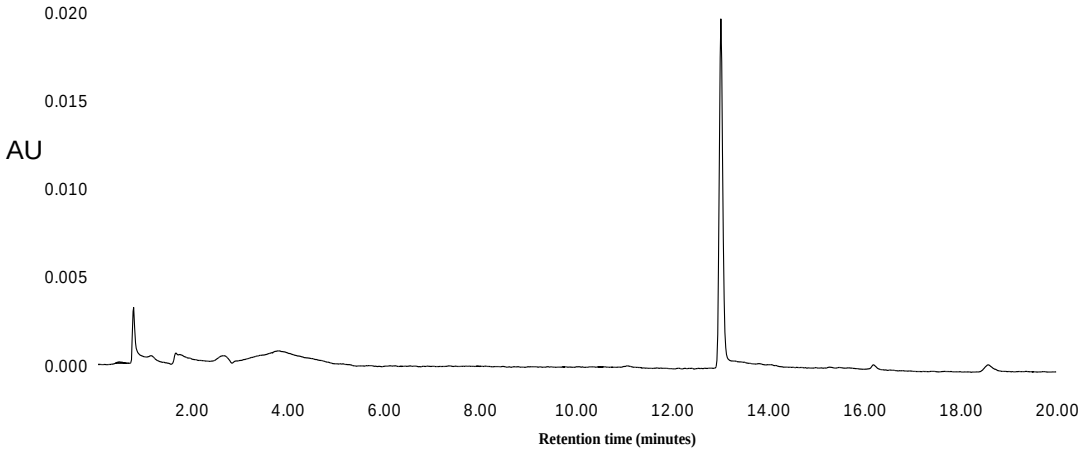

Figure 5-5: HPLC chromatogram of bisphenol-A

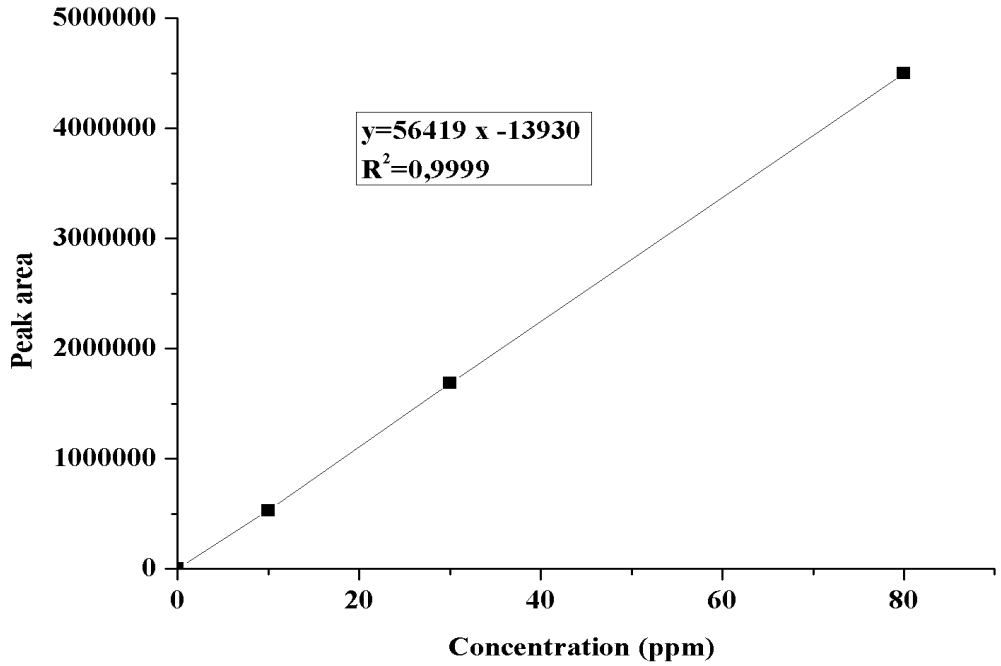

Figure 5-6: Standard calibration curve of 2-nitrophenol (HPLC)

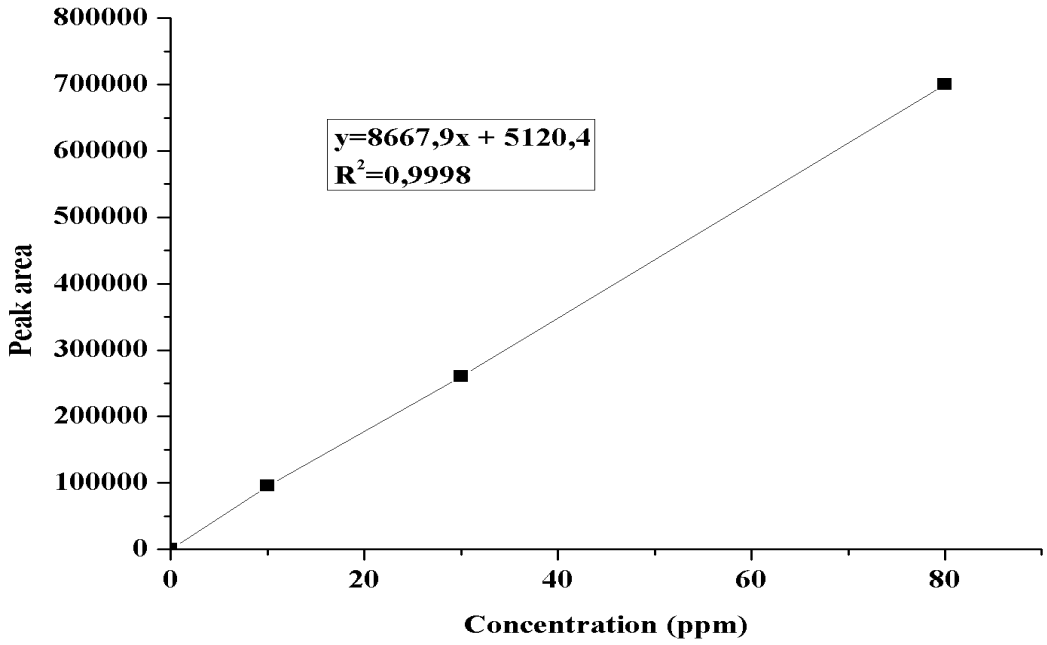

Figure 5-7: Standard calibration curve of bisphenol-A (HPLC)

5.2.4 Investigating the influence of different experimental parameters on the oxidation rate of BPA or 2-NP via DBD system

This section provides information on the experimental parameters studied using DBD only.

5.2.4.1 *Effect of initial solution pH*

In order to establish the optimum pH at which maximum degradation of the modelled pollutants occur, solution pH was investigated as a parameter. The initial solution pH was varied from 3 to 12 for 120 min by adding 0.5 M H_2SO_4 or 0.5 M NaOH dropwise until the desired pH was achieved. The solution pH was measured with a multi-parameter analyser C3010 and prior to that, the pH meter was calibrated based on the manufacturer's instructions. 1.5 L of 10 ppm BPA or 2-NP placed in 2 L beaker were treated with the single cell DBD system. A 2 mL sample aliquot of the treated water was taken at each ten minutes interval and put in 2 mL glass vials, and then analysed by HPLC equipped with a Waters 1525 binary HPLC pump, with absorbance detector set at 280 and 278 nm for BPA or 2-NP respectively.

5.2.4.2 *Effect of initial concentration of the BPA and 2-NP*

In order to determine the optimum concentration at which maximum removal of the modelled pollutants occurred, the initial concentrations of BPA or 2-NP solution were varied in the range of 10-30 ppm maintained at optimum solution pH of 3. 1.5 L of the simulated organic wastewater was subjected to DBD treatment for 120 minutes and sampling was done at intervals of ten minutes during the reaction and 2.0 mL aliquots of the treated solution were withdrawn with a plastic syringe and analysed by HPLC equipped with a Waters 1525 binary HPLC pump, and Waters 2487 dual λ absorbance detector set at 280 and 278 nm respectively.

5.2.4.3 *Effect of the radical scavengers*

60 mg/L each of (Na_2CO_3, Na_2SO_4, NaCl) solution were separately mixed with 1.5 L of BPA or 2-NP solution of known concentration (10 mg/L) at pH 3 in a 2 L beaker. The mixture was subjected to DBD treatment for 120 minutes and sampling was performed every 10 minutes. The residual concentration of BPA or 2-NP in the aliquot of samples withdrawn from the reactor were determined by HPLC equipped with a Waters 1525 binary HPLC pump, Waters 2487 dual λ absorbance detector AT set at 280 nm for both compounds respectively. A Waters Spherisorb C_{18} reversed-phase Liquid chromatography column dimension 150 by 4.6 mm, 5 µ was used for the analysis of BPA and 2-NP concentrations in the treated samples. The detailed HPLC methodology is described in Table 5.1.

5.2.5 Treatment of BPA and 2-NP by combination of DBD reactor and the supported photocatalysts

The schematic diagram of the combined DBD/supported TiO_2 photocatalyst or Ag doped TiO_2 nanocomposites device used for the decomposition of BPA and 2-NP is shown in Figure 5.8. The AC high voltage power supply discharge system connected in series to the DBD reactor provided a constant potential of 8 kV across the electrodes into the reactor vessel containing the simulated organic wastewater. The DBD reactor in Figure 5.6 is the same as shown in Figure 5.1 except that the DBD reactor was positioned at the centre of tubular arrangement of the sample JT7 or JT14 for irradiation by UV light generated during discharge. The whole unit was immersed in a 2 L beaker in order to utilize the ultra-violet light produced by the DBD reactor for photocatalysis. The dimension of the supported catalyst was 19.5 cm by 2 cm which was equivalent to the length of the quartz tube. The rectangular pieces of mesh containing catalysts were joined together with a thread at the edge to form the tubular arrangement. The inner quartz tube was filled with 50 g/L NaCl solution and the electrode (silver) was then connected to AC high voltage. The aqueous NaCl solution in the inner tube acted as discharging electrolyte. In the course of this experiment, the passage of high voltage dielectric barrier electrical discharge in the airgap between the two quartz tubes produced UV light which was used to activate the inserted supported photocatalyst (see Figure 5.8).

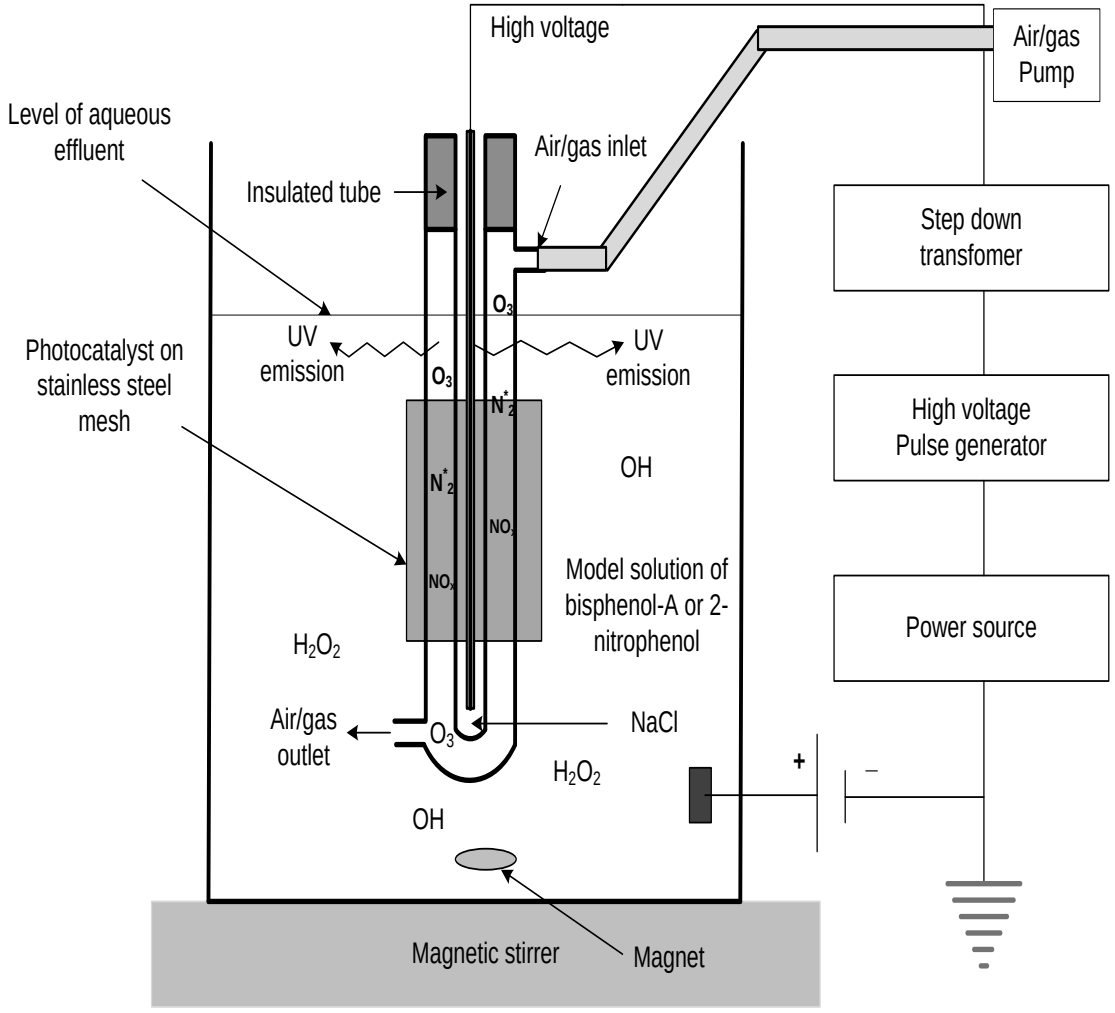

Figure 5-8: The schematic representation of the DBD reactor with supported photocatalyst

The gas flowing through the air gap could be air or oxygen, in this case air was used. The air flow rate was maintained at 3 L/min throughout the period. The ground electrode was equally immersed in the 2 L beaker containing 1.5 L of 10 ppm modelled pollutants. The initial concentration of the simulated organic compounds was 10 ppm and the pH of BPA or 2-NP solution was adjusted to 3 by adding a few drops of 0.5 M NaOH or 0.5 M H_2SO_4 respectively. The experimental set up was then switched on, air was fed into the air gap of the DBD reactor continuously and the produced reactive species were uniformly dispersed within the solution compartment by magnetic stirring. Sampling was done every ten minutes for 120 minutes. In order to prevent possible interference such as indoor electrical light, the experiment was conducted in the dark, apart from the UV generated in situ by the DBD. The residual concentration of 2 mL BPA or 2-NP sampled at 10 min intervals during the experiment was determined using an Agilent HPLC with a C_{18} column and ultraviolet detector operating at 278 nm or 280 nm. All experiments were replicated twice and the average residual concentration was noted.

The control experiment was conducted with supported TiO_2 nanocrystals without the DBD reactor in the dark using 10 ppm solution of BPA or 2-NP. 1.5 L of BPA or 2-NP aqueous solution was placed in a beaker with continuous magnetic stirring at ambient temperature. Sampling was done at 10 min interval and analysis using an Agilent HPLC with a C_{18} column and ultraviolet detector operating at 278 nm or 280 nm. For a comparison, 0.8 g powdery commercial titanium oxide (anatase, Degussa P-25) was uniformly dispersed into aqueous solution of BPA or 2-NP. The DBD reactor containing powder TiO_2 was run for 120 min. Sampling (2 mL) was done at 10 min intervals and subsequently analysed using HPLC methodology described in Table 5.1. Furthermore, the leaching or release of any metallic species such as Ti, Ag, Cr, Fe, Ni from either the catalyst or the support materials during the experiment were measured using ICP-OES.

5.2.6 Reusability and stability test

In order to investigate the reusability and stability potentials of the catalyst, the experimental procedure described in section 5.2.3 was repeated consecutively for four times using the combined DBD and sample JT14 containing freshly prepared 10 ppm BPA or 2-NP solution. After each experiment, sample JT14 was cleaned with Millipore water and air-dried. The mineralogical integrity or stability of the catalysts after each experiment was examined using XRD. The surface morphology and adhesion of the catalysts upon the mesh before and after the repeated experiment was checked using HRSEM.

5.2.7 Determination of Total Organic Carbon

The Total Organic Carbon content (TOC) is used as an indicator parameter during wastewater treatment to provide information on the extent of conversion of organic pollutants in water to harmless inorganic species such as carbon dioxide and water. It is often used to assess the performance of wastewater treatment. In this study, the mineralisation process of BPA or 2-NP was monitored in terms of the reduction in the amount of Total Organic Carbon (TOC) before and after the oxidation process using the adapted standard thermo-catalytic digestion followed by non-dispersive infra-red (NDIR) detection described by Fung et al. (1996). The detailed methodology is provided below.

Prior to analysis, 15 mL of treated water was pipetted into a 25 mL volumetric flask and acidified with 3 mL of 0.2% (v/v) H_3PO_4. This was done to remove or purge the inorganic carbon (IC) such as CO_2 and CO_3^{2-}. The pH of the solution was reduced to 2 and was maintained under purging with purified O_2 for about 10 min at a rate of 100 mL/min^{-1}. The sample was then digested in an autoclave at a temperature of 116ºC for 2 h. Subsequently the digested sample was distilled over 10 g CuO catalyst at about 2-3 mL min^{-1} for 30 min in order to oxidise the volatile organic compounds. In the process of distillation, 0.03 g $K_2S_2O_8$ was also added to oxidise the nonvolatile organic compounds. Thereafter, the total non-purgeable chemically bonded organic carbon that is converted to CO_2 and transported in the purified oxygen streams was measured using nondispersive infrared analyser as the TOC value. The same procedure was repeated for a blank sample and 15 mL carbon-free water was used in place of the sample. The mineralisation rate of BPA or 2-NP solution as a function of TOC was estimated using the relationship below

$$Mineralization\ rate = \frac{Initial\ TOC - Final\ TOC}{Initial\ TOC\ value} * 100$$

5.2.8 Identification of the transformation products

This experiment was conducted to identify the oxidation products of the target compound and to elucidate the degradation mechanism. The Agilent 6230 time of flight liquid chromatograph mass spectrometer (TOF LC-MS) in the negative ionization mode was used for qualitative identification of the intermediates formed during the decomposition of BPA or 2-NP by DBD reactor, or combined DBD/JT14 process. Due to difficulty in the identification of the intermediate compounds at low concentration by LC-MS, 250 ppm each of BPA or 2-NP were separately subjected to DBD treatment. The combined system of DBD/JT14 was utilised to identify the oxidation products of BPA or 2-NP degradation in aqueous solution. The volume of the simulated organic wastewater was 1.5 L and the degradation of BPA or 2-NP into various fragments was monitored for a period of 2 h. Higher concentrations were selected for easy identification of the reaction intermediates and prediction of the degradation pathways.

Sampling was done every 10 minutes when 2 mL aliquot was withdrawn into 2 mL bottles. The 2 mL vials were then sealed and the possible intermediate oxidation products were identified using Agilent 6230 TOF LC-UV and mass spectrometry at 280 and 278 nm respectively. A Thermo chromatographic system (pump + thermostated autosampler Surveyor) equipped with a diode array detector (Surveyor) and an ion trap mass spectrometer DECA XP Ion max was used. The separation of BPA or 2-NP into various fragments was accomplished using a symmetry C8 column and a gradient method with two mobile phases was used. Details of the gradient elution method are contained in Table 5.2.

5.2.9 LC-MS determination of BPA and 2-NP

The intermediate products of BPA and 2-NP were separated and identified using a liquid chromatograph coupled to a mass spectrometer (Agilent 6230 TOF LC-MS). The Agilent 1260 Infinity series used comprised a binary pump, an auto-sampler and an 1100 diode array detector (DAD). The operating program was Mass Hunter software version 3.0. Mobile phases were water (0.1% formic acid) and acetonitrile (0.1% formic acid). Ionization of BPA intermediates was by electron spray ionization (ESI) and ions were captured in the negative mode while ionization of 2-NP was captured in the positive mode. The optimized gradient program used for elution and identification of intermediates on the LC-MS is shown in Table 5.2.

Table 5.2: LC-MS parameters for identification of intermediates

HPLC parameters	Conditions
Chromatograph	Agilent 6230 TOF LC/MS
Detector	Agilent DAD 1100
Column	Waters Symmetry C_8 15mm, 3.9mm 5µ
Injection volume	5 µL
Mobile phase	A: water (1% formic acid)
	B: Acetonitrile (1% formic acid)
Flow-rate	0.4 mL/min
Gradient elution	Time %A %B
	0 85 15
	35 0 100
	47 0 100
	50 85 15
Temperature	26 ºC
Data Collection	Mass Hunter

5.3 RESULTS AND DISCUSSION

5.3.1 Investigating the influence of different experimental parameters on the oxidation rate of BPA or 2-NP via DBD discharge

The results obtained based upon the experiments conducted on the removal and degradation of bisphenol-A (BPA) and 2-nitrophenol (2-NP) by dielectric barrier discharge (DBD) system and combined DBD/photocatalysis are presented in this section.

5.3.1.1 *Effect of initial pH on the removal of bisphenol-A or 2-nitrophenol*

The pH of the solution is one of the important parameters that influence the oxidation of organic compounds in advanced oxidation technologies such as DBD system. Solution pH also affects the oxidative strength of the reactive species such as H_2O_2, O_3, $^{\bullet}O$ and OH radicals amongst others. Based on this background, the influence of the variation of solution pH in the range of 3-12 on the removal of BPA or 2-NP by the DBD system was explored. The desired solution pH value was adjusted by 0.5 M NaOH or 0.5 M H_2SO_4 solution (experimental procedure and conditions have been described in chapter 3). The residual concentration of BPA or 2-NP in aqueous solution was determined using the analytical technique shown in Table 5.2. The results showing the influence of solution pH on the removal of BPA or 2-NP are presented in Figures 5.9 and 5.10 respectively. Figure 5.9 (a) the effect of pH on the removal of BPA degradation with time, (b) change in solution pH during the plasma discharge experiment.

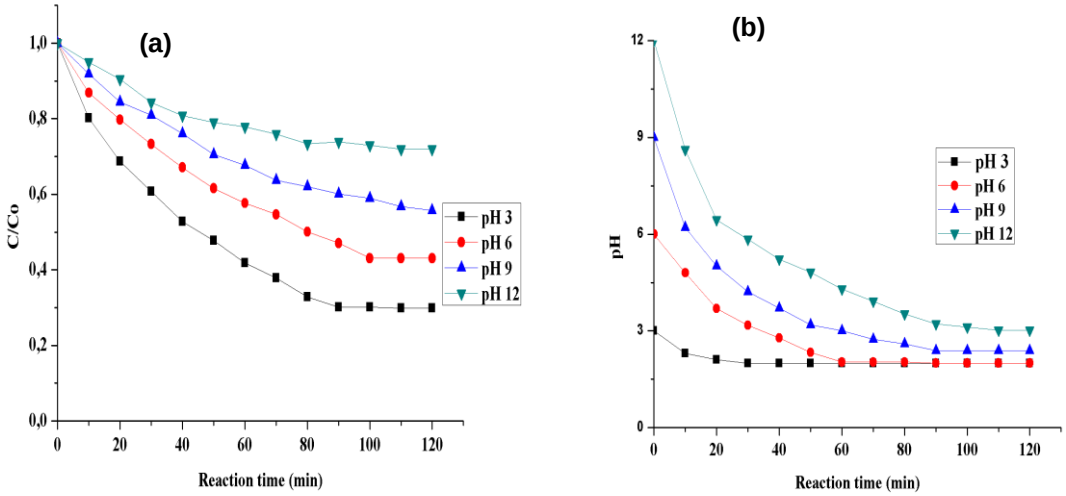

Figure 5-9: (a) Effect of the initial pH value on the degradation of BPA (b) decrease in solution pH values during plasma discharge. Conditions: discharged voltage 8 kV, volume of BPA, 1.5 L, air flow rate 3 L/min, electrode (silver), electrolyte NaCl (50 g/L), concentration of BPA (10 ppm)

While, Figure 5.10 (a) represents 2-NP degradation with treatment time (b) change in solution pH during the plasma discharge experiment.

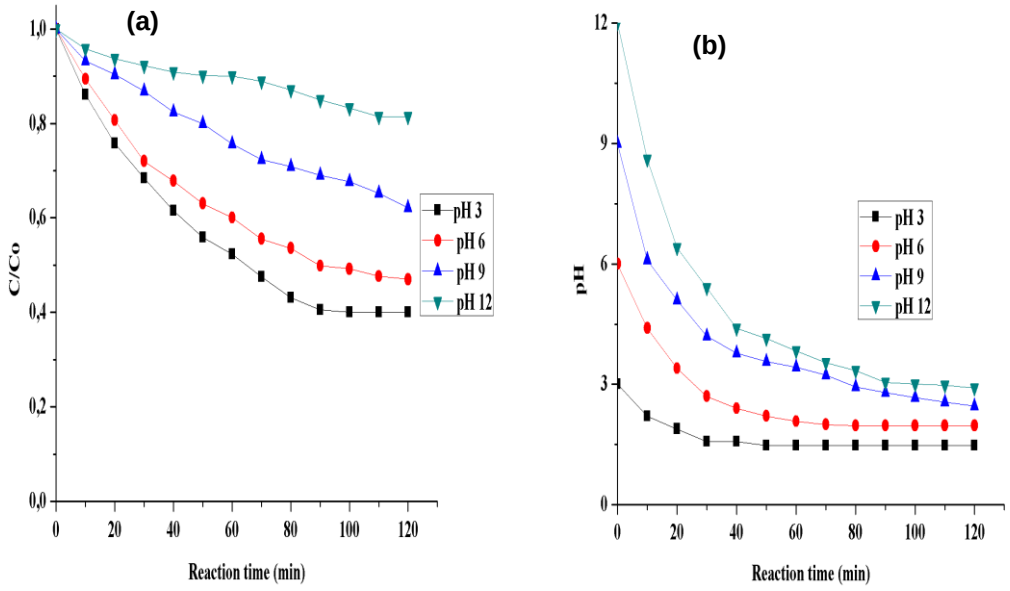

Figure 5-10: (a) Effect of the initial pH value on the degradation of 2-NP (b) decrease in solution pH values during plasma discharge. Conditions: discharged voltage 8 kV, volume of 2-NP, 1.5 L, air flow rate 3 L/min, electrode (silver), electrolyte NaCl (50 g/L), concentration of 2-NP (10 ppm).

As shown in Figures 5.9(a), it can be seen that the removal efficiency of the BPA in the DBD reactor was higher at lower pH than at higher pH. The removal efficiency of BPA at pH 3, 6, 9 and 12 was found to be 70.2%, 57%, 45% and 28.1% respectively after 120 minutes (Figure 5.9 (a)). A similar trend was observed for 2-NP with the lowest removal efficiency observed at pH 12 and the highest at pH 3 (Figure 5.10 (a)). This means that acidic conditions followed by neutral medium favoured the removal of BPA compared to alkaline medium but all solutions tended to become acid over the treatment time even when initially highly alkaline, indicating generation of acidic species during degradation. At low pH, O_3 is stable and remains the dominant species and as such was supposed to be responsible for the mineralisation of BPA or 2-NP in solution in the acidic conditions.

Apart from O_3, OH radicals with higher oxidation potential in acidic conditions or H_2O_2 were responsible for the observed high removal efficiency. This is because a substantial amount of O_3 generated by the DBD escaped from the surface of the solution because the DBD was not a closed system. The open DBD system reduced the concentration of O_3 competing with the target compounds compared to available OH radicals. The other possibility may be due to the consumption of oxygen by nitrous (NO) and nitric oxide (NO_2) which consequently reduced the concentration of O_3 in the system and changed the pH. In addition, studies have shown that OH radicals with higher electrophilic and oxidation potentials attacked the organic pollutants at a rate of 10^6-10^9

times faster than ozone (Rong et al., 2014). However, due to the significant amount of O_3 lost from the system, acidic conditions favoured the generation of the hydroxyl radicals and are deemed responsible for high removal efficiency in acidic rather than alkaline conditions.

It should be noted that the two pollutants exhibited similar removal patterns at different pH values, with BPA having higher removal efficiency than 2-NP. This is because BPA has several bonds that can serve as points of attack where OH, O_3 or H_2O_2 can abstract protons whereas 2-NP has only a few points of attack in the aromatic rings. This showed that BPA was more susceptible to attack and decomposed faster than 2-NP in solution in the DBD system without a catalyst. Furthermore, the extent of removal of a non-coloured pollutant (BPA) was higher than a coloured pollutant (2-NP) irrespective of the solution pH. This observation could be attributed to the inhibitory effect of the colour pigment on the formation of reactive species. Very recently, Zhang et al. (2013) found that non-coloured pollutants such as phenol, and microcystin-LR degraded much faster than a coloured organic compound methyl orange. They argued that coloured organic pollutants inhibited UV-light produced by the plasma system thereby affecting the formation of reactive species in solution.

At a higher pH (basic region), the formation of OH radicals was expected to predominate and accelerate the oxidation of BPA or 2-NP molecules. Yet, lower removal efficiency of both pollutants was observed. The most possible interpretation of low removal efficiency under strongly alkaline conditions (high pH) could perhaps be linked to the generation of CO_2 during the oxidation process of BPA or 2-NP, which perhaps formed carbonate ions (CO_3^{2-}) and HCO_3^-, which tallies with the reducing pH trend observed over time. These carbonate species (CO_3^{2-} and HCO_3^-) are known as radical scavengers and consume OH radicals owing to their high rate constant value. The decrease in the amount of OH radicals in solution affected the removal efficiency. Similar observations were reported by Wang et al. (2007) who found that the OH radicals produced via radical-type chain reaction of O_3 in the basic medium were consumed by carbonate species and reduced the removal efficiency of phenol. Zhang et al. (2003) found that the H_2O_2 dissociated under alkaline conditions to hydroperoxyl radical (HO_2-). The formation of hydroperoxyl radical reduced the OH radicals in solution and affected the degradation rate of 4-NP.

The outcome of this study is however contrary to the findings reported by Lee et al. (2003) and Tay et al. (2012) on BPA oxidation via an ozonation process. The two authors reported that BPA degradation rate increased with the increase in solution pH from 2-12. The reason for the inconsistency in the results reported by these two authors and the outcome of this study was that, radical scavengers (t-BuOH) were added in their work to scavenge and consume available OH radicals. This action eliminated the stronger competition between OH radicals and O_3 for the organic pollutants. Thus, it was demonstrated that only O_3 reacted with BPA. Whereas in this experiment radical scavengers were not added to the DBD system to consume OH, thus a stronger competition among O_3, OH and H_2O_2 for the organic pollutants pertained. It was found that, at low pH, the concentration of OH radicals was higher than that of O_3 due to significant loss of O_3 from the system. Thus, the significant loss of O_3 facilitated the formation of H_2O_2 and OH under acidic conditions in the presence of UV light and favoured the decomposition of the two compounds.

Figure 5.9 (b) and 5.10 (b) represent the variation in solution pH monitored during the oxidation process in the DBD reactor. It was found in both cases that the initial pH values reduced significantly on exposure to plasma discharge especially at higher pH values as reaction time increased. The decrease in the solution pH upon exposure to plasma generated via dry air may be due to the formation of carboxylic and mineral acids. Furthermore, the release of NO_2 by 2-nitrophenol or phenolic fragments from bisphenol-A degradation during the oxidation process may also contribute to the solution acidity and low pH. The reaction mechanisms involved in the formation of nitrogen oxides (NO, NO_2), nitrous and nitric acid during plasma discharge in water are indicated in Section 2.5.6. The presence of OH radicals in the solution may also have accelerated the formation of NO and NO_2 to HNO_2 and HNO_3 respectively, thus contributed to the solution acidity index value.

A similar decrease in solution pH containing sulfadiazine upon exposure to plasma was reported by Rong et al. (2014) and was attributed to the formation of nitrogenous oxides (NO, NO_2), which dissolved in water forming nitrate ion (NO_3-) and nitrite ion (NO_2^-). Further reaction of the nitrate and nitrites ion formed nitric acid (HNO_3), nitrous acid (HNO_2) and sometimes peroxynitrous acid (ONOOH). Liu et al. (2012) found that carbamazepine conversion rate and solution pH decreased during the oxidation process by the DBD due to the presence of NOx species which competed with O_3. Conversely, Tay et al. (2012) reported that the degradation of BPA increase with increases in pH from 2-12 and pH 10.2 was observed as the optimal value where maximum BPA degradation occurred. The authors attributed the increase in BPA oxidation rate with increasing pH to the scavenging effect of t-butanol which prevented OH radicals from interacting with the pollutants.

5.3.1.2 *Effect of initial concentration of BPA or 2-NP*

The influence of different initial concentration of BPA or 2-NP on the degradation efficiency and yield in the range of 10-30 mg/L under the optimal conditions of pH 3.0, discharge voltage 8 kV, air flow rate 3 mL/min were investigated. The detailed experimental procedure and conditions have been described in section 5.2.3. The residual concentration of BPA or 2-NP in aqueous solution was analysed using HPLC conditions shown in Table 5.1. The removal efficiency and degradation yield of BPA as a function of reaction time is shown in Figure 5.11 (a) and (b). Figure 5.12 (a) and (b) illustrates the degradation efficiency and 2-NP degradation yield as a function of reaction time.

As shown in Figure 5.11 (a), the BPA removal efficiency at 10 mg/L concentration under constant solution pH and discharge voltage after 80 minutes reaction time was 70.4%, and however reduced to 58.9% as the BPA concentration increased to 30 mg/L. A similar trend was observed with 2-NP in Figure 5.12 (a), where the removal efficiency of 2-NP reduced significantly from 57.6% to 39.2% under the same experimental conditions. This means that the removal efficiency of BPA or 2-NP was faster at lower concentration than at higher concentration. According to Figure 5.11 (a) and 5.12 (a), it could be seen that at every treatment time, the percentage removal efficiency of BPA or 2-NP decreased with an increase in initial concentration of the BPA or 2-NP. This could be attributed to the fewer number of BPA or 2-NP molecules competing with the available reactive species at low initial concentration during the plasma discharge, allowing more of them to degrade.

On the other hand, at higher pollutant concentration, the number of BPA or 2-NP molecules increased without a corresponding increase in the concentration of free reactive species. As a result, the concentration of available reactive species was less and could not effectively mineralise the large number of BPA or 2-NP molecules into harmless compounds, accordingly being responsible for lower removal efficiency at higher concentration of the pollutants.

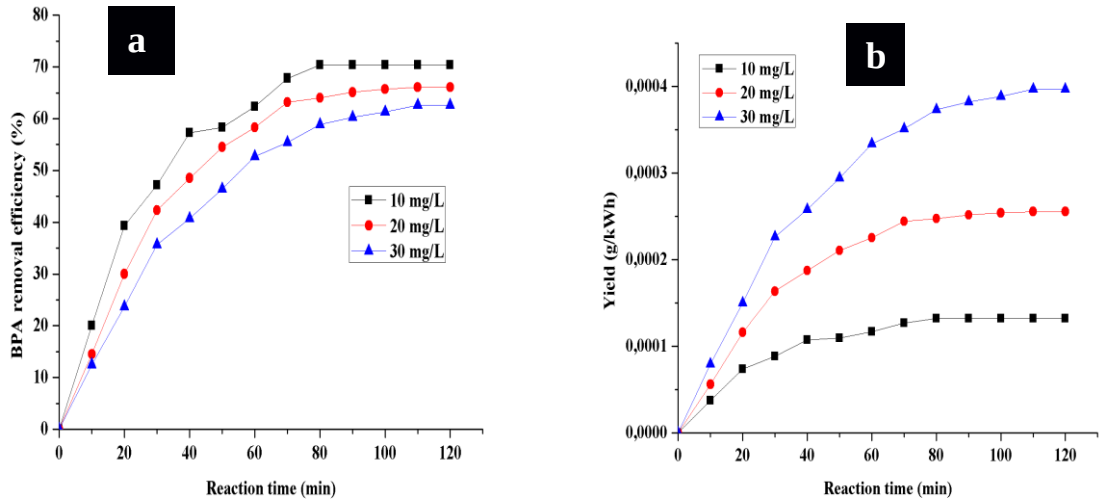

Figure 5-11: Effect of (a) BPA initial concentration (b) BPA degradation yield at different concentration values by the DBD system at discharge voltage 8 kV, pH 3, air flow rate 3.0 mL/min, electrolyte NaCl (50 g/L), volume of BPA (1.5 L), electrode (silver)

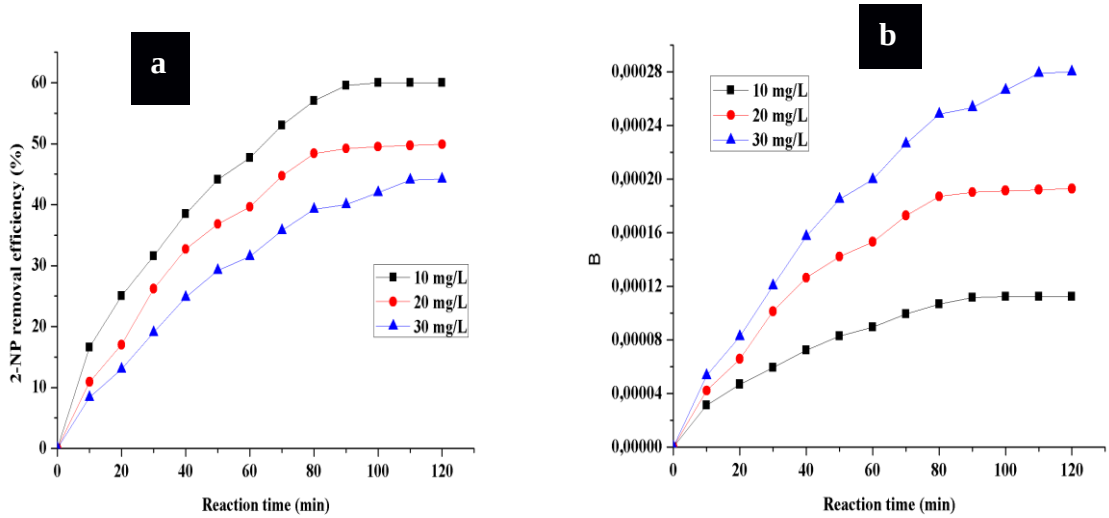

Figure 5-12: Effect of (a) 2-NP initial concentration (b) degradation yield of 2-NP at different concentration values by the DBD system at discharge voltage 8 kV, pH 3, air flow rate 3.0 mL/min, electrolyte NaCl (50 g/L), volume of BPA (1.5 L), electrode (silver)

The other possibility for lower removal efficiency could be traced to the formation of refractory intermediate transformation products at higher pollutant concentration, which strongly competed with the original compound for free reactive species. The competition between the intermediates and initial compounds may have prevented further degradation of the original compound and thus could be responsible for its lower degradation efficiency. The observed trends of decreasing degradation rate with increasing pollutant concentration and vice versa show that the removal efficiency of organic pollutant via plasma discharge depends on the initial concentration in this DBD configuration used, under the applied conditions. This observation is in agreement with previous studies reported by researchers on endocrine disruptors in the literature in spite of the differences in the configuration of the DBD (Gao et al., 2013; Li et al., 2014).

Rong and Sun (2013) utilized wetted wall-corona discharge reactor to degrade sulfadiazine and found that the degradation rate constant (k) of sulfadiazine (SDZ) decreased by an order magnitude of 2 as the pollutant concentration increased from 10-80 mg/L. Rong and co-worker (2013) attributed such decrease in the degradation rate constant at higher SDZ concentration to greater competition between more SDZ molecules and the generated intermediate compounds for the few available OH radicals. It is obvious that the removal efficiency of BPA or 2-NP was strongly affected by the pollutant's concentration and the free radical output of the applied DBD system. Furthermore, the removal efficiency of BPA or 2-NP can equally be explained in terms of degradation yield, which represents the rate of oxidation of the pollutants per unit energy consumed during the process as expressed in the equation below.

$$Y\ (g/kWh) = \frac{\mathrm{C(g/L)} * \mathrm{V(L)} * 1/100 * \mathrm{conversion(\%)}}{\mathrm{P(kW)} * t(h)}$$

Where C(g/L) represents initial concentration of the pollutants, V is the volume of the aqueous solution in Litre, P is the average power dissipated in kW, which is expressed as the product of the discharge voltage (V) and applied current (A), t is the treatment time, while the conversion (%) is the same as removal efficiency at each treatment time.

According to the above equation, the degradation yield of BPA or 2-NP was estimated using a discharge voltage of 8 kV and applied current 5 A. These values changed during the oxidation process and depended on the concentration of the pollutants. Figures 5.11 (b) and 5.12 (b) illustrate the degradation yield of BPA and 2-NP at different initial concentrations. Contrary to the trend observed in Figure 5.11 (a) and 5.12 (a), the degradation yield of BPA or 2-NP increased with increasing pollutant concentrations. According to Figure 5.11 (b), the degradation yield of 10 mg/L BPA solution after 80 minutes treatment time was 1.32×10^{-4} g/kWh, which however increased to 3.73×10^{-4} g/kWh as the concentration increased to 30 mg/L. Similarly, the degradation yield of 2-NP increased from 1.07×10^{-4} g/kWh to 2.48×10^{-4} g/kWh under the same reaction conditions.

This shows that the increase in the degradation yield at higher pollutant concentration did not depend only on the amount of free reactive species in the DBD but on the number of molecules taking part in the reactions. It should be noted that a higher concentration of BPA or 2-NP implies a higher number BPA or 2-NP molecules, which means a higher amount of energy is required to achieve complete degradation. Contrary to what was obtained with removal efficiency at higher concentration of BPA or 2-NP, it was found that increases in the concentration of BPA or 2-NP resulted in a corresponding increase in the discharge energy and hence the degradation yield. This observation supported previous investigation reported for different organic pollutants: 17 β-Estradiol (Gao et al., 2013), 4-chlorobenzoic acid (Lesage et al., 2013), pentoxifylline (Magureanu et al. 2010). These authors attributed the increase in the degradation yield with increasing concentration of organic pollutants to consumption of more energy by the molecules.

The obtained degradation yield in this study was lower than 17 $\times$ 10^{-3} and 15 $\times$ 10^{-3} g/kWh reported for clofibric and phenol by Krause et al. (2009). At the same time, lower than 4.5 and 48 g/kWh for reported for phenol and methylene blue by Grabowski et al. (2006) and Grabowski et al. (2007) respectively. Lesage et al. (2013) reported degradation yield value of 0.87 g/kWh and 0.16 g/kWh for 4-chlorobenzoic acid decomposed by DBD and gliding arc discharge. The differences in the degradation yield were ascribed to the nature of the reactive species produced via each discharge. While DBD produced oxygenated species, gliding arc discharge generated nitrogenated species which consumed OH radicals. Overall, it can be seen that different degradation yields were reported by different researchers, which showed that this parameter depends on several factors such as the nature and structure of organic pollutant, types of DBD, discharge power of the DBD, nature of the feed gas (air or oxygen), and flow rate, amongst others (Magureanu et al. 2008). Thus, considering the fact that the removal efficiency was faster at a lower concentration, 10 mg/L was selected as the optimal initial concentration for both compounds in this study.

5.3.1.3 *Effect of the addition of radical scavengers*

The presence of radical scavengers in solution affects the efficiency of advanced oxidation technologies due to inhibition and consumptions of free radicals. Among radical scavengers or inhibitors are inorganic species such as Na_2CO_3, Na_2SO_4, $NaHCO_3$, $Na_2B_2O_7$, $NaNO_3$, C_3H_9OH, t-C_4H_9OH, Na_3PO_4, and NaCl. In this study, the influence of separate addition of Na_2CO_3, Na_2SO_4 and NaCl on the removal rate of BPA or 2-NP in water by DBD system was examined. The detailed experimental methodology has been provided in Section 5.2.3. The residual concentration of BPA or 2-NP in aqueous solution was analysed using HPLC technique described in Table 5.1. The results of the influence of radical scavengers such as Na_2CO_3, Na_2SO_4 and NaCl on the removal efficiency of BPA or 2-NP are presented in Figures 5.13 (a) and 5.14 (a). While Figures 5.13 (b) and 5.14 (b) illustrate the pseudo-first order kinetic model plot of ln (C/Co) against the reaction time for BPA or 2-NP respectively.

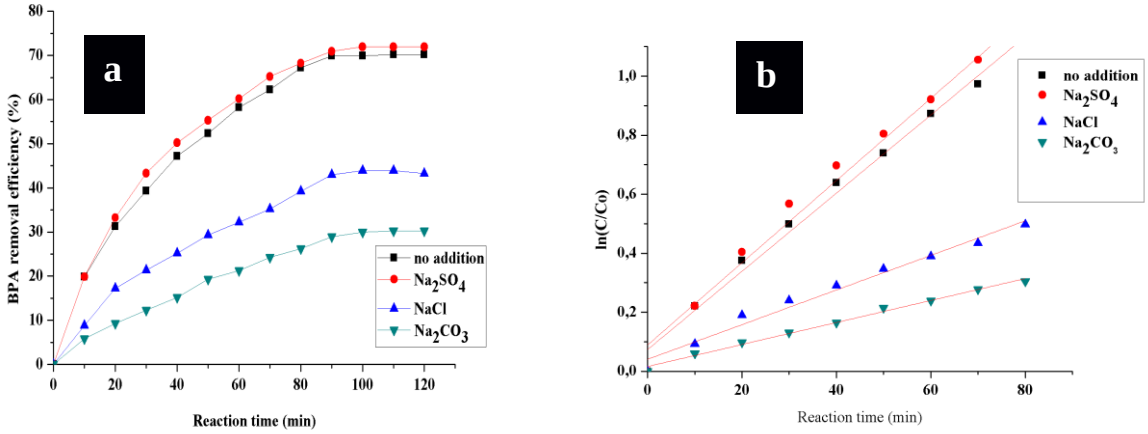

Figure 5-13: Effect of radical scavengers on (a) the removal efficiency of BPA b) degradation kinetics of different radical scavengers on BPA (Discharge voltage 8 kV, BPA concentration 10 mg/L, radical scavengers concentration 60 mg/L, air flow rate 3 mL/min, solution pH 3.0, electrolyte, NaCl (50 g/L), electrode (silver)

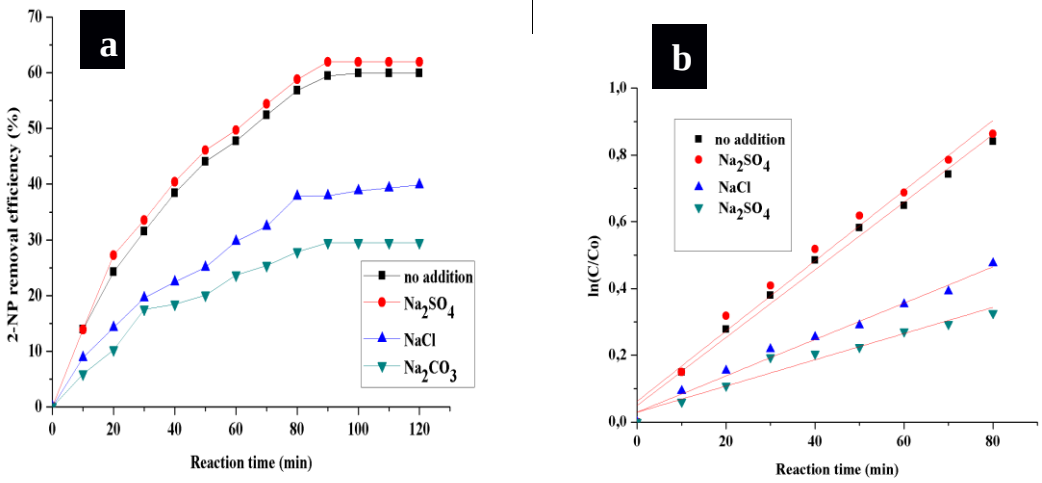

Figure 5-14: Effect of radical scavengers on (a) the removal efficiency of 2-nitrophenol (d) degradation kinetics of different radical scavengers on 2-NP (Discharge voltage 8 kV, 2-NP concentration 10 mg/L, radical scavengers concentration 60 mg/L, air flow rate 3.0, electrolyte, NaCl (50 g/L), electrode (silver).

As shown in Figure 5.13 (a) and 5.14 (a), the BPA or 2-NP removal efficiency decreased in the presence of Na_2CO_3 and NaCl and slightly increased with Na_2SO_4. The BPA removal efficiency was 27.0% and 40% upon the addition of NaCl and Na_2CO_3 after 80 minutes treatment time. Similarly, 2-NP removal efficiency was 22.1% and 30.5% under the same conditions. On the other hand, with the addition of Na_2SO_4, the degradation efficiency of BPA and 2-NP was 71.9% and 61.6% respectively. The addition of Na_2SO_4 slightly enhanced the removal efficiency of BPA or 2-NP by 1.9% and 2.0% respectively.

Notably, among the three radical scavengers, Na_2CO_3 inhibited the removal efficiency of BPA or 2-NP more than the others. The decrease in the removal efficiency gives an indication of a rapid consumption and conversion of the OH radicals into non-active species by the carbonate ions in solution. In contrast, the slight improvement in the removal efficiency of BPA or 2-NP upon Na_2SO_4 could be attributed to the formation of $SO_4^{-\bullet}$ due to reaction of SO_4^{2-} with the OH radicals. The formation of $SO_4^{-\bullet}$ during the oxidation process is shown in the equation (27).

$$SO_4^{2-} + OH^{\bullet} \longrightarrow SO_4^{-\bullet} + OH^{-} \quad (27)$$

Manoj Kumar Reddy et al. (2013) had earlier reported that $SO_4^{-\bullet}$ with oxidation potential of 2.6 V was more reactive than OH radicals with oxidation potential value of 2.8 V. Therefore, the preference or selectivity for $SO_4^{--\bullet}$ by BPA or 2-NP over OH radicals may be based on the contribution of $SO_4^{--\bullet}$ to the electron transfer reaction. This reaction occurred preferably between the pollutant and $SO_4^{-\bullet}$ than with the OH radicals, perhaps involving hydrogen abstraction or addition reactions. Manoj Kumar Reddy et al. (2013) observed similar selectivity behaviour of $SO_4^{-\bullet}$ over OH radicals during the oxidation process in methylene blue by dielectric barrier discharge reactor, where Na_2SO_4 served as a radical scavenger. The increase could simply be as a result of the presence of both OH and $SO_4^{-\bullet}$ radicals in the system. The experimental data on the effect of radical scavengers on BPA or 2-NP removal rate were further fitted into the pseudo-first order kinetic plots illustrated in Figure 5.11(b) and 5.12 (b) respectively. Table 5.3 represents the rate constant and correlation coefficient of the different radical scavengers.

According to Table 5.3, the apparent rate constant (k) of BPA in the presence of Na_2SO_4 was 0.0139 min^{-1}, which was greater than 0.0049 min^{-1} and 0.0031 min^{-1} obtained with NaCl and Na_2CO_3. Similarly, the apparent degradation rate constant (k) for 2-NP upon the addition of 60 mg/L of Na_2SO_4, NaCl and Na_2CO_3 were 0.0084 min^{-1}, 0.004 min^{-1}, 0.0029 min^{-1} respectively. The obtained reaction rate constant (k) for Na_2SO_4 in the presence of BPA or 2-NP was three and four times greater than that observed for NaCl and Na_2CO_3. The higher BPA or 2-NP removal efficiency in the solution containing NaCl over Na_2CO_3 may be linked to the formation of oxidative species such as $Cl_2\bullet^-$ or $ClOH^{\bullet\cdot}$ which are of higher oxidation potential value than CO_3^{2}. The reaction mechanism of formation of $ClOH^{\bullet-}$, is shown in equations 28 and 29.

Table 5.3: The rate constant and correlation coefficient with different radical scavengers

Pollutants	Radical scavengers	Rate constant (min^{-1})	Correlation coefficient (R^2)
	Na_2SO_4	0.0139	0.9434
BPA	NaCl	0.0049	0.9512
	Na_2CO_3	0.0031	0.9641
	No addition	0.0136	0.9421
	Na_2SO_4	0.0083	0.9507
2-NP	NaCl	0.0040	0.9204
	Na_2CO_3	0.0029	0.9041
	No addition	0.0079	0.9393

$$Cl^- + OH^\circ \rightarrow Cl^\circ + OH^- \rightarrow ClOH^{-\circ} \quad (28)$$

$$Cl^\circ + Cl^- \rightarrow Cl_2\circ - \quad (29)$$

Thus, the removal efficiency of BPA or 2-NP by the DBD in the presence of radical scavengers followed the order Na_2SO_4 > NaCl > Na_2CO_3. Zhu et al. (2007) also found that the removal rate of phenol oxidised via pulsed corona discharge decreased from 80% to 30% upon the addition of 60 mg/L radical scavenger Na_2CO_3. The authors ascribed such a significant reduction to rapid reaction between the carbonate ion and the OH radicals, which resulted in termination of the oxidation process. Wang et al. (2007) reported phenol removal efficiency of 63.2% in the presence of 0.5 mmol/L Na_2CO_3, and 77.5% removal efficiency in the absence of a radical scavenger by pulsed corona discharge. Zhang et al. (2003) reported that addition of 10 mM sodium hydrogen carbonate (IV) to a solution containing 4-nitrophenol decreased the degradation rate constant of the compound by a factor of 0.48 compared to 0.29 by Cl^-. The authors attributed the decrease in the degradation rate of 4-NP to the decrease in the concentration of OH radical and consumption of H_2O_2 by sodium hydrogen carbonate (IV). This study shows that radical scavengers such as Na_2CO_3 and NaCl could negatively influence the removal efficiency of BPA or 2-NP in water, which scavengers are expected to be present in wastewater.

5.3.2 Degradation of BPA or 2-NP by combined DBD and supported TiO_2 or AG doped TiO_2 photocatalyst

This section focuses on the incorporation of the supported carbon doped TiO_2 nanocrystals (JT7) and Ag doped TiO_2 nanocomposites (JT14) into the DBD reactor for BPA or 2-NP degradation using the optimum conditions of solution pH and initial pollutant concentration established above.

The objective of this section of the study is to assess the removal and degradation efficiency of BPA or 2-NP by DBD combined with supported TiO_2 nanocrystals (JT7) and Ag doped TiO_2 nanocomposites (JT14). Based on the results presented in chapter 4 on the photocatalytic activities of Ag doped TiO_2 nanocomposites on MB, the optimal supported catalysts were incorporated into the DBD reactor to enhance the BPA or 2-NP mineralization efficiency. In this regard, the removal efficiency of BPA or 2-NP in aqueous solution was investigated using six different approaches. The experiment was conducted using the optimum solution pH and initial concentration of the pollutant obtained in section 5.4.1. The residual concentration of BPA or 2-NP in aqueous solution was determined using the analytical technique described in Table 5.2. The removal efficiencies of BPA or 2-NP via DBD alone or DBD with supported photocatalysts are represented in Figure 5.15 (a) and (b) respectively.

It is apparent from Figure 5.15 (a) and (b) that there was no appreciable removal efficiency for every measurement using stainless steel mesh alone. This indicates that the removal efficiency of BPA or 2-NP did not depend on the support material. In the same vein, the experiment conducted in the dark with the aid of TiO_2 supported nanocrystals, showed only a slight removal efficiency of about 4% for both compounds over the treatment time. This observation could be attributed to adsorption of BPA by the supported TiO_2 photocatalyst rather than photo-oxidation. Thus, adsorption phenomenon on the photocatalyst in the dark did not improve the degradation of BPA or 2-NP in water, showing that irradiation is needed to activate the catalyst. It can also be seen from Figure 5.15 (a) and (b) that the removal efficiency of BPA or 2-NP by the DBD alone at 80 minutes of reaction time was 67.22% and 56.8% respectively. When 0.8 g commercial powder TiO_2 was added to the DBD system, the BPA or 2-NP removal efficiency was 65.1% and 52.2% within the same treatment time as the DBD system on its own, showing the shielding effect of the powder catalyst.

With the incorporation of the supported TiO_2 photocatalyst (JT7) into the DBD reactor, the BPA removal efficiency was 80% within 60 min while 77.5% of 2-NP was removed after 80 min under the same experimental conditions. According to the results, there was a considerable improvement in removal efficiency of BPA or 2-NP in the presence of the stainless steel mesh supported TiO_2 photocatalyst than what was obtained with commercial TiO_2 powder without support in the DBD system. Thus, the prepared supported TiO_2 photocatalyst exhibited considerably higher photocatalytic activity than the standard titania (P25) photocatalyst. Studies have shown that the photocatalytic activity of TiO_2 largely depends on the specific surface area, microstructure and crystallite size (Chong et al., 2010). Additionally, TiO_2 exists in three different polymorphs namely anatase, rutile, and brookite with anatase phase exhibiting higher photocatalytic activity than other phases. The commercial powder TiO_2 used in this study comprised 80% anatase and 20% rutile with specific surface area 56 m^2/g. While, in this study, the synthesized supported TiO_2 photocatalyst (JT7) was purely anatase phase.

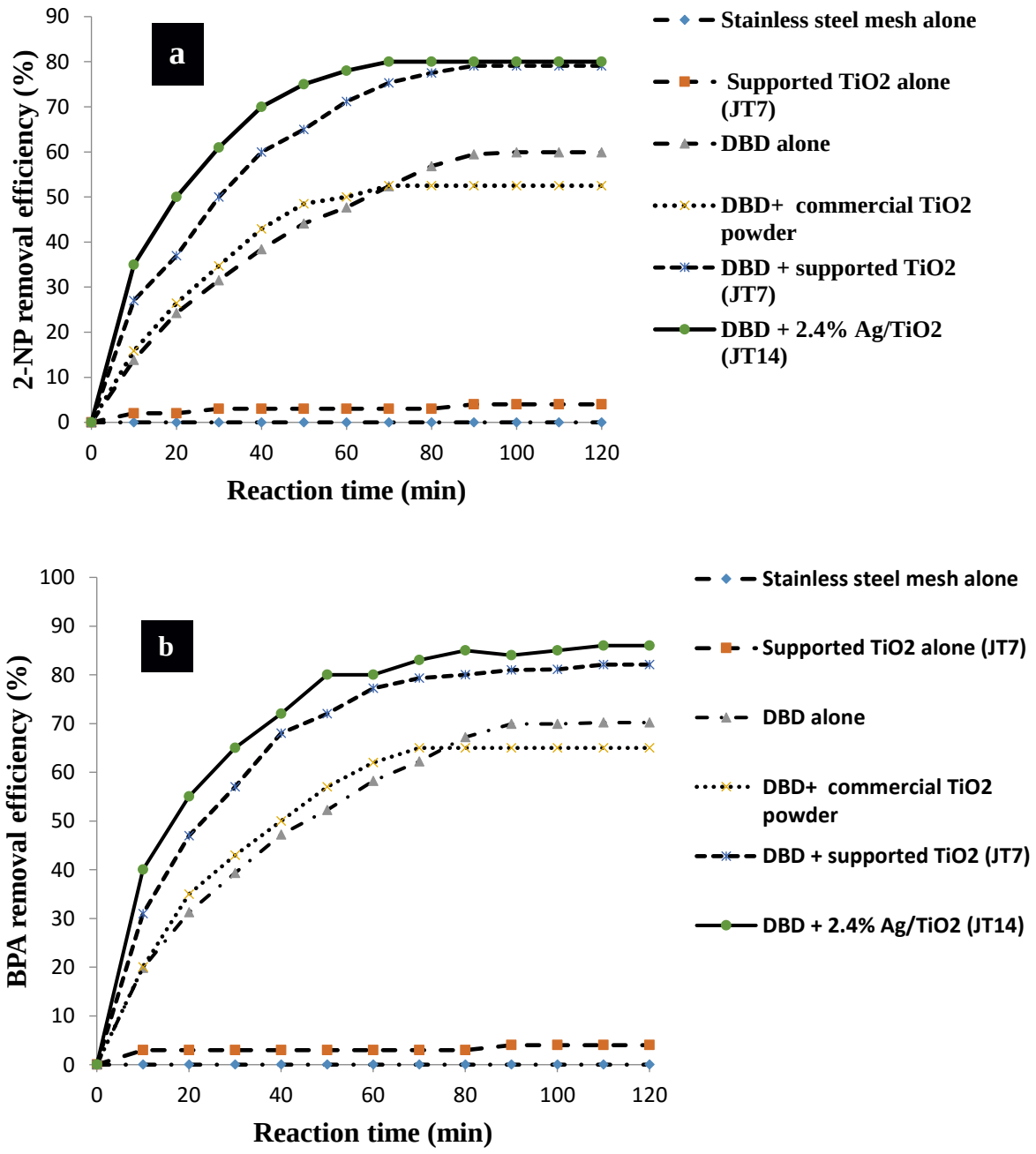

Figure 5-15: Removal efficiency of (a) BPA (b) 2-NP by combined DBD and supported carbon doped TiO_2 (JT7) and Ag loaded carbon doped TiO_2 nanocomposites (JT14). (Experimental conditions, BPA or 2-NP concentration 10 mg/L, discharge voltage 8 kV, air flow rate 3 mL/min, solution pH 3.0, electrode (silver), BPA or 2-NP volume 1.5 L, NaCl electrolyte concentration 50 g/L, mass of supported TiO_2 catalyst ~0.8g, mass of commercial TiO_2 (0.8 g)

Thus, apart from the shadowing effect of the powder catalyst, the pure anatase phase of synthesized TiO_2 may be responsible for the observed higher photocatalytic activity compared to the commercial powder TiO_2. Furthermore, the presence of carbon doping from the PAN precursor used during catalyst preparation may have slowed the electron hole recombination rate or have introduced more active sites on the supported TiO_2 photocatalyst, which in turn could be responsible for the enhanced photocatalytic activity. The substitution effect of carbon on the surface lattice layers of the supported TiO_2 may possibly play a role during the oxidation process of BPA or 2-NP in aqueous solution. This could be due to interaction of the carbon doped supported TiO_2 catalyst (JT7) with the UV light produced by the DBD, which increased the production of OH radicals and enhanced the removal efficiency. Apart from the formation of OH radicals, hydrogen peroxide can also decompose in the presence of ultra-violet light to give OH radicals as shown in equation 30.

$$H_2O_2 + hv \rightarrow 2OH^{\cdot} \quad (30)$$

The OH radicals and other reactive species reacted non-selectively to degrade the contaminants.

With the incorporation of Ag/carbon doped TiO_2 photocatalysts (JT14) into the DBD system, BPA or 2-NP removal efficiency at 80 min was 89.02% or 81% respectively. This shows that the incorporation of supported Ag doped TiO_2 photocatalysts (JT14), further enhanced BPA or 2-NP removal efficiency by 21.8% and 24.2% compared to DBD alone (see Figure 5.15 (a) and (b)).This further corroborates the initial hypothesis that incorporation of supported photocatalyst into the DBD reactor will improve the removal efficiency of BPA or 2-NP. The enhanced BPA or 2-NP removal efficiency by DBD/JT14 compared to DBD/JT7 may be explained as a result of several factors. These factors include the suppression of the electron-hole recombination rate by the Ag or carbon on the TiO_2 surface which could possibly be responsible for the enhanced removal efficiency. Secondly, the trapping of photo-induced electrons as a result of the Schottky barrier created by Ag nanoparticles could facilitate the transfer of electrons to oxygen molecules adsorbed on the surface of the TiO_2 layer and possibly generated more surface hydroxyl radicals, which enhanced BPA oxidation rate. Thirdly, the uniform deposition of Ag nanoparticles on the TiO_2 layer as revealed by HRTEM, allowed effective interaction and activation of the catalyst by UV-light, leading to generation of more hydroxyl radicals and improved removal rate.

The BPA or 2-NP removal efficiency at 80 min of 89.02% or 81% respectively obtained in the present study is greater than 50% diclofenac removal rate reported by Dobrin et al. (2013) with pulse corona discharge alone. This may be due to the nature of generation of free radicals; in this study free radicals were formed via continuous mode while in the study conducted by Dobrin et al. (2013) radicals were formed in a pulsed mode. Similarly, the obtained removal efficiency of BPA or 2-NP in this study is higher than 40% removal efficiency of 4-chlorobenzoic acid via DBD as reported by Lesage et al. (2013). On the contrary, the obtained BPA or 2-NP removal efficiency by the DBD alone was similar compared to 88.8% phenol removal efficiency revealed by Zhang et al. (2012) who utilised pulsed plasma discharge of discharge voltage 16 kV. The differences in the percentage removed could be linked to the type of DBD reactor and importantly the applied discharge voltage of 16 kV which was double that of the 8 kV used in this study.

The BPA or 2-NP removal efficiency obtained using combined DBD with 0.8 g commercial powder TiO_2 was lower than the removal rate obtained via the DBD alone. The decreased in the pollutant removal efficiency may be linked to the turbid nature of the solution caused by the powdery TiO_2, which inhibited the ultraviolet light penetration and reduced the amount of free reactive species. The highest BPA or 2-NP removal efficiency of 89.02% or 81% at 80 min was obtained with combined DBD/supported Ag/carbon doped TiO_2 photocatalysts in this study. The obtained removal rate especially for BPA by the combined DBD and stainless steel mesh supported 2.4% Ag/carbon doped TiO_2 photocatalysts was greater than 50% BPA removed by combined $UV/O_3/TiO_2$ system reported by Colombo et al. (2012). Unfortunately, data and results comparison are complicated due to different experimental conditions such as UV-light intensity, initial concentrations of BPA or 2-NP, reactor configuration, concentration of free reactive species, discharge voltage, solution pH amongst others. Thus, the differences in the removal efficiency could be linked to some of the aforementioned factors.

Besides the aforementioned, studies have shown that the free reactive species such as O_3 and H_2O_2 inhibited the electron-hole recombination rate on the TiO_2 surface and increased the concentration of OH radical (Tang et al., 2013). Therefore, the improved BPA or 2-NP removal rate may be attributed to the existence of a synergetic effect between the two system (DBD and supported Ag/carbon doped TiO_2 nanocomposites) which produced more OH radicals and other reactive species than the DBD alone. The increase in BPA or 2-NP removal efficiency via the combined approach used this study was greater than 5% increment observed for phenol removal with combined pulsed corona discharge/TiO_2 photocatalysis reported by (Wang et al., 2007). The possible reasons for the difference may be explained in terms of free radical production concept, where the combined system used by Wang et al. (2007) produced OH radicals and H_2O_2 only as compared to the combined system used in this study which produced OH radicals, O_3, and H_2O_2.

In spite of the incorporation of supported 2.4% Ag doped TiO_2 photocatalysts (JT14) to the DBD, 100% BPA or 2-NP removal efficiency was not achieved. Therefore, with the current combined DBD system, extension of reaction time may be needed, or increased input discharge voltage or perhaps re-configuration of the DBD reactor by using a closed system to prevent loss of ozone. The next section focusses on the stability and reusability of the supported Ag/carbon doped TiO_2 nanocomposites (JT14).

5.3.3 Leaching test on the catalyst support material

One of the shortcomings of powder TiO_2 nanoparticles is post-filtration or recovery of powder after treatment, this can however be remedied via the development of catalyst on a suitable support materials as was done in this study. However, the stability of the supported catalyst during the photocatalytic environment depends on the integrity of the substrates, in this case, the stainless steel mesh. Stainless steel mesh contains Fe, Cr, and Ni (Bassioni et al., 2015) and it is imperative to determine whether or not these toxic elements leach or are released into the solution on exposure to plasma discharge during the AOT degradation experiment. A control experiment was conducted using the DBD alone without including the TiO_2 photocatalyst supported on a stainless steel to determine the background value of these elements in the treated sample. ICP-OES was used to quantity the concentration of Ti, Cr, Fe, Ni and Ag that leached or released into the solution.

The results obtained using DBD alone without combining it with the supported photocatalyst is presented in Table 5.4. It can be seen from Table 5.4 that the amount of metallic elements in the DBD treated BPA solution was insignificant and in most cases below the detectable limit.

Table 5.4: Concentration of metallic elements in solution using DBD alone without supported photocatalyst

	Concentration of elements (ug/L)				
Time (min)	**Ti**	**Cr**	**Fe**	**Ni**	**Ag**
0	-0,0024	-0,0070	-0,0432	-0,0246	BDL
10	-0,0005	-0,0169	-0,0923	-0,0246	BDL
20	-0,0024	-0,0223	-0,0981	-0,0246	BDL
30	-0,0028	-0,0247	-0,1172	-0,0246	BDL
40	-0,0031	-0,0269	-0,1321	-0,0246	BDL
50	-0,0029	-0,0170	-0,1123	-0,0246	BDL
60	-0,0023	-0,0270	-0,1002	-0,0246	BDL
70	-0,0024	-0,0013	-0,0726	-0,0246	BDL
80	-0,0024	-0,0120	-0,0221	-0,0246	BDL
90	-0,0024	-0,0101	-0,013	-0,0246	BDL
100	-0,0024	-0,0199	-0,032	-0,0246	BDL
110	-0,0024	-0,0146	-0,033	-0,0246	BDL
120	-0,0024	-0,0137	-0,022	-0,0242	BDL

The amount of the metallic species leached into the solution as well as solution pH measured at respective time interval is presented in Figure 5.16. As shown in Figure 5.16, there was no leaching of any metallic species from the substrate within the first 40 minutes upon continuous exposure of the supported catalyst (JT14) to plasma discharge. The only noticeable effect was a slight decrease in solution pH which may be due to the formation of intermediate compounds. Non-leaching within this reaction time probably indicated strong adherence of the catalysts onto the support material. However, after 50 minutes, when the pH had reduced below 2, the leaching of Fe, Cr and Ni was evident and metal concentration differed appreciably in the solution. It is obvious that Fe leached from stainless steel at a much higher concentration followed by Cr and Ni with the least amount. The Ni released rate from the stainless steel mesh was between 0.001 and 0.16 µg/L. The concentration of Fe and Cr increased linearly from 0.2-0.7 µg/L and 0.22-0.5 µg/L at a lower pH value of 2.0. Comparing Table 5.3 and Figure 5.8, the concentration of Fe, Cr, Ni was higher in the combined DBD with supported JT14 than DBD alone. This means that the leaching of Fe, Cr, Ni really emanated from the stainless steel mesh and the metal release rate was dependent on the solution pH.

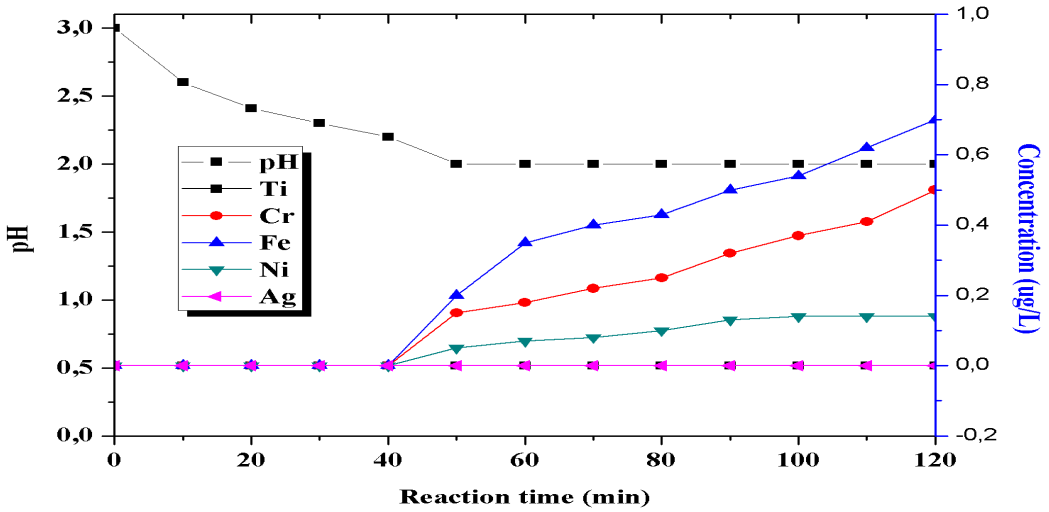

Figure 5-16: Concentration of elements and solution pH at different reaction time during oxidation of BPA or 2-NP by DBD/JT14 (Experimental conditions, same as Figure 5.13).

The leaching of Fe, Cr and possibly Ni into the solution may be linked to the acidic nature of the solution, owing to the formation of nitrous and nitric acid at low pH in water during the plasma discharge. These species form due to degradation of the pollutants or due to breakdown of the N_2 in the air feed to the DBD. It is important to mention that, only one side of the stainless steel mesh was covered with titania and silver layer while the other side was uncoated. It should be noted that there was no leaching of Ti and Ag during the oxidation process, and non-detection of Ti and Ag in solution suggested strong adhesion between the stainless steel mesh and the catalyst. Sometimes, non-detection of elements during analysis depends on the instrument detection limit, it may be that the concentration was too low for the instrument to detect. Since no leaching of Ag and Ti was observed from the coated side, it is possible to conclude that the leaching of Fe, Cr, and Ni emanated from the uncoated side of the mesh.

The leaching or release of Fe, Cr and Ni from the uncoated side of the substrate as a consequence of pH changes in the solution being treated during plasma discharge may be ascribed to the corrosive effect of the new formed mineral or organic acids on the stainless steel mesh. The leaching of Fe, Cr and Ni agrees with the findings of Lesage et al. (2013) who observed the leaching of Cu and Zn from a brass plate during oxidation of 4-chlorobenzoic acid by DBD. The authors attributed the leaching of the two metallic species to corrosion caused by the formation of NO_2^- through reaction of NO_3^- and H^+ in the solution. The presence of NOx and possibly NO_3^- increased the solution acidity level and caused corrosion and consequently leaching of toxic metallic species. According to Lesage et al. (2013), NO_x and NO_3- are radical scavengers, and inhibit or consume OH radicals, O_3 and H_2O_2, thus reduce the degradation efficiency of organic pollutants.

Bagheri et al. (2014) also attributed the leaching of metallic species to weak interaction between the support materials and the catalyst. The leaching of the metallic species as well as the formation of nitrate ion (NO_3^-), carbonate ion (CO_3^{2-}) in the solution thus interfered with the degradation and mineralisation efficiency. Studies have shown that the leached metallic species (Fe, Cr, Ni) sometimes compete with Ti^{4+} based on ionic radii differences and may reduce the performance of the catalyst, which in turn would decrease the degradation efficiency (Fernández et al., 1995). This might be part of the reason for not achieving complete removal BPA or 2-NP with DBD during the testing period despite the incorporation of the various supported photocatalysts in this study. To buttress this fact, Lesage et al. (2013) revealed the occurrence of a secondary reaction between the leached Cu, Zn from a brass plate and reactive species produced by DBD in solution.

The secondary reaction reduced the degradation efficiency from 64% in the absence of a brass plate containing Cu, Zn to 20% in the presence of Cu and Zn. The results confirmed that corrosion of a support material affected the process efficiency. The authors recommended reduction or complete removal of NOx species in the DBD system, since the nitrogenated species consumed the reactive species produced by the DBD. Furthermore, the leaching of Fe, Cr and Ni from the stainless steel mesh into the treated water may be lethal to human health. Although, the amount of Fe, Cr and Ni detected in the treated water was lower than 0.2 mg/L (Fe), 0.05 mg/L (Cr) and 0.02 mg/L (Ni) which are European Union permissible limits for drinking water. Nevertheless, long-term consumption of the treated water should be avoided, were these metals present.

5.3.4 Reusability of the supported Ag doped TiO_2 nanocomposites

One of the fundamental aspects of heterogeneous photocatalysis that cannot be ignored is the concept of reusability and stability of a synthesised catalyst. The stability and reusability of catalyst contribute considerably to the reduction of operational treatment cost. In this regard, the supported 2.4% Ag/carbon doped TiO_2 nanocomposites (JT14) which enhanced the removal efficiency of BPA or 2-NP by 21.8% and 23.2% with DBD reactor was re-used. The detailed experimental procedure on the removal efficiency of BPA or 2-NP using DBD with freshly prepared JT14 and the re-used JT14 was explained earlier. The residual concentration of BPA or 2-NP in aqueous solution was determined using HPLC techniques described in Table 5.1. The results of the reusability test of the DBD with supported Ag doped TiO_2 nanocomposites (JT14) are presented in Figure 5.17 (a) and (b) represent the removal efficiency of BPA or 2-NP by combined DBD with fresh or re-used supported Ag doped TiO_2 nanocomposites (JT14).

As shown in Figure 5.17 (a) and (b), the % removal of BPA or 2-NP at 20 min reaction time was 55% or 50% using combined DBD with the freshly prepared catalyst JT14. At 40 min, the % removal efficiency of BP or 2-NP increased to 72% and 69% respectively using combination of DBD and the freshly prepared JT14. This increase in the removal efficiency of both pollutants was consistent till 80 minutes and no significant increase was observed beyond 80 minutes.

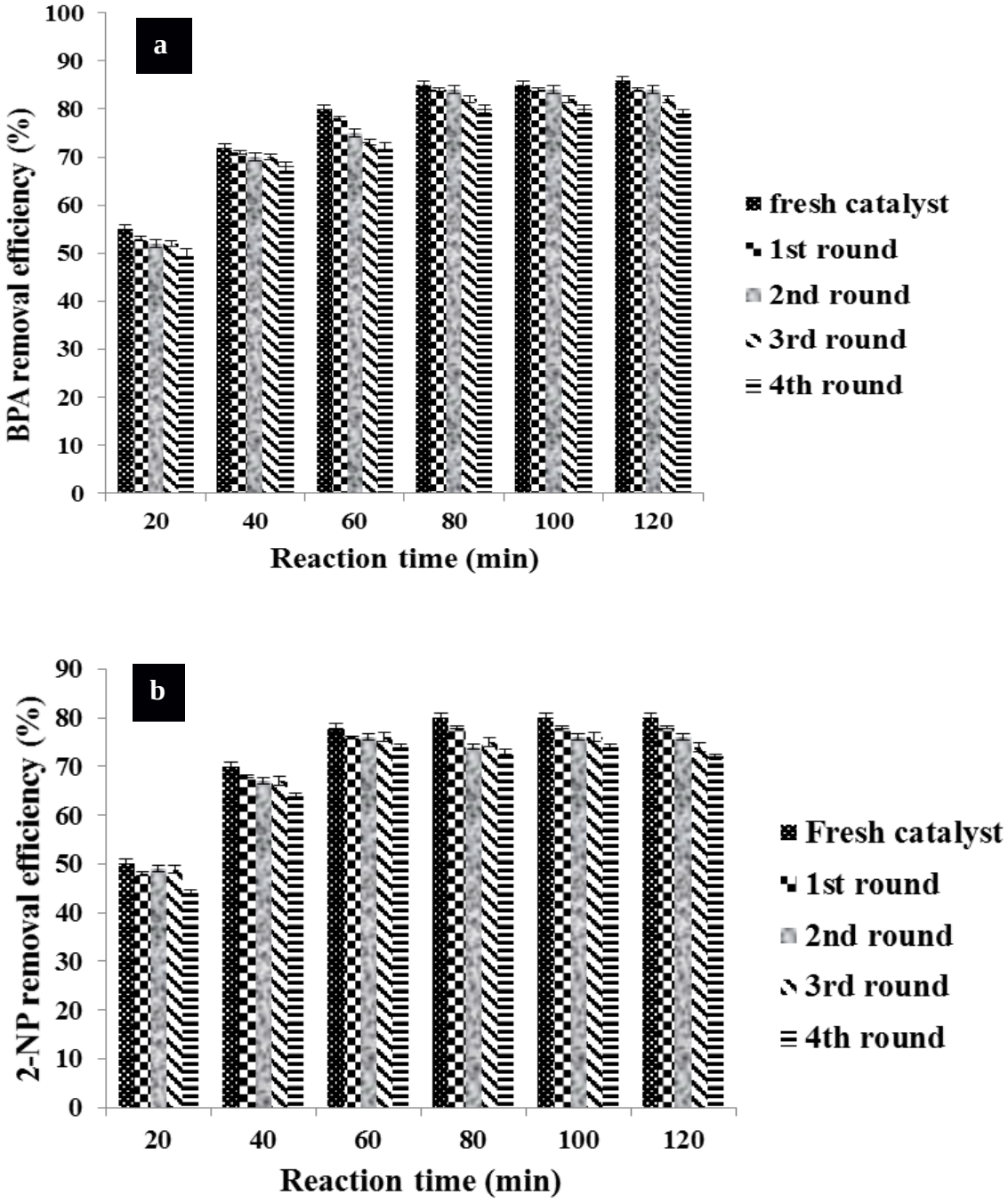

Figure 5-17: Removal efficiency of a) BPA and b) 2-NP using combined DBD with fresh and re-used supported Ag doped TiO_2 nanocomposites (JT14). (Experimental conditions, same as Figure 5.13)

When the catalyst JT14 was re-used for the first time with the DBD, the % removal of BPA or 2-NP at 20 minutes was 53% and 47% respectively, which suggested a slight decrease of 2-3% relative to the fresh catalyst. A similar trend was observed when the catalyst was re-used for the second and third times at each reaction time between 40-120 minutes. This showed that the freshly prepared and re-used supported Ag loaded carbon doped TiO_2 nanocomposites (JT14) exhibited similar or identical catalytic activity as regards the removal of BPA or 2-NP after three consecutive applications. This indicated that the re-used catalyst compared favourably with freshly prepared catalyst, since insignificant differences were observed in the BPA or 2-NP removal efficiency after three consecutive applications.

When the catalyst was re-used for the fourth time irrespective of the reaction time, % removal of BPA or 2-NP was somewhat reduced by less than 10% with respect to the freshly prepared catalyst. It is also obvious that BPA or 2-NP removal rate was rapid for the first 20 minutes and increased with treatment time. This suggested that the catalyst was still stable, not deactivated by the pollutants or intermediates and remained strongly adhered on to the stainless steel mesh. It further demonstrates that the supported Ag/carbon doped TiO_2 photocatalyst (JT14) was not affected by the discharge and as such the catalyst can be used for a long time. The slight decrease of less than 10% after four repeated applications suggested the catalyst to be reusable. The decreased removal efficiency after four repeated applications may be linked to accumulation of low molecular carboxylic acids or intermediate compounds on the TiO_2 surface resulting in partial blockage of the catalytic active sites.

Khan et al. (2013) reported similar stability and photocatalytic activity for both freshly prepared and recycled Ag/TiO_2 nanocomposites with MB removal. Similar findings were reported by Zhao and colleague (2014), in which the reduction of the degradation efficiency of phenol after three successful re-uses was attributed to the over accumulation of transformation products on the catalyst surface. Also, Álvarez et al. (2010) ascribed the loss of catalytic activity of the re-used catalyst to mass losses during separation and possibly leaching of support materials such as Fe from TiO_2/Fe_3O_4 nanocomposites. The next section showed the XRD and HRSEM results of the fresh and re-used catalysts.

5.3.5 Stability of the supported Ag doped TiO_2 nanocomposites after treatment

The stability of a photocatalytic material is considered an essential parameter from both practical and economical perspectives. Based on this, the stability of Ag doped TiO_2 nanocomposites after four repeated applications with plasma discharge for the degradation of BPA or 2-NP was examined using XRD and HRSEM. The detailed experimental procedure on the catalyst preparation and sample analysis has been described in Chapter 3. Figure 5.18 shows the XRD patterns of the original catalyst (JT14) before plasma discharge and after reuse for four times. As shown in Figure 5.18, the XRD pattern of the freshly prepared catalyst (JT14) matched well with the reused Ag doped TiO_2 nanocomposites after four successful applications. This shows that reused catalyst still maintained the same crystalline pure anatase polymorph as the freshly prepared catalyst.

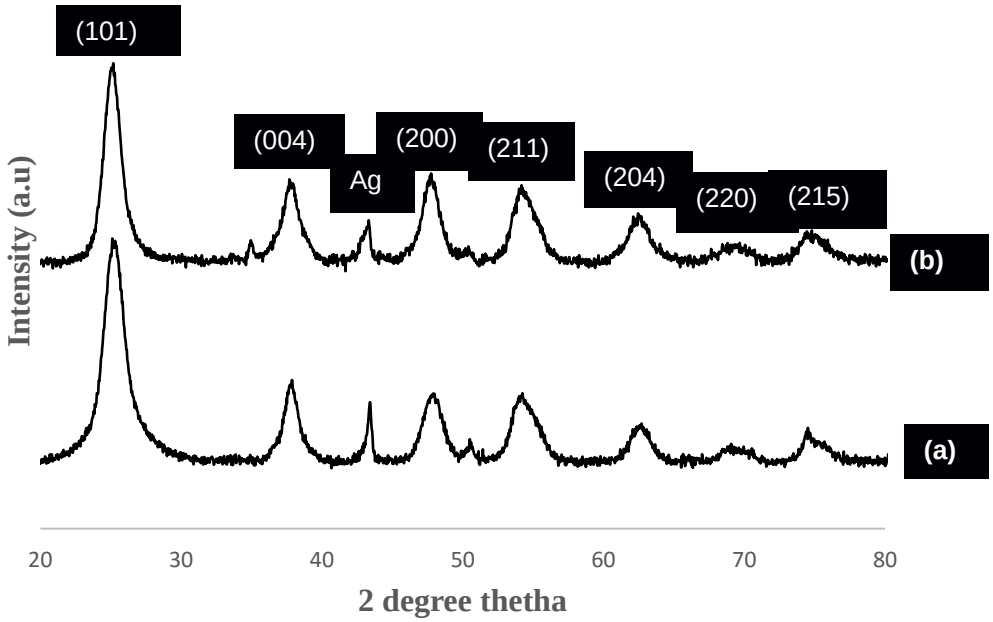

Figure 5-18: XRD patterns of: a) freshly prepared JT14 (b) JT14 after four repeated applications

There was no detection of additional peaks, except a slight decrease in the peak intensity of Ag in the re-used catalyst. This shows that the supported catalyst is photo-irradiation stable and not prone to photo-corrosion in spite of long term discharging. Khan et al. (2013) also reported similar observations with the reused Ag@TiO_2 nanocomposites after two consecutive applications. Furthermore, the HRSEM images of the fresh catalyst before discharge and reused supported catalyst after discharged is presented in Figure 5.19.

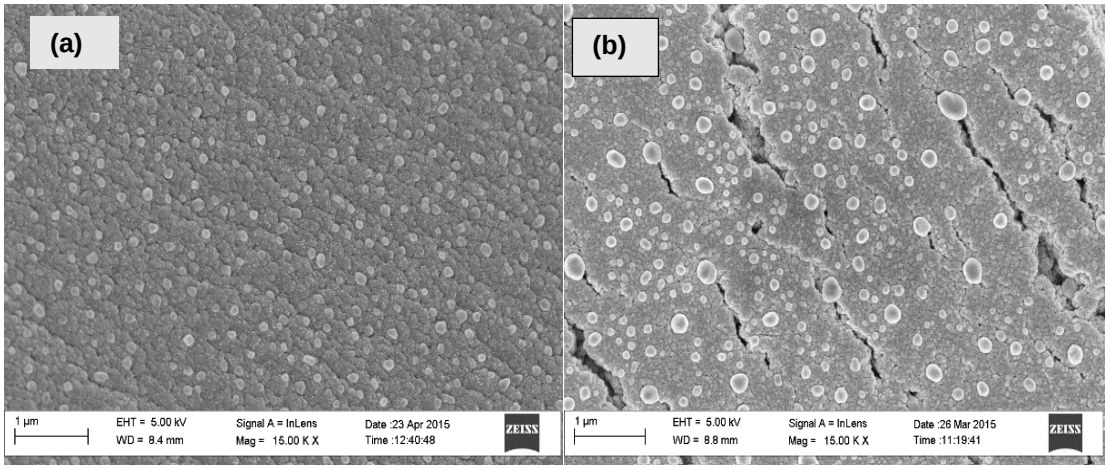

Figure 5-19: HRSEM images of Ag doped TiO_2 nanocomposites (JT14): (a) before plasma discharge (b) after four repeated applications

As shown in Figure 5.19, it is evident that the original particle morphology was still evident after four repeated discharge except for slight cracks or voids and a small amount of Ag sintering. This may be linked to the intense shock waves, exposure to UV light, and free radical attack or the discharge plasma which perhaps resulted in the occasional spark discharge between the DBD reactor and the immersed catalyst. Continuous exposure to plasma discharge often erodes the catalyst surface and created holes or cracks. Zhang et al. (2012) attributed the formation of holes on the catalyst surface during plasma discharge to intense shock waves caused by high-voltage discharge.

5.3.6 Mineralisation of BPA or 2-NP in aqueous solution by DBD and DBD with supported photocatalyst

In order to compare the effectiveness of DBD alone and DBD/supported photocatalyst on the degradation BPA or 2-NP, the mineralization rate was measured in terms of Total organic carbon (TOC) content. The TOC removal efficiency was evaluated using equation 31.

$$TOC\ removal(\%) = \frac{To - Tt}{To} \times 100 \qquad (31)$$

The results of TOC removal of BPA or 2-NP by DBD/supported photocatalysts (JT7 and JT14) is presented in Figure 5.20.

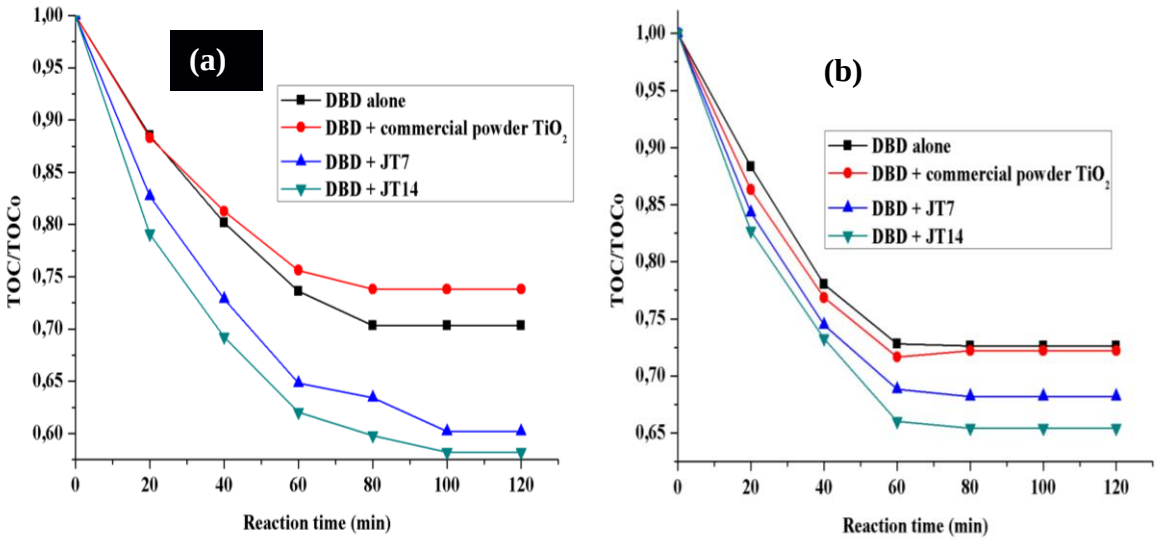

Figure 5-20: TOC removal of (a) BPA (b) 2-NP by DBD and DBD/supported photocatalyst: solution pH 3, discharge voltage 8 kV, concentration of BPA or 2-NP 10 ppm, powder TiO_2 dosage 0.8 g, supported catalyst dosage 0,8 g, solution volume 1.5 L

According to Figure 5.20, it can be seen that the TOC removal for BPA was 29.7% after 80 minutes treatment time with DBD alone and however increased to 39.8% and 41.8% when the DBD was integrated with either supported carbon doped TiO_2 nanocrystals (JT7) or 2.4% Ag loaded carbon doped TiO_2 nanocomposites (JT14) under the same conditions. Also, in Figure 5.18, the TOC removal rate of 2-NP by DBD alone was 27.4% at 80 minutes, and increased to 32.2% and 35.4% in the presence of supported carbon doped TiO_2 nanocrystals (JT7) or 2.4% Ag loaded carbon doped TiO_2 nanocomposites (JT14). It should be noted that there was no significance difference between the TOC values obtained with DBD alone and that of combined DBD with commercial powder TiO_2.

In fact, the TOC value with DBD alone was slightly higher than the latter. This was because the powdered TiO_2 particles hindered transmission of UV-light intensity produced by the DBD, thus reduced the amount of free radicals in solution and hence affected the pollutants mineralisation rate. The TOC value of the solution reduced with increasing treatment time in the presence or absence of a catalyst. The decrease in TOC value demonstrated partial decomposition and elimination of some of the dosed organic pollutants, but not their complete mineralisation. The higher residual TOC values compared to the obtained removal efficiency shown in the case where residual BPA or 2 NP was measured, shows that intermediate organic transformation products had formed during the degradation process which have not yet been directly identified or quantified.

It is difficult to compare the obtained TOC value in this study with the previous reported results in literature due to differences in the applied experimental conditions such as (pollutant initial concentration, applied discharge voltage, volume of the aqueous solution, concentration of the free reactive species, solution characteristics) amongst others, since most of these parameters obviously influence the pollutant mineralisation rate. Nevertheless, the obtained TOC value in this study is higher than 23% TOC removal rate of sulfadiazine by wetted-wall corona discharge reported by Rong and Sun (2013). The difference in the reported TOC value may be linked to the type of the reactive species. The DBD used in this study produced OH, O_3 and H_2O_2 while corona discharge reactor used by Rong and co-worker (2013) produced OH radicals alone. The differences in the TOC value may be based on the number of free reactive species generated by each system.

Furthermore, the 29.4% or 27.4% TOC removal rate of BPA or 2-NP by DBD alone reported in this study is lower than 48% TOC removal percentage of crystal violet by dielectric barrier discharge reactor reported by Manoj Kumar Reddy and Subrahmanyan (2012). The difference in the obtained TOC value may be attributed to the concentration of the pollutants used, discharge voltage, air flow rate. In fact, the discharge voltage and air flow rate of the DBD used by Manoj Kumar Reddy and colleague was 18 kV and 200 mL/min compared to 8 kV and 3 mL/min used in this study. Studies have shown that discharge voltage and air flow rate determine the yield of free radicals, which in turn determine the mineralisation rate. Thus, higher mineralisation reported by Manoj Kumar Reddy and co-worker (2012) may be linked to the impact of the aforementioned parameters. However, for the combined DBD/supported TiO_2 nanocrystals and DBD/supported 2.4% Ag doped TiO_2 nanocomposites, the TOC removal rate was 31.8% and 34.6% respectively. The reason for the increase of TOC removal rate by supported Ag doped titania nanocomposites over the undoped supported titania nanocrystals can be ascribed to the plasmonic silver.

5.3.7 Removal and degradation of organic pollutants by a combined dielectric barrier discharge system

This section chapter contains the results based on the degradation of bisphenol-A (BPA) and 2-nitrophenol (2-NP) by dielectric barrier discharge (DBD) system and combined DBD/JT14.

5.3.7.1 *Identification of intermediates or transformation products*

The identification of intermediate compound or oxidation by-products formed on exposure of organic pollutants to free radicals is somehow tricky and complex. The formation of these intermediates however depends on several operational factors such as pollutant concentration, oxidant dosage and reaction times. Besides, intermediate compounds are unstable and are present at a concentration below a limit detectable by analytical techniques. In this study, the higher concentration approach was adopted to identify the intermediate compounds and predict which of the reactive species was responsible for BPA degradation. Dielectric barrier discharge (DBD) alone and combined DBD/JT14 was utilized to decompose BPA or 2-NP in water, where the degradation experiment was monitored for 2 hr. The detailed experimental procedures and analytical detection techniques can be found in Section 5.2.8. The Agilent 6230 Time of Flight Liquid Chromatograph Mass Spectrometer (TOF LC-MS) in the negative ionization mode was used for qualitative identification of the intermediates at every 20 minutes. The intermediate compounds formed during the degradation of BPA or 2-NP via DBD, DBD/supported photocatalysts (JT14) are explained in the next section.

5.3.7.2 *BPA and BPA oxidation products*

Figure 5.21 (a) illustrates the mass spectra (MS) of BPA standard solution or starting material measured in the electrospray ionization (ESI) negative mode, which contained a sharp peak of deprotonated molecular ion [M-1]-, m/z at 227.10 within 6.5 min. This means that the original mass of BPA was 228.29 but was measured to be 227.10. The LC-UV spectra as shown in Figure 5.21 (b) indicated that BPA had a maximum absorption band at 278 nm. After the exposure of BPA to plasma discharge or radical environment (using either DBD alone or combined DBD/JT14 several other prominent peaks of different relative molecular masses (m/z) were noticed in the aliquot with retention time in the range of 1.9 min to 5.8 min (see Figure 5.22). The lower retention time indicates formation of more polar compounds than BPA. Although, retention times greater than 5.8 min were also noticed which suggested the formation of higher molecular weight species, which could result from secondary reactions among the oxidation by-products of BPA.

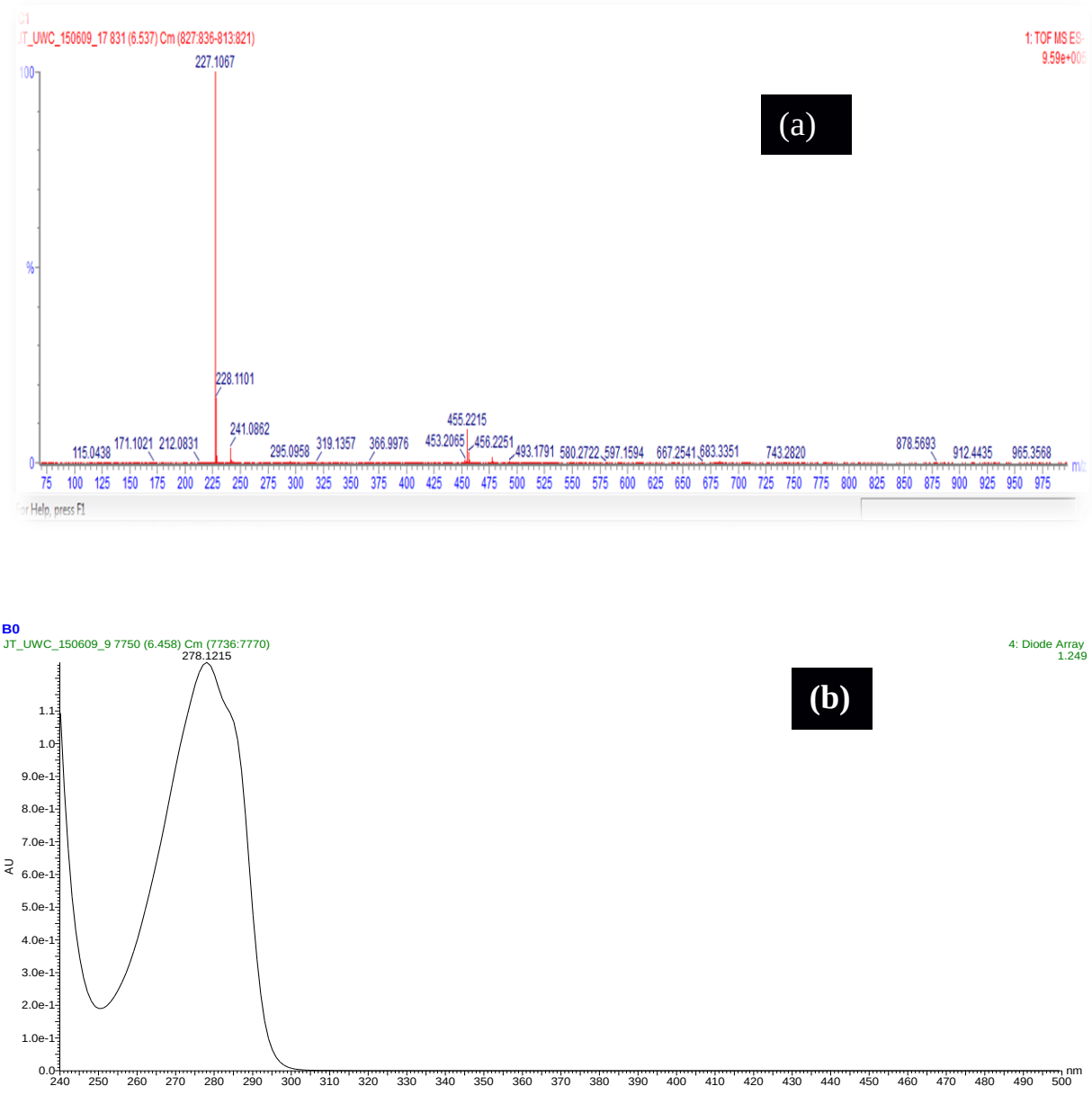

Figure 5-21: (a) LC-MS chromatograph and (b) LC-UV of standard BPA solution prior to oxidation process either by DBD alone or DBD/JT14 process.

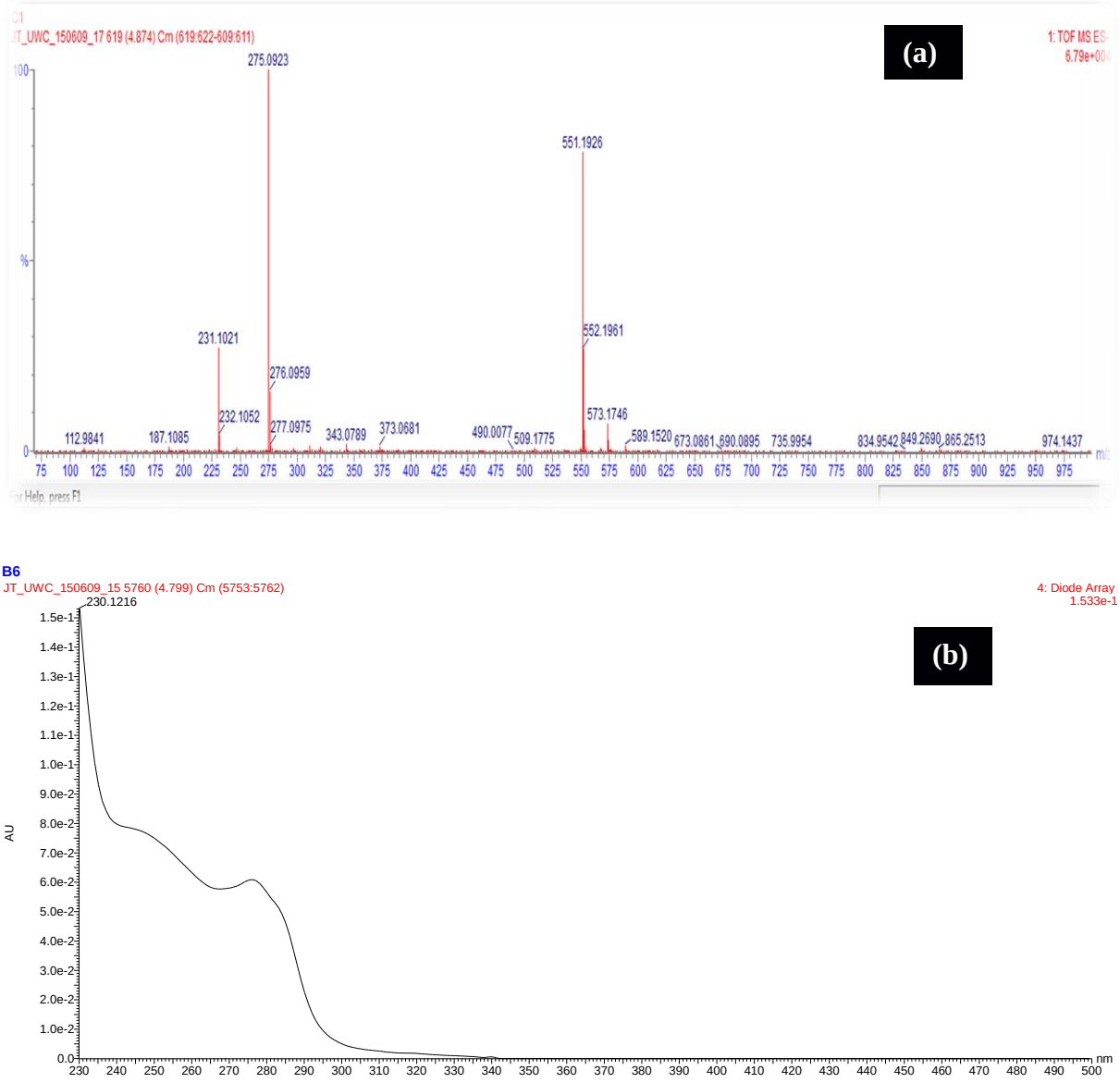

Figure 5-22: (a) LC-MS and (b) LC-UV chromatograph of the intermediates products formed via DBD alone within 20 minutes reaction time.

The LC-MS chromatograph revealed the mass fragmentation pattern (m/z) and relative abundance (%) of identified intermediate compounds via the three treatment approaches as shown in Table 5.5. All the intermediate compounds formed via the two processes are summarised with their proposed chemical structure in Table 5.5. The chemical structures were proposed using the MS library.

Table 5.5: Transformation products of BPA via the two treatment methods

Compounds	Molecular formula	Molecular mass (g/mol)	Theoretical mass [M-H]	Observed fragment ion at m/z value (% abundance)	Acquisition or retention time
Bisphenol-A	$C_{15}H_{16}O_2$	228.29	228.26	227.107 (100)	6.5
BP1	$C_{15}H_{16}0_5$	276. 28	276.24	275.09 (97.50)	4.8
BP2	$C_{14}H_{16}0_3$	232.28	232.24	231.10 (97.50)	4.6
BP3	$C_{30}H_{32}O_{10}$	552.55	552.46	551.19 (97.50)	9.9
BP4	$C_{13}H_{16}O$	188.23	188.26	187.10 (84.5)	4.5
BP5	$C_6H_5NO_3$	139.10	139.09	138.01 (45.62)	4.4
BP6	$C_{15}H_{16}O_3$	244.28	244.25	243.10(97.57)	5.8
BP7	$C_{15}H_{14}O_3$	242.27	242.23	241.89(66.5)	5.0
BP8	$C_{13}H_{14}O_5$	250.24	249.19	249.07 (94.07)	4.3
BP9	$C_{13}H_{14}O_3$	218.24	218.21	217.08 (57.80)	4.0
BP10	$C_{12}H_{14}O_3$	206.21	206.24	205.08 (66.7)	3.9
BP11	$C_9H_{10}NO_4$	196.11	196.18	195.9 (77.8)	3.2
BP12	$C_9H_7O_2$	147.11	147.15	146.9 (14.2)	2.5
BP13	$C_9H_{10}O_3$	166.06	166.14	165.01(82.7)	2.8
BP14	$C_6H_4NO_2$	122.10	123.09	121.02(52.3)	1.9

BP= by-product

Within the first 20 minutes using DBD alone, BPA oxidised to five by-products with main fragment (m/z) value of 275.09, 231.10, 187.10 and 551.19 and 112.98. However, the intermediates with mass fragment ion at m/z 112.98 could not be detected by MS possibly due to low concentration. The LC-MS and LC-UV spectra of the four intermediates are shown in Figure 5.22.

Comparing the LC-UV spectra of ordinary BPA shown in Figure 5.21 (a) with that of Figure 5.22 (b), it can be seen that the intensity of the earlier observed absorption band at 278 nm decreased significantly, which suggested transformation of BPA. Besides, there was an appearance of a weak absorption band in the range of 240-250 nm, and 280 nm which possibly confirmed the identified intermediates compounds. The retention time of three oxidation products shown in Table 6.1 was less than 4.9 min. This means the intermediates that originated from BPA were polar as polar oxidation-byproducts were found to elute faster from the non-polar (C_8) chromatographic column than BPA. The mass difference between 275.09 and fragment ion at m/z 231.10 was 44, which corresponded to the losses of CO_2. While the mass differences between 275.09 and 187.10 was 88, which indicated two consecutive losses of CO_2. The fourth intermediate compound with a higher molecular weight having a fragmentation pattern (m/z) at 551.19 was suspected to be a dimeric or an oligomeric compound. This was a result of secondary reactions between two molecules of 275.09. Based on the obtained fragmentation patterns as demonstrated in the MS spectra and available MS library, the following chemical structure were predicted for BP1, BP2, BP3 and BP4 : 275.09 ($C_{15}H_{16}O_5$), 231.10 ($C_{14}H_{16}O_3$), 187.10 ($C_{13}H_{16}OH$) and 551.19 ($C_{30}H_{30}O_{10}$) respectively using BPA ($C_{15}H_{16}O_2$) as a starting compound.

Furthermore, there was no difference in the range of intermediate compounds formed after 40 minutes using DBD alone (MS spectra not shown), which showed that the compounds were stable and resistant. With DBD alone, at 60 minutes, a new by-product (BP5) with mass fragment ion at m/z 138.01 was observed with other intermediates still in solution (Figure 5.23 (a)).

The LC-UV spectrum of the intermediates having maximum absorption band at 247 and 275 nm is shown in Figure 5.23 (b). The observed fragmentation pattern at m/z 138.01 indicated cleavage of the C-C bond of one of the two aromatic rings in BPA molecules into smaller moieties. The cleavage of one of the two aromatic rings suggested hydrogen abstraction from the methyl group (CH_3) by OH radicals. It should be noted that electron-donating species such as OH^o increase the electron-density of the aromatic rings and made the double bonds more susceptible to subsequent attacks. Based on the available MS library database, the chemical formula of BP5 with fragment ion at m/z 138.01 was predicted to be $C_6H_5NO_3$ (4-nitrophenol). It had earlier been pointed out that DBD produces nitrogenous species such as nitrous and nitrite oxide, which emanated from the feed dry air. The formation of a nitrogenous species suggested reaction of phenolic moieties with NOx in the solution. It should be mentioned that similar intermediate compounds observed in solution at 60 min were still the same as those found at 120 min. This suggested that the intermediates were persistent or resistant to further oxidation by the reactive species. The detailed degradation pathways or reaction mechanism are provided in Section 5.4.7.4.

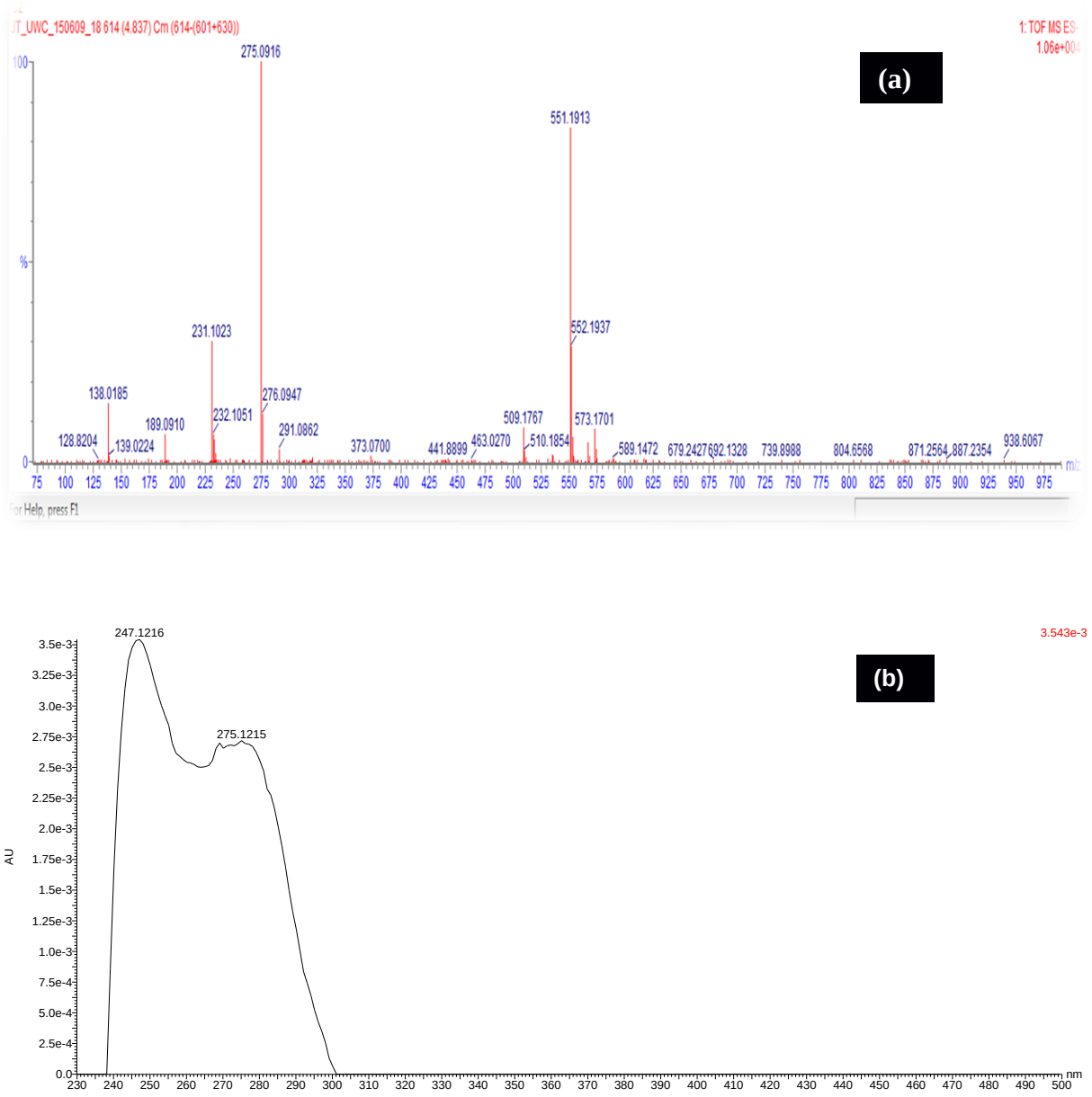

Figure 5-23: (a) LC-MS and (b) LC-UV chromatographs of the intermediates products formed via DBD alone at 60 minutes reaction time

5.3.7.3 *Intermediates compound obtained via DBD/JT14 process*

On the other hand, when combined DBD/JT14 was applied to decompose BPA, unlike what was obtained with DBD, only one intermediate compound was formed within the first 20 minutes. The obtained intermediate compound (BP6) with fragmentation pattern at (m/z) 243.10 is shown in Figure 5.24 (a). Comparing compound BP6 with the parent compound BPA ($C_{15}H_{16}O_2$), it was found that the compound (BP6) has one more additional oxygen which corresponds to an OH^o. Based on this, the chemical structure of BP6 is proposed to be $C_{15}H_{16}O_3$ (mono-hydroxylbisphenol-A) which strongly agreed with UV-spectra shown in Figure 5.24 (b).

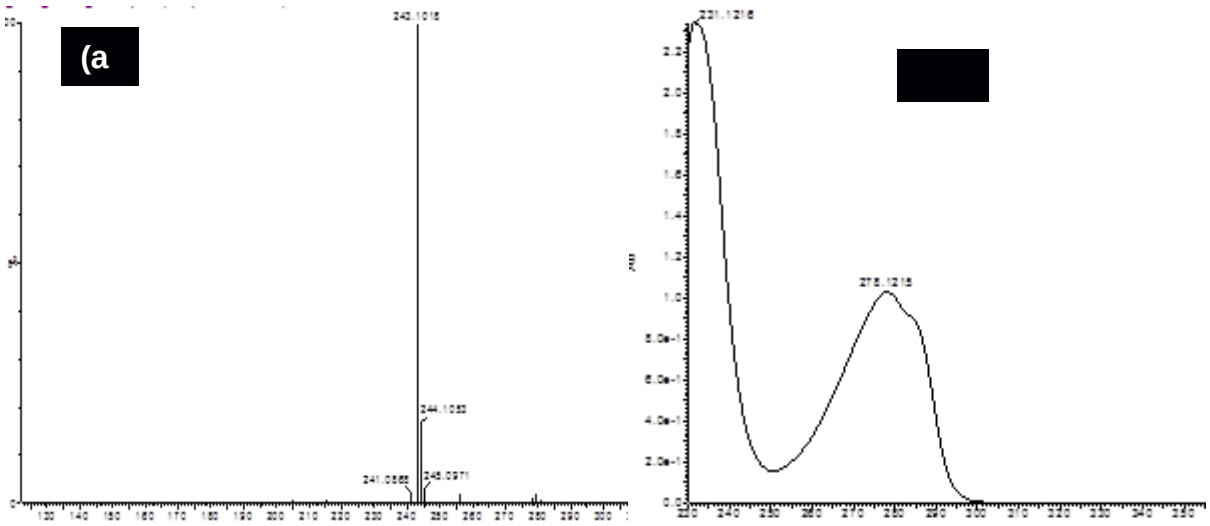

Figure 5-24: (a) LC-MS and (b) LC-UV chromatograph of the intermediates products formed via DBD/JT14 process within 20 minutes reaction time

At 40 minutes, the MS spectra revealed only one peak (not shown), with mass fragment pattern at m/z 241.89. This corresponded to the loss of hydrogen molecules due to oxidation when compared to 243.10. According to the fragmentation patterns, $C_{15}H_{14}O_3$ is proposed as the chemical formula of the BP7. At 60 minutes, three different deprotonated molecular ions were observed on the MS spectra at m/z value of 275.09, 231.10, and 138.01 as shown in Figure 5.25. This corresponds to BP1, BP2 and BP5 which had been previously observed with DBD alone.

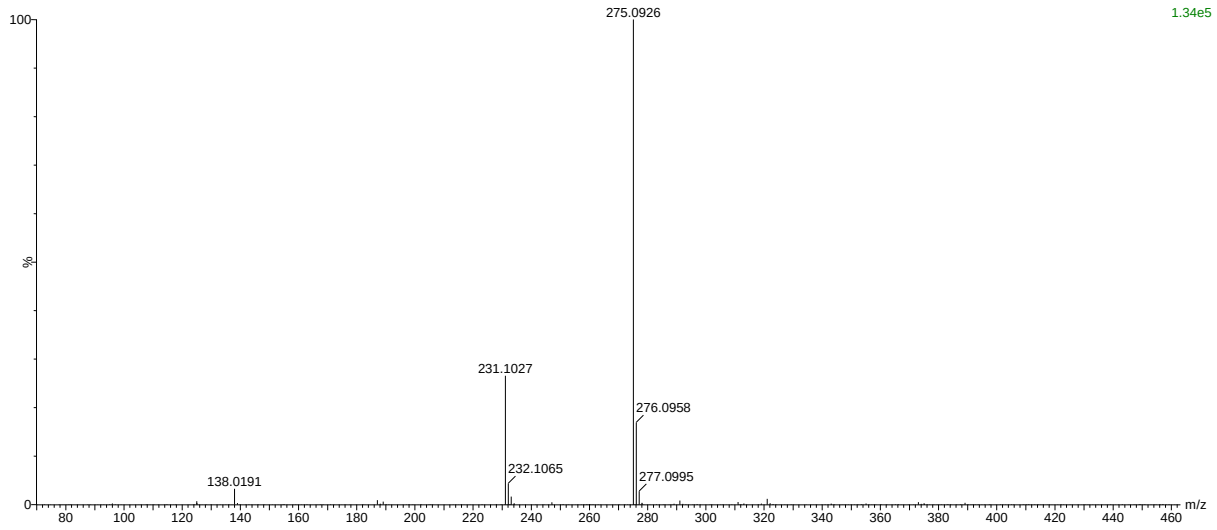

Figure 5-25: LC-MS of the intermediates products formed via DBD/JT14 process at 40 minutes reaction time

At 80 minutes, three fragmentation patterns at m/z 249.07, 217.06 and 205.08 labelled BP8, BP9 and BP10 were found on the MS spectra and the UV-spectra in Figure 5.26 (a) and (b) respectively.

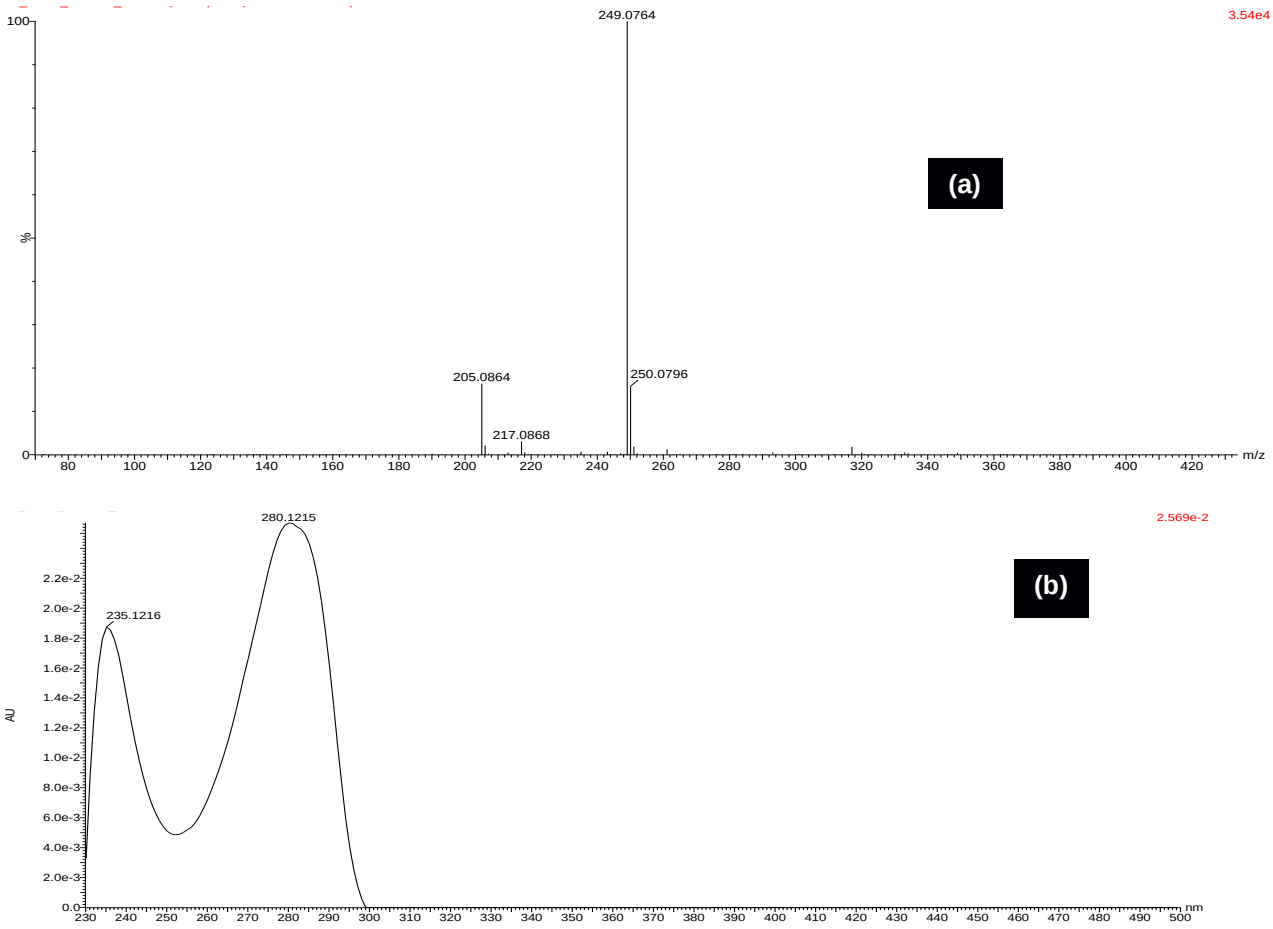

Figure 5-26: (a) LC-MS and (b) LC-UV chromatograph of the intermediates products formed via DBD/supported photocatalyst (JT14) within 80 minutes reaction time

The fragmentation pattern at m/z 249.07 corresponded to loss of the carbonyl group (CO) by a compound with m/z value of 275.09. While the elimination of carbon dioxide (CO_2) by an intermediate with fragmentation pattern at m/z 249.07 produced compound BP10 with m/z at 205.08. As regards the fragmentation patterns at m/z 217.06, the difference between this fragmentation pattern and 249.07 was 32, which corresponded to the loss of oxygen molecules. The following chemical formulas are proposed for BP8 ($C_{13}H_{14}O_5$), BP9 ($C_{13}H_{13}O_3$) and BP10 ($C_{12}H_{14}O_3$). At 120 minutes, with combined DBD/supported photocatalyst (JT14) system, only two mass fragmentation patterns at m/z 165.01 and 121.02 were noticeable as shown in Figure 5.27. The presence of low molecular weight compounds at 120 minutes for the two combined systems suggests the cleavage of the two aromatic rings into a smaller moiety. According to the MS library, the following molecular formulas are proposed: 165.01 ($C_9H_{10}O_3$) and 121.02 ($C_6H_5NO_2$).

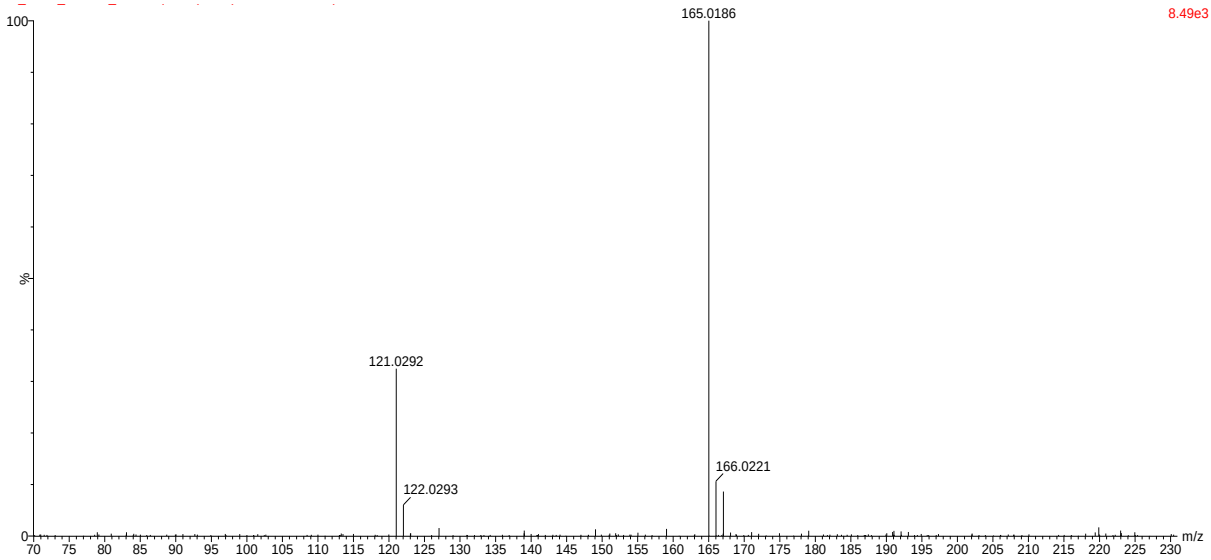

Figure 5-27: LC-MS chromatograph of the intermediates products formed by DBD/supported photocatalysts (JT14) within 120 minutes

As demonstrated in the time scheme experiment shown in Table 5.5, it is evident that the transformation products obtained via the two degradation systems were different. The differences in the number of intermediates also demonstrated that BPA followed different degradation routes or pathways. It should be noted that a higher number of stable and persistent intermediates were obtained via DBD alone, which suggests a high level of persistency or stability of intermediates and can be ascribed to the low concentration of free reactive species generated in the DBD system. On the contrary, similar but fewer intermediate compounds were detected in the combined systems (DBD/supported photocatalyst (JT14). The low number of intermediates in the combined systems compared to DBD alone suggested fast reaction kinetics between the BPA and the reactive species. Most of the persistent intermediates in the DBD system were successfully mineralised into a small fragment ions by the combined DBD/TiO_2 system. The next section focuses on the detailed degradation pathways or routes via the two degradation systems and also on the identification of the reactive species responsible for BPA degradation.

5.3.7.4 *Proposed degradation pathways for the obtained oxidation products from BPA degradation via DBD, DBD/JT14*

It is a well-known fact that DBD produces hydroxyl radicals, ozone, and hydrogen peroxide UV light among others, which reacted with BPA according to their oxidation potential values. Based on the obtained intermediates shown in Table 5.5, a route for the degradation of BPA to BP4 was proposed and illustrated below.

i. Formation of BP1-BP4

The degradation mechanism of BPA which resulted in the formation of BP1-BP4 within 20 minutes is shown in Figure 5.28. As earlier shown in Table 5.5, the number of oxygen increased to 5 when compared to the starting compound with two oxygen, which means three oxygens were added, thus suggesting that the step I in the oxidation of BPA by DBD was ozonation by an electrophilic substitution reaction. This indicates that BP1 ($C_{15}H_{16}O_5$) was formed by direct electrophilic substitution reaction of ozone with BPA to give an ozonide derivative.

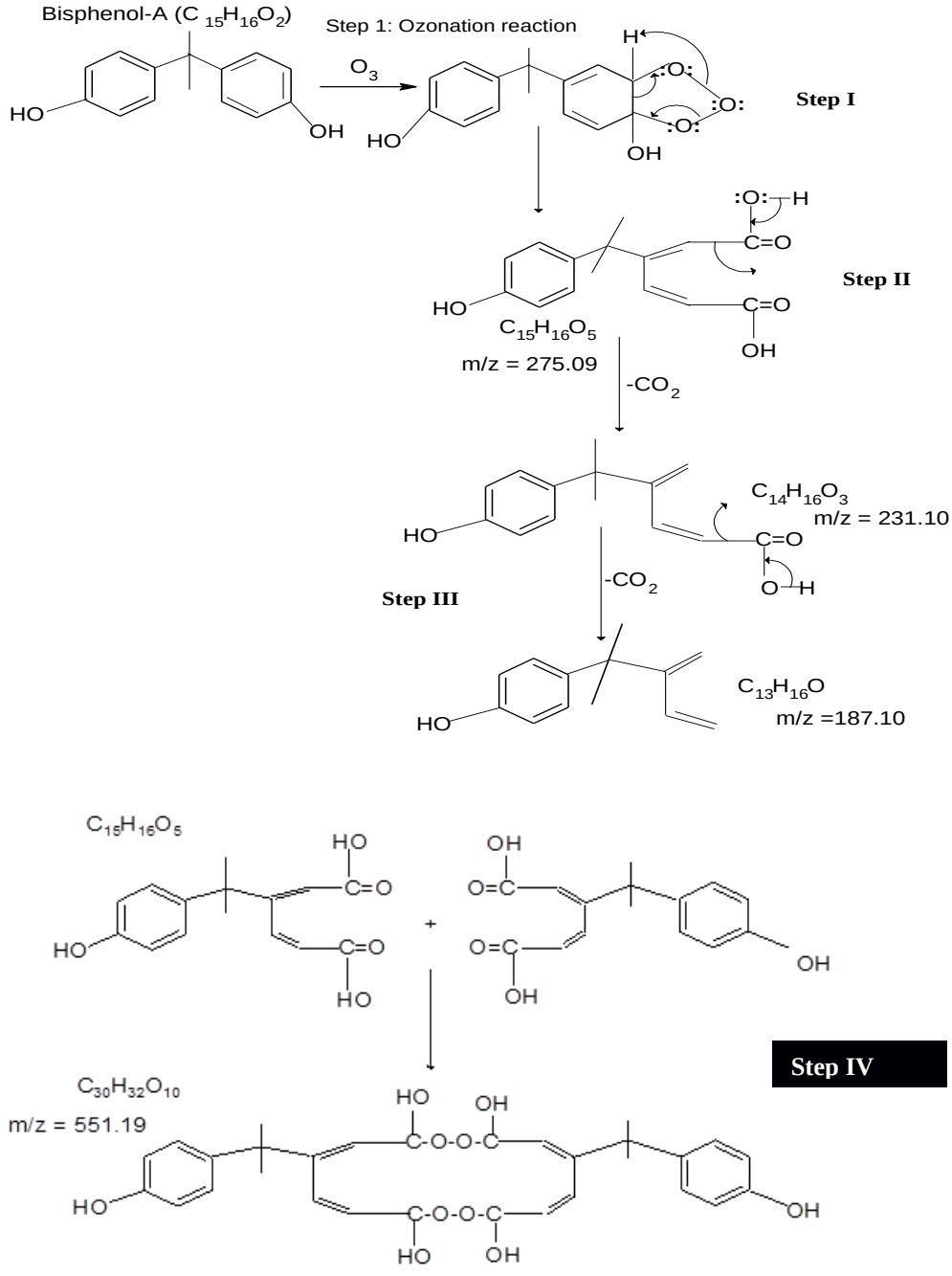

Figure 5-28: Proposed degradation pathways for the formation of BP1-BP4 from BPA using DBD alone.

The ozonide derivative further undergoes intramolecular rearrangement to yield BP1. Step II involved the loss of CO_2 by BP1 ($C_{15}H_{16}O_5$) to give BP2 ($C_{14}H_{16}O_3$), which otherwise is known as a decarboxylation reaction. The third oxidation by-product (BP3) was obtained directly via a double decarboxylation reaction on BP1 ($C_{15}H_{16}O_5$) (Step III). BP4 was a product of the dimerisation reaction involving two similar intermediate compounds. Since the m/z was 551.19 ($C_{30}H_{32}O_{10}$), it was possible to conclude that the step IV was the addition of two $C_{15}H_{16}O_5$. The proposed mechanism has demonstrated that oxidation of BPA proceeds via ozonation, decarboxylation, double decarboxylation and dimerisation reaction to produce recalcitrant intermediate compounds BP1-BP4. The formation of BP1-BP3 via ozonation and photocatalytic process has previously been reported in the literature with exception of BP4 (Colombo et al., 2012: Deborde et al., 2008; Tay et al., 2012).

ii. Formation of BP5-BP7

Furthermore, the proposed degradation pathways for compounds BP5-BP7 is shown in Figure 5.29. As shown in Figure 5.29, it is obvious that compound BP6 ($C_{15}H_{16}O_3$) was formed via two degradation routes: via a hydroxylation step or direct electrophilic substitution of ozone on the aromatic rings of BPA. This indicated that the two reactive species produced by the DBD were probably responsible for the formation of BP6. This corroborates previous studies where it was demonstrated that the mechanistic formation of BP6 proceeds through both hydroxylation and ozonation reactions (Tay et al., 2012). In the same vein, Cardoso da Silva et al. (2013) and Colombo et al. (2012) reported similar intermediate compound during the photodegradation and combined TiO_2/UV/O_3 treatment of BPA. The two authors established that BPA undergoes a hydroxylation reaction to produce the monohydroxylated compound ($C_{15}H_{16}O_3$). Deborde et al. (2008) also reported a similar molecular formula for BP6 during ozonation process of BPA. The oxidation of BP6 (which is removal of hydrogen) by either hydroxyl radicals or ozone produced BP7 ($C_{15}H_{14}O_3$). The attack by hydroxyl radicals on the methyl group (CH_3) in between the two aromatic rings resulted in hydrogen abstraction and C-C bond cleavage, which later produced the phenolic moiety and other residual intermediate compounds. Subsequently, the attack by the nitrogen oxides (NO_2 or NO) produced by DBD on the phenolic moiety, formed 4-nitrophenol as illustrated in Figure 5.29.

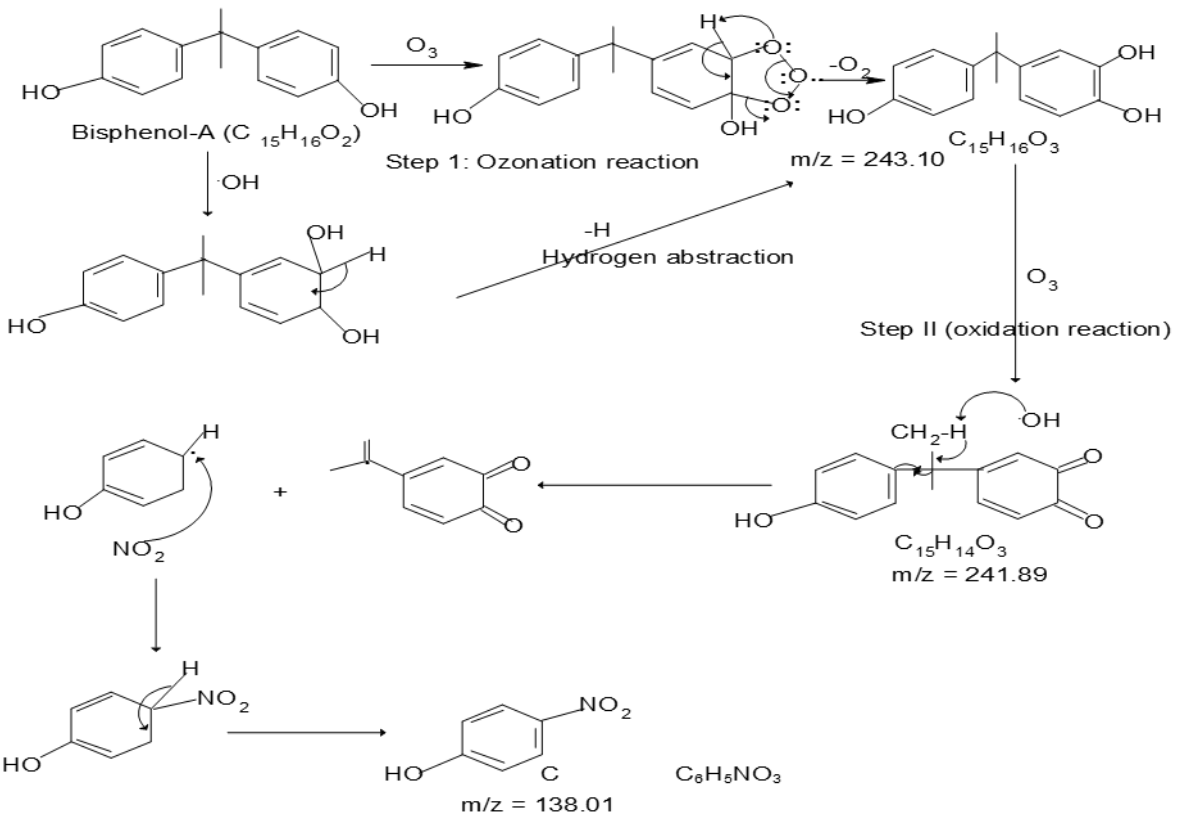

Figure 5-29: Proposed degradation pathways for the formation of BP5-BP7 from BPA using DBD alone and combined DBD/JT14 or DBD/photo-Fenton induced process.

iii. Formation of BP8-BP10

In addition, the degradation routes of BPA leading to the formation of BP8-BP10 are illustrated in Figure 5.30. The step by step attack of BPA molecules by hydroxyl radicals produced mono, bi and polyhydroxylated BPA. The polyhydroxylated BPA undergoes intramolecular rearrangement leading to C-C bond cleavage, loss of H_2 molecules thus forming BP1 ($C_{15}H_{16}O_5$). More so, oxidation of BP1 in the presence of O_3/OH radicals or perhaps H_2O_2 in solution produced BP8 with molecular formula ($C_{13}H_{14}O_5$). This reaction was accompanied with the loss of $C_2H_2O_3$ and atomic oxygen (O). Two consecutive CO_2 eliminations from BP1 and further oxidation in the presence of O_3/OHº yields compound BP9 ($C_{13}H_{14}O_3$). According to Deborde et al. (2008) compound BP9 was categorised as 3-formylacrylic acid derivative. While BP10 ($C_{12}H_{14}O_3$) was obtained from BP8 via CO_2 elimination as illustrated in Figure 5.30.

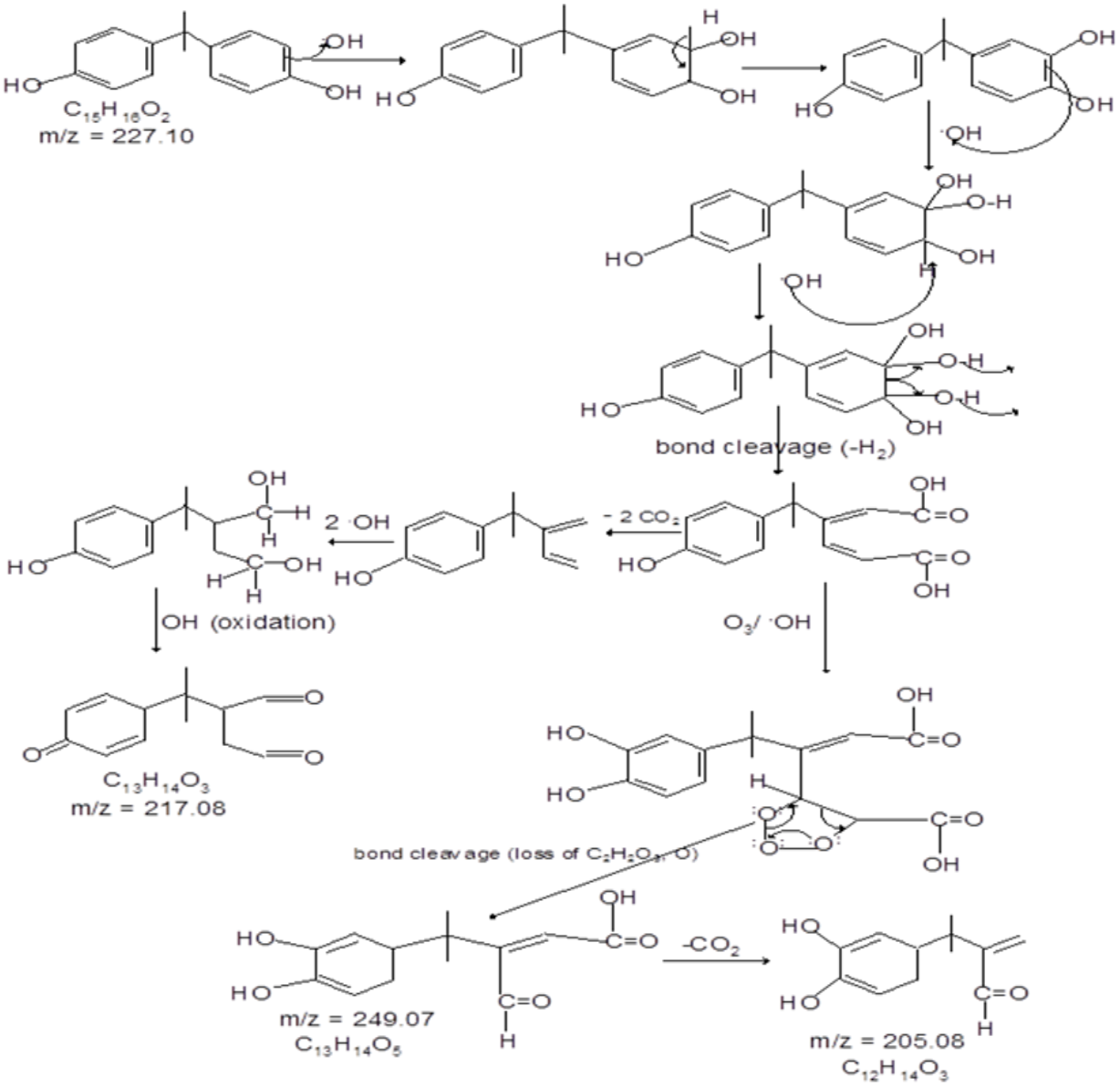

Figure 5-30: Proposed degradation pathways for the formation of BP8-BP10 from BPA using combined DBD with or without JT14

iv *Formation of BP11-BP14*

The formation of BP11-BP14 starting with BP6 is presented in Figure 5.31. As shown in Figure 5.31, the initial hydroxylation of BP6 by hydroxyl radicals or direct attack by OH on the methyl group (CH_3) in between the two aromatic rings, resulted in hydrogen abstraction and subsequently ring cleavage leading to formation of smaller fragments (4-isopropenylcatechol and phenolic ion). The substitution on 4-isopropenylcatechol by one of the nitrogenous species (NO_2) yielded compound BP11 with molecular formula ($C_9H_{11}NO_4$). Likewise, the substitution of nitrous oxide (NO) on the phenolic ion liberated compound BP14 with chemical structure

$C_6H_4NO_2$ (4-nitrosophenolate). The presence of nitrogenous oxide as part of the oxidation-products was a result of dry air used to generate ozone in the DBD system as nitrogen is a component of air. Also, oxidation of 4-isopropenylcatechol involving loss of hydrogen in the presence of $O_3/OH^o/H_2O_2$ produced compound BP12 ($C_9H_8O_2$). Further hydroxylation of BP12 by hydroxyl on the methylene group (CH_2) formed compound BP13 with molecular formula $C_9H_{10}O_3$.

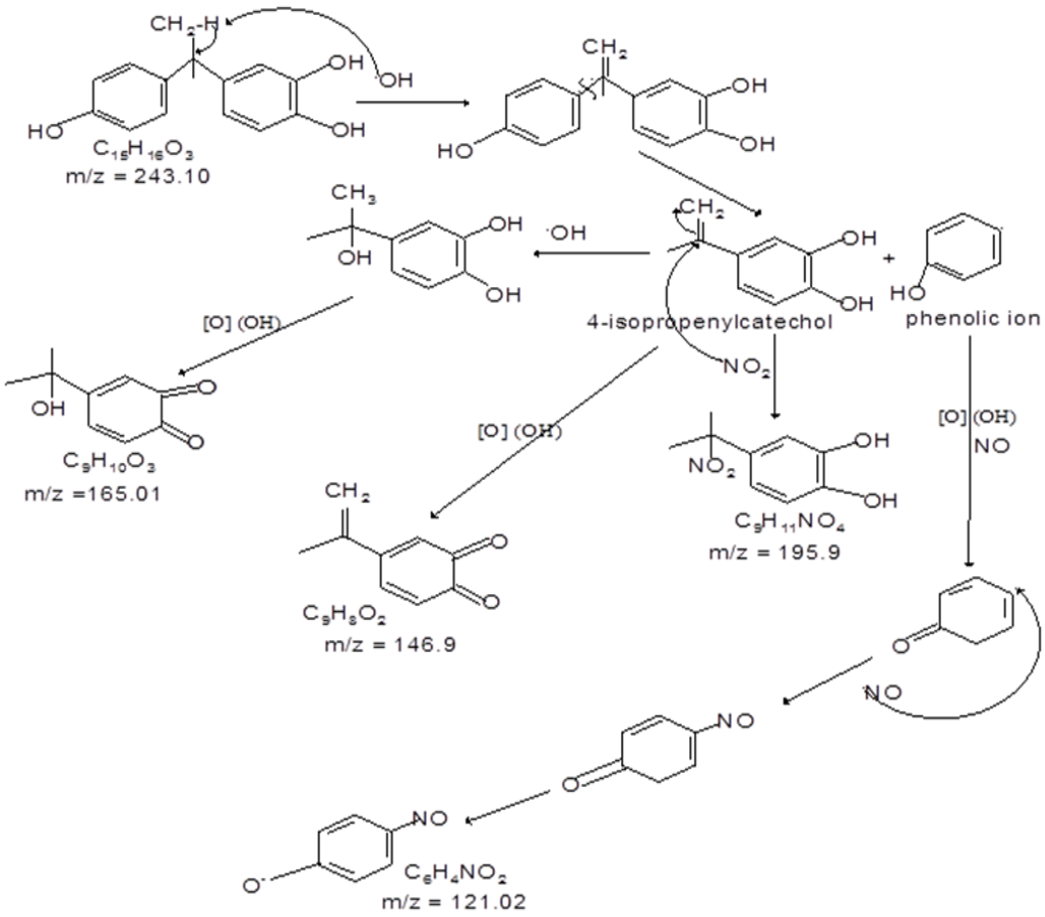

Figure 5-31: Proposed degradation pathways for the formation of BP11-BP14 from BPA using combined DBD with or without supported catalyst

Fourteen major transformation products including oligomeric compounds were identified during BPA oxidation by single and combined advanced oxidation technologies. The following intermediates: BP1-BP4, BP6-BP7 have been extensively reported in the literature (Cardoso da Silva et al., 2014; Colombo et al., 2012; Deborde et al., 2008; Tay et al., 2012). While BP5, BP8, BP9-BP14 have not been reported in the literature. The differences in the intermediates proposed in this study compared to other studies may be attributed to the applied oxidation process and perhaps the types of free reactive species produced by the DBD system. The DBD produced O_3, H_2O_2, OH^o, where air containing nitrogen was used as a source of ozone generation.

Studies conducted by Tay et al. (2012) and Deborde et al. (2008) used the ozonation process alone, Colombo et al. (2012) combined TiO_2/UV/O_3 while Cardoso da Silva et al. (2014) utilized powder commercial TiO_2 with UV to decompose BPA. It is clear from the previous studies that different advanced oxidation processes produce different free radicals and definitely result in different intermediate compounds. Critical analysis of the intermediates showed that BPA decomposed via ozonation step in the DBD while most intermediates in the combined system were proposed via hydroxylation and nitration steps respectively. In all, the degradation of BPA followed different steps: ozonation, hydroxylation, decarboxylation, and dimerisation, double decarboxylation and nitration reaction. It is important to mention that unlike DBD alone, no dimeric or high molecular weight compounds were formed as intermediates in the combined systems. This is in accordance with the results reported by Wang et al. (2007) where there was no formation of oligomeric compounds during the degradation of phenol by combined pulsed plasma discharge and TiO_2 photocatalyst.

Additionally, most of the intermediates obtained with the combined system were of lower molecular mass compared to high molecular weight intermediates obtained with DBD alone. This further demonstrated that the incorporation of the supported photocatalyst with DBD enhanced the mineralisation of BPA much more than with DBD alone. Complete mineralisation of BPA into CO_2 and H_2O was not achieved via the two approaches, which may be attributed to the DBD reactor type and conditions applied.

5.3.7.5 *The obtained intermediates from 2-NP degradation via DBD and DBD/JT14 system*

In this study, the different intermediates of 2-NP obtained via the two treatment processes (DBD alone, or DBD/JT14 were qualitatively analysed by LC-MS TOF Agilent. The detailed experimental procedure and analytical techniques can be found in Chapter three respectively. The LC-MS and LC-UV spectra of the standard 2-nitrophenol solution recorded in the electrospray ionization (ESI) negative mode, revealed a deprotonated molecular ion $[M-1]^-$, m/z at 138.1087 within 5.7 min (Figure 5.32 (a)). This indicates that the original mass of 2-NP was 139.11 but was measured to be 138.1087, indicating loss of a proton (H). The UV spectra of 2-NP shown in Figure 5.32 (b) revealed a slight, sharp and broad absorption band at 232, 276 and 349 nm respectively. Table 5.6 also contains the mass fragmentation pattern (m/z), relative abundance (%) and proposed chemical structure of the identified organic intermediates. The chemical structure of the identified compounds are proposed and compared with the LC-MS library databases.

As shown in Table 5.6, nine different transformation products mostly nitrogenous compounds were obtained via the three degradation systems namely: OBP1 ($C_6H_5NO_4$, 2-nitroresorcinol), OBP2 ($C_6H_5NO_5$, 2-nitrobenzene-1,3,5-triol), OBP3 ($C_6H_2NO_5$, 2-nitro-1,3,5-benzenetriolate), OBP4 ($C_6H_4O_4$, 2,5-dihydroxyl-1,4-benzoquinone), OBP5 ($C_6H_4N_2O_5$, 2,4-dinitrophenol), OBP6 ($C_6H_3NO_4$, 2-nitro-1,4-benzoquinone) OBP7 ($C_6H_5O_3$, 3,5-dihydroxylphenolate), OBP8 ($C_6H_6O_2$, hydroquinone), OBP9 (C_6H_5OH, phenol). The retention time of all the by-products shown in Table 5.6 were less than that of 2-NP, which suggests that most of the intermediates were more polar than the 2-NP.

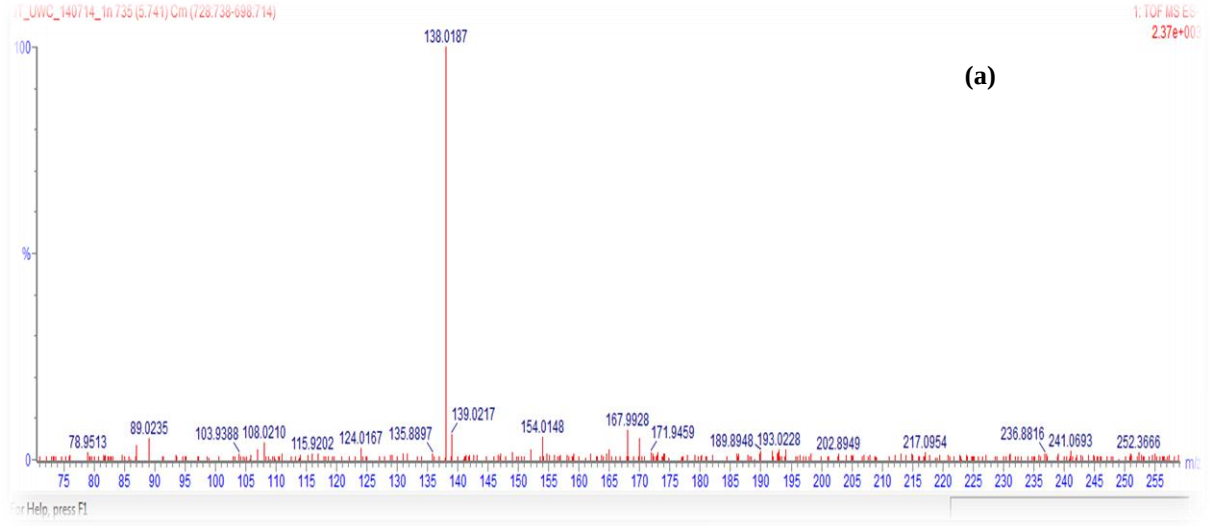

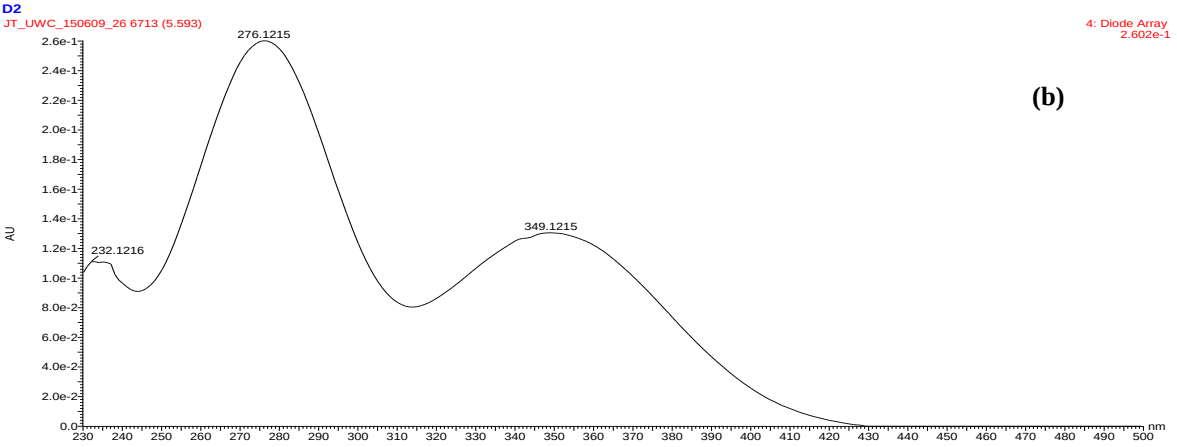

Figure 5-32: (a) LC-MS (b) LC-UV spectra of standard 2-nitrophenol solution prior to degradation experiment

Table 5.6: Transformation products of 2-NP via the three treatment methods

Compounds	Molecular formula	Molecular mass (g/mol)	Theoretical mass [M-H]	Observed fragment ion at m/z value (% abundance)	Acquisition or retention time
2-nitrophenol	$C_6H_5NO_3$	139.11	139.08	138.02 (99.89)	5.7
OBP1	$C_6H_5NO_4$	155.10	155.08	154.01 (100.0)	4.4
OBP2	$C_6H_5NO_5$	171.11	171.04	170.00(100.0)	3.4
OBP3	$C_6H_2NO_5$	168.08	168.05	167.99(98.64)	3.2
OBP4	$C_6H_4O_4$	140.1	140.06	140.00(100.0)	2.9
OBP5	$C_6H_4N_2O_5$	184.11	184.07	183.00(99.99)	5.5
OBP6	$C_6H_3NO_4$	153.09	153.07	152.99 (97.50)	4.2
OBP7	$C_6H_6O_2$	110.11	110.09	110.01(96.07)	1.5
OBP8	$C_6H_5O_3$	125.10	125.08	124.01 (97.30)	4.5
OBP9	C_6H_5OH	94.11	94.09	92.05(66.5)	1.0

OBP= Oxidation by-product

It is evident that the intermediate compounds formed either via the DBD or DBD with JT14 were similar except at 80 minutes. During the oxidation experiments, some of the intermediates disappeared completely while some remained stable and resistant to further degradation. It is also noteworthy mentioning that, $C_6H_4O_3$ and C_6H_5OH were not detected in the DBD alone but were identified with the combined system. Hydroquinone ($C_6H_6O_2$) remained the most persistent among all the intermediates irrespective of the treatment process. This is consistent with the findings of Zhang et al. (2003) who had earlier recognised hydroquinone as one of the most predominant and stable intermediates during the oxidation of p-nitrophenol by UV/H_2O_2. It is important to mention that hydroquinone is unstable and readily oxidised to benzoquinone by the hydroxyl radical. Although, benzoquinone was not detected in this study nevertheless hydroquinone undergoes complete oxidation to form OBP8.

According to Table 5.6, similar intermediate compounds were formed via the two applied processes at 20 minutes. This indicates the possibility of 2-NP being attacked by the same free reactive species. As a matter of fact, 2-NP disappeared completely within 20 minutes and transformed into a compound with a fragment ion at m/z 154.01 shown in Figure 5.33 (a). No other peaks were detected by mass spectrometry. Very importantly,

the mass difference between 154.01 and 138.01 was 16, which showed that the decomposition of 2-NP was initiated by OH radicals. Thus, the first step during the oxidation process of 2-NP either by the DBD or the combined system was hydroxylation (OH radicals) and not both hydroxylation and ozonation observed with BPA. This observation corroborated previous investigations where researchers have demonstrated hydroxylation reaction as the first step during the degradation process of nitrophenols via advanced oxidation technologies (Quiroz et al., 2014; Wei et al., 2011). Based on the available MS library, the chemical structure of the compound is proposed to be 2-nitroresorcinol ($C_6H_5NO_4$,), which agreed with the UV-spectrum shown in Figure 5.33 (b).

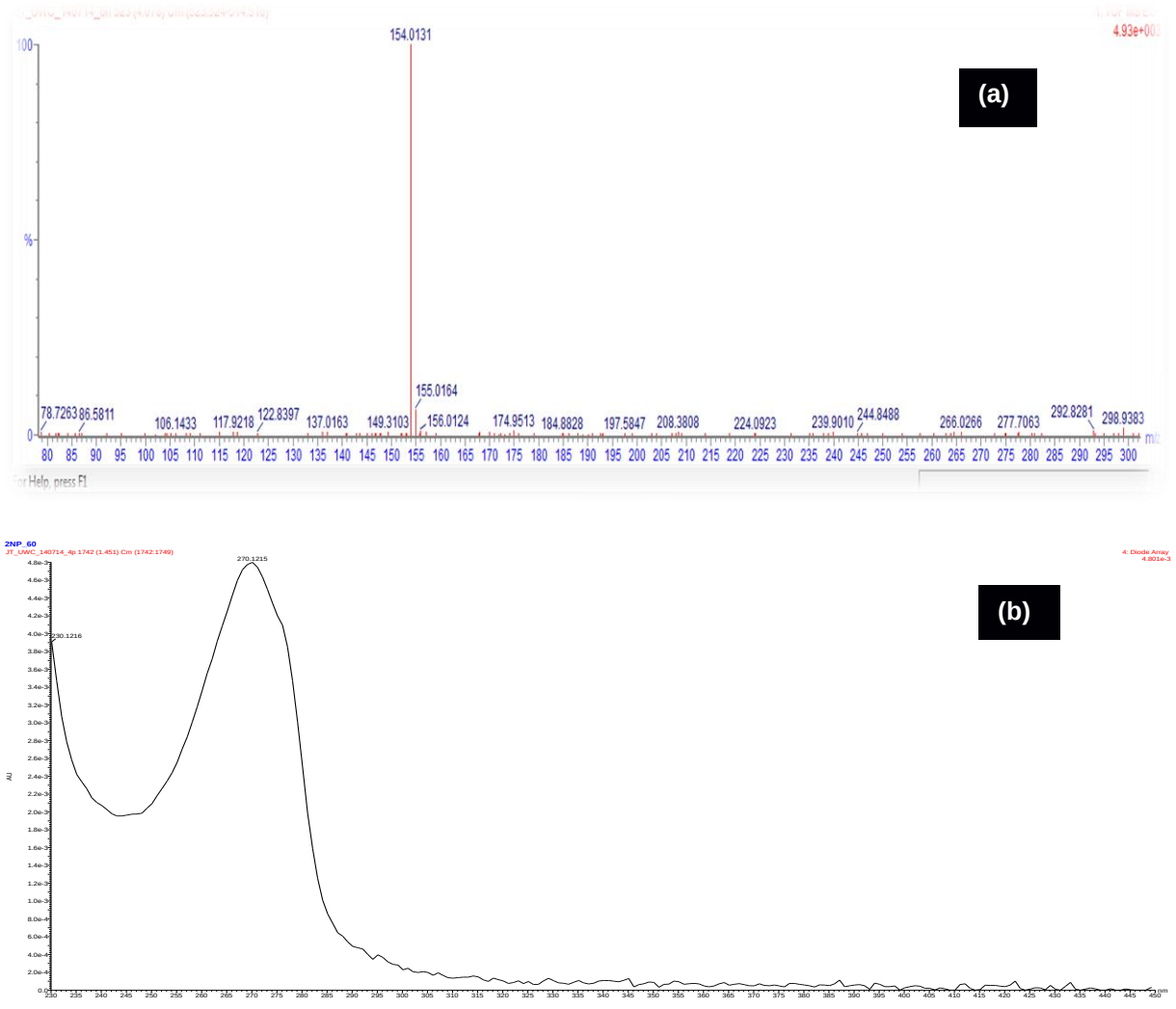

Figure 5-33: (a) LC-MS and (b) LC-UV chromatograph of the intermediates products formed via DBD, DBD/supported photocatalyst within 20 minutes reaction time

Formation of 2-nitrobenzene-1,3,5-triol ($C_6H_5NO_5$), 2-nitro-1,3,5-benzenetriolate ($C_6H_2NO_5$) and 2,5-dihydroxyl-1,4-benzoquinone ($C_6H_4O_4$)

Figures 5.34 (a) and (b) represent the LC-MS and LC-UV chromatograph of the intermediates obtained via DBD alone after 40 minutes. There was a disappearance of the peak observed at 20 minutes and formation of four additional new peaks with the following mass fragment ions at m/z (170.00, 167.99, 151.99 and 140.00). The deprotonated molecular ion at 170.00 corresponded to addition of OH radical to the earlier identified OBP1 having m/z (154.01). This implies a repetitive attacked of the hydroxyl radical on OBP1. The chemical formula $C_6H_5NO_5$ is proposed for OBP2 based on the MS library. Further oxidation of OBP2 vis-a-viz removal of hydrogen certainly resulted in a compound with fragmentation pattern at m/z 167.99. The chemical structure of OBP3 is proposed to be ($C_6H_2NO_5$, 2-nitro-1,3,5-benzenetriolate).

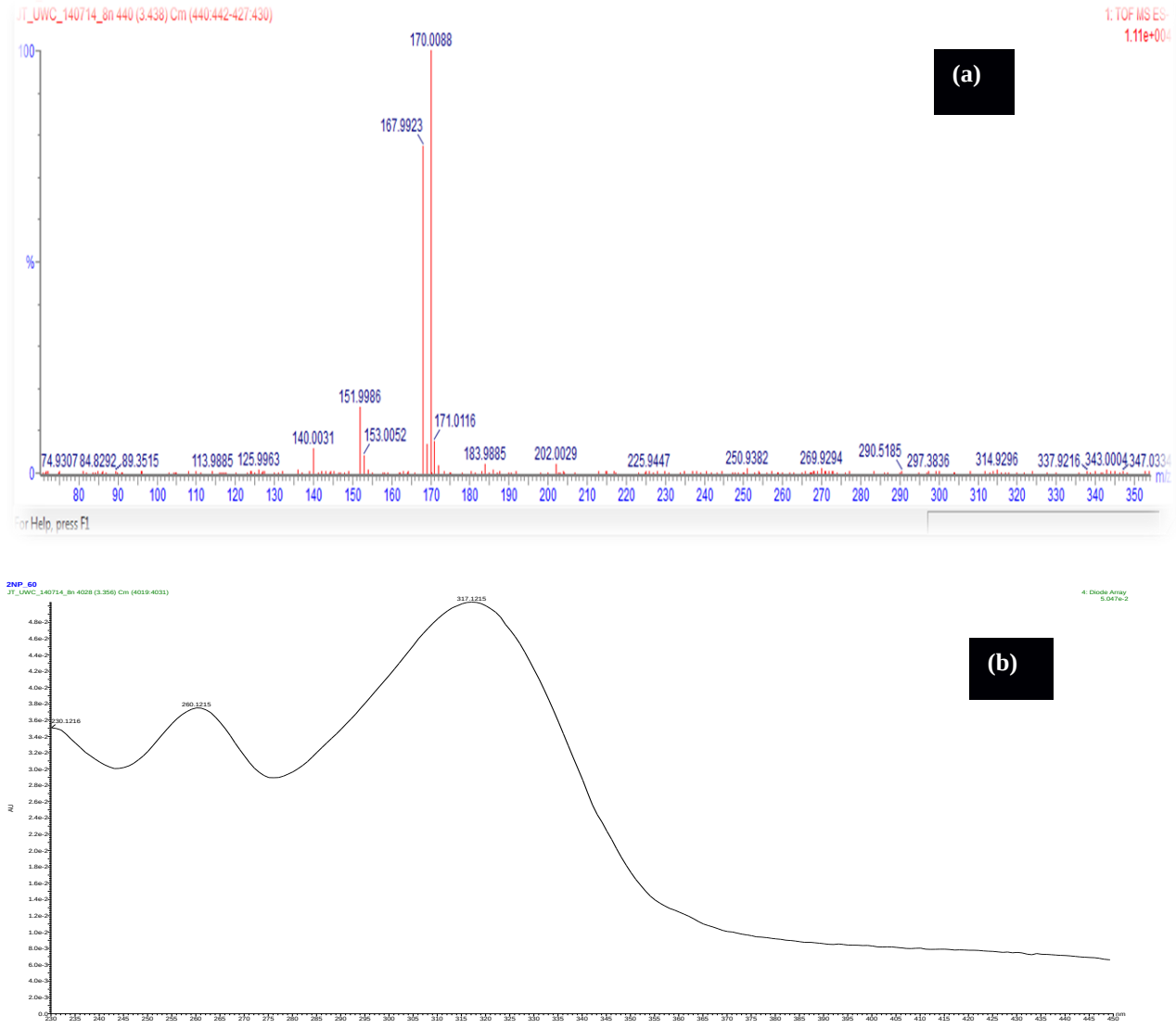

Figure 5-34: (a) LC-MS and (b) LC-UV chromatograph of the intermediates products formed via DBD after 40 minutes reaction time

The fragmentation spectrum at m/z 140.00 corresponded to the elimination of an electron withdrawing group (NO_2) from OBP2 by direct attack by the highly electrophilic OH^o. This was followed by the electrophilic substitution or replacement of a NO_2 group by the OH^o, which showed NO_2 as a good leaving group. The chemistry of the formation of OBP4 basically involved the attack of OH at the ortho position of the benzene ring. It is important to mention that the electrophilic OH radical with high redox potential attacked a carbon atom with the highest electron density within the benzene ring forcing the NO_2 to leave. The presence of both OH and NO_2 groups in 2-NP created a strong electron density on the carbon atom in the para- and ortho-position relative to the OH group. OH group as an electron-donating substituent is known to be an *ortho* (o) and *para* (p) director while NO_2 (electron-withdrawing group) is equally referred to as *meta* (m) director.

Therefore, the OH radical increases the electron density at these two positions in the benzene rings, and because of the ortho/para directory effect, the subsequent attack can occur at either (o) or (p) position, forcing the NO_2 at (o) position to leave and be substituted by the OH^o. Further oxidation (removal of hydrogen) of two phenolic groups attached to the (o) and (p) positions yield the intermediate OBP4. The phenomenon of denitration and hydroxylation are widely reported and considered to be the dominant degradation pathways for 2-NP (Wei et al., 2011). Based on the available MS library, the chemical formula of OBP4 is proposed to $C_6H_4O_4$. However, the chemical structure of the fragment ion at m/z 151.99 could not be established at 40 minutes, probably due to low concentration but however it manifested at 60 minutes. At 60 minutes, some of the intermediates observed at 40 minutes had disappeared and new ones with MS and UV pattern at m/z (183.01, 152.99 and 112.99) were noticed as shown in Figure 5.35 (a) and (b).

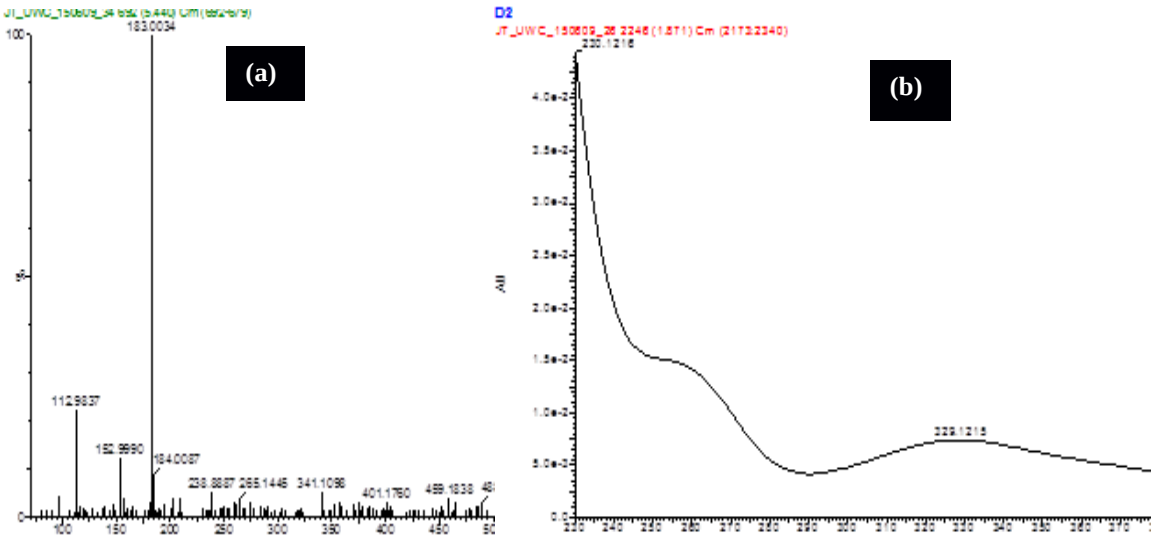

Figure 5-35: (a) LC-MS and (b) LC-UV chromatograph of the intermediates products formed via DBD after 60 minutes reaction time

The mass difference between fragmentation patterns observed at m/z of 183.00 and 138 was 45, which corresponded to the addition of a nitro group (NO_2) at the ortho position. Based on the available MS library, a chemical structure ($C_6H_4N_2O_5$, 2,4-dinitrophenol) is proposed for OBP5. Oxidation of the two phenolic groups in OBP1 ($C_6H_5NO_4$) (removal of hydrogen) in the presence of $OH^o/O_3/H_2O_2$ resulted in OBP6 with a molecular formula of $C_6H_3NO_4$. The de-nitration or removal of the nitro group from OBP1 produced OBP7 with chemical formula $C_6H_6O_2$ (hydroquinone). More so, at 80 and 120 minutes, only OBP5 was identified, which indicates that the compound was stable and resistant to further oxidation.

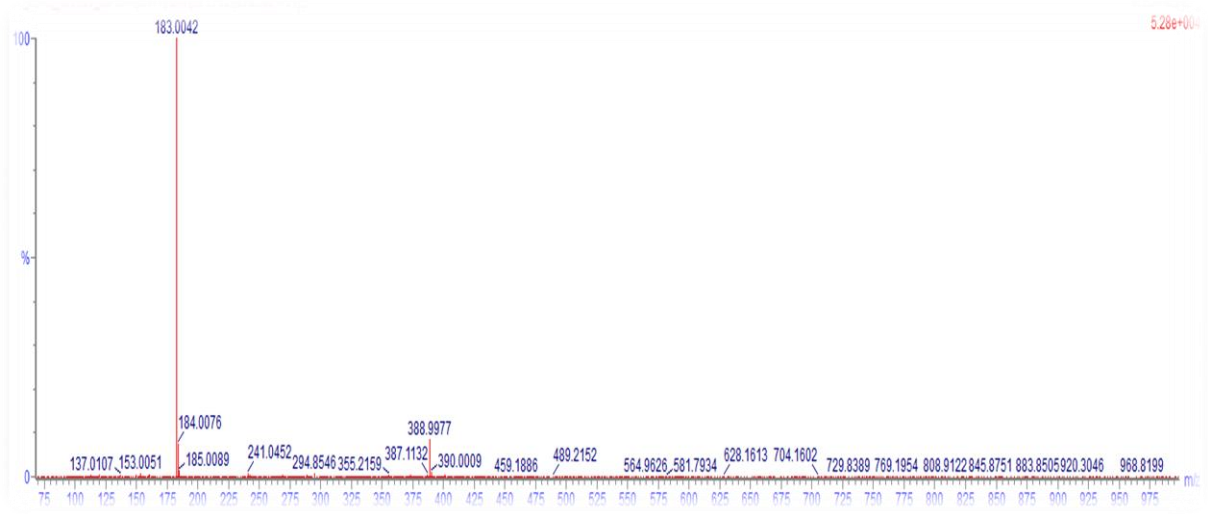

Figure 5-36: LC-MS of the intermediates products formed via DBD after 80 minutes reaction time

Formation of hydroquinone ($C_6H_6O_2$) and phenol (C_6H_5OH).

Critical analyses of the two treatments' performance based on the obtained intermediates enumerated in Table 5.6 indicated that 2-NP was better decomposed via the combined system than DBD alone. This may be due to the higher concentration of reactive species in the combined systems. While OBP8 was formed at 60 minutes, a small fragment of OBP9 was detected at 80 minutes and persisted in solution till 120 minutes. The molar mass of the two compounds were lower in the combined system than the original compound (2-NP) unlike with DBD alone, thus suggested that the addition of the catalyst enhanced the free reactive species in solution and was perhaps responsible for the appearance of peaks with lower m/z value. Also, the final oxidation product obtained via DBD alone was hardly oxidised further after 80 minutes but oxidised into a lower fragment ion with the addition of catalysts. The LC-MS spectrum of the two intermediates are shown in Figure 5.37 (a) and (b).

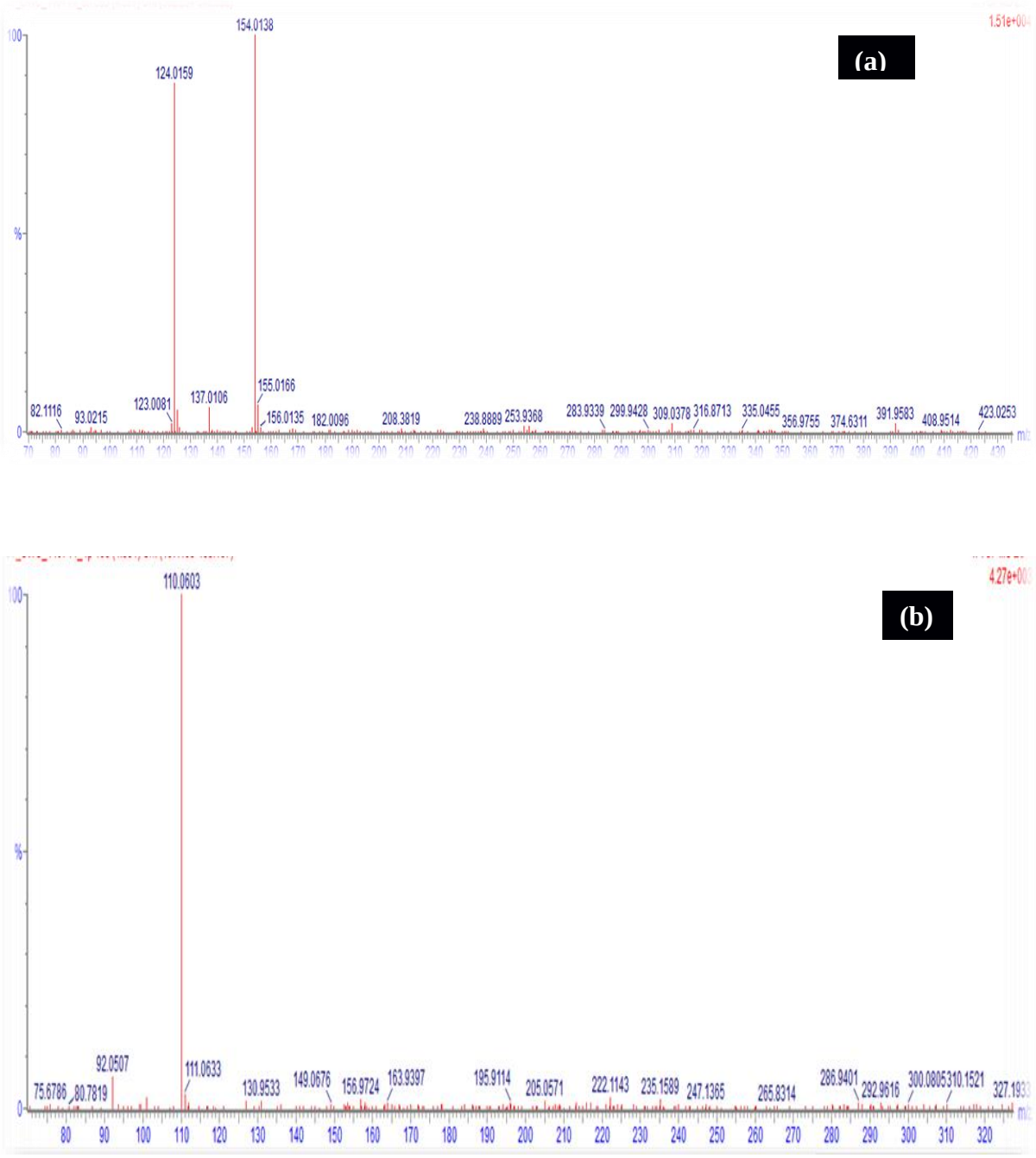

Figure 5-37: LC-MS chromatograph of (a) OBP8 (b) OBP9 formed via combined DBD/photocatalyst at 60 and 120 minutes

As illustrated in Figure 5.37 (a), two fragmentation peaks at m/z 154.01 and 124.01 were observed. The fragmentation pattern at m/z 154.01 was assigned to OBP1. The elimination of NO_2 at the ortho position from OBP1 and substitution by the OH group and further oxidation of the two phenolic OH groups at the ortho and para position formed compound OBP8. The denitration of 2-NP without further substitution and oxidation of the OH group produced a small phenolic fragment shown in Figure 5.38 (b) and labelled as OBP9. The

chemical structure of OBP8 and OBP9 is proposed to be $C_6H_4O_3$ and C_6H_5OH with the aid of MS library. Detailed degradation mechanisms are provided in the next section.

5.3.8 Proposed degradation pathways or routes for 2-NP via DBD alone, or DBD/JT14 induced process

As mentioned earlier, the DBD system produces different reactive species namely OHº, O_3, H_2O_2, O, NO_2, NO and OOH, which are directly or indirectly responsible for the degradation of organic pollutants. In this study, the degradation pathways for 2-NP were proposed based on the obtained intermediates and it was possible to identify which of the reactive species were responsible. Therefore, the degradation mechanism of each intermediate is shown in Figure 5.38.

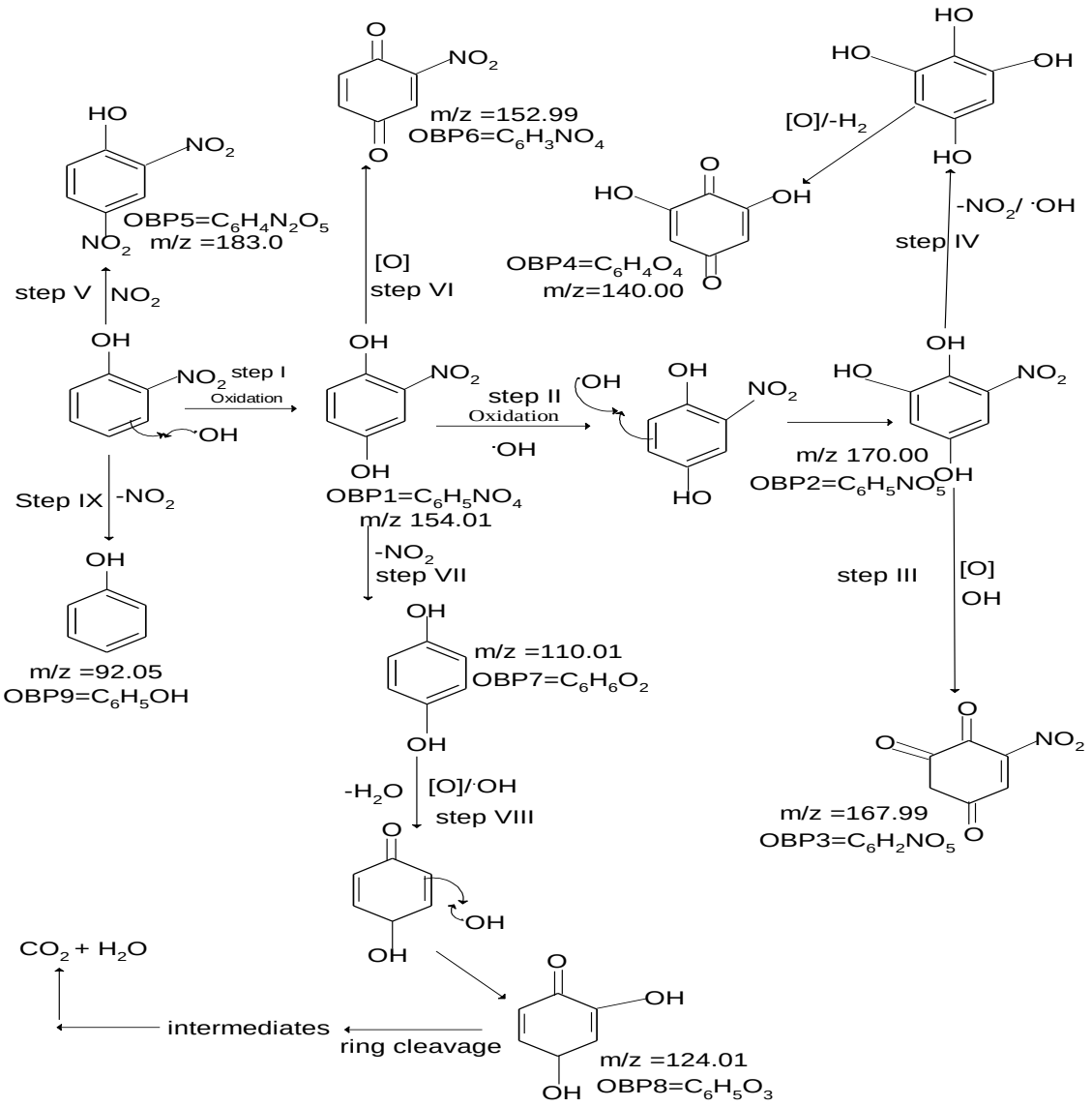

Figure 5-38: Proposed routes for 2-NP degradation by DBD and DBD/supported photocatalysts (JT14)

Three major pathways or routes were identified during the oxidation of 2-NPs namely hydroxylation, nitration and denitration. As demonstrated in Figure 5.38, step I, II, III, IV, VI and VIII, which led to the formation of the intermediates OBP1-OBP4, OBP6, OBP8, corresponded to the hydroxylation reaction. While Step VII and IX which produced OBP7 and OBP9 proceed with the loss of a nitro group, often called the denitration step. Step V represents the nitration step. Notably, the intermediate compounds obtained via step VII, VIII and IX are similar to those reported by Cañizares et al. (2004) who identified benzene derivatives such as phenol and hydroquinone as organic oxidation by-products during oxidation of nitrophenols via electrochemical methods. Furthermore, the oxidation of OBP9 would lead to ring cleavage and formation of carbonyl compounds and carboxylic acid, which in turn would mineralise into CO_2 and H_2O. However, carboxylic acids such as acetic acid, malonic acid, oxalic acid, and glyoxylic acid which have been previously reported (Ammar et al., 2007; Kavitha and Palanivelu, 2005) as part of 2-NP degradation oxidation by-products were not detected in this study. Irrespective of the nature of the intermediate compounds, the degradation mechanism of 2-NP via the two treatments followed hydroxylation, nitration and denitration steps. Based on the proposed mechanism and the identified intermediates, the hydroxyl radical remained the most prominent oxidant responsible for the mineralisation of 2-NPs compared to BPA where both OH^{o} and O_3 played a crucial role. It is imperative to mention that despite the incorporation of different catalysts, complete conversion of the BPA or 2-NP to CO_2 and H_2O was not achieved. This may be attributed to a stronger competition between the various intermediate compounds and original BPA or 2-NP molecules for the free reactive species.

Another possible explanation has to do with the nature of the intermediates, some of these compounds were persistent and resistant to further oxidation and underwent recombination reactions forming oligomeric compounds in the case of BPA. The intermediate compounds were somehow similar despite different treatment processes, suggesting that 2-NP was decomposed by the same reactive species possibly by hydroxyl radicals. Similar observations were reported by Ammar et al. (2007) during the oxidative degradation of 2-NP via electro-Fenton process. Kavitha and Palanivelu (2005) applied the Fenton and the photo-Fenton process to mineralise 2-nitrophenol in water. The authors identified nitrodihydroxylbenzene and nitro-p-benzoquinone as intermediate compounds. Wei et al. (2011) reported tetrahydroxylbenzene as one of the intermediates formed during the electrochemical oxidation of p-nitrophenol.

CHAPTER 6: CONCLUSIONS & RECOMMENDATIONS

6.1 CONCLUSIONS

In the case of the various synthesised TiO_2 nanocrystals supported on stainless steel mesh, the following conclusions were drawn:

- This study has demonstrated, for the first time, the synthesis of stainless steel mesh supported undoped and doped catalyst via sol-gel and thermal evaporation technique
- A promising route for preparing crystalline TiO_2 catalyst developed on a stainless steel mesh was successfully developed via sol-gel method and the results of the various characterization confirmed that the supported TiO_2 photocatalyst was purely anatase phase
- Both the calcination temperature and holding time had an effect on controlling the particle size without affecting the formation of pure anatase phase
- Holding time had an effect on catalyst layer adhesion on the support and 1-3 h was suitable between 300-400°C
- Samples possess photocatalytic activity in different proportion especially supported TiO_2 nanocrystals calcined at 350˚C for 3 hrs, showing the preparation route for photocatalytic metals
- The decolouration of MB was mostly favoured in the acidic region and at low MB concentration
- The MB decolouration efficiency was dependent on solution pH, initial concentration of MB, and calcination temperature and holding time
- The deposition of a plasmonic element such as silver was achieved using thermal evaporation technique. The loading of different amounts of Ag onto TiO_2 surface reduced the band gap energy of TiO_2 which was exhibited by a red-shift of an additional broad absorption band from 352-410 nm
- Thus, the presence of plasmonic metallic silver deposited onto TiO_2 layer might play a crucial role in preventing photoelectron-hole recombination rate emanating from valence and conduction band sphere
- The deposition of 10 nm Ag enhanced the photocatalytic decolouration of MB by 13.3%
- This study has shown that plasmonic Ag deposited on TiO_2 lattice structure improved the MB removal compared to bare TiO_2 nanocrystals
- The photocatalytic decolouration of MB of all the catalysts demonstrated a linear relationship between the MB concentration and irradiation time and fitted well to pseudo first-order kinetic models

- The presence of other organic contaminants in water may result in the decrease in the photocatalytic degradation of the target compound due to competition for active sites by the contaminants on surface of the photocatalyst

In the case of the synthesised TiO_2 nanocrystals supported on fused silica, the study concludes that:

- The differences in the results obtained from change of order of deposition of the plasmon metal in relation to the TiO_2 layer demonstrate that the chemical states and the location of Ag, Cu and Au on TiO_2 play important roles in photodegradation of organic contaminants
- Of all the modified TiO_2 photocatalysts, the highest enhancement was achieved by a bimetallic TiO_2/Au/Ag composite
- Ag plasmon metal composites were more active in UV irradiation whereas Cu plasmon metal composites were more active under visible light irradiation

In this study, the removal and degradation of BPA and 2-NP in aqueous solution by DBD plasma system was investigated. The influence of solution pH, initial concentration of the pollutants and radical scavengers were studied. The incorporation of supported TiO_2 photocatalyst and Ag doped TiO_2 nanocomposites on the mineralization efficiency of BPA or 2-NP were explored. Based on the results obtained the following conclusions were drawn:

- It was found that an increase in solution pH and initial concentration of the pollutants as well as radical scavengers have a negative effect on the removal efficiency of the two compounds 2-NP and BPA
- The removal efficiency of BPA or 2-NP was mostly favoured in acidic conditions and at lower concentrations. Maximum BPA or 2-NP removal efficiency occurred at low pH (3) at optimum concentration of 10 mg/L but removal was not equivalent to demineralisation due to the formation of intermediate degradation products.
- The BPA or 2-NP degradation yield at 30 mg/L concentration of BPA or 2-NP, at 8 kV discharge voltage, solution pH (3), after 80 min treatment time was 3.73×10^{-4} g/kWh or 2.48×10^{-4} g/kWh respectively
- The removal efficiency of BPA or 2-NP in aqueous solution by the DBD alone at 80 minutes of reaction time was 67.22% and 56.8% respectively
- With the incorporation of the supported TiO_2 photocatalyst (JT7) into the DBD reactor, the BPA removal efficiency was 80% while 77.5% of 2-NP was removed under the same experimental conditions

- Furthermore, with the incorporation of 2.4% Ag/carbon doped TiO_2 photocatalysts (JT14) with the DBD system, BPA or 2-NP removal efficiency at 80 min was 89.02% or 81% respectively
- The incorporation of stainless steel supported 2.4% Ag loaded carbon doped TiO_2 nanocomposites enhanced the BPA or 2-NP removal efficiency by 21.8% and 24.2% in relation to DBD alone
- It was shown under the studied conditions that combined advanced oxidation system based on supported 2.4% Ag/carbon doped TiO_2 nanocomposites and dielectric barrier discharge system which produced UV light, was more effective for the high removal and good demineralisation BPA or 2-NP in aqueous solution than DBD alone
- 2.4% Ag/carbon doped TiO_2 nanocomposites were photochemically stable even after four successful applications in the DBD system, thus making this combined advanced oxidation treatment option a strong candidate in wastewater treatment
- However, progressive leaching of the metallic species such as (Fe, Cr, Ni) occurred from the stainless steel mesh depending on solution pH. These species sometimes compete with Ti^{4+} based on ionic radii differences and reduced the performance of the catalyst, which in turn decreased the degradation efficiency.
- Degradation efficiency was better measured from TOC determinations than from quantification of residual pollutants because of the accumulation of intermediate transformation products

Finally, the degradation mechanism of BPA or 2-NP using DBD and combined DBD/JT14 was investigated. Based on the results obtained the following conclusion were drawn:

- The degradation of BPA proceeded via ozonation, hydroxylation, dimerization, and decarboxylation and nitration steps were proposed. While 2-NP proceeded via hydroxylation, nitration and denitration steps respectively.
- Five and three new oxidation products such as (BP5, BP11-BP14) and (OBP2-OBP4) of BPA or 2-NP which have not been previously reported in the literature were identified.
- The DBD alone and combined DBD with catalyst produced more of the OH^{o} than H_2O_2 and O_3.
- The OH^{o} that readily formed in acidic medium was the most significant species responsible for the degradation of BPA and 2-NP.
- The results presented in this study have clearly demonstrated that the combination of the DBD system with a Ag/TiO_2 supported catalyst (JT14) can be applied as a pre or post treatment method to decompose recalcitrant pollutants such as BPA or 2-NP in water.

6.2 RECOMMENDATIONS

In future work:

- It is recommended that the DBD reactor combined with the supported photocatalysts be scaled up to a stage where effective energy balances can be calculated in order to determine process efficiencies compared to other wastewater treatment systems
- As both the fused silica supported and stainless steel supported photocatalysts showed suitable activity in UV light, it is recommended that the fused silica supported catalyst also be evaluated for activity and reusability in the corrosive DBD environment, as it is expected that fused glass will sustain its integrity to a greater extent than stainless steel which was subject to corrosion in low pH environments
- As Cu plasmon metal doped photocatalysts on fused silica showed suitable activity in visible light, it is recommended that supported Cu/TiO_2 or bi and tri metallic systems be tested for their applicability in scaled reactor systems designed to make use of visible light
- Since BPA and 2-NP showed incomplete mineralisation in air due to the formation of recalcitrant intermediates and scavenging species, mechanisms to remove the scavenging species should be developed
- The use of stainless steel mesh was a limitation in this study due to costs of purchasing Ti mesh which was beyond the study budget. Preliminary work with Ti mesh (not shown) shows high promise for long-term stability of the supported photocatalyst and should be used as alterative to the supports chosen in this study
- Were stainless steel mesh to be used as cheap alternative instead of Ti mesh it is recommended that anticorrosion coatings be deposited underneath the photocatalytic layers

The developed combined system showed a high demineralisation efficiency and should be tested for its efficacy to remove other persistent organic contaminants from wastewater.

REFERENCES

Agunbiade, F.O., Moodley, B. (2014). Pharmaceuticals as emerging organic contaminants in Umgeni River water system, KwaZulu-Natal, South Africa. *Environmental Monitoring and Assessment,* 186(11):7273-91

Ahmed, E., Nagaoka, K., Fayez, M., Abdel-Daim, M.M., Samir, H. and Watanabe, G. (2015). Suppressive effects of long-term exposure to p-nitrophenol on gonadal development, hormonal profile with disruption of tissue integrity, and activation of caspase-3 in male Japanese quail (*Coturnix japonica*). *Environmental Science and Pollution Research,* 22(14):10930-42

Ahmed, S., Rasul, M.G., Wayde, N., Martens, Brown, R. and Hashib, M.A. (2011). Advances in Heterogeneous Photocatalytic Degradation of Phenols and Dyes in Wastewater: A Review. *Water Air Soil Pollut*, 215: 3-29.

Al-Rifai, J.H., Khabbaz, H., Schäfer, A.I. (2011). Removal of pharmaceuticals and endocrine disrupting compounds in a water recycling process using reverse osmosis systems. *Separation and Purification Technology*, 77: 60-67

Al-Shamali, S.S. (2013). Photocatalytic Degradation of Methylene Blue in the Presence of TiO_2 Catalyst Assisted Solar Radiation. *Australian Journal of Basic and Applied Sciences*, 7(4): 172-176

Álvarez, P.M., Jaramillo, J., López-Piñero, F. and Plucinski, P.K. (2010). Preparation and characterization of magnetic TiO_2 nanoparticles and their utilization for the degradation of emerging pollutants in water. *Applied Catalysis B: Environmental,* 100: 338-345

Ammar, S., Oturan, N. and Oturan, M.A. (2007). Electrochemical oxidation of 2-nitrophenol in aqueous medium by electro-Fenton technology. J*ournal of Environmental Engineering and Management,* 17(2): 89-96

Aneck-Hahn, N.H., Bornman, M.S., De Jager, C. (2009). Oestrogenic activity in drinking waters from rural area in the Waterberg District, Limpopo Province, South Africa. *Water SA*, 35(3): 245-252

Austin, O., Hart, J., Jarvis, P., MacAdam, J., Parsons, S.A. and Jefferson, B. (2012). Comparison of UV/H_2O_2 and UV/TiO_2 for the degradation of metaldehyde: kinetics and the impact of background organics. Water Research, 46, 5655-5662.

Ba-Abbad, M.M., Kadhum, A.H., Mohamed, A.B., Takriff, M.S. and Sopian, K. (2012). Synthesis and catalytic activity of TiO_2 nanoparticles for photochemical oxidation of concentrated chlorophenols under direct solar radiation. *International Journal of Electrochemical Science*, 7: 4871-4888.

Bagheri, S., Julkapli, N.M. and Abd Hamid, S.B. (2014). Titanium Dioxide as a Catalyst Support in Heterogeneous Catalysis. *Scientific World Journal,* Article ID 727496, 21 pages

Bahnemann, W., Muneer, M. and Haque, M.M. (2007). Titanium dioxide-mediated photocatalysed degradation of few selected organic pollutants in aqueous suspensions, *Catalysis Today,* 124:133-148

Baker, D.R., Kasprzyk-Horden, B. (2013). Spatial and temporal occurrence of pharmaceuticals and illicit drugs in the aqueous environment and during wastewater treatment: New developments. *Science of the Total Environment,* 454-455: 442-456

Balasubramanian, G., Dionysiou, D.D., Suidan, M.T., Baudin, I. and Laîné, J.M. (2004). Evaluating the activities of immobilized TiO_2 powder films for the photocatalytic degradation of organic contaminants in water. *Applied Catalysis B: Environmental*, 47, 73-84

Barakat, M.A., Al-Hutailah, R.I., Qayyum, E., Rashid, J. and Kuhn, J.N. (2013). Pt nanoparticles/TiO_2 for photocatalytic degradation of phenols in wastewater. Environmental Technology, http://dx.doi.org/10.1080/09593330.2013.820796

Bassioni, G., Korin, A. and Salama, A.E. (2015). Stainless Steel as a Source of Potential Hazard due to Metal Leaching into Beverages. *International. Journal of. Electrochemical. Science,* 10: 3792-3802

Behnajady, M.A., Eskandarloo, H., Modirshahla, N., Shokri, M. (2011). Investigation of the effect of sol-gel synthesis variables on structural and photocatalytic properties of TiO_2 nanoparticles. *Desalination,* 278: 10-17

Behnajady, M.M. (2008). Enhancement of photocatalytic activity of TiO_2 nanoparticles by Silver doping: Photodeposition versus Liquid impregnation methods. *Global NEST Journal,* 10(1): 1-7.

Bell, K.Y., Wells, M.J.M., Traexler K.A., Pellegrin, M., Morse, A. and Bandy, J. (2011). Emerging Pollutants. *Water Environment Research*, 83: 1906-1984

Bergman, A., Heindel, J.J., Jobling, S., Kidd, K.A., Zoeller, R.T. (2013). State of the Science of Endocrine Disrupting Chemicals 2012. Summary for Decision-Makers. Pp. 7

Bestetti, M, Sacco, D, Brunella, M.F., Franz, S., Amadelli, R. and Samiolo, L. (2010). Photocatalytic degradation activity of titanium dioxide sol-gel coatings on stainless steel wire meshes. *Materials Chemistry and Physics*, 124: 1225-1231

Bhatkhnade, D.S., Kamble, S.P., Sawant, S.B., Pangarkar, V.G. (2004). Photocatalytic and photochemical degradation of nitrobenzene using artificial ultraviolet light. *Chem. Eng. J*. 102: 283-290.

Bian, W., Song, X., Liu, D., Zhang, J. & Chen, X. (2011). The intermediate products in the degradation of 4-chlorophenol by pulsed high voltage discharge in water. *Journal of Hazardous Materials*, 192(3), 1330-1339

Boehncke, A., Koennecker, G., Mangelsdorf, I. and Wibbertmann, A. (2000). Mononitrophenols: World Health Organization, Concise International Chemical Assessment Document 20. ISSN 1020-6167, Pp. 5

Boithias, L., Acuña, V., Vergoñós, L., Ziv, G., Marcé, R. and Sabater, S. (2014). Assessment of the water supply: demand ratios in a Mediterranean basin under different global change scenarios and mitigation alternatives. *Science of the Total Environment*, 470-471: 567-577

Boparai, H.K., Joseph, M. and O'Carroll, D.M. (2013). Cadmium (Cd^{2+}) removal by nano zerovalent iron: Surface analysis, effects of solution chemistry and surface complexation modelling. *Environmental Science and Pollution Research,* 20:6210-6221

Brezova, V., Blaskova, A., Borsova, E., Ceppan, M., Fiala R. (1995). The influence of dissolved metal ions on the photocatalytic degradation of phenol in aqueous TiO_2 suspensions, *J. Mol. Catal. A: Chem.* 98 109-116.

Bruce, G.M., Pleus, R.C., Snyder, S.A. (2010). Toxicological relevance of pharmaceuticals in drinking water. *Environmental Science and Technology*, 44:5619-26.

Bruggeman, P.J. & Locke, B.R. (2013). Assessment of Potential Applications of Plasma with Liquid Water, in Low Temperature Plasma Technology: Methods and Applications, P. Chu, and X. Lu (Eds.), Taylor and Francis Group, pp. 368-369.

Bull, R.J., Crook, J., Whittaker, M., Cotruvo, J.A. (2011). Therapeutic dose as the point of departure in assessing potential health hazards from drugs in drinking water and recycled municipal wastewater. *Regulatory Toxicology and Pharmacology,* 60: 1-19

Burger, A.E.B., Moolman, A.P.M. (2006). First Phase of an Endocrine Research Programme for South African Water Systems. *Water Practice & Technology,* 1(2): 35-42

Byranvand, M.M., Kharat, A.N., Fatholahi, L. and Beiranvand, Z.M. (2013). A review on the synthesis of nano-TiO_2 via different methods. *Journal of Nanoscience*, 3: 1-9

Cañizares, P., Saez, C., Lobato, J. and Rodrigo, M.A. (2004). Electrochemical treatment of 2,4-dinitrophenol aqueous , H., Shi, T., Tang, T and Li, J. (2008). Preparation of Ag-doped TiO_2 nanoparticles for photocatalytic degradation of acetamiprid in water. *J Chem Technol Biotechnol*, 83:546-552

Cardoso da Silva, J.C., Reis Teodoro, J.A., Franco Afonso, R.J.C., Aquino, S.F. and Augusti, R. (2014). Photodegradation of bisphenol Ain aqueous medium: Monitoring and identification of by-products by liquid chromatography coupled to high-resolution mass spectrometry. *Rapid Communication in. Mass Spectrometry,* 28: 987-994

Carlucci, C., Xu, H., Scremin, B.F., Giannini, C., Altamura, D., Carlino, E., Videtta, V., Conciauro, F., Gigli, G. and Ciccarella, G. (2014). Selective synthesis of TiO_2 nanocrystals with morphology control with the microwave-solvothermal method. *Cryst Eng. Comm*, 16: 1817-1824

Carson, R.L. (1962). Silent Spring, Houghton, Mifflin Boston

Carson, R.L. (2002). Silent Spring – 40th Anniversary Edition. Boston: Mariner

Chang, B.V., Yuan, S.Y. and Chiou, C.C. (2011). Biodegradation of bisphenol-A in river sediment. *Journal of Environmental Science Health A*, 46(9):931-937

Chang, J.A., Vithal, M., Baek, I.C. and Seok, S.I.I. (2009). Morphological and phase evolution of TiO_2 nanocrystals prepared from peroxotitanate complex aqueous solution: Influence of acetic acid. *Journal of Solid State Chemistry*, 182: 749-756

Chavadey, S., Kaitubolpaiboon, W., Rangsunvigit, P., Sreethawong, T. and Mol, J.A. (2007). Combined multistage corona discharge and catalytic system for gaseous benzene removal. *Catal. A.Chem*, 263,128-136.

Chen, D., Du, G., Zhu, Q. and Zhou, F. (2013). Synthesis and characterization of TiO_2 pillared montmorillonites: Application for methylene blue degradation. *Journal of Colloid and Interface Science*, 409: 151-157

Chen, J.Q., Wang, D., Zhu, M.-X. & Gao, C.-J. (2007). Photocatalytic degradation of dimethoate using nanosized TiO_2 powder. *Desalination,* 207:87-94.

Chen, T.C., Shue, M.F., Yeh, Y.L. and, Kao T.J. (2010). Bisphenol A occurred in Kao-Pin River and its tributaries in Taiwan. *Environmental Monitoring and Assessment*, 161:135-45.

Chen, Y.W. and Lee, D.S. (2014). Photocatalytic Destruction of Methylene Blue on $Ag@TiO_2$ with Core/Shell Structure. Open Access Library Journal, 1: e504. http://dx.doi.org/10.4236/oalib.1100504

Cheng, M.M., Ma, W.H. Li, J., Huang, Y.P. and Zhao, J.C. (2004). Visible light-assisted degradation of dye pollutants over Fe(III)-loaded resin in the presence of H_2O_2 at neutral pH values, *Environ. Sci. Technol*. 38:1569-1575

Chiarello, G.L., Aguirre, M.H., Selli, E. (2010). Hydrogen production by photocatalytic steam reforming of methanol on noble metal-modified TiO_2. *Journal of Catalysis,* 273: 182-190

Choi, J., Park, H., Hoffmann, M.R. (2009). Effects of Single metal-ion doping on the visible light photo-reactivity of TiO_2. *Journal of Physical Chemistry*, C, 17-55

Chong, M.N. and Jin, B. (2012). Photocatalytic treatment of high concentration carbamazepine in synthetic hospital wastewater. *Journal of Hazardous Materials*, 199-200: 135-142

Chong, M.N., Jin, B., Chow, C.W.K. and Saint, C.P. (2010). Recent developments in photocatalytic water treatment technology: a review. *Water Resources*, 44: 2997-3027.

Chong, M.N., Sharma, A.K., Burn, S. and Saint, C.P. (2012). Feasibility study on the application of advanced oxidation technologies for decentralised wastewater treatment. *Journal of Cleaner Production*, 35: 230-238

Clemente, Z., Castro, V.L., Jonsson, C.M. and Fraceto, L.F. (2012). Ecotoxicology of Nano-TiO_2 – An Evaluation of its Toxicity to Organisms of Aquatic Ecosystems. *Int. J. Environ. Res*., 6(1):33-50

Colombo, A., Cappelletti, G., Ardizzone, S., Biraghi, I., Bianchi, C.L., Meron, D., Pirola, C. and Spadavecchia, F. (2012). Bisphenol A endocrine disruptor complete degradation using TiO_2 photocatalysis with ozone. *Environmental Chemistry Letter*: 10: 55-60

Cong, Y., Li, X., Qin, Y., Dong, Z., Yuan, G., Cui, Z. and Lai, X. (2011). Carbon-doped TiO_2 coating on multiwalled carbon nanotubes with higher visible light photocatalytic activity. *Applied Catalysis B: Environmental*, 107:128-134

Corbari, L. (2008). Iron oxide deposits associated with the ectosymbiotic bacteria in the hydrothermal vent shrimp *Rimicaris exoculata*. *Biogeosciences*, 5: 1295-1310.

Crane, R.A., Dickinsona, M., Popescub, I.C. and Scott, T.B. (2011). Magnetite and zero-valent iron nanoparticles for the remediation of uranium contaminated environmental water. *Water Research*, 45: 2931-2942

Daghrir, R. and Drogui, P. (2013). Tetracycline antibiotics in the environment: a review. Environmental Chemistry Letters, 11:209-227

Dai, K., Chen, H., Peng, T., Ke, D., Yi, H. (2007). Photocatalytic degradation of methyl orange in aqueous suspension of mesoporous titania nanoparticles. *Chemosphere*, 69: 1361-1367

Dalrymple, O.K., Stefanakos. E., Trotz, M.A. and Yogi, G.D. (2010). A review of the mechanisms and modeling of photocatalytic disinfection. *Applied Catalysis B: Environmental*, 98:27-38.

Dalrymple, O.K., Yeh, H. and Trotz, M.A. (2007). Removing pharmaceuticals and endocrine-disrupting compounds from wastewater by photocatalysis, *Journal of Chemical Technology & Biotechnology*, 82 (2): 121-134

Dang, T.M.D., Le, T.T.T., Fribourg-Blanc, E., Dang, M.C. (2011). Synthesis and optical properties of copper nanoparticles prepared by a chemical reduction method, *Adv. Nat. Sci.: Nanosci. Nanotechnol., 2 1-6.*

Daniel, L.S., Nagai, H., Sato, M. (2013). Photoelectrochemical property and the mechanism of plasmonic Ag-NP/TiO_2 composite thin films with high silver content fabricated using molecular precursor method. *J. Mater. Sci*. doi:10.1007/s10853-013-7533-0.

Deborde, M., Rabouana, S., Mazelliera, P., Duguet, J.P. and Legube, B. (2008). Oxidation of bisphenol A by ozone in aqueous solution. *Water Research*, 42: 4299-4308

Department of Water Affairs (DWA). (2012). The Annual National State of water resources report October 2011 to September 2012. Department of Water Affairs. Pretoria, South Africa

Dhananjeyan, M.R., Kandavelu, V., Renganathan, R. (1997). An investigation of the effects of Cu2+ and heat treatment on TiO_2 photo-oxidation of certain pyrimidines, J. Mol. Catal. A: Chem. 158 577-582.

Di Paolo, A., Marci, G., Palmisano, L., Schiavello, M., Uosaki, K., Ikeda, S. and Ohtani, B. (2009). Preparation of polycrystalline TiO_2 photocatalysts impregnated with various transition metal ions: Characterization and photocatalytic activity for the degradation of 4-nitrophenol. *J. Phys. Chem. B,* 106: 637-645

Diamanti-Kandarakis, E., Bourguignon, J.P., Giudice, L.C., Hauser, R., Prins, G.S., Soto, A.M., Zoeller, R.T. and Gore, A.C. (2009). "Endocrine-disrupting chemicals: an Endocrine Society scientific statement". *Endocrine Review*, 30 (4): 293-342

Dmitruk, U., Piascik, M., Taboryska, B. and Dojlido, J (2008). Persistent organic pollutants (POPs) in bottom sediments of the Vistula River, Poland. *Clean* 36: 222-229

Dobrin, D., Bradu, C., Magureanu, M., Mandache, N.B. and Parvulescu, V.I. (2013). Degradation of diclofenac in water using a pulsed corona discharge. *Chemical Engineering Journal,* 234: 389-396

Dolat, N.Q., Kusiak-Nejman, E., Morawski, A.W., Puma Li, G. (2012). One step, hydrothermal synthesis of nitrogen, carbon co-doped titanium dioxide (N, C TiO_2) photocatalyst. Effects of alcohol degree and chain length as carbon dopant precursors on photocatalytic activity and catalyst deactivation. *Appli.Catal.B: Environment*, 115-116: 81-89

Domínguez-Espíndola, R.B., Silva-Martínez, S., Ortiz-Hernández, M.L., Román-Zubillaga, J.L. and Guardián-Tapia, R. (2012). Photocatalytic disinfection of municipal wastewater using TiO_2 film and Ag/TiO_2 powders under UV and solar light irradiation. *Mexican Journal of Scientific Research,* 2 (2): 2013, 60-68

Duong, H.T., Kadokami, K., Pan, S., Matsuura, N., Nguyen, T.Q. (2014). Screening and analysis of 940 organic micro-pollutants in river sediments in Vietnam using an automated identification and quantification database system for GC-MS. *Chemosphere,* 107:462-72.

Elmolla, E.S. and Chaudhuri, M. (2010). Comparison of different advanced oxidation process for treatment of antibiotics aqueous solution. *Desalination,* 256: 43-47

Ewa Kowalska, O.O., Prieto, M., Ryu, A., Bunsho, O. (2010). Visible-light-induced photocatalysis through surface plasmon excitation of gold on titania surfaces. *Physical Chemistry Chemical Physics*, 12: 2344-2355

Fabiola Méndez-Arriaga, Jaime Gimenez, and Santiago Esplugas. (2008). Photolysis and TiO_2 Photocatalytic Treatment of Naproxen: Degradation, Mineralization, Intermediates and Toxicity. *J. Adv. Oxid. Technol***,** 11(3): 436-445

Fang, X., Mark, G. and Von Sonntag, C. (1996). “OH radical formation by ultrasound in aqueous solutions Part I: chemistry underlying the tereophthalae dosimeter,” *Ultrasonic Sonochemistry,* 3: 57-63

Fatoki, O.S., Bornman, M., Ravandhalala, L., Chimuka, L., Genthe, B., Adeniyi, A. (2010). Phthalate ester plasticizers in freshwater systems of Venda, South Africa and potential health effects. *Water SA,* 36 (1): 117-.

Fatoki, O.S. and Opeolu, B.O. (2009). Studies on the occurrence and quantification of phenolic endocrine disruptors in water. *Scientific Research and Essay,* 4 (12): 1415-1422

Fawell, J. and Ong, C.N. (2012). Emerging contaminants and the implications for drinking water. *International Journal of Water Resources Development*, 28(2): 247-263

Fent, K. (2008). Pharmaceuticals in the environment: Sources, Fate, Effects, and Risks. Springer-Verlag, Pp. 174-203 (Chapter Effects of Pharmaceuticals on Aquatic organisms).

Fent, K., Weston, A.A., Caminada, D. (2006). Ecotoxicology of human pharmaceuticals. *Aquatic Toxicology,* 76:122-159.

Fernández, A., Lassaletta, G., Jimknez, V.M., Justo, A., GonzSlez-Elipe, A.R., Herrmann, J.M., Tahiri, H. and Ait-Ichou, Y. (1995). Preparation and characterization of $Ti0_2$ photocatalysts supported on various rigid supports (glass, quartz and stainless steel). Comparative studies of photocatalytic activity in water purification. *Applied Catalysis B: Environmental,* 7: 49-63

Fernandez, M. (2010). Endocrine disruptors and semen quality. Presentation at ESHRE Annual Meeting, Rome, Italy.

Flint, S., Markle, T., Thompson, S. and Wallace, E. (2012). Bisphenol A exposure, effects, and policy: A wildlife perspective. *Journal of Environmental Management*, 104: 19-34.

Friedmann, D., Mendive, C. & Bahnemann. D. (2010). TiO_2 for water treatment. Parameters affecting the kinetics and mechanisms of photocatalysis. *Applied Catalysis B: Environmental.* 99: 398-406

Fujishima, A., Zhang, X. and Tryk, D.A. (2008). TiO_2 photocatalysis and related surface phenomena. *Surf. Sci. Rep*. 63: 515-582

Fukushima, M., Tatsumi, K. and Moimoto, K. (2000). Influence of Fe (III) and humic acid on the phototodegradation of pentachlorophenol. *Environ. Toxicol. Chem*. 19, 1711-1716

Fung, Y.S., Wu, Z. and Dao, K.L. (1996). Determination of Total Organic Carbon in Water by Thermal Combustion-Ion Chromatography. *Analytical Chemistry*, 68:2186-2190

Gao, L., Sun, L., Wan, S., Yu, Z. and Li, M. (2013). Degradation kinetics and mechanism of emerging contaminants in water by dielectric barrier discharge non-thermal plasma: The case of 17b-Estradiol. *Chemical Engineering Journal* 228: 790-798

Gaya, U.I. and Abdullah, A.H. (2008). Heterogeneous photocatalytic degradation of organic contaminants over titanium dioxide: a review of fundamentals, progress and problems. *J. Photochem. Photobiol. C: Photochem. Rev.* 9: 1-12

Geens, T., Goeyens, L. and Covaci, A. (2011). Are potential sources for human exposure to bisphenol-A overlooked? *International Journal of Hygiene and Environmental Health*, 214: 339-347

Georgi, A., Schierz, A. Trommler, U., Horwitz, C.P., Collins, T.J and Kopinke, F.D. (2007). Humic acid modified Fenton reagent for enhancement of the working pH range. *Appl. Catal. B-Environ*. 72: 26-36.

Gogate, P.R. and Pandit, A.B. (2004). A review of imperative technologies for wastewater. *Chemosphere,* 73: 848-853.

Grabowski, L.R., Van Veldhuizen, E.M., Pemen, A.J.M. and Rutgers, W.R. (2007). Breakdown of methylene blue and methyl orange by pulsed corona discharge. *Plasma Sources Science and. Technology.* 16, 226-232.

Gupta, S.B. (2007). Investigation of a Physical Disinfection Process Based on Pulsed Underwater Corona Discharges. Unpublished PhD thesis submitted to Forschungszentrum Karlsruhe, Institute for Pulsed Power and Microwave Technology (IHM), Karlsruhe, Germany

Gupta, S.M. and Tripathi, M. (2012). A review on the synthesis of TiO_2 nanoparticles by solution route. *Cen. Eur. J. Chem,* 10(2): 279-294

Habibi, S., Fatemi, S., Izadyar, S. and Mousavand, T. (2012). TiO_2 nanoparticle layer formation on ceramic support, a statistical approach to control influential synthesis parameters. *Powder Technology,* 229:51-60

Han, C., Luque, R. and Dionysiou, D.D. (2012). Facile preparation of controllable size monodisperse anatase titania nanoparticles. *Chem. Commun*, 48, 1860-1862.

Hänel, A., Moreń, P., Zaleska, A. and Hupka, J. (2010). Photocatalytic activity of TiO_2 immobilized on glass beads. *Physicochemical Problem of Mineral Processing*, 45: 49-56

He, F., Ma, F., Li, J., Li, T. and Li, G. (2014). Effect of calcination temperature on the structural properties and photocatalytic activities of solvothermal synthesized TiO_2 hollow nanoparticles. *Ceramic International*, 40: 6441-6446

Hedayati, M.K., Faupel, F., Elbahri, M. (2014). Review of Plasmonic Nanocomposite Metamaterial Absorber. *Mater.* 7 1221-1248

Hen D.H., Huang, F.Z., Cao, L., Cheng Y.B. and Caruso, R.A. (2012). Spiky mesoporous anatase titania beads: A metastable ammonium titanate-mediated synthesis. *Chem. Eur. J*. 18: 13762-13769.

Hintsho, Nomso, Petrik, Leslie, Alexander Nechaev, Salam Titinchi, and Patrick Ndungu (2014). Photo-catalytic activity of titanium dioxide carbon nanotube nano-composites modified with silver and palladium nanoparticles. *Applied CatalysisB:Environmental*, 156-157: 273-283

Hoeben, W.F.L.M., van Veldhuizen, E.M., Classens, H.A. and Rutgers, W.R. (1997). Degradation of Phenol and Atrizine in Water by Pulsed Corona Discharges. 13th International Symposium on Plasma Chemistry, August 18-22, Beijing, China.

Houtman, C.J. (2010). Emerging contaminants in surface waters and their relevance for the production of drinking water in Europe. *Journal of Integrative Environmental Sciences,* 7(4), 271-295.

Huang, H.H., Lu, M.C. and Chen, J.N. (2001). Catalytic decomposition of hydrogen peroxide and 2-chlorophenol with iron oxides, *Water Res*. 35:2291-2299.

Huang, X., El-Sayed, M.A. (2010). Gold nanoparticles: Optical properties and implementations in cancer diagnosis and photothermal therapy, J. Adv. Res. 1 13-28.

Huang, Y.Q., Wong, C.K.C., Zheng, J.S., Bouwman, H., Barra, R., Wahlström, B., Neretin, L. and Wong, M.H. (2012). Bisphenol A (bisphenol A) in China: a review of sources, environmental levels, and potential human health impacts. *Environmental. International.* 42: 91-99

Hughes, S.R., Kay, P., Brown, L.E. (2013). Global synthesis and critical evaluation of pharmaceutical data sets collected from river systems. *Environmental Science and Technology,* 47: 661-677

Hussain, S., Shaikh, S. and Farooqui, M. (2013). COD reduction of waste water streams of active pharmaceutical ingredient – Atenolol manufacturing unit by advanced oxidation-Fenton process. *Journal of Saudi Chemical Society,* 17: 199-202

Ismail, A.A. and Bahnemann, D.W. (2011). Mesoporous titania photocatalysts: Preparation, characterization and reaction mechanisms. *J. Mater. Chem*. 2011, 21, 11686-11707.

Ismail, A.A., Bahnemann, D.W., Robben, L., Yarovyi, V. and Wark, M. (2010). Palladium doped porous titania photocatalysts: Impact of mesoporous order and crystallinity. *Chem. Mat.* 22: 108-116.

Jackson, J., Sutton, R. (2008). Sources of endocrine disrupting chemicals in urban wastewater, Oakland, CA. *Science of The Total Environment,* 405, 153-160

Jagadale, T.C., Takale, S.P., Sonawane, R.S., Joshi, H.M., Patil, S.I., Kale, B.B., Ogale, S.B. (2008). N-doped TiO_2 nanoparticle based visible light photocatalyst by modified peroxide sol-gel method. *Journal Phys. Chem.*, 14596-14602

Jen, J.F., Leu, M.F. and Yang, T.C. (1998). Determination of hydroxyl radicals in an advanced oxidation process with salicylic acid trapping and liquid chromatography. *Journal of Chromatography A,* 796: 283-288

Jia, C., Wang, Y., Zhang, C., Kong, S., Qin, Q. and Yao, S.K. (2012). Photocatalytic Degradation of Bisphenol A in Aqueous Suspensions of Titanium Dioxide. *Environmental Engineering Science*, 29(7): 630-637

Jiang, B., Qiu, J.Z.S., Mingbo, W., Yan, Q.Z.Z. and Xue, Q. (2014). Review on electrical discharge plasma technology for wastewater remediation. *Chemical Engineering Journal*, 236,348-368.

Jiang, J.Q., Zhou, Z., Sharma, V.K. (2013). Occurrence, transportation, monitoring and treatment of emerging micro-pollutants in waste water – A review from global views. *Microchemical Journal,* 110: 292-300

Jin, L. and Dai, B. (2012). TiO_2 activation using acid-treated vermiculite as a support: Characteristics and photoreactivity. *Appl. Surf. Sci*. 258: 3386-3392.

Jo, J.O. and Mok, Y.S. (2009). In-situ production of ozone and ultraviolet light using a barrier discharge reactor for wastewater treatment. *Journal of Zhejiang University Science A,* 10(9):1359-1366

Joo, J.B., Zhang, Q., Dahl, M., Lee, I., Goebl, J., Zaera, F. and Yin, Y.D. (2012). Control of the nanoscale crystallinity in mesoporous TiO_2 shells for enhanced photocatalytic activity. *Energy. Environ. Sci*. 5: 6321-6327

Kanakaraju, D,. Glass, B.D., Oelgemoller, M. (2014). Titanium dioxide photocatalysis for pharmaceutical wastewater treatment. *Environmental Chemistry Letter,* 12:27-47

Karami, A. (2010). Synthesis of TiO_2 nano powder by the sol-gel method and its use as a photocatalyst. *Journal of Iran Chemical Society*, 7: S154-S160

Kasiri, M.B., Aleboyeh, H. and Aleboyeh, A. (2008). Degradation of Acid Blue 74 using Fe-ZSM5 Zeolite as a heterogeneous photo-Fenton catalyst, *Appl. Catal.* B 84: 9-15.

Kasprzyk-Hordern. B., Dinsdale, R.M., Guwy, A.J. (2009). The removal of pharmaceuticals, personal cares products, endocrine disruptors and illicit drugs during wastewater treatment and its impact on the quality of receiving waters. *Water Research,* 43(2): 363-380

Kathryn, M., Onesios, A.E., Jim, T., Yu, A.E. and Bouwer, E.J. (2009). Biodegradation and removal of pharmaceuticals and personal care products in treatment systems: a review. *Biodegradation*, 20,441-466.

Kavitha, M., Gopinathan, C and Pandi, P. (2013). Synthesis and characterization of TiO_2 Nanopowders in hydrothermal and sol-gel method. *International Journal of Advancement in Research and Technology*, 2(4): 102-108

Kavitha, V. and Palanivelu, K. (2005). Degradation of nitrophenols by Fenton and photo-Fenton processes. *Journal of Photochemistry and Photobiology A: Chemistry,* 170: 83-95

Keller, A.A., Garner, K., Miller, R.J. and Lenihan, H.S. (2012). Toxicity of Nano-Zero Valent Iron to Freshwater and Marine Organisms. *PLOS ONE* 7(8): e43983.doi:10.1371/journal.pone.0043983

Khan, M.M., Ansari, S.A., Amal, M.I., Lee, J. and Cho, M.H. (2013). Highly visible light active Ag@TiO_2 nanocomposites synthesized using an electrochemically active biofilm: a novel biogenic approach. *Nanoscale*, 5: 4427-4435.

Kirkpatrick, M. and Locke, B.R. (2005). Hydrogen, Oxygen, and Hydrogen Peroxide Formation in Electrohydraulic Discharge. I*ndustrial and Engineering Chemistry Research,* 44: 4243-4248

Klauson, D., Babkina, J., Stepanova, K., Krichevskaya, M., Preis, S. (2010).Aqueous photocatalytic oxidation of amoxicillin. *Catal. Today,* 151: 39-45.

Klavarioti, M., Mantzavinos, D. & Kassinos, D. (2009). Removal of residual pharmaceuticals from aqueous systems by advanced oxidation processes. *Environment International*, 35:402-417.

Kleiman-Shwarsctein, A., Hu, Y.S., Forman, A.J., Stucky, G.D. and McFarland, E. (2008). Electrodeposition of α-Fe_2O_3 doped with Mo or Cr as photoanodes for photocatalytic water splitting. *J. Phys. Chem. C,* 112, 15900-15907

Kleywegt, S., Pileggi, V., Yang, P., Hao, C., Zhao, X., Rocks, C., Thach, S., Cheung, P., Whitehead, B. (2011). Pharmaceuticals, hormones and bisphenol-A in untreated source and finished drinking water in Ontario, Canada – Occurrence and treatment efficiency. *Science of the Total Environment,* 409: 1481-1488

Kostedt, W.L., Ismail, A.A. and Mazyck, D.W. (2008). Impact of Heat Treatment and Composition of ZnO-TiO_2 Nanoparticles for Photocatalytic Oxidation of an Azo Dye. *Ind. Eng. Chem. Res*, 47:1483-1487.

Krause, H., Schweiger, B., Schuhmacher, J., Scholl, S. and Steinfeld, U. (2009). Degradation of the endocrine disrupting chemicals (EDCs) carbamazepine, clofibric acid, and isopromide by corona discharge over water. *Chemosphere*, 75(2):163-168.

Kümmerer, K. (2011). Emerging Contaminants versus Micro-pollutants. *Clean – Soil, Air, Water*, 39 (10), 889-890

Lee, J., Park, H. and Yoon, J. (2003). Ozonation characteristics of bisphenol-A in water. *Environmental Technology*, 24(2): 241-248

Lee, S.Y. and Park, S.J. (2013). TiO_2 photocatalyst for water treatment applications: Review. *Journal of Industrial and Engineering Chemistry* (Article in press) http://dx.doi.org/10.1016/j.jiec.2013.07.012

Lei, L.C., Zhang, Y., Zhang, X.W., Du, Y.X., Dai, Q.Z. and Han, S. (2007). Degradation performance of 4-chlorophenol as a typical organic pollutant by a pulsed high voltage discharge system. *Industrial and Engineering Chemistry Research,* 46: 5469-5477.

Leong, K.H., Monash, P., Ibrahim, S. and Saravanan, P. (2014). Solar photocatalytic activity of anatase TiO_2 nanocrystals synthesised by non-hydrolitic sol-gel method. *Solar Energy*, 101: 321-332

Lesage, O., Falk, L., Tatoulian, M., Mantovani, D. and Ognier, S. (2013). Treatment of 4-chlorobenzoic acid by plasma-based advanced oxidation processes. *Chemical Engineering and Processing: Process Intensification,* 72: 82-89

Li, J., Zhou, Z., Wang, H., Li, G. & Yan, W. (2007). Research on decoloration of dye wastewater by combination of pulsed discharge plasma and TiO_2 nanoparticles. *Desalination*, 212,123-128.

Li, S., Ma, X., Jiang, Y. and Cao, X. (2014). Acetamiprid removal in wastewater by the low-temperature plasma using dielectric barrier discharge. *Ecotoxicology and Environmental Safety* 106:146-153

Li., X.B., Qianfeng Liu, XiaoYing Jiang, Jianhua Huang. (2012). Enhanced Photocatalytic Activity of Ga-N Co-doped Anatase TiO_2 for Water Decomposition to Hydrogen. *Int. J. Electrochem. Sci.,* 7:11519-11527

Liu, Y., Mei, S., Iya-Sou, D., Cavadias, S. and Ognier, S. (2012). Carbamazepine removal from water by dielectric barrier discharge: Comparison of ex situ and in situ discharge on water. *Chemical Engineering and Processing*, 56: 10-18

Locke, B.R., Sato, M., Sunka, P., Hoffmann, M.R., and Chang, J.S. (2006). Electrohydraulic discharge and non-thermal plasma for water treatment. *Industrial and Engineering Chemistry Research*, 45(3), 882-905.

Luiz, D.B., Genena, A.K., José, H.J., Moreira, R.F. and Schröder, H.F. (2009). Tertiary treatment of slaughterhouse effluent: degradation kinetics applying UV radiation or H_2O_2/UV. *Water Science and Technology*, 60(7):1869-1874

Magureanu, M., Bogdan, N., Piroi, D., Mandche, N.B., and Parvulescu, V. (2013). Pulsed Corona Discharge for Degradation of Methylene Blue in Water. *Plasma Chemistry and Plasma Processing,* 33: 51-64

Magureanu, M., Piroi, D., Mandache, N.B., David, V., Medvedovici, A. and Parvulescu, V.I. (2010). Degradation of pharmaceutical compound pentoxifylline in water by non-thermal plasma treatment. *Water Research,* 44: 3445-3453

Magureanu, M., Piroi, D., Mandache, N.B., David, V., Medvedovici, A., Parvulescu, V.I. and Bradu, C. (2011). Degradation of antibiotics in water by non-thermal plasma treatment. *Water Research*, 45: 3407-3416

Maletz, S., Floehr, T., Beier, S., Klumper, C., Brouwer, A., Behnisch, P., Higley, E., Giesy, J.P., Hecker, M., Gebhardt, L.V., Pinnekamp, J. and Hollert, H. (2013). In vitro characterization of the effectiveness of enhanced sewage treatment processes to eliminate endocrine activity of hospital effluents. *Water Research,* 47,1545-1557.

Malik, M.A. (2010). Water purification by plasmas: which reactors are most energy efficient? *Plasma Chemistry and Plasma Processing,* 30,21-31.

Manickum, T. and John, W. (2014). Occurrence, fate and environmental risk assessment of endocrine disrupting compounds at the wastewater treatment works in Pietermaritzburg (South Africa). *Science of the Total Environment*, 468-469: 584-597

Manoj, A., Lazar., Shaji Varghese and Santhosh S. Nair (2012). Photocatalytic Water Treatment by Titanium Dioxide: Recent Updates. *Catalysts*, 2: 572-601

Manoj Kumar Reddy, P. and Subrahmanyam, C. (2012). Green Approach for Wastewater Treatment – Degradation and Mineralization of Aqueous Organic Pollutants by Discharge Plasma. *Industrial Engineering and Chemical Research,* 51: 11097-11103

Marcoux, M.A., Matias, M., Olivier, F., Keck, G. (2013). Review and prospect of emerging contaminants in waste – Key issues and challenges linked to their presence in wastewater treatment schemes: General aspects and focus on nanoparticles. *Waste Management*, 33: 2147-2156.

Matongo, S., Birungi, G., Moodley, B., Ndungu, P. (2015). Occurrence of selected pharmaceuticals in water and sediment of Umgeni River, KwaZulu-Natal, South Africa. *Environmental Science and Pollution Research,* 22(13):10298-308

Michałowicz, J. (2014). Bisphenol A – Sources, toxicity and biotransformation. *Environmental Toxicology and Pharmacology*, 37: 738-758

Monreal, H.A., Chacon-Nava., Arce-Colunga, U., Martinez, C.A., Casillas, P.G., Martınez-Villafane, A. (2009). Sol-gel preparation of titanium dioxidenanoparticles in presence of a linear polysaccharide. *Micro and Nano Letters.,* 4(4): 187-191

Mouele, E.S.M. (2014). Water treatment using electrohydraulic discharge system. Unpublished MSc thesis to the Department of Chemistry, University of the Western Cape, South Africa. Pp. 63-66

Nainani, R., Thakur, P. and Chaskar, M. (2012). Synthesis of Silver Doped TiO_2 Nanoparticles for the improved Photocatalytic Degradation of Methyl Orange. *Journal of Materials Science and Engineering B*, 2 (1): 52-58

Nakada, K. and Fujishima, A. (2012). TiO_2 photocatalysis: Design and applications. *J. Photochem. Photobiol. C* 13: 169-189.

Nam, H.-J., Amemiya, T., Murabayashi, M. and Itoh, K. (2004). Photocatalytic activity of sol-gel TiO_2 thin films on various kinds of glass substrates: the effects of Na+ and primary particle size, *The Journal of Physical Chemistry B*, 108, 8254-8259

Ochuma, I.J., Fishwick, R.P., Wood, J., Winterbottom, J.M. (2007). Optimisation of degradation conditions of 1,8-diazabicyclo[5. 4.0]undec-7-ene in water and reaction kinetics analysis using a co-current downflow contactor photocatalytic reactor. *Appl. Catal. B: Environ*. 73, 259-268.

Oller, I., Malato, S. and Sánchez-Pérez, J.A. (2011). Combination of Advanced Oxidation Processes and biological treatments for wastewater decontamination – A review. *Science of the Total Environment*, 409 (20), 4141-4166

Olujimi, O.O., Fatoki, O.S., Odendaal, J.P., Daso, A.P. (2012). Chemical monitoring and temporal variation in levels of endocrine disrupting chemicals (priority phenols and phthalate esters) from selected wastewater treatment plant and freshwater systems in Republic of South Africa. *Microchemical Journal,* 101: 11-23

Olujimi, O.O., Fatoki, O.S., Odendaal, J.P. and Okonkwo, J.O. (2010). Endocrine disrupting chemicals (phenol and phthalates) in the South African environment: A need for more monitoring. Review. *Water SA*, 36(5), 671-682.

Padhye, L.P., Yao, H., Kung'u, F.T., Huang, C.H. (2014). Year-long evaluation on the occurrence and fate of pharmaceuticals, personal care products, and endocrine disrupting chemicals in an urban drinking water treatment plant. *Water Research*, 51: 266-276.

Palominos, R., Freer, J., Mondaca, M.A., Mansilla, H.D. (2008). Evidence for hole participation during photocatalytic oxidation of the antibiotic flumequine. *J. Photochem. Photobiol.* A 193: 139-145

Pan, J.H., Dou H.Q., Xiong, Z.G., Xu, C., Ma, J.Z. and Zhao, X.S. (2010). Porous photocatalysts for advanced water purifications. *J. Mater. Chem*. 20: 4512-4528.

Pardeshi, S.K. and Patil, A.B. (2009). Effect of morphology and crystallite size on solar photocatalytic activity of zinc oxide synthesized by solution free mechanochemical method. *Journal of Molecular Catalysis A: Chemical,* 308: 32-40

Pomiès, M., Choubert, J-M., Wisniewski, C., Coquery, M. (2013). Modelling of micropollutant removal in biological wastewater treatments: A review. *Science of the Total Environment* 443: 733-748

Qu, G., Liang, D., Qu, D., Huang, Y., Liu, T., Mao, H., Ji, P. and Huang, D. (2013). Simultaneous removal of cadmium ions and phenol from water solution by pulsed corona discharge plasma combined with activated carbon, *Chemical Engineering Journal*, 228:28-35

Quiroz, M., Sánchez-Salas, J.L., Reyna, S., Bandala, E.R., Peralta-Hernández, J.M. and Martínez-Huitle, C.A. (2014). Degradation of 1-hydroxy-2,4-dinitrobenzene from aqueous solutions by electrochemical oxidation: Role of anodic material. *Journal of Hazardous Materials,* 268: 6-13

Rahman, M.F., Yanful, E.K. and Jasim, S.Y. (2009). Occurrences of endocrine disrupting compounds and pharmaceuticals in the aquatic environment and their removal from drinking water: Challenges in the context of the developing world. *Desalination*, 248: 578-585

Ribeiro, R.S., Silva, A.M.T., Figueiredo, J.L, Faria, J.L. and Gomes, H.T. (2013).Removal of 2-nitrophenol by catalytic wet peroxide oxidation using carbon Materials with different morphological and chemical properties. *Applied Catalysis B: Environmental*, 140-141: 356-362

Richardson, S.D. (2008). Environmental mass spectrometry: emerging contaminants and current issues. *Anal. Chem.* 80: 4373-4402

Richardson, S.D. and Ternes, T.A. (2011). Water analysis: emerging contaminants and current issues. *Analytical Chemistry,* 83 (12): 4614-4648.

Rivera-Utrilla, J., Sánchez-Polo, M., Ferro-García, M.A., Prados-Joya, G., Ocampo-Pérez, R. (2014). Pharmaceuticals as emerging contaminants and their removal from water. A review: *Chemosphere,* 93: 1268-1287

Robben, L., Ismail, A.A., Lohmeier, S.J., Feldhoff, A., Bahnemann, D.W. and Buhl, J.C. (2012). Facile synthesis of highly ordered mesoporous and well crystalline TiO_2: Impact of different gas atmosphere and calcination temperatures on structural properties*. Chem. Mat*., 24:1268-1275.

Rocha, S., Domingues, V.F., Fernandes, V.C., Gameiro, P., Pinho, C., Delerue-Matos, C., and Mansilha, C. (2013). Occurrence of Bisphenol A, Estrone, 17b-Estradiol and 17a-Ethinylestradiol in Portuguese Rivers. *Bulletin Environmental Contamination and Toxicology,* 90:73-78

Rogers, J.A., Metz, L. and Wee Yong, V. (2013). Review: Endocrine disrupting chemicals and immune responses: A focus on bisphenol-A and its potential mechanisms. *Molecular Immunology*, 53:421-430.

Rong, S. and Sun, Y. (2013). Wetted-wall corona discharge induced degradation of sulfadiazine antibiotics in aqueous solution. *Journal of Chemistry Technology and Biotechnology*, 89: 1351-1359

Rong, S.P., Sun, Y.B. and Zhao, Z.H. (2014). Degradation of sulfadiazine antibiotics by water falling film dielectric barrier discharge. *Chinese Chemical Letters*, 25: 187-192

Saggioro, E.M., Oliveira, A.S., Pavesi, T., Maia, C.G., Ferreira, L.F.V., Moreira, J.C. (2011). Use of Titanium Dioxide Photocatalysis in the Remediation of Model Textile Wastewaters Containing Azo Dyes, *Molecules.* 16:10370-10386

Sahni, M. and Locke, B.R. (2006). Quantification of Hydroxyl Radicals Produced in Aqueous Phase Pulsed Electrical Discharge Reactors. *Industrial Engineering and Chemical Research,* 45: 5819-5825

Santiago, E., Bila, D.M., Krause, L.G.T. and Dezotti, M. (2007). Ozonation and advanced oxidation technologies to remove endocrine disrupting chemicals (EDCs) and pharmaceutical and personal care products (PPCPs) in water effluent. *Journal of Hazardous Materials*, 149,631-642.

Scott, J.P. and Ollis, D.F. (1995). Integration of chemical and biological oxidation processes for water treatment: review and recommendations. *Environmental Progress*, 14(2), 88-103.

Shannon, M.A., Bohn, P.W., Elimelech, M., Georgiadis, J.G., Mariñas, B.J. & Mayes, A.M. (2008). Science and technology for water purification in the coming decades*. Nature*, 452(20), 301-310.

Sharma, H.S. and Sharma, A. (2007). Nanoparticles aggravate heat stress induced cognitive deficits, blood-brain barrier disruption, endema formation and brain pathology. *Prog. Brain Res.* 162:245-273

Sharma, S., Ruparelia, J.P. and Patel, M.L. (2011). A general review on advanced oxidation processes for waste water treatment. Paper presented at the Institute of Technology, Nirma University, Ahmedabad, 382-481, 08-10

Sheikhnejad-Bishe, O., Zhao, F., Rajabtabar-Darvishi, A., Khodadad, E, Mostofizadeh, A. and Huang, Y. (2014). Influence of temperature and surfactant on the photocatalytic performance of TiO_2 Nanoparticles. *Int. J. Electrochem. Sci.*, 9: 4230-4240

Shen, C, Wang, Y.J., Xu, J.H. and Luo, G.S. (2012). Facile synthesis and photocatalytic properties of TiO_2 nanoparticles supported on porous glass beads. *Chemical Engineering Journal,* 209: 478-485

Sobana, N., Muruganadham, M., Swaminathan, M. (2006). Nano-Ag particles doped TiO_2 for efficient photodegradation of direct azo dyes. *Journal of Molecular Catalysis A: Chemical*, 258, 124-132.

Stanford, B.D., Trenholm, R.A., Holady, J.C., Vanderford, B.J., Synder, S.A. (2010). Estrogenic activity of US drinking waters: a relative exposure comparison. *Journal of the American Water Works Association,* 110(11): 55-65

Stasinakis, A.S. (2008). Use of selected advanced oxidation processes (AOPS) for wastewater treatment – a mini review. *Global NEST Journal,* 10(3), 376-385

Strauch, K.A. (2011). Invisible pollution: The impact of pharmaceuticals in the water supply. *AAOHN Journal,* 59(12): 525-532

Stuart, M., Lapworth, D., Crane, E., Hart, A. (2012). Review of risk from potential emerging contaminants in UK groundwater. *Science of the Total Environment*, 416: 1-21

Subrahmanyam, A., Biju, K.P., Rajesh, P., Jagadeesh Kumar, K., Raveendra Kiran, M. (2012). Surface modification of sol gel TiO_2 surface with sputtered metallic silver for sun light photocatalytic activity: Initial studies. *Solar Energy Materials and Solar Cells*, 101: 241-248

Suwanchawalit, C., Chanhom, P., Sriprang, P., Wongnawa, S. (2011). Ag-Doped TiO_2 photocatalyst for dye decolorization under UV. *Pure and Applied Chemistry International conference*, pp.375-405

Suwarnkar, M.B., Dhabbe, R.S., Kadam, A.N., Garadkar, K.M. (2014). Enhanced photocatalytic activity of Ag doped TiO_2 nanoparticles synthesized by a microwave assisted method. *Ceramic International* 40(4): 5489-5496

Tahara, M. and Okubo, M. (2012). Detection of Free Radicals Produced by a Pulsed Streamer Corona Discharge in Solution Using Electron Spin Resonance. Proceeding 2012 Joint Electrostatics Conference held on June 12-14, 2012 at Cambridge, ON, Canada. Pp.1-12

Tai, C., Peng, J.F., Liu, J.F., Jiang, G.B. and Zou, H. (2004). Determination of hydroxyl radicals in advanced oxidation processes with dimethyl sulfoxide trapping and liquid chromatography. *Analytica Chimica Acta,* 527: 73-80

Tang, S., Lu, N., Li, J., Shang, K. and Wu, Y. (2013). Improved phenol decomposition and simultaneous regeneration of granular activated carbon by the addition of a titanium dioxide catalyst under a dielectric barrier discharge plasma. *Carbon*, 53: 380-390

Tay, K.S., Abd.Rahman, N. and Radzi Bin Abas, M. (2013). Degradation of bisphenol A by ozonation: rate constants, influence of inorganic anions, and by-products. *Maejo International Journal of Science and Technology,* 6(01): 77-94

Teoh, W.Y., Amal, R. and Scott, J. (2012).Progress in heterogenous photocatalysis: From classical radical chemistry to engineering nanomaterials and solar reactors. *J. Phys. Chem. Lett*. 3, 629-639

Teppala, S., Madhavan, S. and Shankar, A. (2012). Bisphenol A and metabolic syndrome: results from NHANES., http://dx.doi.org/10. 1155/2012/598180.

Topp, E., Monteiro, S.C., Beck, A., Coelho, B.B., Boxall, A.B.A., Duenk, P.W., Kleywegt, S., Lapen, D.R., Payne, M., Sabourin, L., Li, H.X., Metcalfe, C.D. (2008). Runoff of pharmaceuticals and personal care products following application of biosolids to an agricultural field. *Science of the Total Environment,* 396: 52-59

Tryba, B., Piszcz, M., Morawski, A.W. (2009). Photocatalytic activity of TiO_2-WO composites. *International Journal of Photoenergy,* Article ID 297319, 7.

Tsai, W.T., Leeb, M.K., Suc, T.Y. and Yuan, M.C. (2009). Photodegradation of bisphenol-A in a batch TiO_2 suspension reactor. *Journal of Hazardous Materials*, 168,269-275.

Tsoi, K.M., Dai, Q., Alman, B.A., Chan, W.C. (2013). Are quantum dots toxic? Exploring the discrepancy between cell culture and animal studies. *Acc Chem Res*. 46(3):662-71

UN Millennium Project (2005). “Innovation: Applying Knowledge in Development,” Task Force on Science, Technology, and Innovation, http://www.unmillenniumproject.org/ reports/reports2.htm

UN/FAO (2007). Water scarcity. Challenge of the twenty-first century. Pp 1

UNDP (2006). Human Development Report 2006.

US Environmental Protection Agency (2007). Memorandum to EDSTAC Members RE: Definition of "Endocrine Disruptor". Washington D.C., USA

USEPA (2010). Bisphenol-A Action Plan. Washington D.C., USA. (CASRN 80-05-7) CA Index Name: Phenol, 4,4′- (1-methylethylidene) bis-. 2010-3-29

USGS (US Geological Survey) (2014). Emerging Contaminants In the Environment: Accessed October 2014. http://toxics.usgs.gov/regional/emc/

Van Doorslaer, X., Dewulf, J., Van Langenhove, H., Demeestere, K. (2014). Fluoroquinolone antibiotics: An emerging class of environmental micropollutants. Science of the Total Environment, 500-501: 250-269

Wahyudiono, S., Machmudah, and Goto, M. (2013). Pulsed discharge plasma over a water surface induces decoloration of dyes. *Journal of Physics: Conference Series* 441: 012008

Wang, C., Shi, H. and Li, Y. (2015). Synthesis and characterization of natural zeolite supported Cr-doped TiO_2 photocatalysts. *Applied Surface Science*, 258: 4328-4333

Wang, H., Chu, J., Ou, H., Zhao, R. and Han, J. (2009). Analysis of TiO_2 photocatalysis in a pulsed discharge system for phenol degradation. *Journal of Electrostatic,* 67: 886-889.

Wang, H., Li, J., Quan, X. and Wu, Y. (2008). Enhanced generation of oxidative species and phenol degradation in a discharge plasma system coupled with TiO_2 photocatalysis. *Applied Catalysis B: Environmental*, 83:72-77

Wang, H., Li, J., Quan, X., Wu, Y., Li, G. and Wang, F. (2007). Formation of hydrogen peroxide and degradation of phenol in synergistic system of pulsed corona discharge combined with TiO_2 photocatalysis. *Journal of Hazardous Materials,* 141: 336-343

Wang, H., Niu, J., Long, X. and He, Y. (2008). Sonophotocatalytic degradation of methyl orange by nano-sized Ag/TiO_2 particles in aqueous solutions. *Ultrasonics Sonochemistry*, 15: 386-392

Wang, T., Li, M., Chen, B., Xu, M. and Xu. Y. (2012). Urinary Bisphenol A (BPA) Concentration Associates with Obesity and Insulin Resistance. *Journal of Clinical Endocrinology Metabolism*, 97: E223-E227.

Wang, W., Lu, C., Ni, Y., Peng, F. and Xu, Z. (2012). Enhanced performance of {001} facets dominated mesoporous TiO_2 photocatalyst composed of high-reactive nanocrystals and mesoporous spheres. *Appl. Surf. Sci.*doi:10.1016/j.apsusc.2012.11.025.

Wankhade, A.V., Gaikwad, G.S., Dhonde, M.G., Khaty, N.T. and Thakare, S.R (2013). Removal of Organic Pollutant from Water by Heterogenous Photocatalysis: A Review. *Research Journal of Chemistry and Environment,* 17 (1): 84-94

Wei, L., Shifu. C., Wei, Z. and Sujuan, Z. (2009). Titanium dioxide mediated photocatalytic degradation of methamidophos in aqueous phase. *Journal of Hazardous Materials*, 164: 154-160

Wei, L., Zhu, H., Mao, H. and Gan, F. (2011). Electrochemical oxidation process combined with UV photolysis for the mineralization of nitrophenol in saline wastewater. *Separation and Purification Technology,* 77:18-25

Wei, T.Y., Yang, Y.Y., Wan C.C. (1992). Kinetics of photo-catalytic oxidation of phenol on TiO_2 surface, *J. Photochem. Photobiol., A.* 69: 241-249.

Weir, A., Westerhoff, P., Fabricus, L., Hristovski, K. and Von Goetz, N. (2012). Titanium dioxide nanoparticles in food and personal care products. *Environ. Sci. Technol*. 46, 2242-2250.

Whang, T.J., Hsieh, M.T., Shi, T.E. and Kuei, C.H. (2012). UV-Irradiated Photocatalytic Degradation of Nitrobenzene by Titania Binding on Quartz Tube. *International Journal of Photoenergy*. Article ID 681941, 8 pages

WHO (2011). Pharmaceuticals in drinking-water. Report No.: WHO/HSE/WSH/11.05. Geneva, Switzerland: World Health Organization; 2011 [Available from: http://www.who.int/water_sanitation_health/publications/2011/pharmaceuticals_20110601.pdf].

WHO/UNEP. (2013). State of the science of endocrine disrupting chemicals – 2012. An assessment of the state of the science of endocrine disruptors prepared by a group of experts for the United Nations Environment Programme (UNEP) and WHO. Accessed at http://www.who.int/ceh/publications/endocrine/en/

Wu, R., Chena, C., Chen, M., Lu, C. (2009).Titanium dioxide-mediated heterogeneous photocatalytic degradation of terbufos: Parameter study and reaction pathways. *Journal of Hazardous Materials*, 162: 945-953

Yan, Q., Gao, X., Huang, L., Gan, X.M., Zhang, Y.X., Chen, Y.P., Peng, X.Y., Guo, J.S. (2014). Occurrence and fate of pharmaceutically active compounds in the largest municipal wastewater treatment plant in Southwest China: Mass balance analysis and consumption back-calculated model. *Chemosphere,* 99: 160-170

Yang, H., Ke, Z., Rongrong, S., Xianwei, L., Xiaodan, D. and Yongmei, Y. (2006). Sol-gel synthesis of TiO_2 Nanoparticles and photocatalytic degradation of methyl orange in aqueous TiO_2 suspensions. *Journal of Alloys and Compounds*, 413, 302-306.

Yang, Y., Wang, H., Li, J., Benqiao He, Tonghua Wang, and Shijun Liao. (2012). Novel Functionalized Nano-TiO_2 Loading Electrocatalytic Membrane for Oily Wastewater Treatment. *Environ. Sci. Technol.,* 46: 6815−6821

Yeh, C.K.J., Chen, W.S. and Chen, W.Y. (2004). Production of hydroxyl radicals from the decomposition of hydrogen peroxide catalyzed by various iron oxides at pH 7, Pract. Period Hazard. Toxic. Radioact. *Waste Manage*. 8:161-165.

Zhang, J., Liu, D., Bian, W. & Chen, X. (2012). Degradation of 2, 4-dichorophenol by pulsed high voltage discharge in water. *Desalination,* 304:49-56

Zhang, W., Xiao, X., An, T., Song, Z., Fu, J., Sheng, G. and Cui, M. (2003). Kinetics, degradation pathway and reaction mechanism of advanced oxidation of 4-nitrophenol in water by a UV/H_2O_2 process. *Journal of Chemistry Technology Biotechnol*ogy, 78:788-794

Zhang, Y., Xin, Q., Cong, Y., Wang, Q. and Jiang, B. (2013). Application of TiO_2 nanotubes with pulsed plasma for phenol degradation. *Chemical Engineering Journal*, 215-216: 261-268

Zhang, Y., Xu, H. and Xin, Q. (2012). Enhanced Phenol Degradation by Pulsed Plasma Cooperated with TiO_2 Nanotubes Film. *2012 Asia Pacific Conference on Environmental Science and Technology, Advances in Biomedical Engineering*, 6: 376-379

Zhang, Y., Zhang, R., Ma, W., Zhang, X., Wang, L. and Guan, Z. (2013). Purification of water by bipolar pulsed discharge plasma combined with TiO_2 catalysis. J*ournal of Physics: Conference Series,* 418, 121-25

Zhang, Y. and Zhou, J.L. (2008). Occurrence and removal of endocrine disrupting chemicals in wastewater treatment I: Oxidation technologies at ambient conditions, *Adv. Environ. Res.,* 8:501-551.

Zhao, Z., Sun, Z.C., Zhao, H.F., Zheng M., Du, P., Zhao, J.L. and Fan, H.Y. (2012). Phase control of hierarchically structured mesoporous anatase TiO_2 microspheres covered with {001} facets*. J. Mater. Chem*., 22: 21965-21971.

Zhao, D., Wang, J., Zhang, Z., Zhao, X., Zhang, J. (2009). TiO_2 /NaY composite as photocatalyst for degradation of omethoate. *Chem.Res.Chinese Universities*, 25(4): 543-549

Zheng, J.M., Song, G., Kim, C.W., Kang, Y.S. (2014). One-step transformation of Cu to Cu2O in alkaline solution, *RSC Adv.* 4: 18616.

Zhu, B. and Zou, L. (2009). Trapping and decomposing of colour compounds from recycled water by TiO_2 coated activated carbon. *J. Environ. Manag*. 90: 3217-3225.

Zhu, J., Yang, D., Geng, J., Chen, D. and Jiang, Z. (2008). Synthesis and characterization of bamboo-like CdS/TiO_2 nanotubes composites with enhanced visible-light photocatalytic activity. *Journal Nanoparticle Research,* 10,729.

Zhu, L., Wang, Y., Ren, Z., Liu, G. & Kang, K. (2013). The degradation of organic pollutants by bubble discharge in water. *Plasma Science and Technology*, 15(10), 1053-1058.

Zhu, X., Yuan, C., Bao, Y., Yang, J. and Wu, Y. (2005). Photocatalytic degradation of pesticide pyridaben on TiO_2 particles. *Journal of Molecular Catalysis: Chemical*, 229: 95-105

Ziv-Gal, A., Zelieann, C., Wang, W. and Flaws, J. (2013). Bisphenol A inhibits cultured mouse ovarian follicle growth partially via the aryl hydrocarbon receptor signaling pathway. *Reproductive Toxicology*. 42: 58-67.